UNIVERSITY OF SOUTHAMPTON

FACULTY OF ENGINEERING, SCIENCE AND MATHEMATICS

School of Chemistry

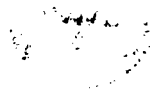

Controlled Surface Modification of Supported Platinum Group Metal Catalysts

by

Peter Philip Wells

Thesis for the degree of Doctor of Philosophy

March 2007

And when I finished the painting & looked at that poor leatherjacket which now lay dead on the table I began to wonder whether, as each fish died, the world was reduced in the amount of love that you might know for such a creature. Whether there was that much less wonder & beauty left to go around as each fish was hauled up in the net. And if we kept on taking & plundering & killing, if the world kept on becoming ever more impoverished of love & wonder & beauty in consequence, what, in the end, would be left?

It began to worry me, you see, this destruction of fish, this attrition of love that we were blindly bringing about, & I imagined a world of the future as a barren sameness in which everyone had gorged so much fish that no more remained, & where Science knew absolutely every species & phylum & genus, but no-one knew love because it had disappeared along with the fish.

Life is a mystery, Old Gould used say, quoting yet another Dutch painter, & love the mystery within the mystery.

But with the fish gone, what joyful leap and splash would signal where these circles now began?

R. Flanagan

UNIVERSITY OF SOUTHAMPTON

ABSTRACT

FACULTY OF ENGINEERING, SCIENCE AND MATHEMATICS

School of Chemistry

Doctor of Philosophy

CONTROLLED SURFACE MODIFICATION OF SUPPORTED PLATINUM GROUP METAL CATALYSTS

By Peter Philip Wells

The development of proton exchange membrane fuel cell (PEMFC) technologies relies upon many catalytic processes. The ability to specifically modify the surface of a catalyst with a secondary metal is beneficial as it could lead to increased performance and improved mechanistic knowledge.

Co and Cr surface modified Pt/C catalysts have been prepared by the controlled surface reaction between the reduced Pt surface and an organometallic precursor of the secondary metal. It was found, using X-ray absorption spectroscopy (XAS), X-ray diffraction (XRD), and transmission electron microscopy (TEM) that the secondary metal was targeting the Pt surface sites, but that additional heat treatments were required to form an alloy. Oxygen reduction testing using a rotating disk electrode (RDE) demonstrated that the Pt_3M alloy phase was required for the catalysts to exhibit a 2 to 3 fold enhancement towards the ORR. No enhancement was observed when the secondary metal was present at the surface of the catalyst in an unalloyed state. Pt modified Pd/C catalysts were prepared to reduce the Pt metal content whilst retaining its catalytic activity towards the oxygen reduction reaction (ORR). The Pt mass activities of the Pt/Pd/C catalysts towards the ORR were less than the 40 wt % Pt/C catalyst used as a comparison. It is believed that a larger Pd core particle is required to achieve improved Pt mass activities.

$CeO_x/Pt/Al_2O_3$ catalysts were prepared for the water gas shift reaction and offered improved performance in comparison to Pt/Al_2O_3, but less than Pt/CeO_2. X-ray absorption near edge spectroscopy (XANES) was used to confirm that Pt facilitated the reduction of Ce(IV) to Ce(III) in atmospheres of air, H_2 and CO. It is proposed that the increase in activity observed on increasing the CeO_x loading is consistent with the formate mechanism.

TABLE OF CONTENTS

Chapter One: Introduction **1**

1 General Introduction **1**
1.1 Energy Resources and Environmental Concerns 1
1.2 The History of the Fuel Cell 2
1.3 Applications 3
2 Fuel Cell Principles **4**
3 Types of Fuel Cell **6**
3.1 Alkaline Fuel Cells (AFCs) 6
3.2 Phosphoric Acid Fuel Cell (PAFCs) 7
3.3 Molten Carbonate Fuel Cells (MCFCs) 7
3.4 Solid Oxide Fuel Cells (SOFCs) 8
4 Proton Exchange Membrane Fuel Cells (PEMFCs) **9**
4.1 PEMFC Structure 9
4.2 Anode Fuels for the PEMFC 10
4.2.1 Pure Hydrogen 10
4.2.2 Reformate 11
4.2.3 Methanol (DMFCs) 12
4.3 The Membrane 14
4.4 Gas Diffusion Electrode 15
4.5 Anode Catalysts 16
4.6 Cathode Catalysts 17
5 Aims and Objectives **17**
6 References **19**

Chapter Two: Experimental Methods and Techniques **22**

1 Reagents and Materials **22**
2 Controlled Surface Modification **23**
2.1 Controlled Surface Modification Apparatus 24
2.2 Controlled Surface Modification Experimental Procedure 25
2.3 Heat Treatment of Catalysts 26
3 Electrochemical Methods **26**
3.1 Voltammetric Techniques 26
3.1.1 Pt Voltammetry 27
3.2 Half Cell Studies 30
3.2.1 Preparation of Porous Gas Diffusion Electrodes (PGDE) 30
3.2.2 Equipment and Apparatus 31
3.2.3 Cyclic Voltammetry 32
3.2.4 CO Stripping Investigations 32
3.3 Rotating Disk Electrode (RDE) Studies 32
3.3.1 General Principles 32
3.3.2 Electrode Preparation 34

3.3.3 Equipment and Apparatus 34
3.3.4 RDE Experimental Procedure 35
3.4 Mini Cell Testing 36
3.4.1 Membrane Electrode Assembly (MEA) Preparation 36
3.4.2 Equipment and Apparatus 37
3.4.3 Mini Cell Testing Procedure 38
4 X-Ray Absorption Spectroscopy 39
4.1 Theoretical Aspects of XAS 39
4.1.1 General Principles 39
4.1.2 Progression of EXAFS Theory 43
4.1.3 EXAFS Equations 44
4.1.4 Data Analysis 46
4.2 Experimental Aspects of XAS 50
4.2.1 X-ray Radiation Source 50
4.2.2 Experimental Stations 7.1 and 16.5 53
4.2.3 XAS Transmission Experiments 54
4.2.4 XAS Fluorescence Experiments 56
4.2.5 Gas Treatment Cell 57
5. X-Ray Diffraction 59
5.1 Theoretical Aspects of XRD 59
5.2 Experimental aspects of XRD 60
6. Transmission Electron Microscopy (TEM) and Energy Dispersive X-Ray Analysis (EDX) 61
6.1 Theoretical Aspects of TEM and EDX 61
6.2 Experimental Aspects of TEM and EDX 62
7 Fixed Bed Reactor Testing 62
7.1 Equipment and Apparatus 62
7.2 Water Gas Shift Testing Procedure 63
7.3 CO Oxidation testing procedure 64
8. References 65

Chapter Three: Cr and Co Modified Pt/C Catalysts for the Oxygen Reduction Reaction. 67

1 Introduction 67
2 Experimental Details 73
2.1 Catalyst Preparation 73
2.2 Electrochemical Characterisation 74
2.2.1 Cyclic Voltammetry 74
2.2.2 Oxygen Reduction Testing 74
2.3 XAS Studies 74
2.3.1 Cr and Co K edge Investigations 74
2.3.2 Pt L_2 and L_3 edge Investigations 74
2.3.3 Fractional d-band Vacancy Determination 75
2.4 XRD, TEM, and ICP-AES Analysis 77
3 Results and Discussion 78
3.1 ICP-AES Analysis 78

3.2 XRD Analysis 79
3.3 TEM EDX Analysis 82
3.4 Cyclic Voltammetry - Half Cell Studies 86
3.5.1 XANES – 2nd Metal K edge 92
3.5.2 XANES – Pt L_2 and L_3 edges 95
3.5.3 EXAFS – Cr K edge Studies 100
3.5.4 EXAFS – Pt L_3 edge Studies of Cr Modified Catalysts 110
3.5.5 EXAFS – Pt L_3 and Co K edge Studies of Co Modified Catalysts 121
3.6 Catalytic Activity Towards the ORR 127
3.6.1 ORR Testing Using the RDE 127
4. Conclusions 136
5. References 138

Chapter Four: Pt and Pd Surface Modified Catalysts for the Oxygen Reduction Reaction. 141

1 Introduction 141
2 Experimental Details 145
2.1 Catalyst Preparation 145
2.2 Electrochemical Characterisation 146
2.3 XAS Studies 147
2.4 XRD, TEM, and ICP-AES Analysis 147
3 Results and Discussion 148
3.1 ICP-AES Analysis 148
3.2 XRD Analysis 148
3.3 TEM EDX Analysis 151
3.4 Electrochemical Characterisation 160
3.4.1 Cyclic Voltammetry – Half Cell Studies 160
3.4.2 Hydride Storage Properties 167
3.5 EXAFS Analysis of Pd/Pt/C catalysts 170
3.6 Mini Cell Testing 185
5 Conclusions 190
6 References 192

Chapter Five: CeO_x Modified Pt/Al_2O_3 Catalysts 194

1 Introduction 194
2 Experimental Details 200
2.1 Catalyst Preparation 200
2.2 XAS Studies 201
2.3 WGS and CO Oxidation testing 202
2.4 TEM, CO Chemisorption and ICP-AES Analysis 202
3 Results and Discussion 203
3.1 ICP-AES Analysis 203
3.2 TEM EDX Analysis 204
3.3 CO Chemisorption 210

3.4 XANES Analysis 211
3.5 WGS Testing 216
3.6 CO Oxidation Testing 218
4 Conclusions 222
5 References 223

Chapter Six: Conclusions and Further work 226
References 227

ACKNOWLEDGEMENTS

Firstly, I would like to thank my supervisors Dr. Andrea Russell and Dr. Eleanor Crabb for all their helpful advice, support, and encouragement they have provided for me throughout the course of my PhD. Special thanks must also go to all of those who have helped me at Johnson Matthey: Dave Thompsett, Alvaro Amieiro, Sarah Ball, Brian Theobald, Janet Fisher, Sarah Hudson, Emma Schofield, and Dogan Ozkaya. For all their help at Daresbury, I would like to thank: Bob Bilsborrow, Fred Mosselmans, Steve Fiddy, and Chris Corrigan. For the amazing job they do I would also like to thank the staff of the mechanical workshop and the glassblowers, who have provided me with many pieces of equipment.

I would like to take this opportunity to thank the members of the Russell group whom I have worked with over the last three and a half years. Firstly, the other two members of my Daresbury dream team, Richard and Colin. Thanks to Richard for the enthusiasm he exuded towards EXAFS, which inspired us all, and for being a great sporting competitor (I'm sure I beat you at something at least once); and to Colin for providing enormous amounts of entertainment, albeit not intentionally, the bottom lip quiver, stalling on motorways (any road actually), reversing into stationary vehicles, crunching challenges on Guy, and meetings with the big brown bear are all things I'll remember very fondly. Thanks to Dave Joun Gilbert Quin (the master of medieval times) for being a great friend, introducing me to the joys of chest and arms and his amazing knowledge of obscure deviant practices; to Suzanne, for successfully transcending the non-physical, yet near impenetrable, floor 6 divide, of which otherwise I would never have got to know one of the nicest people I could possibly hope to meet; to Kate, for always giving me the option (hmmm) of whether to buy her a small or large glass of wine, wanted/unwanted advice on hair styles, and her delicate tone of voice; to Helen for her no nonsense approach and awesome chilli plants; to Fab, for providing jokes about 'skinny coke', and for being a great advertisement for Drink Aware initiatives. I would also like to thank; Abbe (and Julian of course), Gurjit, Piotr, Gael, Praba, and Dai. Thanks to all for making my time here a really enjoyable experience.

Chapter One: Introduction

This chapter will briefly review current fuel cell technology, highlighting the theoretical aspects of their operation and the current issues hindering their progression as a realistic alternative to current energy sources. Specific literature reviews pertinent to the work undertaken in this study will be presented at the beginning of each chapter.

1 General Introduction

1.1 Energy Resources and Environmental Concerns

The issue of climate change as a result of green house gas emissions is currently being brought to the public's attention. The major contributor to the increased levels of green house gases in the atmosphere, is the burning of fossil fuels for the production of energy. Furthermore, not only are there concerns about the climatic impact of using fossil fuels, but also there are issues regarding other environmental hazards and dwindling fuel reserves, which are creating an unstable global energy market. Thus, it is desirable to find a viable alternative to the use of fossil fuels. The environmental impact of burning fossil fuels arises as NO_x, SO_x, CO_2, and particulate matter are released into the atmosphere. The major focus is on CO_2 emissions which contribute most significantly to the greenhouse effect. The other environmental concerns are not inconsequential. Particulate matter of a certain size can penetrate deep into the lungs and stay there for a sustained period of time. These particulates are often laced with polyaromatic hydrocarbons which are carcinogenic. Hence the release of particulate matter into the atmosphere has been linked to lung cancer [1]. Levels of SO_x in the atmosphere are of great concern because they can condense with water to form droplets of H_2SO_4. This is responsible for environmental effects such as acid rain. High levels of SO_x in the atmosphere have been responsible for many deaths. One of the most notable examples in the UK is the great London smog of 1952, which killed thousands of people. It was this incident which triggered a wave of clean air acts in the UK. More stringent legislation is

continually reducing the permitted amount of harmful emissions. Some of the most progressive legislation pertaining to air pollution is in California, which has the worst air pollution of any state in the USA. The legislation is driving the production of more environmentally friendly motor vehicles, and states that by 2010 at least 22000 (10 % of cars sold or leased in California) zero or near zero emission vehicles need to be made available [2]. One alternative to the combustion engine which also produces zero emissions is the fuel cell.

1.2 The History of the Fuel Cell

Sir William Grove is commonly accepted as being the first person to discover the fuel cell effect, although similar research was reported by Schoenbein a month prior to Grove [3]. Schoenbein found [4] that a voltage was measured between two Pt foils immersed in separate tubes of hydrogen saturated and oxygen saturated dilute sulphuric acid. The explanation of the observed effect incorporated many theories of the age, which were later discounted and as such led to a lack of clarity in the reasoning behind the findings. Grove reported [5] a very similar observation and described it more appropriately as a "gaseous voltaic battery" which has led to him being accredited with the discovery of the fuel cell. In reality both men played pioneering roles in the development of fuel cell technology with much collaboration [3]. In 1842 Grove published his work on the first operational fuel cell, connecting 4 glass cells filled with sulphuric acid, which were coupled in series, utilising thin Pt electrodes [6].

Although work continued on fuel cell technology, it took in excess of 100 years to find a practical use. The development of fuel cells for practical applications was due largely in part to the important work carried out by Francis Bacon. Bacon developed a high pressure fuel cell which could withstand pressures up to 210 bar and temperatures of 200 °C. The cell used Ni gauze electrodes which were activated by alternately oxidising in air and hydrogen, separated by a potassium hydroxide soaked asbestos layer [7]. Numerous pitfalls were encountered with the development of the cell and it was not until 1959 that a practical fuel cell stack was demonstrated [8]. The American company Pratt & Whitney Aircraft licensed the technology in 1961 and soon received an order

from the National Aeronautics and Space Administration (NASA) to develop fuel cells for the Apollo space missions. A device which produced electricity, heat, and water had obvious benefits over other power sources such as batteries. Although the space programme provided an application where fuel cells could be used, it did not result in an immediate transition to mainstream technologies. The prohibitive economics which blight the use of precious metals in commercial operations is not of consequence for the space program, and thus the Pt loading was too high for most applications. Furthermore, the alkaline electrolyte used is sensitive to carbon dioxide, and therefore requires pure hydrogen and oxygen to be used at the anode and cathode, respectively.

To overcome these problems, numerous types of fuel cell have been developed (to be discussed in detail in section 2) as well as efforts to improve the component materials and reduce the noble metal content. One of the types of fuel cell which has received a lot of attention is the proton exchange membrane fuel cell (PEMFC). In this instance, significant strides have been made in reducing the noble metal content since the 1960s with the required Pt load being reduced from around 4 mg cm^{-2} to 0.4 mg cm^{-2} [9-11].

1.3 Applications

The economic markets where present day fuel cell technologies aim to be important contributors include the transportation, stationary power, and portable power areas [12]. The automotive sector is by far the largest potential market utilising PEMFC technology. Fuel cells have advantages over an internal combustion engine, as they have increased energy efficiency and have zero or near zero emissions. Many prototype fuel cell cars and buses have been developed and have been trialled in many cities. The use of fuel cells for stationary power applications is also a realistic market, with small scale stationary energy production having many benefits. Small scale energy production plants are quick to set-up and do not face the same environmental concerns and public resistance as large scale power plants. Also large power plants suffer from the daily fluctuations of energy demand which are encountered in urban areas. The fuel cell that has received much attention for stationary

power generation is the Solid Oxide Fuel Cell (SOFC). The portable power market refers to small systems, which at present are commonly powered by batteries. The Direct Methanol Fuel Cell (DMFC) can now achieve power densities comparable to secondary battery technologies and can achieve much larger operation times [13]. The most notable example of DMFCs infiltrating this market, is in the application of powering laptop computers.

2 Fuel Cell Principles

Fuel cells and batteries are similar in the sense that they convert chemical energy to electrical energy, without the need of a combustion step. They differ, as unlike the battery, the fuel cell is not a closed system and relies upon a continual external supply of fuel. Using a PEMFC as an example, hydrogen is oxidised into protons and electrons at the anode (equation 1), with the reduction of oxygen occurring at the cathode (equation 2). The two electrodes are separated by an ion conducting electrolyte (in this case proton conducting), facilitating the flow of ions from anode to cathode. The net result of these processes is the production of electrical current and the formation of water as the by-product (equation 3).

When hydrogen is the fuel, the anode reaction is:

$$H_2 \longrightarrow 2H^+ + 2e^- \qquad E^\circ = 0 \text{ V vs. RHE} \qquad \textbf{Equation 1}$$

After the electrons pass through the external circuit, they arrive at the cathode where oxygen is reduced to give water:

$$O_2 + 4H^+ + 4e^- \longrightarrow 2H_2O \qquad E^\circ = 1.23 \text{ V vs. RHE} \qquad \textbf{Equation 2}$$

The overall equation for the reaction is as follows:

$$2H_2 + O_2 \longrightarrow 2H_2O \qquad E^\circ = 1.23 \text{ V vs. RHE} \qquad \textbf{Equation 3}$$

The operation of a PEMFC is represented schematically in figure 1.

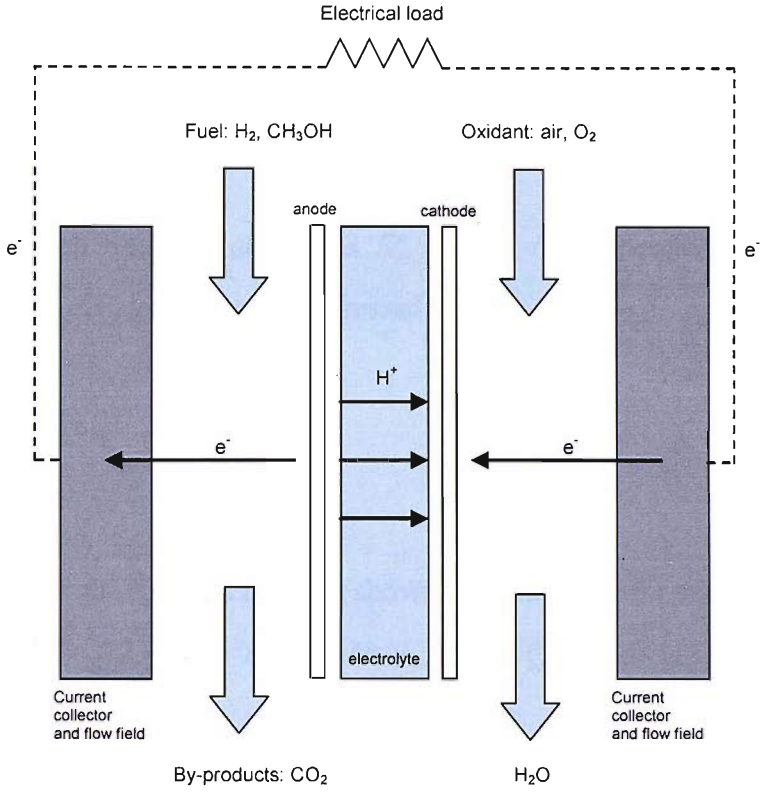

Figure 1 **Schematic diagram of a PEM fuel cell.**

The maximum electrical energy obtainable is determined by the product of the reversible cell potential, E, and the charge, Q, where $Q = nF$ and is thus given by a change in the Gibbs free energy:

$$\Delta G = -nFE \qquad \textbf{Equation 4}$$

where ΔG is the Gibbs free energy (kJ mol^{-1}), n is the number of electrons transferred per mole of reactants, F is the Faraday constant (96485 C mol^{-1}), and E is the cell voltage for the specific chemical reaction [14].

The reaction enthalpy and reaction entropy must also be considered to calculate thermodynamic efficiencies. The Gibbs-Helmholtz relation can be used to relate the different terms:

$$\Delta G = \Delta H - T\Delta S \qquad \textbf{Equation 5}$$

The thermodynamic or ideal efficiency of energy conversion, ξ_{th}, is related to the reaction enthalpy by the following equation:

$$\xi_{th} = \frac{\Delta G}{\Delta H} = 1 - \frac{T\Delta S}{\Delta H} \qquad \textbf{Equation 6}$$

If the thermal cell voltage is defined as $E_H^o = -\Delta H / nF$, then the thermodynamic efficiency can be expressed as:

$$\xi_{th} = \frac{E^o}{E_H^o} \qquad \textbf{Equation 7}$$

For example, for the fuel cell reaction shown in equation 3, for standard conditions, $E^o = 1.23\ V$ and E_H^o = 1.48 V, giving ξ_{th} = 0.83 [15].

3 Types of Fuel Cell

The development of fuel cell technology has led to different types of fuel cell system, characterised by the electrolytic medium separating the electrode interfaces, and the temperature at which the fuel cells can operate effectively. The different types of fuel cells are described herein.

3.1 Alkaline Fuel Cells (AFCs)

The greater efficiency of the reduction of O_2 to OH^- in alkaline media results in the alkaline fuel cell (AFC) having the highest electrical efficiency of all the fuel cells [10]. AFCs typically operate between 60 to 90 °C and are classed as one of the low temperature fuel cells. The electrolyte media used is aqueous KOH (30 – 45 wt %) stabilised within a matrix, which is usually a gel-like material. As mentioned previously the electrolytic media is very sensitive to CO_2, as they react together to form carbonates. These carbonates then act to block the electrolytic pathways [16]. Thus pure gases of hydrogen and oxygen need to be used at the anode and cathode, respectively. At the cathode, oxygen is reduced to

hydroxyl ions which then diffuse to the anode. At the anode the hydroxyl ions combine with the oxidised hydrogen to form water. The water travels then from the anode to cathode where it reacts with oxygen and the incoming electrons to regenerate the hydroxyl ions.

3.2 Phosphoric Acid Fuel Cell (PAFCs)

The PAFC is a product which has already experienced a high degree of commercialisation, mostly as large stationary power units and small combined heat and power (CHP) systems for places such as hospitals. Phosphoric acid acts as the electrolytic medium, and due to only partial dissociation at room temperature, the ion conductivity is low. When operating at temperatures between 150 and 200 °C (still classed as a low temperature fuel cell), the ion conductivity is greatly enhanced, although it results in much longer start-up times. Hydrogen is split at the anode to protons and electrons, with the protons migrating across the electrolyte towards the cathode. At the cathode, oxygen is reduced, with the oxide species combining with the protons to form water, and the resulting electrons travelling around the circuit. The advantage of the PAFC is the improved tolerance that it offers towards CO_2 compared to the AFC.

3.3 Molten Carbonate Fuel Cells (MCFCs)

MCFCs are operated with high operating temperatures in the range of 600 to 700 °C and are classed as a high temperature fuel cell. Ni based catalysts are used at both the anode and the cathode, which are placed either side of an electrolyte comprising of a mixture of molten carbonate salts stabilised by an alumina based matrix. At these high temperatures, the molten carbonate electrolyte is conductive to carbonate ions. The high operating temperatures used avoid the need for a separate fuel processor as the cell itself can act as an internal reformer. Thus, hydrocarbon based fuels can be directly converted into hydrogen. The CO_2 by product that is formed does not hinder the cell performance as with the AFC, but instead reacts with the reduced oxide species at the cathode to form carbonate ions, which then migrate across to the anode. At the anode, the carbonate ions react with the oxidised hydrogen to reform CO_2 and

also H_2O. The main application of MCFCs are in stationary power generation, in part due to the high electrical efficiencies which can be achieved, the ability to operate with external reforming (hence a wide range of fuels can be used) and the prohibitive size and start-up which time make them impractical for other uses.

3.4 Solid Oxide Fuel Cells (SOFCs)

SOFCs are another branch of high temperature fuel cell and commonly operate at temperatures between 800 and 1000 °C. SOFCs use ceramic materials as the electrolyte. The choice of electrolyte is dependent on the operating temperature. At high operating temperatures, yttria-stabilised materials are used due to their ability to withstand the harsh thermal conditions. At lower operating temperatures more conductive materials need to be used, such as ceria based electrolytes. Operating at these high temperatures, the issue of slow oxygen reduction kinetics becomes negligible and $LaSrMnO_3$ (LSM) cathodes are most commonly used. Some SOFC cell designs have both oxidant and fuel going to both electrodes; therefore it is necessary to have a cathode which can not oxidise the fuel, such as LSM. Like the MCFC, Ni based catalysts are used at the anode. The SOFC also foregoes the need of requiring an external reforming step. At the cathode, oxygen is reduced to oxide ions, which migrate through oxygen vacancies of the electrolyte to the anode. At the anode, the oxide ions combine with hydrogen to form water.

Both of the high temperature fuel cells are tolerant to CO and CO_2 and do not require expensive precious metal catalysts, which is an advantage compared to the low temperature fuel cells. The SOFC does not experience problems of a leaking electrolyte as is occasionally encountered for the MCFC, and is of smaller size, as CO_2 does not need to be recycled. However, the SOFC has problems of its own. The high temperatures used, results in thermal expansion of the electrolyte, causing sealing problems, and a reduced life time of the fuel cell, thus there is a drive to produce SOFCs that operate at slightly lower temperatures, around 600 °C [10].

4 Proton Exchange Membrane Fuel Cells (PEMFCs)

The proton exchange membrane fuel cell (PEMFC) has experienced the most attention in recent years, primarily due to the high performance it offers but also because of the simplicity of the system. The PEMFC most commonly operates using hydrogen and oxygen (air) as the anode and cathode feed gases, respectively. The hydrogen can be delivered in a pure form or as reformate, a mixture of H_2, CO, and CO_2, which is obtained by reforming hydrocarbons. The anode fuel can also be methanol, and this type of fuel cell is termed the direct methanol fuel cell (DMFC).

4.1 PEMFC Structure

A diagram showing the structure of a PEMFC is shown in figure 2.

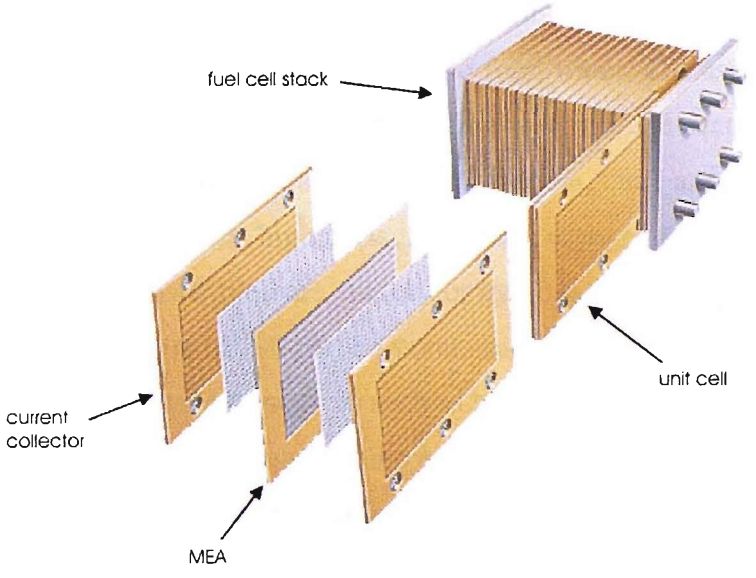

Figure 2 **Expanded view showing the structure of a fuel cell stack and unit cell for a PEMFC [17].**

The core component of a PEMFC is the membrane electrode assembly (MEA). The MEA consists of a proton conducting membrane sandwiched between the anode and cathode. The electrodes consist of a porous gas diffusion backing layer coated on one side with a layer of catalyst. The catalyst side is placed facing the membrane. The MEA is situated between two current collectors, with

the current collectors also acting as flow fields. The flow fields machined into the current collector plate allow for the even distribution of the reactant gases to the electrode interfaces. One MEA is not sufficient in isolation to provide the required power for the majority of applications. Therefore, the individual MEA unit cells are connected in series to create a fuel cell stack.

4.2 Anode Fuels for the PEMFC

The following section describes the most common types of anode fuel sources for PEMFCs, in each case oxygen (air) is used as the cathode fuel.

4.2.1 Pure Hydrogen

The electrochemical reactions taking place at the anode and the cathode have already been described in equations 1 and 2, respectively, and can achieve an overall cell potential of 1.23 V. After the hydrogen is oxidised into protons and electrons, the protons cross the proton exchange membrane towards the cathode where they combine with the reduced oxygen to form water. The use of pure hydrogen as a fuel presents a problem with regard to its storage because it exists as a gas at standard temperature and pressure. At present, there are three principle storage technologies: high pressure storage, cryogenic storage, and hydride storage. Composite pressure vessels for hydrogen storage are available with working pressures up to 700 bar, however, due to their size and weight, they are only practical for large automotives such as buses [18]. Liquid hydrogen has the advantage of decreased storage volume and weight and a longer driving range compared to pressurised hydrogen, but is hindered by the large amount of energy required to liquefy hydrogen and the specialist equipment required to handle liquid hydrogen [19]. There are many alloys and intermetallic compounds which have reversible hydriding properties. At present, the best hydride storage devices have H-densities less than 2 wt % and cannot compete with compressed hydrogen storage [20].

4.2.2 Reformate

To overcome the problems associated with using pure hydrogen one option is to employ a reforming step before the anode feed gas enters the PEMFC, allowing liquid hydrocarbons to be used as the fuel. This produces a fuel, termed reformate, which is primarily hydrogen, but also contains very significant amounts of CO and CO_2. Methanol is a small hydrocarbon and so produces less carbon dioxide and is easier to reform than longer chain molecules, and will be used here to illustrate the principle of reforming. The two predominant methods for producing reformate are partial oxidation and steam reforming. Partial oxidation is an exothermic reaction involving partial burning of the fuel to produce carbon dioxide and hydrogen:

$$CH_3OH + \tfrac{1}{2}O_2 \longrightarrow CO_2 + 2H_2 \qquad \textbf{Equation 8}$$

Steam reforming is endothermic and combines the fuel with steam to produce the same products:

$$CH_3OH + H_2O \longrightarrow CO_2 + 3H_2 \qquad \textbf{Equation 9}$$

Steam reforming produces more molar equivalents of hydrogen in comparison to the partial oxidation. However, as the reaction is endothermic an input of energy is required.

At the same time as producing the desired hydrogen, the conditions are also suitable for the reverse water gas shift reaction (RWGS) [21]:

$$CO_2 + H_2 \longrightarrow CO + H_2O \qquad \textbf{Equation 10}$$

The production of CO as a result of the RWGS is a major drawback for the use of reformate. Even trace levels of CO around the ppm level, act as a catalyst poison at the Pt based catalysts used at the anode. The CO acts as a poison by strongly binding to the surface of Pt and thus reducing the number of sites

available for the oxidation of hydrogen. The levels of CO can be reduced by using multi stage clean-up process involving preferential oxidation (PROX), low temperature WGS (LTS), and high temperature WGS (HTS), achieving levels of CO less than 10 ppm [22, 23].

4.2.3 Methanol (DMFCs)

Many of the problems encountered with using hydrogen in its pure form or as reformate, can be overcome by using methanol as the anode fuel. There are no complicated storage problems and the need for complex reforming systems is removed. The use of pure H_2 or reformate can result in poor humidification of the membrane (to be discussed in section 4.3), increasing the cell resistance and thus the overall performance. The fuels need to be carefully humidified to counteract this problem. Using a fuel stream of a dilute methanol-water mixture negates the need for humidification and heat management hardware modules. The processes occurring at the anode and cathode are shown in equations 11 and 12, respectively.

$$CH_3OH + H_2O \longrightarrow CO_2 + 6H^+ + 6e^- \qquad E^0 = 0.05V \text{ vs. RHE} \qquad \textbf{Equation 11}$$

$$3/2O_2 + 6H^+ \longrightarrow 3H_2O \qquad E^0 = 1.23 \text{ V vs. RHE} \qquad \textbf{Equation 12}$$

The overall reaction is therefore:

$$CH_3OH + H_2O + 3/2O_2 \longrightarrow CO_2 + 3H_2O \qquad E^0 = 1.18 \text{ V vs. RHE} \qquad \textbf{Equation 13}$$

The theoretical efficiency, ξ_{th}, for this process is 0.97 compared to that of 0.83 with hydrogen [15]. Despite this increase in efficiency, the power density obtainable from a DMFC is only a third of a conventional PEMFC system [13]. The problems associated with a DMFC are: poor electrode kinetics at the anode; the stability and permeability of current membranes to methanol, with the crossover of methanol not only reducing the utilisation of the fuel but also reducing the already poor oxygen reduction kinetics [24]. Increasing the

membrane thickness can greatly reduce the amount of methanol crossover but there is a trade off as this also increases the cell resistance. Using Pt based catalysts the processes taking place at the anode are described in equations 14 to 18.

$$Pt + CH_3OH \longrightarrow Pt - (CH_3OH)_{ads} \quad \textbf{Equation 14}$$

$$Pt - (CH_3OH)_{ads} \longrightarrow Pt - (CH_3O)_{ads} + H^+ + e^- \quad \textbf{Equation 15}$$

$$Pt - (CH_3O)_{ads} \longrightarrow Pt - (CH_2O)_{ads} + H^+ + e^- \quad \textbf{Equation 16}$$

$$Pt - (CH_2O)_{ads} \longrightarrow Pt - (CHO)_{ads} + H^+ + e^- \quad \textbf{Equation 17}$$

$$Pt - (CHO)_{ads} \longrightarrow Pt - (CO)_{ads} + H^+ + e^- \quad \textbf{Equation 18}$$

Initially, methanol adsorbs at Pt surface sites followed by the sequential removal of a proton and electron. The adsorption of methanol requires multiple Pt adsorption sites, and thus the surface needs to be free of adsorbed hydrogen. This occurs around 0.2 V vs. RHE on polycrystalline Pt. As with reformate, adsorbed CO species on Pt act as a catalyst poison. The formation of the $Pt - CHO_{ads}$ and $Pt - CO_{ads}$ species have been found using infrared spectroscopy [25, 26]. It has been proposed that the removal of adsorbed CO in DMFCs occurs as shown in equation 19 [24].

$$Pt - OH_{ads} + Pt - (CO)_{ads} \longrightarrow CO_2 + H^+ + e^- \quad \textbf{Equation 19}$$

This process requires the formation of oxide species from the dissociation of water, which does not occur on a Pt surface until potentials above 0.4 to 0.45 V vs. RHE are attained [27]. These processes result in polarisation losses at the anode and are one of the limitations of DMFCs.

4.3 The Membrane

The membrane in a PEMFC needs to be non-permeable to the reactant gases, allow for the flow of protons from anode to cathode, to be electronically insulating so as no charge is lost, and to be inert to the oxidising and reducing environments experienced. At present, a solid polymer membrane, called Nafion® is used. Nafion® has a polytetrafluoroethylene (PTFE)-based hydrophobic backbone with sulphonated hydrophilic sidechains, as shown in figure 3:

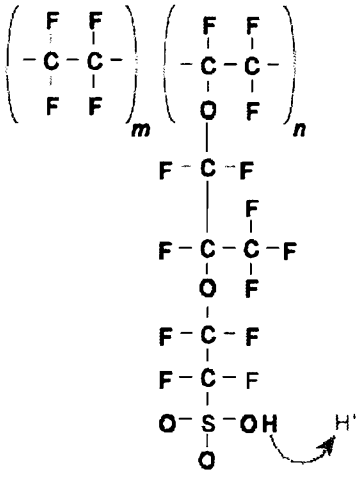

Figure 3 **Chemical structure of Nafion® where the ratio *n* to *m* (i.e. active sites to inactive chain monomers) determines the acidity of the electrolyte.**

Before the development of Nafion®, other membranes including phenolic membranes, partially sulphonated polystyrene sulphonic acid, and polystyrene-divinylbenzene sulfonic acid were all considered [9]. However, each of the membranes had poor proton conductivity and were not inert to the oxidising environments they experienced due to the high potential of the cathode. The use of Nafion® overcame these problems as the presence of highly electronegative fluorine atoms bonded to the same carbon atom as the SO_3H group, leads to super acid properties and high proton conductivities. The degradation of the membrane was also reduced as CF_2 groups are very stable in both reducing and oxidising environments [9].

Water management plays a very important role in the use of Nafion® membranes. The presence of the sulphonic acid group facilitates ion exchange and thus allows for the reorientation of water molecules, and provides the desired high proton conductivities. At high temperatures and high current density operation the membrane dehydrates, resulting in an increased cell resistance as a consequence of decreased proton conductivity [28, 29]. The use of humidified gases and thinner Nafion® membranes with inherently higher conductivities can remedy the affect of dehydration [29].

In DMFCs, methanol crossover is also an important consideration as it hinders the already sluggish oxygen reduction reaction. The common way to reduce methanol crossover is to increase the thickness of the membrane [30]. This results in a decrease in the proton conductivity. New membrane production methods have been able to produce membranes of 2 μm thickness which have the same resistance to methanol crossover as conventional 7 μm thick membranes [29].

4.4 Gas Diffusion Electrode

For PEMFCs, Pt based catalysts are used for both anodic and cathodic processes. Due to the high cost of precious metal catalysts, there is a drive to reduce the metal loading. To maximise the effective Pt metal surface area, small Pt particles (around 4 nm) are supported on carbon (e.g. XC-72R). Carbon is a good choice for the support because of: the relative ease of obtaining uniformly highly dispersed Pt particles; good conductivity and stability under fuel cell operating conditions; and the increased stability they offer compared to the agglomeration which occurs for non-supported Pt under fuel cell operating conditions [31].

The carbon supported catalyst layer is then screen printed (other methods of forming the catalyst layer are also used) onto a gas diffusion layer in the form of a slurry containing the catalyst, alcoholic solution, and the membrane ionomer. The membrane ionomer acts to bind the catalyst layer together but also facilitates good contact with the membrane giving rise to improved proton conductivities.

The gas diffusion layer is commonly porous carbon paper including a small amount of hydrophobic substrate such as polytetrafluoroethylene (PTFE). The porous carbon paper allows for the diffusion of gases and acts as a current collector. The hydrophobic substrate prevents water accumulating within the pores and limiting the diffusion rate of the gases. The reason for this arrangement is to maximise the three-phase boundary between the supply of gas, the catalyst particle and the ionic conductor and is shown in figure 4.

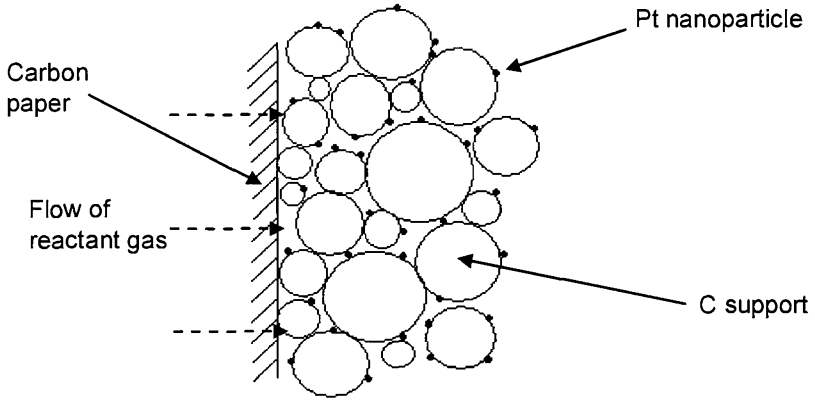

Figure 4 **Cross-section through a typical gas diffusion electrode [10].**

4.5 Anode Catalysts

The oxidation of hydrogen on Pt is a very facile process with only a small overpotential of approximately 20 mV observed for the process. As mentioned previously (section 4.2.2), CO in the reformate fuel stream acts as a catalyst poison towards Pt. Thus, there is a drive to develop catalysts with an increased tolerance to CO, with PtRu alloys being the most prominent example of this. The electrooxidation of adsorbed CO occurs at 0.25 V vs. RHE for PtRu alloys, which is 0.2 V less positive than Pt alone [32]. Pt alloys of W, Co, Sn, Mo, and Cr have also been studied [12]. A promoted or bifunctional mechanism to explain the improved CO tolerance, was first proposed by Watanabe and Motoo [33] and is shown in equations 20 and 21. The process involves CO adsorbing on the surface of Pt sites and being oxidised by oxide or hydroxide species adsorbed on neighbouring Ru sites. As CO is mobile on the Pt surface, holes in the CO

surface with free Pt islands are formed, allowing for the oxidation of hydrogen to occur at a very high rate [34].

$$Ru + H_2O \longrightarrow Ru - OH + H^+ + e^- \quad \textbf{Equation 20}$$

$$Pt - CO + Ru - OH \longrightarrow CO_2 + H^+ + e^- + Pt + Ru \quad \textbf{Equation 21}$$

An electronic mechanism has also been proposed. It is suggested that the enhancement arises due to electronic effects reducing the adsorption strength of CO on PtRu alloys [12].

4.6 Cathode Catalysts

Pt based catalysts are also used at the cathode for the oxygen reduction reaction (ORR). There is a large overpotential associated with this process (approximately 400 mV), and when using pure H_2 at the anode, this overpotential represents the key loss of efficiency for a fuel cell. Oxygen reduction is a far more complex process than hydrogen oxidation. These complexities can be attributed to the relative stronger bond strength of the O-O bond, the stability of intermediates such as Pt-O and Pt-OH, and the fact that the process involves the transfer of four electrons rather than two. Pt alloyed with Cr, Co, Ni, Fe, and Ti have been shown to offer improved kinetics over pure Pt alone. The mechanism by which the reaction is enhanced is still not completely understood, although it is believed that changes in the geometric and electronic properties of the catalyst are involved [35-39].

5 Aims and Objectives

The concise review presented thus far has highlighted the potential that the PEMFC system has to offer as well as drawing attention to the current challenges hindering its progression to commercialisation. The work presented in this thesis involves the preparation of model catalytic systems to facilitate a better understanding of important catalytic processes relevant to the PEMFC. The

controlled surface modification technique developed by Crabb *et al.* [40-44] will be used to modify the surface of supported platinum group metal catalysts with a secondary metal component. A range of techniques will be used to characterise the catalyst structure including: X-ray absorption spectroscopy (XAS), X-ray diffraction (XRD), transmission electron microscopy (TEM) and cyclic voltammetry (CV).

The greatest inefficiency in a PEMFC is the poor kinetic performance of the oxygen reduction reaction (ORR) taking place at the cathode. Pt alloys with first row transition metals such as Cr and Co have shown a 2 to 3 fold enhancement compared to Pt alone, although the origin of the enhancement is not fully understood. It is believed that changes in the surface properties of the catalyst play an important role in the improved performance offered by Pt alloys. Chapter 3 details the preparation of Cr and Co modified Pt/C catalysts using the method developed by Crabb *et al.* [40-44]. These model catalytic systems will be used to correlate catalyst structure and performance so as to gain an insight into the mechanism by which Pt alloys exhibit enhanced ORR activity

There is a continued drive to reduce the Pt loading as well as to gain improved kinetic performance towards the ORR. Pt modified Pd single crystals have been shown to offer increased kinetics over pure Pt and provide a means of drastically reducing the Pt metal content if translated to supported catalysts [45]. The controlled surface modification procedure has been used to develop Pt modified Pd/C catalysts and are detailed in chapter 4. The Pd modified Pt/C system is also discussed.

With levels of CO around the ppm level acting as a catalyst poison towards Pt based catalysts, a multi-stage clean up process is used to reduce the levels of CO in H_2 fuel streams to less than 10 ppm. Part of this process involves the water gas shift reaction (WGS). The Pt/CeO_2 system offers many benefits compared to conventional Cu / ZnO catalysts used for the WGS reaction for fuel cell applications. The controlled surface modification procedure has been used to deposit Ce onto the surface of Pt/Al_2O_3 and is described in chapter 5. These Ce

modified Pt/Al_2O_3 catalysts should allow the interaction between Pt and ceria to be probed as well as providing a potentially more stable catalyst.

6 References

1. anon, Air Quality in the UK, Parliament Office of Science and Technology, Postnote, 188, 2002
2. *State of California Bill AB 2061*. 2001.
3. Bossel, U., *The birth of the fuel cell*. 2000.
4. Schoenbein, C.F., Phil. Mag., 1839. **14**: p. 43.
5. Grove, W.R., Phil. Mag., 1839. **14**: p. 127.
6. Grove, W.R., Phil. Mag., 1842. **21**: p. 417.
7. Sandstede, G., E.J. Cairns, V.S. Bagotsky, and K. Wiesener, *Chapter 12: History of low temperature fuel cells*, in *Handbook of Fuel Cells - Volume 1: Fundamentals and Survey of Systems*. 2003, John Wiley and Sons.
8. Bacon, F.T. *The high pressure hydrogen/oxygen fuel cell*. in *Fuel Cells, Symposium of the ACS*. 1960. Atlantic City.
9. Costamagna, P. and S. Srinivasan, J. Power Sources, 2001. **102**(1-2): p. 242.
10. Carrette, L., K.A. Friedrich, and U. Stimming, ChemPhysChem, 2000. **1**(4): p. 162.
11. Antolini, E., J. Appl. Electrochem., 2004. **34**(6): p. 563.
12. Hoogers, G. and D. Thompsett, Cattech, 2000. **3**: p. 106.
13. Hogarth, M.P. and T.R. Ralph, Platinum metals Rev., 2003. **46**(4): p. 146.
14. Winter, M. and R.J. Brodd, Chem. Rev., 2004. **104**(10): p. 4245.
15. Vielstich, W., *Chapter 4: Ideal and effective efficiencies of cell reactions and comparison to carnot cycles*, in *Handbook of Fuel Cells - Volume 1: Fundamentals, Technology and Applications*. 2003, John Wiley &Sons Ltd.
16. Cifrain, M. and K. Kordesch, *Chapter 14: Hydrogen/oxygen (Air) fuel cells with alkaline electrolyte*, in *Handbook of Fuel Cells - Volume 1:*

Fundamentals, Technology and Applications. 2003, John Wiley & Sons, Ltd.

17. www.xcellsis.com. [cited.
18. Funck, R., *Chapter 6: High Pressure Storage*, in *Handbook of Fuel Cells - Volume 3: Fuel Cell Technology and Applications*. 2003, John Wiley & Sons. .
19. Wolf, J., *Chapter 7: Liquid hydrogen technology for Vehicles*, in *Handbook of Fuel Cells - Volume 3: Fuel Cell Technology and Applications*. 2003, John Wiley & Sons.
20. Sandrock, G., *Chapter 8: Hydride Storage*, in *Handbook of Fuel Cells - Volume 3: Fuel cell technology and applications*. 2003, John Wiley & Sons.
21. Hansen, J.B., *Chapter 12: Methanol reformer design considerations*, in *Handbook of Fuel Cells - Volume 3 Fuel cell technology and applications*. 2003, John Wiley & Sons.
22. Ladebeck, J.R. and J.P. Wagner, *Chapter 16: Catalyst Development for Water Gas Shift*, in *Handbook of Fuel Cells - Volume 3: Fuel cell technology and applications*. 2003, John Wiley & Sons.
23. Farrauto, R., S. Hwang, L. Shore, and W. Ruettinger, Ann. Rev. Mater. Res., 2003. **33**: p. 1.
24. Hamnett, A., *Chapter 18: Direct methanol fuel cells*, in *Handbook of Fuel Cells - Volume 1: Fundamentals and Survey of Systems*. 2003, John Wiley & Sons
25. Iwasita, T. and F.C. Nart, J. Electroanal. Chem., 1991. **317**(1-2): p. 291.
26. Christensen, P.A., A. Hamnett, J. Munk, and G.L. Troughton, J. Electroanal. Chem., 1994. **370**(1-2): p. 251.
27. Iwasita, T., Electrochimica Acta, 2002. **47**(22-23): p. 3663.
28. Doyle, M. and G. Rajendran, *Chapter 30: Perfluronated membranes*, in *Handbook of Fuel Cells: Volume 3: Fuel Cell Technology and applications*. 2003, John Wiley & Sons.
29. Banerjee, S. and D.E. Curtin, J. Fluor. Chem., 2004. **125**(8): p. 1211.

30. Neergat, M., K.A. Friedrich, and U. Stimming, *Chapter 63: New materials for DMFC MEAs*, in *Handbook of fuel cells - Volume 4: Fuel cell technology and applications*. 2003, John Wiley & Sons.
31. Tada, T., *Chapter 38: High dispersion catalysts including novel carbon supports*, in *Handbook of fuel cells - Volume 3: Fuel cell technology and applications*. 2003, John Wiley & Sons.
32. Ralph, T.R. and M.P. Hogarth, Platinum metals Rev., 2002. **46**(3): p. 117.
33. Watanabe, M. and S. Motoo, J. Electroanal. Chem., 1975. **60**: p. 275.
34. Ruth, K., M. Vogt, and R. Zuber, *Chapter 39: Development of CO-tolerant catalysts*, in *Handbook of Fuel Cells - Volume 3: Fuel cell technology and applications*. 2003, John Wiley & Sons.
35. Jalan, V. and E.J. Taylor, J. Electrochem. Soc., 1983. **130**(11): p. 2299.
36. Mukerjee, S. and S. Srinivasan, J. Electroanal. Chem., 1993. **357**: p. 201.
37. Mukerjee, S., S. Srinivasan, M.P. Soriaga, and J. McBreen, J. Electrochem. Soc., 1995. **142**(5): p. 1409.
38. Toda, T., H. Igarashi, H. Uchida, and M. Watanabe, J. Electrochem. Soc., 1999. **146**(10): p. 3750.
39. Toda, T., H. Igarashi, and M. Watanabe, J. Electroanal. Chem., 1999. **460**(1-2): p. 258.
40. Crabb, E.M., M.K. Ravikumar, D. Thompsett, M. Hurford, A. Rose, and A.E. Russell, Phys. Chem. Chem. Phys., 2004. **6**(8): p. 1792.
41. Crabb, E.M., M.K. Ravikumar, Y. Qian, A.E. Russell, S. Maniguet, J. Yao, D. Thompsett, M. Hurford, and S.C. Ball, Electrochem. Solid State Lett., 2002. **5**(1): p. A5.
42. Crabb, E.M. and M.K. Ravikumar, Electrochim. Acta, 2001. **46**(7): p. 1033.
43. Crabb, E.M., R. Marshall, and D. Thompsett, J. Electrochem. Soc., 2000. **147**(12): p. 4440.
44. Crabb, E.M. and R. Marshall, Appl. Catal. A-Gen., 2001. **217**(1-2): p. 41.
45. Zhang, J., Y. Mo, M.B. Vukmirovic, R. Klie, K. Sasaki, and R.R. Adzic, J. Phys. Chem. B, 2004. **108**(30): p. 10955.

Chapter Two: Experimental Methods and Techniques

Detailed information regarding the theoretical and practical aspects of the experimental work undertaken in this project is presented in this chapter. This includes descriptions of: catalyst preparation, electrode fabrication, electrochemical studies, X-ray absorption spectroscopy, and fixed bed reactor testing.

1 Reagents and Materials

The materials and reagents used within this study, along with their suppliers, are detailed below in table 1.

Table 1 **List of the reagents / materials used and their suppliers**

Reagent / Material	**Supplier**
20 wt % Pt supported on carbon	Johnson Matthey Technology Centre
18.8 wt % Pd supported on carbon	Johnson Matthey Technology Centre
4 wt % Pt supported on γ - Al_2O_3	Johnson Matthey Technology Centre
γ - Al_2O_3	Johnson Matthey Technology Centre
XC-72R carbon black	Cabot Corporation
Bulk Pt-M supported on carbon	Johnson Matthey Technology Centre
Nafion® solution 5 wt % in alcohol	Aldrich
TGHP-090 carbon paper	Johnson Matthey Technology Centre
Concentrated sulphuric acid (98%)	Fisher
Toluene (Lab reagent grade)	Fisher
n – heptane (Lab reagent grade)	Fisher
Chloroform (Lab reagent grade)	Fisher
Propan-2-ol (Lab reagent grade)	Fisher
Bisbenzene chromium	STREM Chemcials
Biscyclopentadienyl chromium	STREM Chemicals

Chromium (III) acetylacetonate	Aldrich
Biscyclopentadienyl Cobalt	STREM Chemicals
Cerium (III) acetylacetonate monohydrate	Aldrich
Palladium (II) acetylacetonate	Aldrich
Platinum (II) acetylacetonate	Alfa Aesar

2 Controlled Surface Modification

Many catalytic processes utilise bimetallic catalysts for improved performance. The origin of the enhancement is sometimes not fully understood and is generally attributed to geometric effects [1] or changes in electronic properties [2]. Both of these processes are sensitive to the surface structure of the bimetallic catalyst. The ability to tailor the surface structure of these materials is of the utmost importance to fully understand the reaction mechanisms and subsequently improve performance. Traditional methods for preparing bimetallic catalysts such as impregnation, electrochemical deposition, and precipitation lack the required specificity to deposit the secondary metal onto the surface sites of the primary metal in a controlled manner. One method which offers this specificity is the reaction between the reduced surface of the primary metal and an organometallic compound of the secondary metal. Work by Basset *et al.* looked at the reactions between supported Ru, Rh, and Pt metals and alkyl complexes of Ge, Sn, Pb, Se and Zn [3-5], the method was called surface organometallic chemistry (SOMC). The procedure exploited the interaction between the organometallic complex and the metal surface in the presence of a partial pressure of hydrogen. It was deduced that different types of materials could be obtained as a result of the modification of the primary metal depending on the reaction conditions used:

(a) The organometallic compound has only partially reacted, with clusters of unreacted material present on the primary metal surface.
(b) All the organometallic compound has reacted and the secondary metal is present as adatoms on the primary metal surface.

(c) The adatoms of the secondary metal can be thermally incorporated into the particle to form an alloy.

Work by Crabb *et al.* transferred this novel preparatory method into the design of fuel cell electrocatalysts. Carbon supported Pt particles were modified with Ge, Sn, Ru, and Mo using alkyl, allyl and metallocene compounds for use as CO electro-oxidation catalysts [6-9]. As the method used organometallics other than alkyl complexes these reactions are known as controlled surface reactions (CSR). The reaction was assumed to be initiated by the physisorption of the organometallic species onto the reduced surface of the primary metal. Subsequent heating under hydrogen was believed to cleave the organic fragment, leaving behind adatoms on specific crystallographic sites. Thermal treatment of the resulting catalyst was used to obtain the surface alloy. The work presented in this study utilises the method developed by Crabb *et al.* to prepare novel catalysts for the oxygen reduction and water gas shift reactions.

2.1 Controlled Surface Modification Apparatus

The apparatus used for the preparation of catalysts detailed in this study is shown below in figure 1.

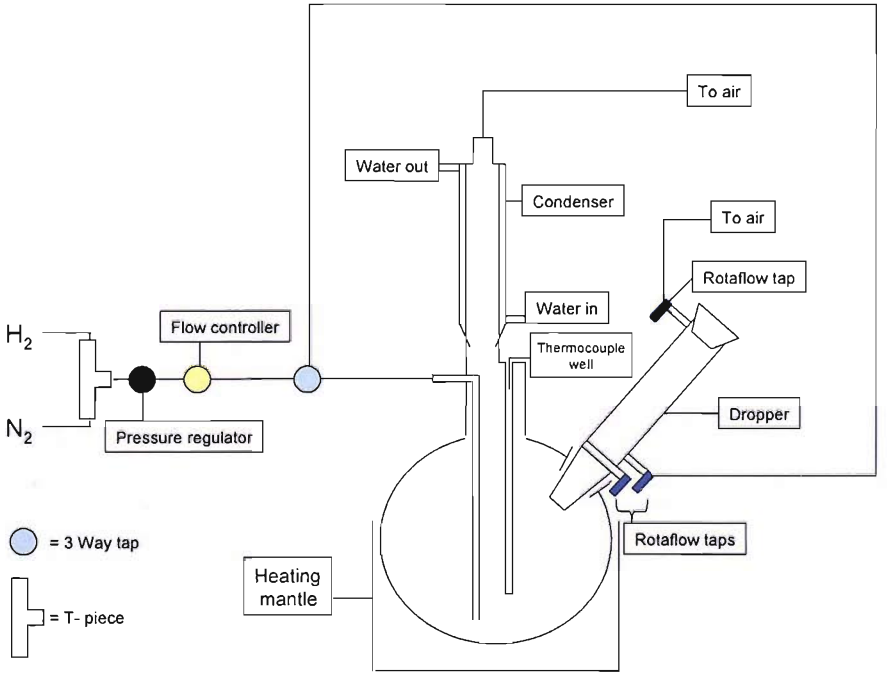

Figure 1 **Schematic diagram of the controlled surface modification reactor.**

The reactor used was specifically designed for the preparation of catalysts via the controlled surface modification route. The apparatus consists of a series of glassware interconnected by PTFE tubing. A key feature of the apparatus is the removable dropper for the addition of dissolved organometallic compounds. As it is removable, air sensitive materials can be prepared in the glove box and then transferred to the reactor without being exposed to air. The three-way tap allows for the dropper to be purged of any dissolved oxygen before addition of the precursor to the pre-reduced surface. The same orientation of gas flow to purge the contents of the dropper is also used to transfer the precursor.

2.2 Controlled Surface Modification Experimental Procedure

The reactor (figure 1) was loaded with the starting catalyst, M_1/C or M_1/Al_2O_3 and purged with $N_2(g)$ for 1 hour to remove oxygen from the system. The catalyst was then reduced under flowing $H_2(g)$ (flow 60-100 cm^3 min^{-1}), heating to a temperature of 200 °C for carbon supported catalysts and 350 °C for alumina supported catalysts. This temperature was maintained for 3 hours at which point the reactor was cooled to room temperature under $H_2(g)$. The required amount of organometallic precursor was calculated using the equation below;

$$\text{Mass precursor} = \frac{\text{wt \% } M_1 \times \text{mass } M_1/C \times D \times x \times \text{RMM Precursor}}{\text{RAM } M_1}$$

Equation 1

where D is the dispersion of M_1 and x is the desired monolayer coverage.

The organometallics were dissolved in the appropriate solvent (n-heptane for metallocenes, and toluene for acac complexes) and added to the dropper. After purging the saturator with $N_2(g)$ for 10-15 min. the contents of the dropper were transferred to the reactor. $H_2(g)$ was then passed through the reactor whilst stirring and heating at 90 °C for 8 hours. The reactor was then allowed to cool and flushed with $N_2(g)$ for 30 min. The contents of the reactor were discharged,

filtered, and washed with the appropriate solvent (n-heptane or toluene). The catalyst was placed on a watch glass, and dried in a fume cupboard in air. The dried catalyst was returned to the cleaned reactor and the initial reduction step repeated.

2.3 Heat Treatment of Catalysts

Some catalysts were exposed to additional thermal treatment to form an alloy phase. A portion of the catalyst was placed in an alumina boat and loaded into a horizontal tube furnace. The tube was purged with N_2 (g) for 30 min and the gas then switched to a 10% H_2 / N_2 mixture, at a flow rate of 60 cm^3 min^{-1}. The temperature was increased from room temperature to the desired temperature at a heating rate of 5 °C min^{-1} and held there for 1 hour and then allowed to cool back to room temperature. Prior to discharging the catalyst, the gas was switched back to N_2(g) and the tube purged for 30 min.

3 Electrochemical Methods

Instrumental electrochemical techniques provide important methods in the study of fuel cell electrocatalysts. The techniques are employed to characterise the structural and electronic properties of the material as well as to assess their catalytic activity. The different methodologies used as part of this project are detailed within this section. The voltammetry of a polycrystalline Pt electrode is presented and the details of the electrochemical cells used for the carbon supported catalysts are discussed.

3.1 Voltammetric Techniques

Voltammetry comprises a group of electroanalytical methods in which information about an electrochemical process is derived from the measurement of current as a function of the applied potential. The current response observed is dependent on the charge transfer processes taking place at the surface of the working electrode. The simplest of these methods is linear sweep voltammetry

(LSV). In LSV the potential is swept from an initial potential, E_1, to a final potential, E_2, at a known sweep rate, v. Cyclic voltammetry (CV) is an extension of LSV also includes the return to the initial potential, E_1 or to another potential, E_3. More sophisticated voltammetric experiments can utilise an initial phase where the potential is held at a set potential to saturate the working electrode surface with an adsorbed species. The uses of voltammetric methods to probe the electrochemical reactions of Pt in an acidic environment are detailed in the following sections.

3.1.1 Pt Voltammetry

The CV of a polycrystalline Pt surface as shown in figure 2 contains a number of different features, which can be divided up into three separate regions, as indicated by the letters a to c in the figure. A 3 electrode cell was used with Pt wire as the counter electrode, and a mercury mercurous sulphate reference electrode.

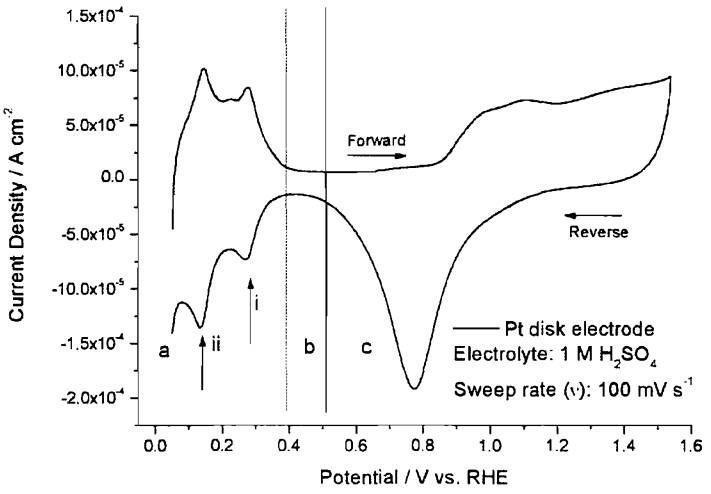

Figure 2 **CV of a 5 mm diameter Pt disk electrode. The voltammogram shown is the 2nd cycle, starting at 0.05 V vs. RHE, sweeping to 1.5 V vs. RHE and back.**

Region a is the hydrogen region. The peaks observed in the forward scan represent the desorption of hydrogen from the Pt surface. For the reverse scan peaks i and ii corresponds to the adsorption of hydrogen (equation 2). The

position of the peaks correlates to the relative strength of the hydrogen adsorption. Peak i corresponds to the more strongly adsorbed hydrogen as a greater overpotential is required to remove it in the forward scan. Peak ii therefore represents the weakly adsorbed hydrogen. The area underneath the hydrogen adsorption peaks can be used to calculate the Pt surface area as hydrogen will adsorb to complete a full monolayer on Pt surfaces. The peak forming at the lowest potential is the start of hydrogen evolution. It is important not to use the desorption peaks to calculate the Pt surface area for carbon supported catalysts as evolved hydrogen can remain trapped in the catalyst structure and then be reoxidised in the subsequent forward scan. This is less of a problem for a smooth Pt disk electrode.

$$Pt + H^+ + e^- \rightarrow Pt\text{-}H_{ads} \qquad \textbf{Equation 2}$$

Region b is the double layer region. The double layer arises due to the segregation of charge which occurs at the interface between the working electrode and the electrolyte. As the potential is swept the charges migrate towards the working electrode producing the observed charging current. The current observed is proportional to the scan rate. At high scan rates the current from the double layer charging is no longer negligible in comparison to the faradaic current. As a consequence most voltammetric experiments undertaken in this study utilise a scan rate of 10 mV s^{-1}.

Region c is the oxide region. In the forward scan the peak starting at approximately 0.88 V vs. RHE is the response observed for an oxide layer forming on Pt (equation 3). Once the Pt surface has been saturated with oxide, a place exchange mechanism occurs where oxygen at the surface of Pt moves into the bulk of the particle. The Pt can then continue to form an oxide layer after the surface is initially saturated. On the reverse scan, the peak at 0.78 V vs. RHE is the oxide stripping peak (equation 4). The position and area under this peak is dependent on the length of time spent in the oxide region and the upper potential limit of the voltammogram. As the area under this peak does not solely reflect the Pt surface it should not be used for surface area determination.

$$Pt + H_2O \rightarrow Pt - OH_{ads} + H^+ + e^- \quad \textbf{Equation 3}$$

$$Pt - OH_{ads} \rightarrow PtO + H^+ + e^- \quad \textbf{Equation 4}$$

When a monolayer of CO is adsorbed onto a Pt surface (figure 3) there is a very noticeable change in the voltammetric response.

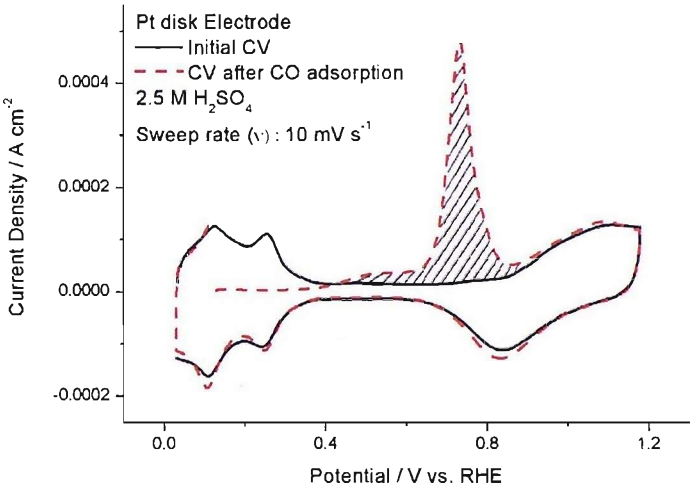

Figure 3 **Cyclic voltammograms of a Pt disk electrode before and after CO adsorption.**

A monolayer of adsorbed CO blocks the surface for any other electrochemical reactions in the hydrogen region. This is a demonstrated by a complete suppression of the hydrogen desorption region for the CV of Pt with adsorbed CO. The large peak at 0.73 V vs. RHE is the oxidation of CO to CO_2 (equation 5). This peak potential is 0.83 V more positive than the standard reversible potential and indicates the very strong bonding interaction between CO and Pt. This highlights the problem for PEMFCs, where CO in a reformate anode feed acts as a catalyst poison and hinders the oxidation of hydrogen. Once the CO has been removed from the Pt surface the normal hydrogen adsorption and desorption features return in the subsequent scan.

$$Pt - CO + H_2O \rightarrow Pt + CO_2 + 2H^+ + 2e^- \quad \textbf{Equation 5}$$

As CO adsorption on a Pt surface is limited to a single monolayer coverage, the area under the CO adsorption peak can be used to determine the available Pt surface area. The charge associated with a monolayer of CO on a Pt surface is 420 μC cm^{-2} Pt. The active surface area of Pt present is simply the ratio between the measured charge for CO oxidation and the constant charge for a monolayer of CO on a cm^2 of Pt (equation 6).

$$Pt_{area} = \frac{\text{Measured CO Charge } / \mu C}{420\ \mu C\ cm^{-2}\ Pt} \qquad \textbf{Equation 6}$$

This can then be normalised to express the amount of Pt surface area present as a function of mass Pt present (equation 7).

$$Pt_{area_m}\ (m^2\ Pt\ g^{-1}\ Pt) = \frac{Pt_{area}\ (m^2\ Pt)}{\text{Pt loading}\,(g\ Pt\ m^{-2}) \times \text{Electrode area}\,(m^2)} \qquad \textbf{Equation 7}$$

3.2 Half Cell Studies

3.2.1 Preparation of Porous Gas Diffusion Electrodes (PGDE)

The required amount of catalyst (~ 100 mg) was dispersed in a small amount of purified water (purified using a Barnstead Nanopure system – giving water with a conductivity of 18 MΩ cm) (~ 0.5 ml). To the solution was added a required amount of 5 wt% Nafion® in alcohol suspension, to prepare a dry catalyst containing 15 wt% Nafion® solids. The resulting mixture was mixed using a Fisher PowerGen 125 homogeniser and subsequently painted onto a circular piece of carbon paper (TGHP 090) with an area of 5.31 cm^2. The carbon paper was painted, dried on a hot plate, and then weighed. This process was repeated until a Pt loading of 0.35 mg cm^{-2} was obtained. The electrodes were hot pressed at 10 bar and 100 °C for 3 min. Electrodes of the appropriate size (1.32 cm^2) were cut out of the larger sheet and boiled in triply distilled water to ensure a fully hydrated state.

3.2.2 Equipment and Apparatus

A detailed drawing of the electrochemical cell used in these studies is shown below in figure 4.

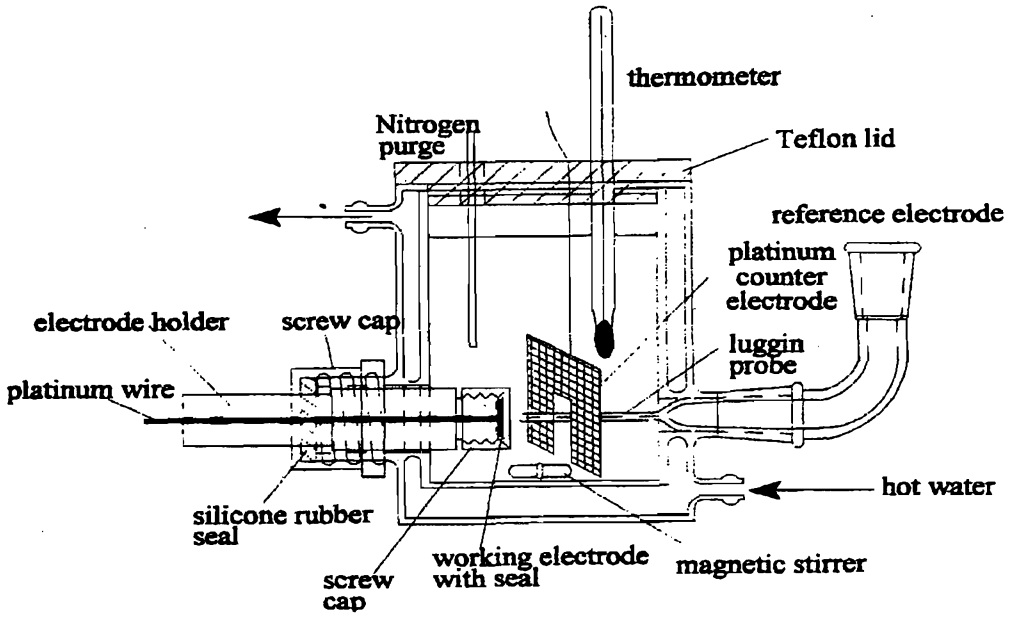

Figure 4 **Example of the three electrode electrochemical cell used to test fuel cell catalysts [10].**

The cell used is a 3 electrode electrochemical cell. The potential is applied between the working electrode (WE) and reference electrode (RE), with the current being measured between the WE and the counter electrode (CE). All the electrodes are connected to an Autolab PGSTAT30 potentiostat. The PGDE was held in position at the WE by a screw-on flange. A platinum wire was used as an electrical contact to the back of the WE. The WE holder was mounted in a glass cell with a capacity of 150 cm^3, which had an integrated water jacket for temperature control. A mercury mercurous sulphate (MMS), Hg/Hg_2SO_4 RE was used and Pt gauze acted as the CE. The RE was calibrated regularly prior to use by comparison to a dynamic hydrogen/Pt electrode in the same electrolyte used for the measurement (RHE). All potentials reported in this thesis are corrected to the RHE scale. A Luggin capillary was used with the MMS reference electrode to reduce errors in potential due to solution resistance.

3.2.3 Cyclic Voltammetry

The cell was set-up as detailed in section 3.2.2 and filled with 2.5 M H_2SO_4. Concentrated H_2SO_4 was supplied by Fisher Chemicals and then diluted with purified water to obtain the desired concentration. The electrolyte was purged with $N_2(g)$ for 20 min to remove any dissolved oxygen, after which $N_2(g)$ was flowed over the surface of the electrolyte, by retracting the purging tube. Cyclic voltammograms were generally acquired from 0.05 V ⇆ 1.2 V vs. RHE with a scan rate of 10 mV s^{-1}. These parameters were chosen as to include all the features demonstrated by a Pt based WE in an acid environment as depicted in section 3.1.1.

3.2.4 CO Stripping Investigations

The set-up was the same as detailed in the previous section. To prepare an electrode with a monolayer of adsorbed CO, a pre-conditioning phase was employed. The electrode was held at 0.05 V vs. RHE for 1 hr, with CO being purged through the electrolyte for 30 min to adsorb CO on to the Pt surface. For the second 30 min, $N_2(g)$ was purged through the system to remove any dissolved CO, ensuring that any CO oxidation observed in the voltammetric response is from CO adsorbed on the Pt surface only. Cyclic voltammograms were then acquired from 0.05 V ⇆ 1.2 V vs. MMS with a scan rate of 10 mV s^{-1}.

3.3 Rotating Disk Electrode (RDE) Studies

3.3.1 General Principles

The rotating disk electrode (RDE) is one of the few systems where the hydrodynamic and convective diffusion equations have been solved for the steady state. As the RDE rotates, it pulls the solution towards the disc and then flings it out towards the sides as it approaches the electrode surface. The RDE keeps the concentration of all species at their bulk value throughout the whole of the solution except at the electrode surface. At the electrode surface a boundary layer exists where the electrolyte within this layer is stagnant and flux of species

to this layer is via diffusion only. The rate of this diffusion is dependent upon the rotation rate of the disk; this can be attributed to a decrease in the boundary layer thickness at increased rotation rates. The Levich equation (equation 8) describes the relationship between the observed limiting current (for an oxidation), I_L, and the rotation rate, ω, when the surface concentration of the electroactive species is equal to zero.

$$I_L = 0.62nFD^{2/3}\upsilon^{-1/6}c^{\infty}\omega^{1/2} \qquad \textbf{Equation 8}$$

Where I_L is the limiting current density (A cm^{-2}), n, the number of electrons involved in the process, F, the faraday constant (C mol^{-1}) , D, the diffusion coefficient (cm^2 s^{-1}), υ, the kinematic (cm^2 s^{-1}), c^{∞}, the concentration of electroactive species in the bulk solution (mol cm^{-3}), ω, the angular rotation rate of the disc (RPM), and 0.62 a constant, the value of which depends on the units of the other variables in the equation.

A plot of I_L against $\omega^{1/2}$ should therefore be linear and pass through the origin and is used to confirm that the RDE experiment is operating under defined hydrodynamic control.

At any potential the current observed (for a reduction) can be expressed via the kinetic equation (equation 9),

$$-I = nF\vec{k}c_O^{\sigma} \qquad \textbf{Equation 9}$$

where $\vec{k}$ is the rate constant for the electron transfer reaction and c_O^{∞} is the concentration of electroactive species in the bulk solution. If the Nernst diffusion layer model (equation 10) is assumed, then equation 9 becomes:

$$-I = nF\,k_m\left(c_O^{\infty} - c_O^{\sigma}\right) \qquad \textbf{Equation 10}$$

where k_m is the mass transport coefficient, and c_O^σ is the concentration of the electroactive species at the electrode surface.

Combining equations 9 and 10 gives:

$$-\frac{1}{I} = \frac{1}{nF\vec{k}c_O^\infty} + \frac{1}{nFk_m c_O^\infty} \qquad \textbf{Equation 11}$$

which can be simplified to:

$$\frac{1}{I} = \frac{1}{I_k} + \frac{1}{I_L} \qquad \textbf{Equation 12}$$

where I_L is the diffusion limited current density and I_k is the true kinetic current density [11]. Hence the kinetic current can separated out from any mass transport effects.

3.3.2 Electrode Preparation

Prior to applying the catalyst suspension the glassy carbon electrode was polished to a 0.05 μm mirror finish and sonicated in triply distilled water to remove any particulates affixed to the disk. A mixture of 10 mg catalyst and 10 ml chloroform was mixed using an ultrasonic bath for 30 min to form a suspension of well dispersed catalyst. A 5 μL aliquot of this solution was deposited onto the surface of a glassy carbon rotating disk electrode (area = 0.196 cm^2) and allowed to dry. A 5 μL solution of 5 wt % Nafion® in low weight alcohol (50 μL) and IPA (4950 μL) was deposited onto the catalyst layer and allowed to dry in air at room temperature for 30 min.

3.3.3 Equipment and Apparatus

The RDE was attached to a PINE AFMSRX modulated speed rotator and mounted into the RDE cell (figure 5). As with the PGDE studies, all electrodes were connected to a Autolab PGSTAT30 potentiostat and a MMS RE, and Pt gauze counter electrode was used.

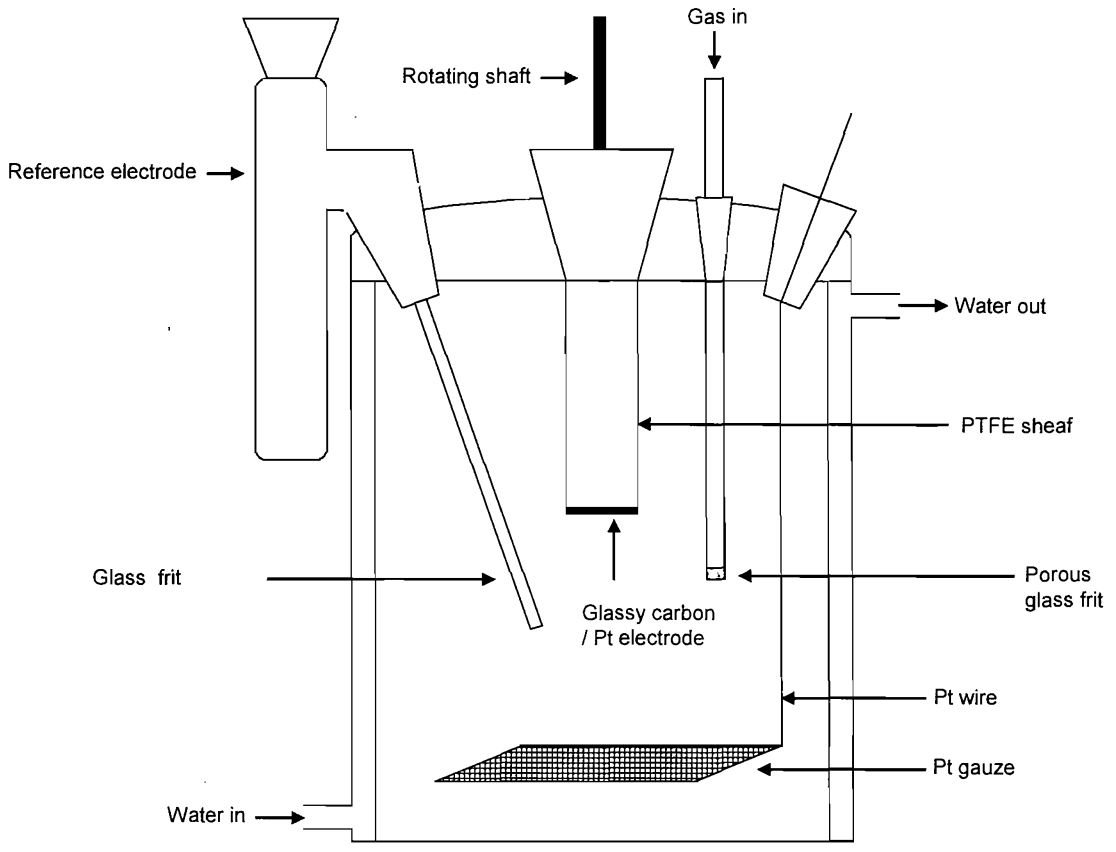

Figure 5 **Electrochemical cell for RDE measurements.**

3.3.4 RDE Experimental Procedure

The RDE cell was set-up as detailed in section 3.3.3 and filled with 1M H_2SO_4. Concentrated H_2SO_4 was supplied by Fisher Chemicals and then diluted with purified water to obtain the desired concentration. The electrolyte was then purged with $N_2(g)$ whilst rotating the electrode at 1000 RPM for 20 min. Cyclic voltammograms were then generally acquired from 0.05 V ⇆ 1.2 V vs. RHE with a scan rate of 10 mV s^{-1}. The available Pt surface area was determined by carrying out a CO stripping experiment. The potential was held constant at 0.05 V vs. RHE for 45 min. For the first 15 min, CO(g) was purged through the solution whilst rotating the electrode at 1000 RPM. For the remaining 30 min, $N_2(g)$ was purged through the solution whilst rotating the electrode at 1000 RPM. Prior to acquiring any CVs, any trapped bubbles on the electrode surface were removed and the rotation rate of the electrode was set to 0 RPM. Cyclic

voltammograms were then generally acquired from 0.05 V ⇆ 1.2 V vs. RHE with a scan rate of 10 mV s^{-1}.

Before carrying out oxygen reduction measurements the electrolyte was purged with $O_2(g)$ for 30 min whilst rotating the electrode at 1000 RPM. Prior to acquiring any CVs, any trapped bubbles on the electrode surface were removed. Cyclic voltammograms were then acquired between 1.0 V and 0.05 V vs. RHE with a scan rate of 2 mV s^{-1}, whilst flowing $O_2(g)$ over the surface of the electrolyte using rotation rates of 900, 1600, 2500, and 3600 RPM. In between measurements, the electrolyte was purged with $O_2(g)$ whilst rotating the electrode at 1000 RPM.

3.4 Mini Cell Testing

The RDE was used as the primary method for assessing the performance of cathodic ORR catalysts. Another way of testing fuel cell electrocatalysts is in a miniaturised fuel cell (mini cell).

3.4.1 Membrane Electrode Assembly (MEA) Preparation

MEAs were prepared by first painting electrodes in a similar way to the paintbrush procedure described previously. The ink mixture prepared was a combination of catalyst, and 11.8 % Nafion® in water. The amount of Nafion® solids added was 75 wt % of the total amount of carbon in the catalyst. The inks were then well mixed using a Silverson (laboratory stirrer) for 10 min. The painting method described in section 3.2.1 was then used to prepare 3.14 cm^2 electrodes with a total metal loading of 0.4 mg cm^{-2}. The MEA was then assembled by sandwiching a 3 x 3 cm^2 square of Flemion® SH30 membrane in between the painted cathode electrode and a screen printed 40 wt % Pt/C electrode (0.4 mg Pt cm^{-2}) for the anode. The MEA was then placed between PTFE and paper sheets, as in figure 6, and hot pressed at 150 °C and 60 psi for 2 min.

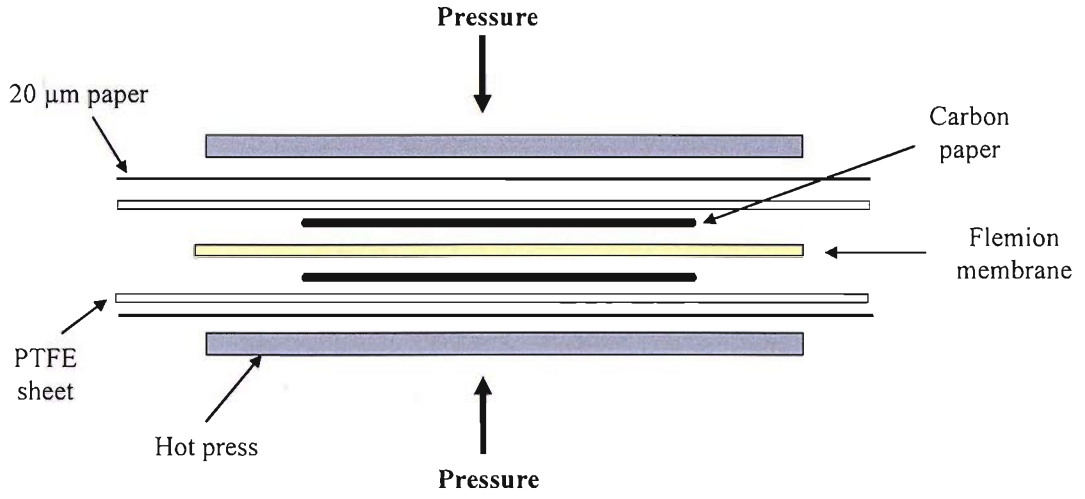

Figure 6 **Schematic diagram of the MEA pressing procedure**

3.4.2 Equipment and Apparatus

The mini cell used for the testing of fuel cell electrocatalysts is detailed in figure 7.

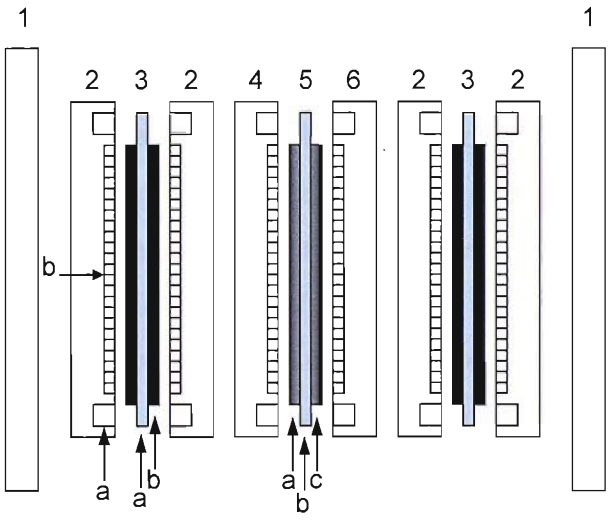

Key:
1: Perspex end plate
2: Graphite end with (a) H_2O water channel and (b) gas flow field
3: Membrane substrate assembly. (a) Toray paper dipped in nafion. (b) Nafion membrane
4: Anode graphite flow field for gas humidification
5: Membrane electrode assembly. (a) Toray paper backed anode catalyst layer. (b) Nafion membrane. (c) Toray paper backed cathode catalyst layer
6: Cathode graphite flow field for gas humidification

Figure 7 **Schematic diagram of the mini cell used.**

The cell is made up of three sets of graphitic plates held together with two Perspex end plates. The graphite plates also act as flow fields, allowing for the access and removal of reactant gases, and contain a water channel to allow for the mini cell to be operated temperatures. The central set of graphitic plates act

us current collectors and are placed either side of the MEA. The set of graphitic plates either side of the central pair include membrane substrate assemblies, which allow for the humidification of the reactant gases. The water channel is connected to a water bath, which pumps water at 80 °C through the system. The MEA is placed between the graphite plates and compressed to a level of 80 % of the initial thickness.

3.4.3 Mini Cell Testing Procedure

The mini cell was operated at 80 °C using humidified reactant gases of hydrogen and oxygen. Gas flow rates of 60 cm^3 min^{-1} were used for both the anode and cathode, with the both sides of the mini cell pressurised to 25 psi. The cathode was set as the working electrode with anode set as the counter/reference electrode. Initially nitrogen was supplied to both sides to purge the system of air whilst the mini cell was allowed to reach its operating temperature. The anode feed gas was switched to $H_2(g)$ until a stable open circuit potential was maintained. At this point the cell was polarised at 0.5 V to check for the degree of hydrogen crossover, with currents less than 40 mA being recorded.

The cathode gas stream was then switched to $O_2(g)$, and left until the open circuit potential had stabilised. The electrode was then conditioned to achieve a fully hydrated state. The potential was initially held at 0.7 V for 10 seconds before being cycled 10 times between 0.95 and 0.65 V, stepping at 0.05 V intervals, holding at each point for 5 seconds. After the preconditioning oxygen reduction polarisation curves were acquired. The potential was initially held at 0.65 V for 150 seconds, and then cycled 2 times between 0.95 and 0.65 V, stepping at 0.025 V intervals, holding at each potential for 30 sec.

The available CO area of the cathode was determined using CO stripping voltammetry. The Potential was held at 0.125 V for 2700 seconds. For the first 180 seconds CO(g) was supplied to the cathode as the reactant gas, after which point the gas was switched to $N_2(g)$. The potential was then swept to 1 V, and then cycled between 1 V and 0.075 V three times at a sweep rate of 10 mV s^{-1}.

4 X-Ray Absorption Spectroscopy

X-ray absorption spectroscopy (XAS) can be subdivided into two sections; X-ray Absorption Near Edge Structure (XANES) and Extended X-ray Absorption Fine Structure (EXAFS). Both the XANES and the EXAFS are powerful characterisation techniques for determining structural parameters of materials without any long range order. XAS has been used as part of this study to gain information about the structural properties of the catalysts prepared by the CSR method.

4.1 Theoretical Aspects of XAS

4.1.1 General Principles

As X-rays pass through a material there is an attenuation in the intensity of the X-rays. This loss in X-ray intensity is proportional to the incident intensity of the X-rays (I_0) and the path length (x). This relationship can be expressed as shown below (equation 13):

$$dI = -\mu I\, dx \qquad \textbf{Equation 13}$$

where I is the intensity of the X-rays and μ is the linear absorption coefficient, which is a function of the photon energy, E. Integrating over the path length, x, results in the Beer Lambert equation (equation 14):

$$I = I_o e^{-\mu(E)x} \qquad \textbf{Equation 14}$$

The absorption of X-rays by the material will decrease with increasing photon energy until a critical energy is reached. At this point a sudden rise in X-ray absorption occurs. This feature is the absorption edge and is attributable to the excitation of a core electron of the absorber into an excited state or the continuum. The ejected photoelectron is released with kinetic energy, E_k:

$$E_k = h\nu - E_{binding} \qquad \textbf{Equation 15}$$

The X-ray absorption coefficient, μ, dictates the intensity of the absorption edge and is proportional to the probability of the absorption of a photon as dictated by Fermi's golden rule (equation 16) [12].

$$\mu \propto \sum_f \left|\langle \psi_f | p \cdot A(r) | \psi_i \rangle\right|^2 \delta\left(E_f - E_i - \hbar\omega\right) \qquad \textbf{Equation 16}$$

ψ_i and ψ_f describe the initial and final states respectively, p represents the momentum operator and A(r), the vector potential of the incident electromagnetic field.

The overall process is termed the photoelectric effect, with the designation of the absorption edge dependent on the principle quantum number of the orbital from which the electron was ejected (figure 8).

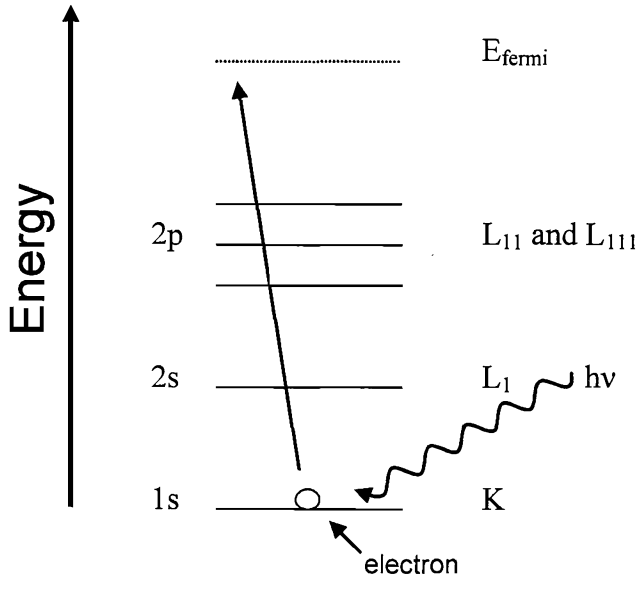

Figure 8 **Schematic diagram of the photoelectric effect - excitation of a 1s electron giving rise to the K edge.**

The outgoing photoelectron can be described as a spherical wave function with wave vector, k:

$$k = \sqrt{\left(\frac{8\pi^2 m_e}{h^2}\right)(h\nu - E_0)} \qquad \textbf{Equation 17}$$

where, m_e, is the electron mass, and E_0 is the zero point energy, which is usually taken to be the inflection point of the absorption edge.

A typical XAS spectrum is shown below, highlighting the absorption edge, the XANES region and the EXAFS region (figure 9).

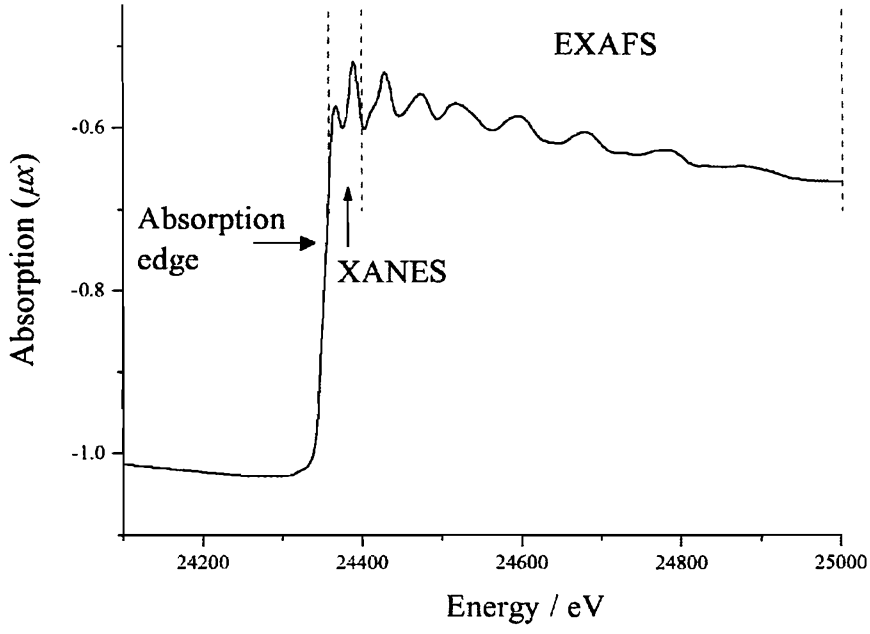

Figure 9 **XAS spectrum of a Pd foil at the Pd K-edge.**

The XANES region arises mainly due to electronic transitions from the core level to higher unfilled or partially filled orbitals, e.g. $s \rightarrow p$, or $p \rightarrow d$ and can extend up to 50 eV past the absorption edge. The XANES region is quite complex with effects such as multiple scattering and distortions of the excited state contributing

to the overal spectrum. As a consequence, the majority of XANES analysis is limited to a semi-quantitative interpretation, rather than being fully modelled.

Some absorption edges have a very large initial peak after the absorption edge. This peak is termed the 'white line' as it appeared as a bright white line in early XAS experiments involving photographic plates. The appearance of the white line is associated with electronic transitions to orbitals with a high density of states [13]. Differences in the Pt L_2 and L_3 white lines have been used to calculate the fractional d-electron occupancy of Pt based alloys [2, 13, 14]. Detailed explanation of the method used for the semi-quantitative determination of unoccupied d-electron states will be discussed later.

The oscillatory variation of the absorption of X-rays as a function of energy beyond the absorption edge is the EXAFS region. The emitted photoelectron can be backscattered by the neighbouring atoms. As a result, the final state wave function depends on both the outgoing and the backscattered waves.

$$\psi_f = \psi_{outgoing} + \psi_{backscattered} \qquad \textbf{Equation 18}$$

The EXAFS arises due to the interference (figure 10) between the forward scattered and backscattered photoelectrons and can extend up 1000 eV past the absorption edge.

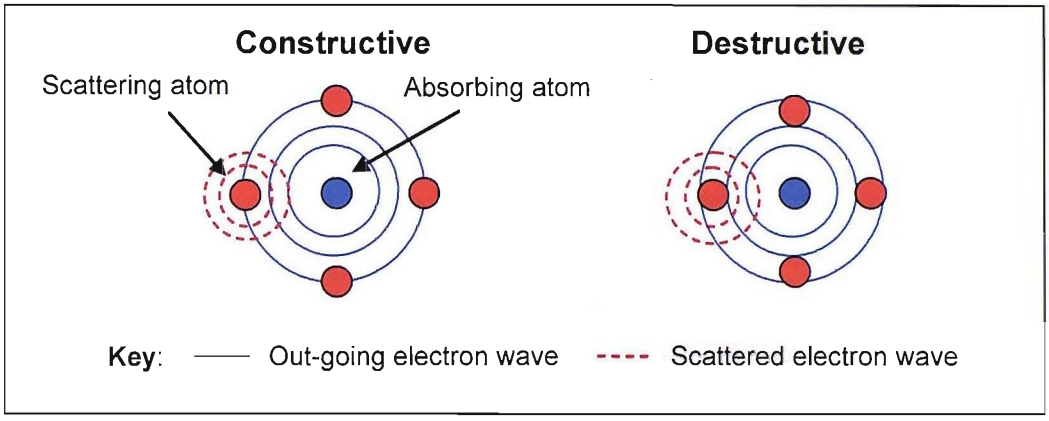

Figure 10 **Schematic of the interference patterns in the final state wave-functions (The rings represent the maxima of the forward scattered and back scattered waves).**

The variation of the absorption coefficient, μ_{tot}, as a result of this interference can be defined as follows:

$$\mu_{tot} = \mu_0 \cdot (1 + \chi) \qquad \textbf{Equation 18}$$

where μ_0 is the background absorption of a free atom as a result of elastic and inelastic X-ray scatter. The EXAFS oscillations are given by χ and are defined as the normalized oscillatory part of μ. The EXAFS can be extracted from the data as a function of the wavevector, k, in the following equation:

$$\chi(k) = \frac{\mu_{tot}(k) - \mu_0(k)}{\mu_0(k)} \qquad \textbf{Equation 19}$$

4.1.2 Progression of EXAFS Theory

Work by Friche in the 1920's was the first to report the EXAFS oscillations in XAS spectra [15]. However, it was not until Sayer *et al.* applied a point scattering theory to experimental EXAFS data that structural information could be derived [16]. This work was expanded on by Lee *et al.* [17], giving rise to a point scattering plane wave approximation. This was applied to EXAFS of well

known crystalline systems and the experimentally determined parameters were found to be in good agreement with those already known. The theory assumes that the distance to the neighbouring atom is much larger than the atomic radius of the central atom. As such, the spherical wave can be approximated as a plane wave, greatly simplifying the derivation of structural parameters. This theory does not hold true for low values of k below 3 $Å^{-1}$ and has led to more advanced simulations using spherical or curved wave theory. The plane wave approximation also assumes that single scattering effects dominate, i.e. the photoelectron is only scattered once before returning to the central atom. However, there are systems where multiple scattering (figure 11) greatly affects the EXAFS.

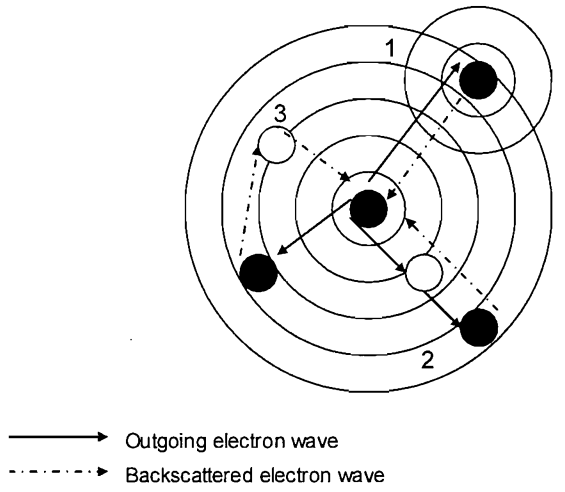

Figure 11 **1) single scattering path; 2) and 3) multiple scattering paths**

To be able to extract any structural information beyond the first coordination shell, the effects of multiple scattering need to be taken into account. Lee *et al.* [17] also described a quantitative means of incorporating multiple scattering effects into EXAFS theory, which has been expanded on in recent years [12].

4.1.3 EXAFS Equations

The pioneering work of Sayers *et al.* [16] is still the basis on which current analyses are performed. The EXAFS function, $\chi(k)$, can be represented as a summation of the sine waves produced from the outgoing photoelectron

wavefunction, together with the backscattered wavefunction from each co-ordination shell, of atom type, j (equation 20).

$$\chi(k) = \sum_{j=1}^{shells} A_j(k) \sin \delta_j(k) \qquad \textbf{Equation 20}$$

The amplitude term, A_j, can be described as (Equation 21):

$$A_j(k) = \frac{N_j}{kR_j^2} S_0^2 F_j(k) e^{-2k^2\sigma_j^2} e^{\frac{-2R_j}{\lambda(k)}} \qquad \textbf{Equation 21}$$

where: N_j is the number of atoms of type j at distance R_j from the absorber atom.

S_0 is the amplitude reduction factor. This describes multi-electron processes and central atom shake-up and shake-off as a result of relaxation after photoionisation [18].

F_j is the backscattering amplitude from the jth atom, and is element specific. F_j can be extracted from reference compounds or calculated theoretically [18]. In the work presented in this thesis, theoretical calculations were used.

$e^{-2k^2\sigma_j^2}$ is the Debye Waller term and partially arises due to thermal influences causing fluctuations in the positions of the atoms from the equilibrium atomic positions.

σ_j^2 is the relative mean squared disorder along the distance between the absorbing atom and neighbouring atom, j due to thermal and static motions. The result of this term is to dampen the amplitude of χ at high regions of k.

$e^{\frac{-2R_j}{\lambda(k)}}$ accounts for the finite lifetime of the excited state, with λ representing the mean free path of the photoelectron.

The EXAFS function also contains a phase component reflecting the effects that interatomic distances and energy have on the oscillatory structure:

$$\sin\delta(k) = \sin\left(2kR_j + \varphi_j(k)\right) \qquad \textbf{Equation 22}$$

where R_j is the interatomic distance between the absorber atom and the backscattering atom and $\varphi_j(k)$ is the back scattering phase shift, which can be expressed as follows:

$$\varphi_j(k) = 2\varphi_{absorber}(k) + \varphi_{backscatterer}(k) \qquad \textbf{Equation 23}$$

The absorber contributes twice the amount to the phase factor as the back scattering atom. This is because the photoelectron sees the potential created by this atom twice. As with the case of F_j earlier, the phase shift can be extracted from reference compounds or calculated theoretically.

In summation, the EXAFS formula can be used to extract structural parameters from the experimental data. It allows for the distance to the neighbouring atom, coordination number, and Debye Waller factor to be calculated.

4.1.4 Data Analysis

The data processing of the raw XAS spectra was achieved using the Daresbury suite of programs, including, EXCALIB and EXBROOK. The first step of the data processing is to read the raw data file into the EXCALIB program. As the data is initialised, the energy scale is converted from the position of the monochromater into the more useful electronvolt scale. When the data has been acquired in fluorescence mode (section 4.2.4) the response from each individual detector channel can be viewed. If the data from a single channel is deemed unsatisfactory, it can be set a weighting of zero and will not contribute to the overall XAS spectrum. The EXCALIB program also allows for the summing together of multiple scans acquired for the same experiment to increase the signal to noise ratio.

The role of the EXBROOK program is to normalise the data into a form where the EXAFS part of the spectrum can be used to derive structural parameters. The

first step in this process is to subtract the pre-edge background from the data. To remove the pre-edge background absorption two quadratics are fitted, one to the pre-edge slope and one to the post-edge region. The line of best fit is subtracted from the spectrum and the edge jump set to a value of one (figure 12) to standardise the intensity scale. The edge jump is defined as the distance between the linear pre-edge and smooth post-edge background extrapolated to E_0.

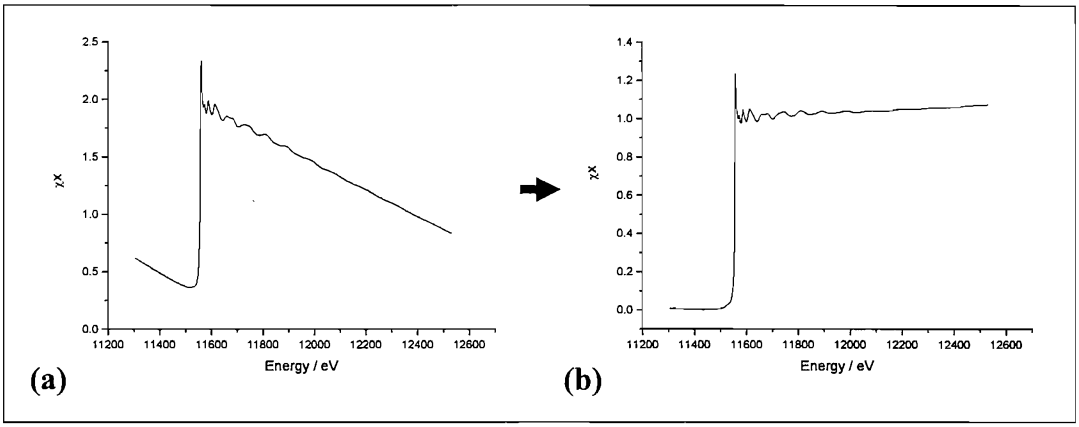

Figure 12 **Raw XAS data (a) before and (b) after pre-edge background subtraction and normalisation.**

The energy scale is then set relative to the position of E_0, where the energy at E_0 is set as 0 eV (figure 13). Unless there is a sharp pre-edge feature, E_0 is taken as the maximum of the first derivative of the XAS spectrum as shown in figure 11.

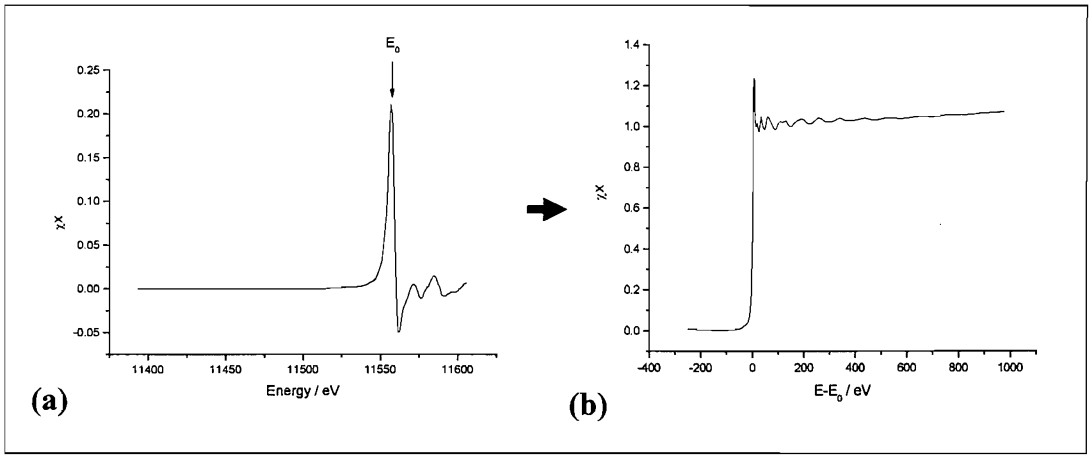

Figure 13 **(a) E_0 identification using the first derivative and (b) the rescaled XAS spectrum.**

The final step of the data processing in EXBROOK is to extract the EXAFS oscillations from the absorption spectrum and remove the contribution due to μ_0 (equation 18). The post-edge background absorption is approximated by fitting a cubic spline using the method developed by Cook and Sayers [19]. It is imperative that the cubic spline does not follow the spectrum too closely or some of the data will be lost in the background removal. The cubic spline technique is applicable to EXAFS data as there is a continuous control in the smoothing of the cubic spline. The cubic spline function (equation 24) [19, 20] contains a smoothing factor, SM, which determines the spline function of background, BCK, and a weight factor, WE, which can be used to enhance the high k part of the spectrum. The start of the background subtraction is set to occur at the start of the EXAFS region, which is normally 50 eV past the absorption edge. The end product of the background removal is a chi plot where the amplitude of the oscillations is evenly distributed above and below the axis (figure 14). The Fourier transform of the chi plot reflects the radial distribution function of neighbours surrounding the absorbing atom. In optimising the background, the Fourier transform should normally have an amplitude for the first peak between 1.8 and 3 Å maximised, with any contributions below 1 Å minimised.

$$\sum_{i=1}^{NPTS} \frac{(\mu_i - BCK_i)^2}{e^{-WEk_i^2}} \leq SM \qquad \textbf{Equation 24}$$

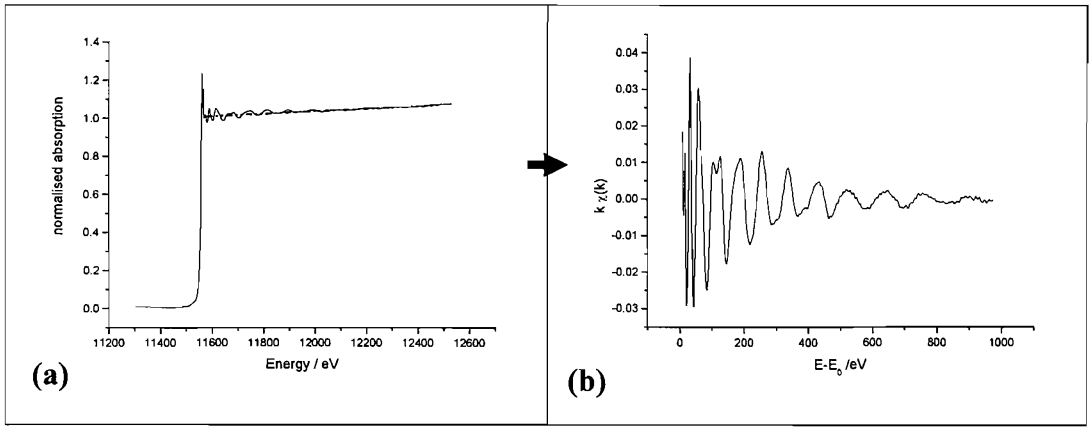

Figure 14 **(a) Selection of cubic spline for post-edge background removal (b) and the resulting chi plot.**

Once the data has been processed, it can be read into EXCURV98 [21] where the chi plot can be fitted to obtain structural parameters. The EXCURV98 program simulates EXAFS spectra using rapid curve wave theory [22] and Rehr Albers theory [12, 23, 24] from the parameters of the radial shells of atoms surrounding the central atom. When the data is read into EXCURV98, the energy scale is converted (equation 25) from eV to k space ($Å^{-1}$), which evens out the amplitude across the energy range. The resulting chi plot is then showed along with its corresponding Fourier transform (figure 15).

$$k = \sqrt{\left(\frac{8\pi^2 m_e}{h^2}\right)(h\nu - E_0)} \qquad \textbf{Equation 25}$$

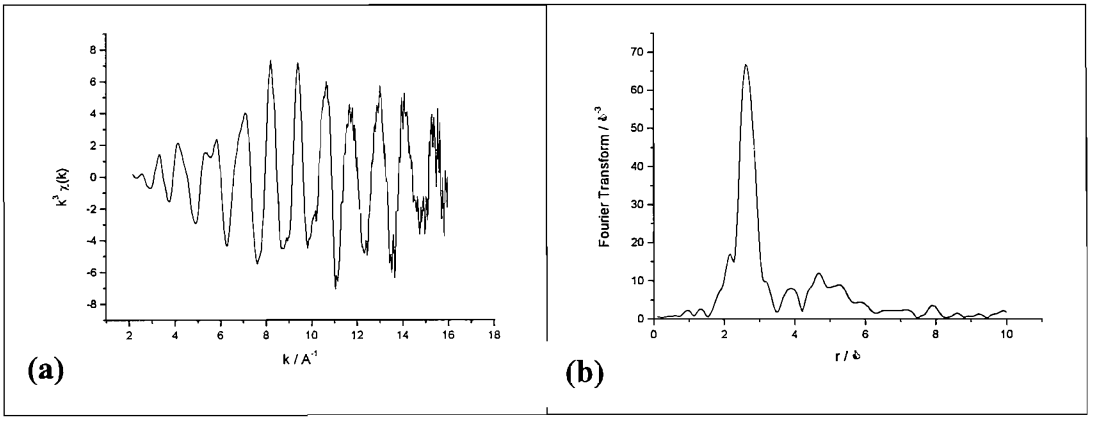

Figure 15 **(a) Chi data (b) and its corresponding Fourier transform.**

The simulated EXAFS spectrum is generated by EXCURV98 by using probable values for the: coordination number (N), distance to the nearest neighbour (r), the Debye Waller term ($2\sigma^2$) and the shift in Fermi energy (E_f). These values are then refined using a least-squares minimum of the fit index. The goodness of fit is represented by the R_{EXAFS} value (equation 26).

$$R_{EXAFS} = \sum_i^N \frac{1}{\sigma_i}\left(\left|\chi_i^{\exp}(k) - \chi_i^{fit}(k)\right|\right) \times 100\% \qquad \textbf{Equation 26}$$

where N is the number of data points, σ_i the standard deviation for each data point, i, and $\chi_i^{exp}(k)$ and $\chi_i^{th}(k)$, the experimental and theoretical EXAFS, respectively. An R_{EXAFS} value between 20 – 30 % is usually considered to be a reasonable fit, although larger values are deemed acceptable if the data is noisy. Errors in the parameters are estimated from standard deviations. The number of statistically justified free parameters, n, that may be fitted should also be taken into account when fitting the data. This is estimated using the Nyqvist theorem (equation 27):

$$n = \frac{2\Delta k \Delta r}{\pi} + 1 \qquad \textbf{Equation 27}$$

where Δk and Δr are the ranges in k- and r-space over which there is useful data.

There is a variation in the amplitude of the EXAFS oscillations with respect to k, with the amplitude being less at high k space. The EXAFS function can be multiplied by k^i, where i = 1, 2, or 3. This allows the emphasis of the chi plot to be tilted in favour of high or low Z (where Z is the atomic number) neighbours. A weighting of 1 is used for low Z neighbours, 3 for high Z neighbours, and 2 being used as a compromise between low and high Z neighbours.

4.2 Experimental Aspects of XAS

4.2.1 X-ray Radiation Source

Traditionally, X-rays are produced when there is a sudden deceleration of fast moving electrons when they are aimed towards a target material, as is the case with the X-ray tube. The majority of electrons undergo multiple collisions and transfer part of their energy to the target material. As a result, a continuous Bremstrahlung spectrum of X-rays is produced, which is also commonly termed as white radiation. The spectrum produced also contains characteristic lines due to emission of core electrons within the target material, but it is the white

radiation which is used for XAS studies. Synchrotron radiation sources have revolutionised experimental X-ray studies due the advantages offered: high intensity X-rays, 10^6 more intense then conventional sources; tunability over a wide energy range with a continuous spectrum; high degree of collimation; and the plane-polarization of the X-rays produced [25].

In a synchrotron an electron beam, travelling near the speed of light, is contained within a storage ring (at ultra high vacuum) by a set of bending magnets. When the beam is bent by the magnets, the beam is accelerated and results in the release of high energy radiation. As the electrons are travelling near the speed of light, the radiation pattern is distorted by relativistic effects. The subsequent radiation pattern changes to a narrow cone in the direction of the motion of the electron beam. This radiation can then be harnessed to carry out a range of scientific experiments. The characteristic wavelength of the radiation is governed by the radius of curvature and the energy of the particles (equations 28 and 29).

$$\lambda_C = \frac{4\pi r}{3\gamma^3} \qquad \textbf{Equation 28}$$

$$\gamma = \frac{E}{M_e c^2} \qquad \textbf{Equation 29}$$

where λ_c, is the critical wavelength (m), r, the radius of curvature (m), E, the energy of the electron (kg m^2 s^{-2}), M_e, the mass of an electron (kg), and c is the speed of light (m s^{-1})

All XAS experiments undertaken as part of this investigation were carried out at the SRS (figure 16) at Daresbury Laboratory, Warrington, UK.

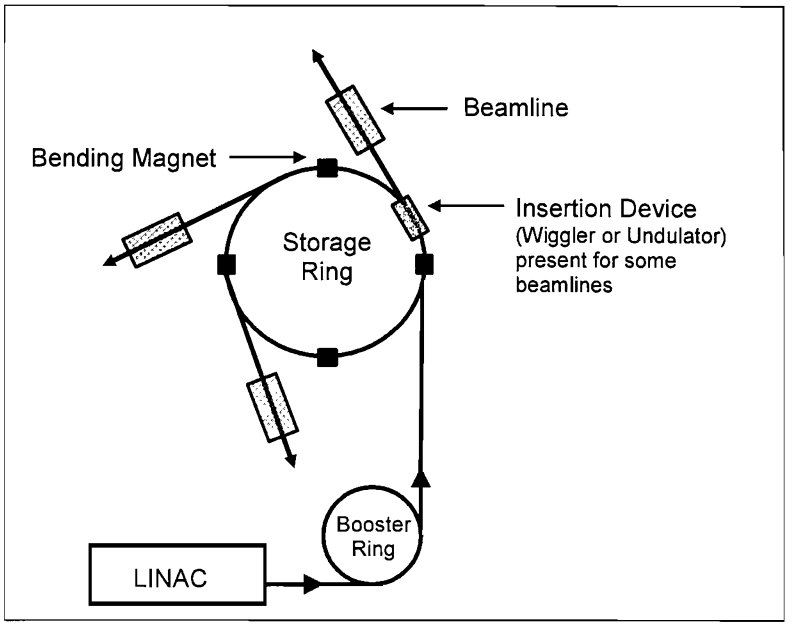

Figure 16 **A Schematic diagram of the SRS at Daresbury laboratory [26] (not to scale, with most of the bending magnets not shown).**

The LINAC (Linear Accelerator) produces an electron beam which is accelerated by the interaction with microwaves produced by a klystron. On achieving an energy of 12 MeV, the electron beam is injected into the booster ring. The electrons are further accelerated to an energy of 600 MeV, at which point the beam is injected into the main storage ring. The klystron then acts to cause the electrons to travel around the storage ring in a series of bunches, with a set distance between each bunch; typically nanosecond pulses of electrons separated by a few microseconds. The energy of these electron pulses is around 2 GeV. The beam is then contained within the storage ring by a set of bending magnets, which as mentioned earlier, causes an acceleration of the electrons and a release of high energy radiation. The microwaves produced by the klystron are required to keep the electron beam in orbit.

The critical energy of the SRS can be increased by inserting devices in between the bending magnets. Wigglers and undulaters are typical insertion devices used. A wiggler is a three pole magnet, and when the electron beam travels through the wiggler it is forced to follow a chicane type path. This reduces the radius of curvature, and shifts the characteristic wavelength to lower values (higher energy). An undulater uses an array of permanent magnets above and below the path of the electron beam. As the beam passes through the magnets, its trajectory

oscillates in the horizontal plane. Interference effects in undulater radiation yield resonance peaks in the output spectrum. Variation in the distances between the magnets and the electron beam allow the radiation achieved to be optimised for a given experiment. As a general rule, undulaters are used for soft X-ray experiments whereas wigglers are used for hard X-ray experiments.

The storage ring is operated under ultra high vacuum (UHV) conditions, typically 10^{-10} mbar. However, the energy of the beam still decays due to collisions with any remaining gas molecules. As a consequence a new beam has to be injected periodically.

4.2.2 Experimental Stations 7.1 and 16.5

The experimental stations used for the XAS studies were stations 7.1 and 16.5 at the Daresbury Laboratory. These beamlines were chosen due to the energy of the X-rays produced at each station and their suitability towards the absorption edges being probed.

Station 7.1 utilises a harmonic rejecting sagitally focusing double crystal Si(111) monochromator to acquire XAS data in the range of 4 keV to 10 keV. The sagital focusing allows for the X-ray beam to be maintained as a focused spot by dynamically bending the crystal whilst carrying out XAS experiments. This gives rise to an increase of X-ray flux and, as a consequence, improved signal to noise ratio. The fluorescence detector uses a monolithic structure nine-channel array on a germanium wafer with a diameter of 21.8 mm. This detector design led to an increase in the total active area of the detector compared to conventional multi channel detectors, yielding a high photon count rate and improved resolution [27].

Station 16.5 is designed for the study of ultra dilute samples and is on a 6 T Wiggler beamline, and utilises a water cooled double crystal Si(220) monochromator to acquire XAS measurements in the range of 7 KeV to 40 keV. Vertical collimation is achieved using a 1.2 m uncoated plane mirror. The second

crystal is dynamically bent to provide horizontal focus. The fluorescence detector on the station is an Ortec 30-element Ge Solid state detector.

Both stations use the double crystal geometry of the monochromators to select a single, well –defined energy from the X-ray source. The Bragg relation (equation 30) relates reflections from a crystal plane as a function of the incident angle, $\theta_{i,,}$ and is used to select the well defined photon energy.

$$n\lambda = 2d\sin(\theta_i) \qquad \textbf{Equation 30}$$

where λ is the wavelength of light, d is the spacing of the atoms in the crystal and θ_i is the angle of incidence. The second crystal is positioned at the same angle as the first crystal to correct for the angular deflection. The first order reflection is the most intense and is used for the XAS experiments. However, higher order harmonics can also be present in the reflected beam. The higher order harmonic reflections have a smaller angle of acceptance compared to the first order reflection. Therefore, the fundamental reflection has a large overlap of acceptance angle compared to the higher harmonic reflections [28]. Consequently, by detuning the second crystal some of the harmonic content can be reduced. This process is called harmonic rejection. Typically a harmonic rejection of 50 % was used for the lower energy edges such as the Pt $L_{3,}$ Cr K, Co K and Ce L_3, and a value of 70 % was used for the higher energy edges such as the Pd K. By convention, the value chosen, 50 % or 70 % represents the fraction of the maximum signal retained following detuning of the second crystal.

4.2.3 XAS Transmission Experiments

The simplest mode of XAS data acquisition is the transmission experiment. A transmission experiment measures the variation in absorption of X-rays as the energy of the incident photons is systematically increased. A basic set-up for this type of experiment is shown below (figure 17).

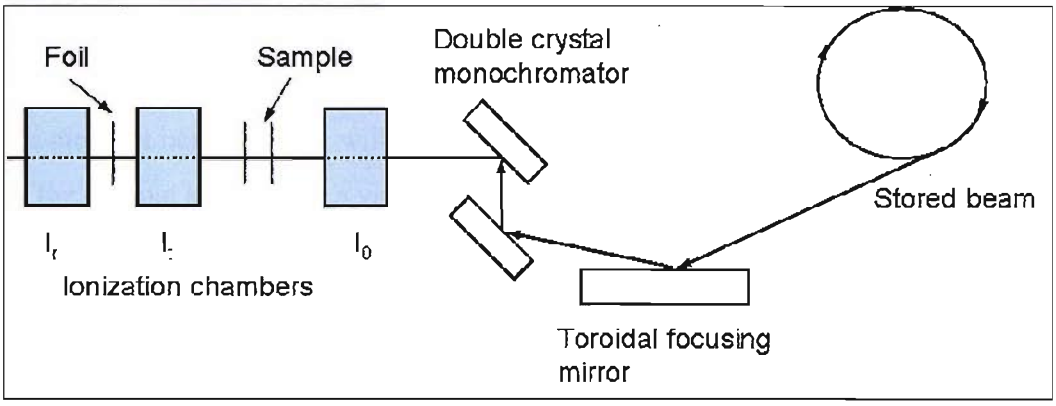

Figure 17 **Typical set-up for a transmission XAS experiment**

The role of the ion chambers is to measure the intensity of the X-ray beam. I_0 measures the incident intensity, I_t measures the intensity of the X-rays after passing through the sample, and I_r measures the intensity of X-rays after passing through the sample and a Pt reference foil. Each ion chamber is filled with a mixture of inert gas, set to absorb a specific amount of incident flux. I_0 is set to absorb 20 %, where as I_r and I_t are both set to absorb 80 %. The ion chambers contain two metal plates, with a constant potential applied between them, so that ions are attracted to the negative side and the electrons to the positive. The size of the resultant current that flows is therefore directly related to the number of photons entering the chamber. The absorption of the X-rays by the sample is given by $\ln(I_o/I_t)$.

The role of I_r is to act as a reference chamber so that the energy of the X-rays can be calibrated against a metal foil. Sometimes the energy readings can shift very slightly with time. For XANES studies where the edge position contains important information, it is imperative to have an internal calibration so that energy values can be assigned with a large amount of confidence.

Transmission experiments are typically used when there is a suitably large enough concentration of the element being probed within the sample. If the sample is too dilute then the resulting absorption of X-rays will be particularly weak, resulting in a poor signal to noise ratio. However, if the sample prepared contains too much of the element under study then all the X-rays will be absorbed. It is important when conducting an XAS experiment to consider all the

constituents present in the sample (including sample diluents), their relative proportions, and their absorption coefficients. Ideally the absorption edge (μx) of the element being probed will have a value of 0.3 to 1, with the total absorption of the sample kept below a value of 2.5. If the absorption of the sample is too high then self-absorption effects occur. This gives rise to errors in the determination of coordination numbers from EXAFS spectra. The mass of sample required to yield the desired edge step can be calculated using the equation below (equation 31)

$$mass = \frac{(\mu x)(area)}{(\mu / \rho)} \qquad \textbf{Equation 31}$$

where (μ / ρ) is the mass absorption coefficient of the element of interest, with ρ being the density. Values for mass absorption coefficient have been calculated by McMaster *et al.* [29] and have been used in this study to calculate the absorbance of the samples used.

If possible, transmission is the desired mode of data acquisition due to its simplicity and lack of statistical noise. However, there are some areas where care needs to be taken when conducting transmission experiments. For example, when preparing pellets used in the gas treatment cell (section 4.2.5), it is vital to make sure there are no pin holes present in the end pellet. Pin holes allow some of the incident X-rays to pass through the sample unabated, which affects the data acquired in transmission.

4.2.4 XAS Fluorescence Experiments

When the sample is too dilute, the absorbance by the target element is low, and the absorbance of the matrix may dominate the end spectrum. At this point it is not possible to conduct a suitable transmission experiment, so the data can be acquired in fluorescence mode (figure 18). The photoelectric effect produces a core hole in an atom of the target element. This core hole then becomes filled by an outer shell electron. The energy difference between the outer shell and the

inner shell is emitted as fluorescent radiation characteristic of the target element. The fluorescence EXAFS signal consists of only a small fraction of the total absorption and is proportional to the incident intensity as follows:

$$\mu(E) = \frac{I_{fluorescence}}{I_o} \qquad \textbf{Equation 32}$$

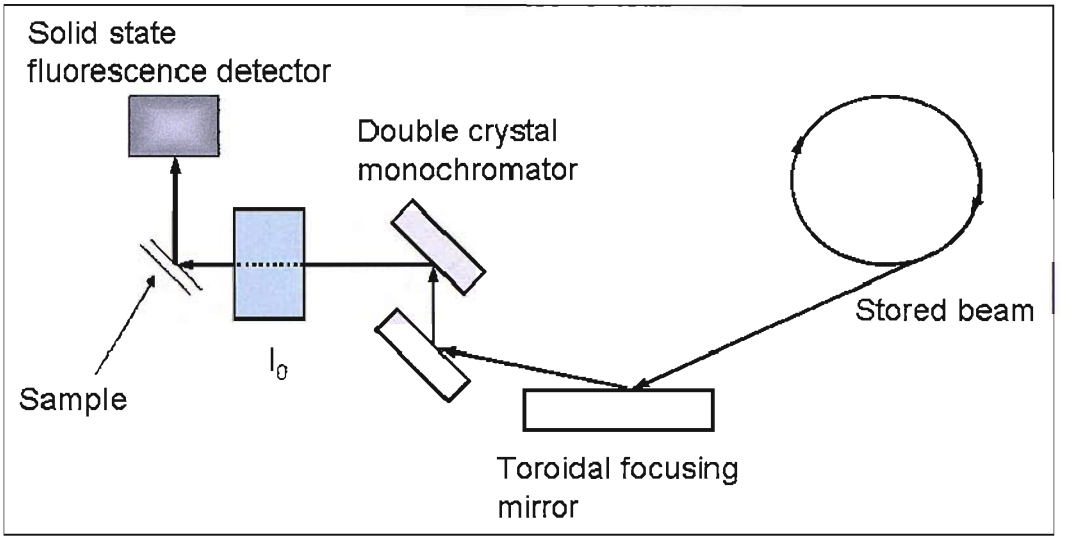

Figure 18 **Typical set-up for a fluorescence XAS experiment.**

As can be seen above (figure 16), the sample is aligned at 45 ° to the incident radiation to maximise the solid angle. The fluorescence radiation is detected using various types of solid state detector. The fluorescence radiation has a specific energy which is different from that of the radiation, which arises due to scattering processes which is similar to the energy of the incident beam. Solid state detectors can discriminate between radiation of different energies and have resolutions around 100 eV. Since the background radiation is significantly larger than the fluorescent radiation the detectors are easily saturated. Care must therefore be applied when positioning the fluorescence detector, assuring that the detector is close enough to yield enough signal without causing saturation.

4.2.5 Gas Treatment Cell

For conventional XAS experiments not involving electrochemical cells, the Pt based catalysts to be studied were prepared as BN pellets. The preparation of

pellets involves grinding a set amount of catalyst and BN to form a homogenous mixture and then compacting this in a purpose built press to form a self supporting wafer. BN was used in preference to polyethylene due to the better gas flow through the pellet. The pellet holder used in the pressing process can then be transferred to a gas treatment cell (figure 19).

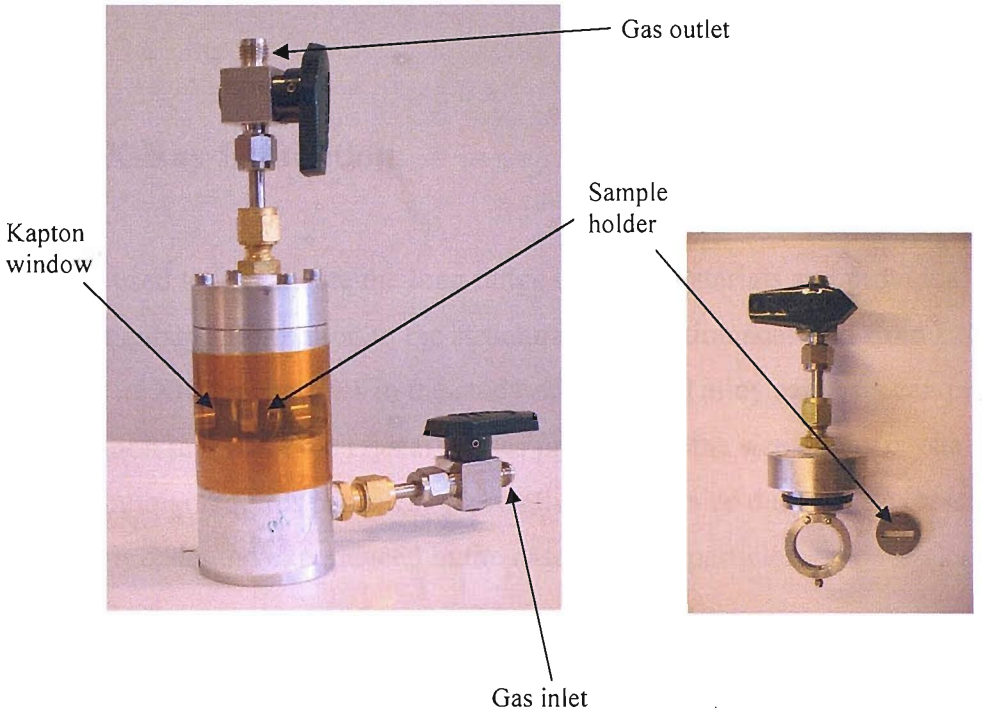

Figure 19 **Gas treatment cell, highlighting gas inlet and outlet, Kapton windows, and the sample holder.**

The gas treatment cell contains a gas inlet and gas outlet port so that different gases can be purged through the cell. The gas can be contained within the cell by shutting the outlet and inlet ports. The cell consists of a series of Kapton windows to allow for the entry and exit of the X-ray beam. As can be seen in figure 19, the sample holder is mounted into a removable arm. The angle of the arm with respect to the cell can be varied, so the cell can be set-up for both transmission and fluorescence experiments. When aligning the sample in the X-ray beam, checks were made using photographic paper to confirm that the beam passed through the cell without clipping the sample holder. When working on station 7.1 at the Cr and Co K edge, high density polyethylene sample holders were used to reduce the effect of scatter. On station 16.5, where the Pt L_3 and Pd K edges were investigated, sample holders made of steel were used.

When exposing the sample to different gas environments, the cell was purged with the desired gas for ~ 1 hour before closing the gas taps. All gas treatments were performed away from the beamline for safety reasons. The cell was also leak checked prior to use. At the end of an experiment the cell was purged with N_2(g) for 30 min before opening to air.

5. X-Ray Diffraction

XRD is used to investigate the long range order of materials and provides complimentary information to the structural information achieved from EXAFS. The use of XRD techniques in the study of metal and alloy catalysts can provide information regarding the crystal phases present and the size of any crystallites. The technique requires particles of a relatively large size due to the excessive X-ray line broadening experienced in the case of small particles.

5.1 Theoretical Aspects of XRD

As an X-ray beam is targeted at the sample, the electron density around the nuclei causes the X-rays to be scattered. The lattice planes of the crystals act like mirrors with the X-rays reflecting off each successive crystal plane. If the glancing angle of the X-rays gives rise to a path-length difference between reflections of successive mirror planes which is equal to an integer number of wavelengths, then a maximum due to constructive interference occurs [32]. This condition can be expressed using Bragg's law:

$$n\lambda = 2d_{hkl}\sin\theta \qquad \textbf{Equation 33}$$

where λ is the wavelength, θ is the diffraction angle, d_{hkl} is the spacing of the planes (hkl) and n is an integer. The Pt catalysts are not single crystals; they consist of many small crystallites with random orientations. For every set of

crystal planes, one or more crystals will be in the correct orientation to give the correct Bragg angle to satisfy Bragg's law.

Given that the intermolecular spacing, d_{hkl}, (assuming an fcc structure) is as follows:

$$d_{hkl} = \frac{a}{\sqrt{h^2 + k^2 + l^2}} \qquad \textbf{Equation 34}$$

then Bragg's law can be used to determine the lattice parameter, a, once the fcc peak positions, θ_{hkl}, have been identified.

$$\sin^2 \theta_{hkl} = \frac{\lambda^2}{4a^2}(h^2 + k^2 + l^2) \qquad \textbf{Equation 35}$$

As mentioned previously, the diffraction lines broaden on decreasing particle size. This broadening can be used to give an estimate of the particle size, by measuring the FWHM value of the peak after a background has been subtracted and a Gaussian peak fitted. From the FWHM value, the average particle size, L, can be estimated using the Scherrer equation:

$$L = \frac{0.9\,\lambda}{B_{2\theta}\cos\theta_{\max}} \qquad \textbf{Equation 36}$$

where λ is the wavelength and $B_{2\theta}$ is the measured broadening in radians.

5.2 Experimental aspects of XRD

All XRD data reported as part of this work were carried out at the Johnson Matthey Technology Centre, by one of their technicians.

6. Transmission Electron Microscopy (TEM) and Energy Dispersive X-Ray Analysis (EDX)

The use of TEM in the study of supported metal and alloy catalysts can be used to provide information regarding the shape and size of the particles including the particle size distribution. The EDX function allows for the proportions of the different components of the alloy to be assessed at different points across the particle, and on different particles. If the EDX shows that the components are in similar proportion throughout the particle for a number of particles, it suggests that the sample is well alloyed.

6.1 Theoretical Aspects of TEM and EDX

A typical TEM system is a microscope column type arrangement where the illumination is provided by an electron gun at the top which is focussed onto the specimen by a series of electromagnetic lenses. The specimen has to be a very thin sample, with a thickness less than 2000 Å. The image of the sample can be viewed physically by looking at a viewing screen, usually a simple layer of X-ray fluorescent material, through a lead glass window. The microscope is also fitted with a camera which must work in the vacuum within the microscope, typically 1×10^{-5} mbar [33].

Bombardment of a specimen with high energy electrons results in a characteristic emission of X-rays. The wavelengths of the X-rays are dependent upon the atoms that are present in the sample. Each element has characteristic X-ray lines relating to the excitation of a core electron to a higher energy level. Analysis of these characteristic emission lines allows for the relative proportion of each constituent to be determined. The detector normally consists of a small semi-conductor such as Si, held in a position so that the X-ray emission from the sample falls upon it. In the case of a TEM system, the detector is normally placed within the objective lens. The detector works by exciting electrons into the conduction band of the silicon, leaving an identical number of positively charged holes in the outer-electron shells. The number of electron-hole pairs generated is proportional to the energy of the X-ray photon being detected [33].

6.2 Experimental Aspects of TEM and EDX

All TEM EDX data reported as part of this work were carried out at the Johnson Matthey Technology Centre, by one of their technicians.

7 Fixed Bed Reactor Testing

Fixed bed reactor testing was employed to assess the performance of modified Pt/γ-alumina samples for the gas phase water gas shift reaction (WGS) and CO oxidation. Different partial pressures of CO were used in the case of the CO oxidation testing to determine the reaction order.

7.1 Equipment and Apparatus

Both tests were carried out using the reactor detailed below (figure 20). An enlarged schematic of the reactor tube (figure 21) is also included, showing the positions of the three thermocouples.

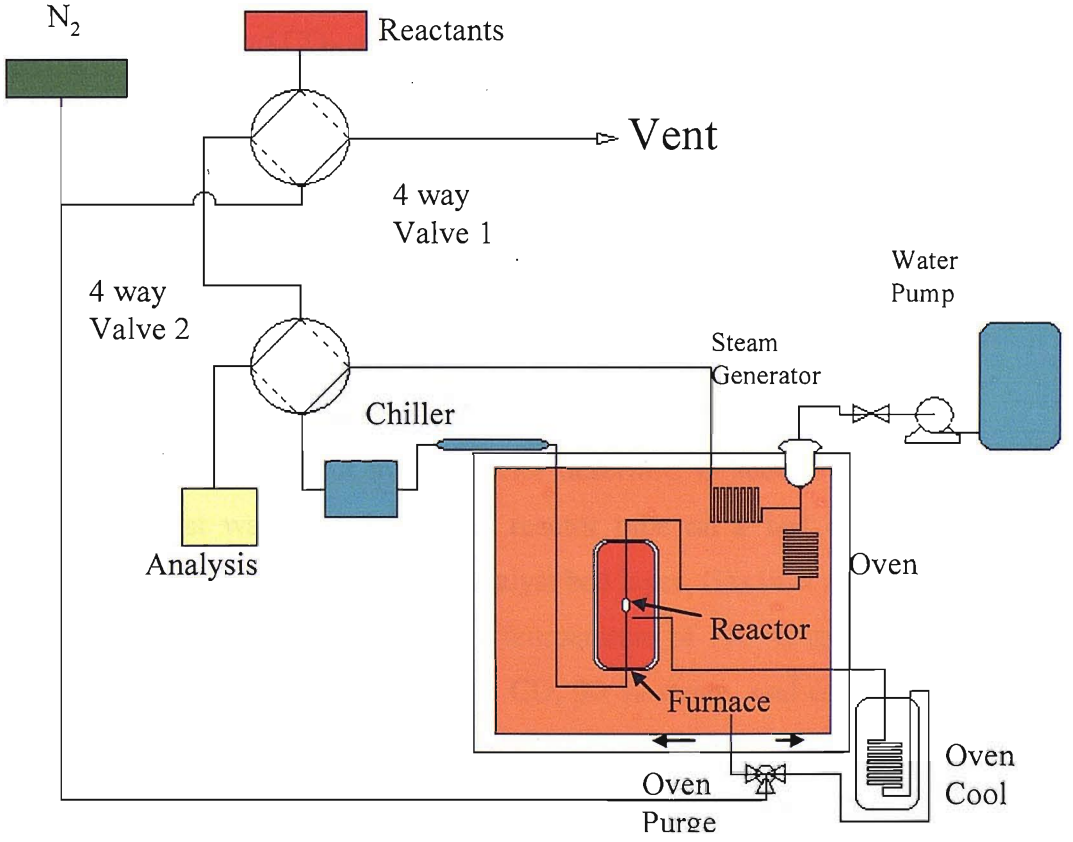

Figure 20 **Schematic diagram for the reactor used for the WGS and CO oxidation testing.**

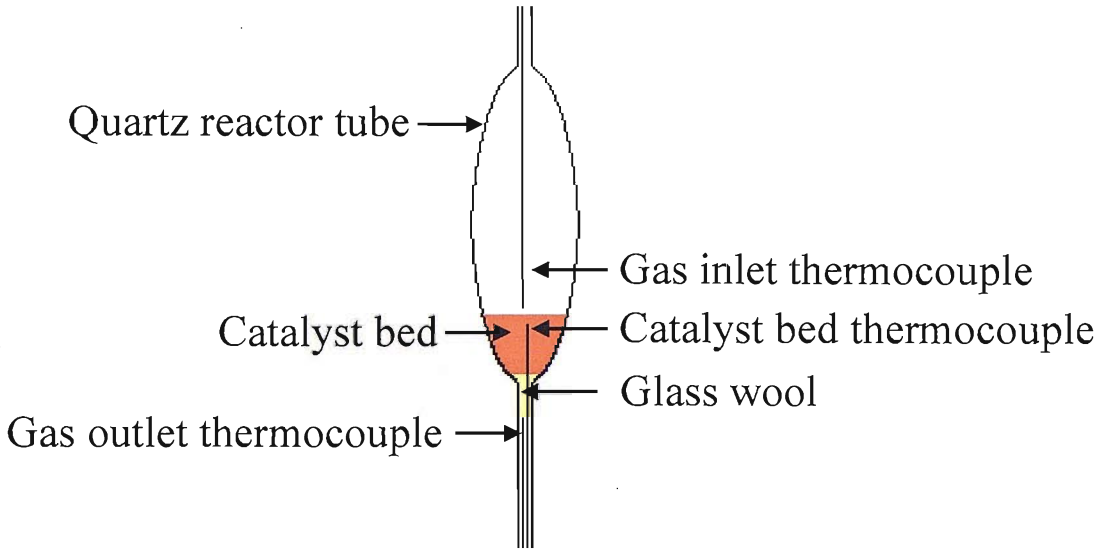

Figure 21 **Schematic diagram of the reactor chamber showing the positions of the three thermocouples.**

The analysis was performed using a Maihak s710 analyzer comprising of a H_2 detector and IR CO and CO_2 sensors. The pump used is a calibrated Watson Marlow Sand. The reactor is in a Lenton oven so as to avoid any line condensation when steam is one of the feed gases. Three thermocouples are placed inside the reactor chamber to monitor the temperature of the gas inlet, gas outlet and the catalyst bed.

7.2 Water Gas Shift Testing Procedure

WGS testing was carried out in the reactor described in section 7.1. 0.45 g of pelletised catalyst was loaded into the reactor tube on a bed of glass wool, ensuring the thermocouple was in the catalyst bed layer. Gas inlet and outlet lines were enclosed in an oven operating at a temperature of 110 °C to prevent water condensation. The inlet gases were 5 % CO, 30 % steam, and 65 % N_2 with a total flow of 300 cm^3 min^{-1}. The heating rate was 5 °C min^{-1} and the maximum temperature set to 500 °C. The exit gases were monitored by the analyser.

7.3 CO Oxidation testing procedure

CO oxidation testing was carried out in the reactor described in section 7.1. 0.2 g of pelletised catalyst was loaded into the reactor tube on a bed of glass wool, ensuring the thermocouple was in the catalyst bed layer. The inlet gases were a mixture of N_2, 1% CO in N_2, and air with a total flow of 300 cm^3 min^{-1}. The flow of air was kept constant and the flows of N_2 and CO were adjusted to control the mole fraction of CO. The temperature was ramped manually, the procedure involved simultaneously heating the furnace and cooling with liquid nitrogen to facilitate a very slow heating rate and combat the exothermic reaction conditions. The exit gases were monitored by the analyser.

8. References

1. Jalan, V. and E.J. Taylor, J. Electrochem. Soc., 1983. **130**(11): p. 2299.
2. Mukerjee, S., S. Srinivasan, M.P. Soriaga, and J. McBreen, J. Electrochem. Soc., 1995. **142**(5): p. 1409.
3. Candy, J.P., B. Didillon, E.L. Smith, T.B. Shay, and J.M. Basset, Journal of Molecular Catalysis, 1994. **86**(1-3): p. 179.
4. Didillon, B., J.P. Candy, F. Lepeletier, O.A. Ferretti, and J.M. Basset, *Surface Organometallic Chemistry on Metals - Selective Hydrogenation of Citral on Silica-Supported Rhodium Modified by Tetra-N-Butyl Germanium, Tin and Lead*, in *Heterogeneous Catalysis and Fine Chemicals Iii*. 1993. p. 147.
5. Lefebvre, F.D., J.P. Candy, C.C. Santini, and J.M. Basset, Topics in Catalysis, 1997. **4**(3-4): p. 211.
6. Crabb, E.M., R. Marshall, and D. Thompsett, J. Electrochem. Soc., 2000. **147**(12): p. 4440.
7. Crabb, E.M. and M.K. Ravikumar, Electrochim. Acta, 2001. **46**(7): p. 1033.
8. Crabb, E.M., M.K. Ravikumar, Y. Qian, A.E. Russell, S. Maniguet, J. Yao, D. Thompsett, M. Hurford, and S.C. Ball, Electrochem. Solid State Lett., 2002. **5**(1): p. A5.
9. Crabb, E.M., M.K. Ravikumar, D. Thompsett, M. Hurford, A. Rose, and A.E. Russell, Phys. Chem. Chem. Phys., 2004. **6**(8): p. 1792.
10. Hogarth, M.P., The Development of the Direct Methanol Fuel Cell, PhD Thesis, 1995, University of Newcastle upon Tyne
11. Schmidt, T.J. and H.A. Gasteiger, *Rotating thin-film method for supported catalysts*, in *Handbook of fuel cells*. 2003.
12. Rehr, J.J. and R.C. Albers, Rev. Mod. Phys., 2000. **72**(3): p. 621.
13. Brown, M., E.A. Stern, and R.E. Peierls, Phys. Rev. B, 1977. **15**(2): p. 738.
14. Mansour, A.N., J.W. Cook, and D.E. Sayers, J. Phys. Chem., 1984. **88**(11): p. 2330.
15. Lytle, F.W., J. Synchrot. Radiat., 1999. **6**: p. 123.

16. Sayers, D.E., E.A. Stern, and F.W. Lytle, Phys. Rev. Lett., 1971. **27**(18): p. 1204.
17. Lee, P.A. and J.B. Pendry, Phys. Rev. B, 1975. **11**(8): p. 2795.
18. Russell, A.E. and A. Rose, Chem. Rev., 2004. **104**(10): p. 4613.
19. Cook, J.W. and D.E. Sayers, Journal of Applied Physics, 1981. **52**(8): p. 5024.
20. van Dorssen, G.E., *New developments in XAFS spectroscopy*. 1999.
21. Binsted, N., *EXCURV98: CCLRC Daresbury Laboratory computer program*. 1998.
22. Gurman, S.J., N. Binsted, and I. Ross, Journal of Physics C-Solid State Physics, 1984. **17**(1): p. 143.
23. Rehr, J.J. and R.C. Albers, Phys. Rev. B, 1990. **41**(12): p. 8139.
24. Rehr, J.J., R.C. Albers, and S.I. Zabinsky, Phys. Rev. Lett., 1992. **69**(23): p. 3397.
25. Teo, B.K., *EXAFS: Basic Principles and Data Analysis*. Inorganic Chemistry Concepts. Vol. 9. 1986: Springer-Verlag.
26. Rose, A., Structural Effects in Fuel Cell Electrocatalysts, PhD Thesis, 2004, University of Southampton
27. Derbyshire, G. and K.C. Cheung, J. Synchrot. Radiat., 1999. **6**: p. 62.
28. Kampers, F.W.H., *EXAFS in Catalysis: Instrumentation and Applications;*. 1998: Technical University of Eindhoven.
29. McMaster, W.H., *Compilation of X-ray Cross-Sections, National Bureau of standards, for calculation of X-ray cross sections*.
30. Herron, M.E., S.E. Doyle, S. Pizzini, K.J. Roberts, J. Robinson, G. Hards, and F.C. Walsh, J. Electroanal. Chem., 1992. **324**(1-2): p. 243.
31. Maniguet, S., R.J. Mathew, and A.E. Russell, J. Phys. Chem. B, 2000. **104**(9): p. 1998.
32. Aitkins, P.W., *Physical Chemistry*. 6 ed. 1998: Oxford University Press.
33. Goodhew, P.J., J. Humphreys, and R. Beanland, *Electron microscopy and analysis*. 3 ed. 2001: Taylor & Francis.

Chapter Three: Cr and Co Modified Pt/C Catalysts for the Oxygen Reduction Reaction.

1 Introduction

A major loss in the performance of a proton exchange membrane fuel cell (PEMFC) is the reduction of oxygen taking place at the cathode. The overpotential associated with this process is around 400 mV. This greatly exceeds the 20 mV overpotential associated with the oxidation of hydrogen when using pure $H_{2(g)}$ as the fuel at the anode. The reduction of oxygen on Pt based catalysts in acidic media can proceed via a direct reduction process (equation 1), yielding water as the product, or by an indirect route via a peroxide intermediate (equations 2-4).

$$O_2 + 4H^+ + 4e^- \longrightarrow 2H_2O \qquad E^0_{O_2/H_2O} = 1.23\,V \qquad \textbf{Equation 1}$$

$$O_2 + 2H^+ + 2e^- \longrightarrow H_2O_2 \qquad E^0_{O_2/H_2O_2} = 0.682\,V \qquad \textbf{Equation 2}$$

The intermediate peroxide can then undergo a further reduction,

$$H_2O_2 + 2H^+ + 2e^- \longrightarrow 2H_2O \qquad E^0_{H_2O_2/H_2O} = 1.77\,V \qquad \textbf{Equation 3}$$

Or a chemical decomposition,

$$2H_2O_2 \longrightarrow 2H_2O + O_2 \qquad \textbf{Equation 4}$$

The direct four electron pathway offers the greatest cell potential and is, therefore the most desirable outcome. It is considered to be the most common pathway for the ORR on Pt based catalysts. However, a detailed mechanism for this process is still not fully resolved. Yeager used the inorganic chemistry of complexes adsorbed onto an electrode surface to look at some of the possible interactions of transition metal surfaces with O_2 [1]. The interactions available

are detailed in figure 1 and include: a Griffiths model adsorption (pathway I) involving a lateral interaction between the π orbitals of O_2 with the d_z^2 orbitals of the metal, with back bonding from partially filled d_{xy} and d_{yz} orbitals of the metal to the π^* antibonding orbitals of O_2; an end on single bond σ-type interaction (Pauling model) (pathway II); or a bridge model where an O_2 molecule is adsorbed over two metal sites (pathway III).

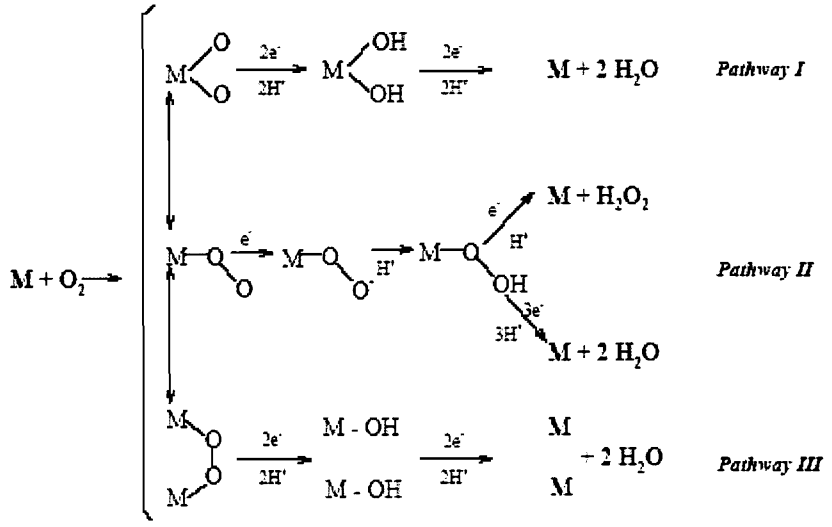

Figure 1 **Reaction pathways resulting from three proposed models for intermediate adsorption states in the ORR [1].**

The performance of any catalytic process is governed by the number of active sites the catalyst possesses and the turnover frequency of each site. The number of active sites for the electrocatalysts can be increased by dispersing small nanoparticles of Pt on a high surface area carbon powder. Carbon is chosen over other supports due to its electrical conductivity. The greater the dispersion, the larger the available Pt surface area. The ORR is a highly structure sensitive reaction as work by Kinoshita has shown [2]. Platinum particles consist of a distribution of surface sites including (111) and (100) crystal facets, in addition to corner and edge sites. Kinoshita showed that the specific activity of Pt towards the ORR increased with increasing particle size, coinciding with an increase in the relative contribution of the (111) and (100) crystal facets and a decrease in corner and edge sites. However, the mass averaged distribution of (111) and (100) crystal facets reaches a maximum for particles of diameter ~ 3.5 nm, which

Kinoshita then correlated to the mass activities observed towards the ORR for a range of Pt particle sizes. Subsequent work by Markovic *et al.* [3] looked at the performance of different Pt crystal faces towards the ORR in different electrolytes using single crystal electrodes. The adsorption of anions on the surface of Pt was also shown to be structure sensitive. As a consequence, the activity of different Pt crystal facets towards the ORR increased in the order (111) << (100) < (110) for sulphuric acid, but increased in the order (100) < (110) < (111) when in KOH. When using sulphuric acid there is a highly structure specific adsorption of sulphate / bisulphate anions on (111) crystal facets which inhibits the performance of these sites towards the ORR.

One of the ways to increase the activity of Pt towards the ORR is by alloying with other metals. Work looking at improved ORR catalysts in PAFCs carried out by Jalan and Taylor [4] suggested that the activity of these alloys was due to geometrical considerations. They proposed that by introducing a second metal into the Pt lattice, the Pt-Pt interatomic distances on the surface of the catalyst would be altered. It was suggested that an important part of the reaction mechanism involved O_2 adsorbing at two Pt sites, followed by breakage of the O-O bond. The spacing between different Pt sites at the surface should thus affect the reaction rate and an optimum distance should exist. Jalan and Taylor looked at a range of Pt alloys and showed a linear correlation between interatomic separation and specific activity towards the ORR. The work found that PtCr catalysts showed the highest specific activity towards the ORR compared to the other Pt alloys studied.

This early work on the enhancement towards the ORR offered by PtCr alloys was contested by other research groups. Glass *et al.* [5] investigated a range of PtCr alloys of different compositions, suggesting that increased Cr content should decrease the Pt-Pt spacing. The performance of these catalysts towards the ORR did not correlate with the Pt-Pt interatomic spacing and furthermore showed no improved performance over pure Pt. The work did show some differences in electrochemical behaviour between the Pt and PtCr systems, most notably differences in OH coverage and open circuit potential. Paffet *et al.* [6] also disputed the enhancement offered by PtCr catalysts. Although a slight

improvement in performance was observed for PtCr alloys it was attributed to a roughening of the surface, and an increase in Pt surface area. It was proposed that during the experiments, Cr(III) at the surface, which is present as an oxide or hydroxide, is dissolved as a Cr(VI) solution species at a certain potential. This causes a roughening of the surface, and a corresponding increase in the number of active sites.

Mukerjee and Srinivasan [7] looked at carbon supported Pt alloys of Cr, Co, and Ni and noted a two to three fold enhancement towards the ORR under PEMFC operating conditions over Pt alone. The work showed that the specific activity of the alloys increased, even though they had an increased particle size, and thus a smaller available active area than pure Pt for similar metal loadings, expressed as wt %. This improvement was attributed to the formation of superlattices of the type Pt_3Cr, Pt_3Co, and Pt_3Ni. These superlattices exhibited the same cubic fcc structure of Pt but with lattice contractions. The work also showed that the alloying component was not evenly distributed and remained on the surface in an oxide form. Mukerjee *et al.* [8] then used *in-situ* XAS measurements to relate structural and electronic properties of carbon supported Pt alloy catalysts with their activity towards the ORR. White line analysis of the Pt L_3 and L_2 edges was used to calculate the Pt d-orbital vacancy per atom in an electrochemical environment at potentials of 0.54 and 0.84 V vs. SHE. The work showed that both the Pt d-orbital vacancy per atom and Pt-Pt distance exhibit a volcano type behaviour with respect to electrocatalytic activity towards the ORR, suggesting that there is a symbiotic relationship between Pt-Pt distance and d-orbital vacancy. The PtCr/C catalyst was shown to sit at the top of this volcano plot. PtCr alloys have continually been shown to be active towards the ORR and also exhibit a large degree of methanol tolerance making them applicable as DMFC cathode catalysts [9-11]. The work by Mukerjee *et al.* also showed that the Pt/C catalyst showed a large change in fractional d-band vacancy with respect to the alloy catalysts when the potential was increased from 0.54 to 0.84 V vs. SHE. This was attributed to an increase of adsorbed surface OH on the Pt/C compared to the alloys. Prior to the XAS measurements by Mukerjee *et al.* [8] the catalysts were acid leached to remove any unalloyed oxides. However, this same acid

leaching step was not used prior to the electrochemical analysis. Therefore the results must be handled with a degree of caution.

Work by Toda *et al.* [12, 13] looked at the performance of Pt alloyed with Ni, Co, and Fe, where the surface of the alloy has a Pt enriched layer (Pt skin). XPS was used to show that the surface Pt had an increased d-band vacancy without having a contraction in the Pt-Pt spacing. Large enhancements towards the ORR were observed for all the alloys. The enhancement was attributed to the change in d-electron vacancy of the Pt skin by the underlying bulk alloy. More precisely it was suggested that this change in electronic property, assuming a lateral interaction between O_2 and Pt, promotes the 2π donation from O_2 to surface Pt. This results in stronger O_2 adsorption and a weakening of the O-O bond. Scission follows immediately when there is back donation from the Pt d-orbitals to π^* orbitals on O_2.

Other research suggests that changes in electronic properties of surface Pt sites aids the ORR by impeding the formation of adsorbed OH [14-16]. It is proposed that the activation of water to yield Pt-OH hinders the ORR by blocking Pt absorption sites. It is thought that this electronic modification of Pt on alloying has the ability to shift the onset potential of water activation.

The enhancement towards the ORR exhibited by Pt alloys is still not fully understood. Current research is still trying to relate surface structures and changes in electronic properties to the improved activity observed for the ORR [17-21]. The development of model systems on small particles rather than single crystals is required to facilitate a better understanding of the origins of the enhancement towards the ORR. Many of the mechanisms proposed for the ORR suggest that it is the surface interactions between the two alloying components which give rise to the enhancement. It is therefore desirable to prepare supported bimetallic catalysts where the secondary metal is exclusively at the surface of the first metal. Traditional methods for producing bimetallic catalysts such as impregnation, electrochemical deposition and precipitation lack the selectivity to deposit the second metal specifically onto the Pt sites.

In this study, the controlled surface modification procedure developed by Crabb *et al.* [22-26] and detailed in chapter 2, section 2, was used to prepare Pt/C catalysts with surfaces modified with Cr and Co. Previous work using the controlled surface modification procedure for fuel cell electrocatalyst preparation has been used to study Pt/C catalysts modified with Sn [25], Ge [24], Mo [23] and Ru.[22] All of the systems prepared exhibited a lower onset potential for the electrooxidation of CO compared to Pt/C alone. Initial work on the PtSn system showed that this means of preparation formed a catalyst with a better activity than conventionally prepared PtSn alloys. *In-situ* EXAFS studies were used to assess the Ru modified Pt/C system [22]. XAS provides an ideal means to study bimetallic fuel cell electrocatalysts [27, 28], as the local structure around each of the alloying components can be determined, along with the oxidation state. The EXAFS results showed that at open circuit potential Ru was present as an oxide but in intimate contact with the Pt [22]. XRD was also used to show that there was no evidence of PtRu alloying. Work performed by Qian [29] has previously looked at a series of modified Pt/C catalysts with Co, Cr, Fe and Ni for use as ORR electrocatalysts. For each metal, the metallocene analogue was used as the precursor for the modification. Qian [29] has shown that the catalysts exhibit encouraging performance towards the ORR, with the optimum monolayer fraction of Co and Cr found to be 0.66. The promising results shown by Qian [29] are sufficient to warrant further attention, in particular a full physical characterisation of the catalysts, so that the structure can be accurately linked to activity.

The Co and Cr modified Pt/C catalysts (to be denoted as Co/Pt/C and Cr/Pt/C) prepared in this chapter have been assessed for their performance towards the ORR using a RDE assembly and have been characterised using XANES, EXAFS, cyclic voltammetry, XRD and TEM.

2 Experimental Details

2.1 Catalyst Preparation

Cr/Pt/C and Co/Pt/C catalysts were prepared as detailed in chapter 2, section 2.2. Modifications were made to a 20 wt % Pt/C (XC-72R) catalyst with a calculated dispersion of 0.48. For the Cr/Pt/C catalysts two different precursors were used for the deposition; chromocene ($Cr(Cp)_2$), and bisbenzene chromium ($Cr(Ph)_2$). For the Co/Pt/C catalyst, cobaltocene ($Co(Cp)_2$) was used as the precursor. The table below gives details of the catalysts prepared, the desired monolayer coverage, and the heat treatments carried out.

Table 1 **Details of catalysts prepared**

Catalyst	Equivalent monolayers	Precursor	Heat treatments / °C	Initial colour of solution	End colour of filtrate
Cr/Pt/C	0.66	$Cr(Cp)_2$	750, 900	Dark green*	colourless
Cr/Pt/C	0.66	$Cr(Ph)_2$	750, 900	Light green	colourless
Cr/Pt/C	0.16	$Cr(Ph)_2$	750, 900	Light green	colourless
Co/Pt/C	0.66	$Co(Cp)_2$	750, 900	Dark brown	colourless

*The solution was a mixture of dissolved and undissolved precursor

Conventionally prepared PtCr/C and PtCo/C alloys were supplied by Johnson Matthey to facilitate a comparison with the surface modified catalysts. Control reactions were also carried out to show that the precursor was specifically targeting Pt sites and not the carbon support. In each case the filtrate ran through the same colour as it entered the reactor vessel, thus indicating that no reaction was observed. The 20 wt % Pt/C (XC-72R) was also subjected to the 750 and 900 °C heat treatments to facilitate a more representative comparison.

2.2 Electrochemical Characterisation

2.2.1 Cyclic Voltammetry

The electrochemical properties of the catalysts were characterised using the standard 3 electrode half cell detailed in chapter 2, section 3.2.2, with button electrodes prepared according to chapter 2, section 3.2.1.

2.2.2 Oxygen Reduction Testing

The performance of the catalysts towards the ORR was assessed using an RDE assembly as detailed in chapter 2, section 3.3.

2.3 XAS Studies

2.3.1 Cr and Co K edge Investigations

Cr and Co K edge XAS spectra were acquired on station 7.1 at the SRS, Daresbury Laboratory. Station 7.1 utilises a double crystal Si(111) monochromator for EXAFS in the range of 4 keV to 10 keV. EXAFS of the catalyst materials were acquired in fluorescence mode using a liquid nitrogen cooled 9 element Ge solid state detector. Reference EXAFS of metal foils and oxide standards were acquired in transmission mode. All catalysts were prepared as BN pellets for XAS measurements.

2.3.2 Pt L_2 and L_3 edge Investigations

Pt L_2 and L_3 edge XAS spectra were acquired on station 16.5 at the SRS, Daresbury Laboratory. Station 16.5 is on a 6T Wiggler line, and utilises a double crystal Si(220) monochromator to acquire EXAFS in the range of 7 KeV to 40 KeV. EXAFS of the catalyst materials were acquired in fluorescence mode using a liquid nitrogen cooled 30 element Ge solid state detector. Reference EXAFS of metal foils and oxide standards were acquired in transmission mode. All catalysts were prepared as BN pellets for XAS measurements.

2.3.3 Fractional d-band Vacancy Determination

The white lines of the Pt L_3 and L_2 edges in XAS spectra are due to the transitions from $2p_{3/2}$ states to $5d_{3/2}$ and $5d_{5/2}$ states, and from $2p_{1/2}$ states to $5d_{3/2}$ states respectively. These transitions are restricted by certain selection rules; $\Delta L = \pm 1$ and $\Delta J = 0, \pm 1$ where L is the orbital angular momentum quantum number and J is the total orbital angular momentum quantum number [30]. Using these selection rules, it can be seen that transitions to s states are also possible. However, the occurrence of white lines is mainly due to high density of final states. The d symmetric portion of the density of states tends to be large and narrow whereas the s symmetric portion tends to be small and spread out. Thus the white line can be attributed solely to the $p \rightarrow d$ transitions [31]. For a Pt atom, it can be seen that the empty state in the 5d shell has a J value of 5/2. The Pt L_2 white line is therefore much less intense as there are no transitions to states where J = 5/2. The ratio of final states of $d_{5/2}$ and $d_{3/2}$ has been found to be 14:1 [31]. It can be seen that the intensity of L_3, and to a lesser extent L_2 edges, is related to the overall d-band vacancy. An increase in d-band vacancy has been associated with an enhanced performance towards the ORR for Pt based catalysts. The fractional d electron vacancy, f_d, of the absorber atoms is defined as follows:

$$f_d = (\Delta A_3 + 1.11\ \Delta A_2)/(A_{3,r} + 1.11A_{2,r}) \qquad \textbf{Equation 5}$$

where ΔA_3 and ΔA_2 represent the difference in areas under the L_3 and L_2 edges with the corresponding reference spectra (obtained using a Pt foil). The quantity $A_{3,r} + 1.11A_{2,r}$ is the combined area per unoccupied d electron and is a constant for the absorbing atom being probed.

The quantitative analysis of d-electron character was performed as detailed by Mansour *et al.* [30]. The three critical components of the data analysis are the removal of the background absorption, the alignment of the sample and reference spectra, and the normalisation of the sample and reference spectra. The alignment of edges is achieved by adjusting the energy scales of the spectra so that 0 eV corresponds to the inflection point of the edge (figure 2).

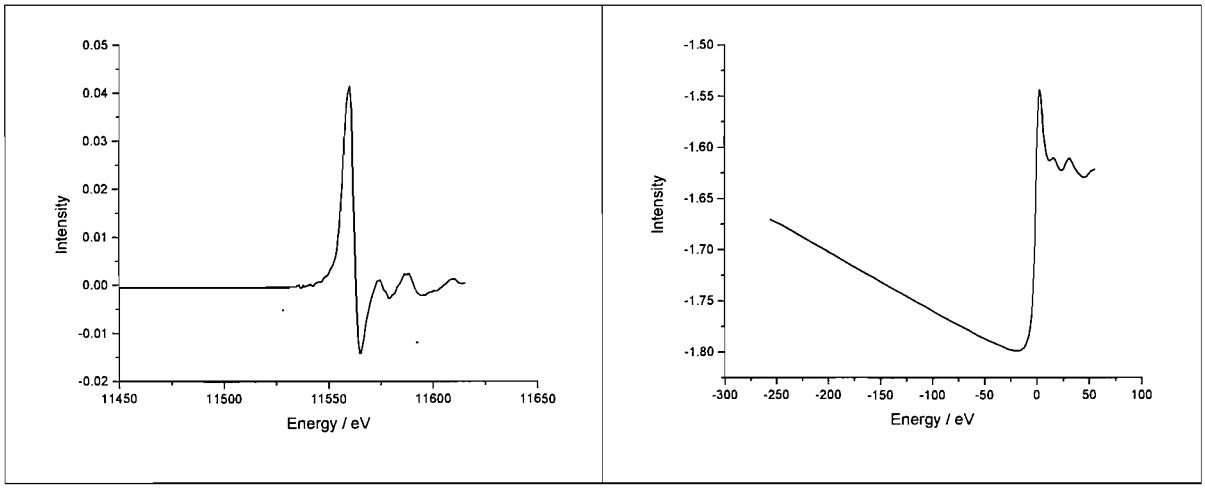

Figure 2 **Alignment of the energy scale relative to the inflection point of the absorption edge.**

The removal of background absorption is achieved by fitting a linear gradient to the pre-edge slope and subtracting the gradient from the spectrum (figure 3).

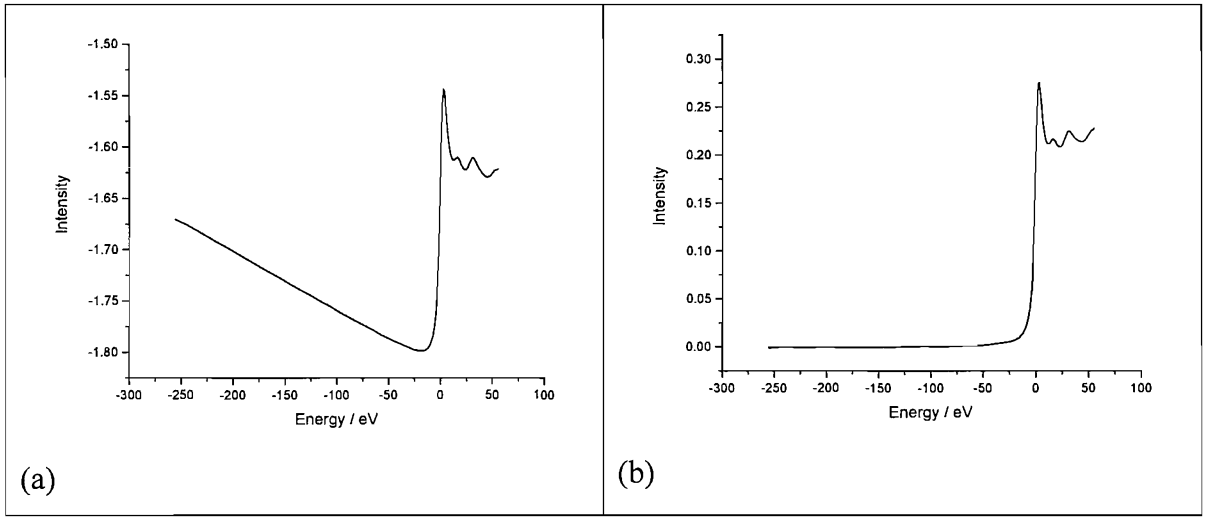

Figure 3 **XAS Data from the Pt L_3 edge (a) before and (b) after removal of the pre-edge background absorption.**

The normalisation of spectra is performed by adjusting the energy scale of the L_2 and L_3 edges so that the EXAFS oscillations are aligned. This procedure is used, as theoretically the EXAFS oscillations for both the L_2 and L_3 edges should be the same. The final step is to normalise the data by setting the intensity of one of the inflection points of the EXAFS oscillations above 40 eV to 1 (figure 4).

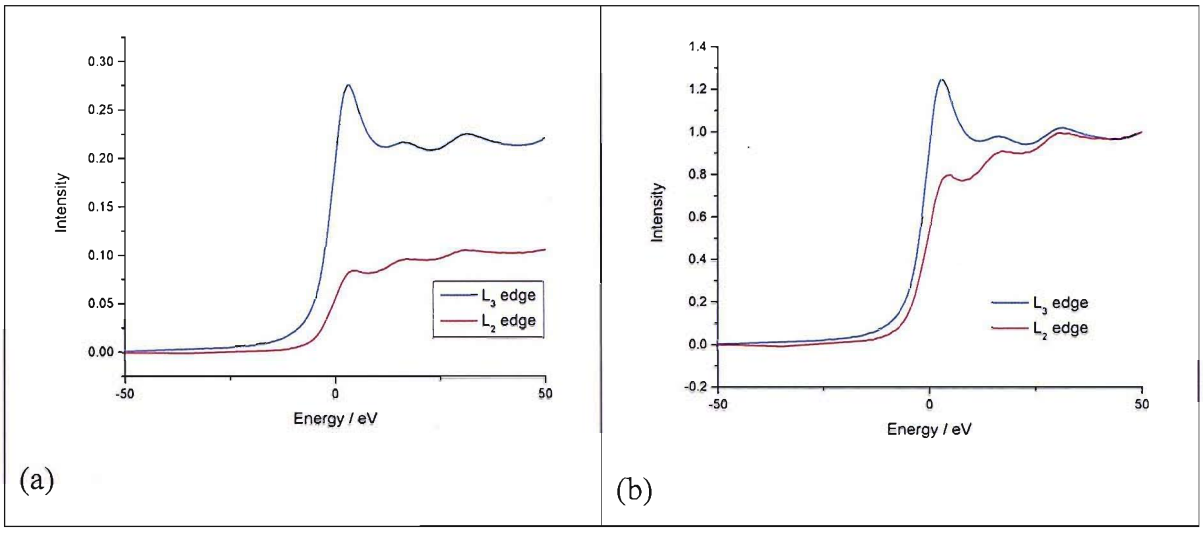

Figure 4 **Pt L_3 and L_2 edge spectra (a) before and (b) after data normalisation.**

The areas used to calculate ΔA_3 and ΔA_2 were determined by integrating the area which extends from -10eV → 13eV under the absorption edge for the normalised spectra. The value for $A_{3,r}$ was found by first calculating the areas under the L_3 and L_2 edges of Pt foil from -10eV → 40eV. The difference in areas was then multiplied by the ratio of $(h_{5/2} + h_{3/2}) / h_{5/2}$, where h_J= the number of unoccupied d states that are characterized by the angular momentum quantum number J. This ratio corrects for the white line weight at the L_2 x-ray absorption edge. The area $A_{2,r}$ is then estimated by multiplying the difference in areas by the ratio $h_{3/2} / h_{5/2}$. Finally, all areas calculated (ΔA_3, ΔA_2, $A_{3,r}$, and $A_{2,r}$) were multiplied by the x-ray absorption cross section at the absorption edge and the density of absorbing material. Values of 117.1 $cm^2\ g^{-1}$ and 54.2 $cm^2\ g^{-1}$ were used for the absorption cross section of the Pt L_3 and L_2 edges, respectively. The density of Pt used was 21.09 g cm^{-3}. The total number of d states per Pt atom can then be calculated as follows:

$$(h_J)_{t,s} = (1.0 + f_d)\ (h_J)_{t,r} \qquad \textbf{Equation 6}$$

where $(h_J)_{t,r}$ has been shown to be 0.3 [31].

2.4 XRD, TEM, and ICP-AES Analysis

All samples were submitted to Johnson Matthey Technology Centre, Sonning Common, where the analyses were performed.

The XRD analysis used a Bruker AXS D-500 diffractometer with a 40 position sample changer, a Ni filtered Cu K_α X-ray source, a scan range of 15 to 95°2θ with a 0.02° step size, and a scan rate of 0.25° 2θ per minute.

Powder samples for TEM EDX were crushed between two glass slides and samples positioned onto a lacey carbon coated copper 'finder' grid with the aid of a micro manipulator. The samples were examined in a Tecnai F20 Transmission Electron Microscope. Both bright field and high resolution electron microscopy modes were used.

3 Results and Discussion

3.1 ICP-AES Analysis

Elemental analysis of the prepared catalysts was carried out using ICP-AES. The experimental values, along with the theoretically calculated values based on the theoretical yield of the modification reaction, are shown below (table 2).

Table 2 **Elemental analysis of prepared M_2/Pt/C catalysts**

Sample	Wt % Pt Theoretical	Wt % Pt Experimental	Wt % M_2 Theoretical	Wt % M_2 Experimental
0.66 Cr/Pt/C*	19.60	19.89	1.67	1.89
0.166 Cr/Pt/C *	19.67	-	0.42	-
0.66 Co/Pt/C	19.62	19.30	1.88	0.88

* represents catalysts prepared by the bisbenzene chromium route

The work done previously by Qian [29] has shown that Cr/Pt/C samples prepared using the $Cr(Cp)_2$ precursor are successful in depositing the expected amount of Cr so were not submitted for elemental analysis. In general, the ICP-AES results are in good agreement with the theoretical values. This suggests that all the secondary metal is being deposited on the Pt/C. In the case where the

experimental value is greater than the theoretical value this can be rationalised by the accuracy of the balance used for the air sensitive compounds and the error in the measurement. Unfortunately, the balance in the glove box was only accurate to ± 0.01 g and could not be substituted for a more accurate balance. The 0.66 Co/Pt/C catalyst has a Co content of 0.88 wt % compared to the theoretical estimation of 1.88 wt %. It is not clear if this represents a failure to deposit the entirety of the Co, or is a combined artefact of the two sources of error mentioned above. The 0.166 Cr/Pt/C catalyst was not submitted for ICP-AES analysis as the 0.66 Cr/Pt/C catalysts showed that the deposition procedure was successful and the small fraction of Cr present in the sample would lead to a great amount of error in the measurement.

3.2 XRD Analysis

Whereas EXAFS provides information regarding the average local structure of the catalyst, XRD is used to investigate the long range order of materials. Of particular interest in this study, is the ability to identify the presence of separate metal and oxide phases. XRD can also be used to determine the lattice parameter and the crystallite size using Scherrer's equation.

The XRD analysis of the Pt/C samples annealed at 750 °C and 900 °C show that the catalyst in both cases is made up of poorly crystalline Pt, with a range of crystallite sizes. This distribution of crystallite sizes makes it difficult to accurately predict the particle size of the catalyst. The same can also be said for the 0.66 Cr/Pt/C sample annealed at 200 °C prepared by the $Cr(Ph)_2$ route.

However, the 750 and 900 °C (figure 5a) annealed samples of the same catalyst have very different characteristics. The 750 °C annealed sample is mainly composed of a poorly crystalline cubic phase close in crystallographic parameters to Pt/C. Also present is a second poorly crystalline cubic phase similar in crystallographic parameters to cubic Pt_3Cr. Subtle differences between the observed phase and the reference pattern could indicate the presence of a solid solution and/or stoichiometric differences. In addition, a trace amount of Cr_2O_3 is also present. The 900 °C annealed sample is composed of one phase, which is similar in crystallographic parameters to the cubic Pt_3Cr phase.

A very similar pattern is observed for the Co/Pt/C catalysts (figure 5b). The 200 °C annealed catalyst has the same XRD interpretation as the Pt/C catalysts and the Cr/Pt/C catalyst annealed at 200 °C. The 750 °C annealed sample is mainly composed of a poorly crystalline cubic phase close in crystallographic parameters to Pt/C, with a minor amount of Pt_3Co also present. The sample consists of a range of particle sizes and as such an accurate estimation of the particle size could not be determined. The 900 °C annealed sample consists of a single poorly crystalline cubic phase, most likely to be an undocumented PtCo phase. Where possible the lattice parameter and particle size have been calculated and are presented below in table 3.

Table 3 **Lattice parameters and particle size for 0.66 Cr/Pt/C and Co/Pt/C catalysts determined using XRD**

Sample	Lattice parameter / Å	Particle size / nm
0.66 Cr/Pt/C 750 °C	3.89	3.8
0.66 Cr/Pt/C 900 °C	3.89	5.9
0.66 Co/Pt/C 750 °C	3.89	6.9

Although only a limited number of samples were appropriate for particle size estimation using XRD the values obtained contain a greater level of information with regards to the vales determined using TEM. The values of the XRD derived particle size are specific to the Pt_3M phase whereas the particle size from TEM is an average of all the metallic particles whether they be, Pt, Pt_3M or M.

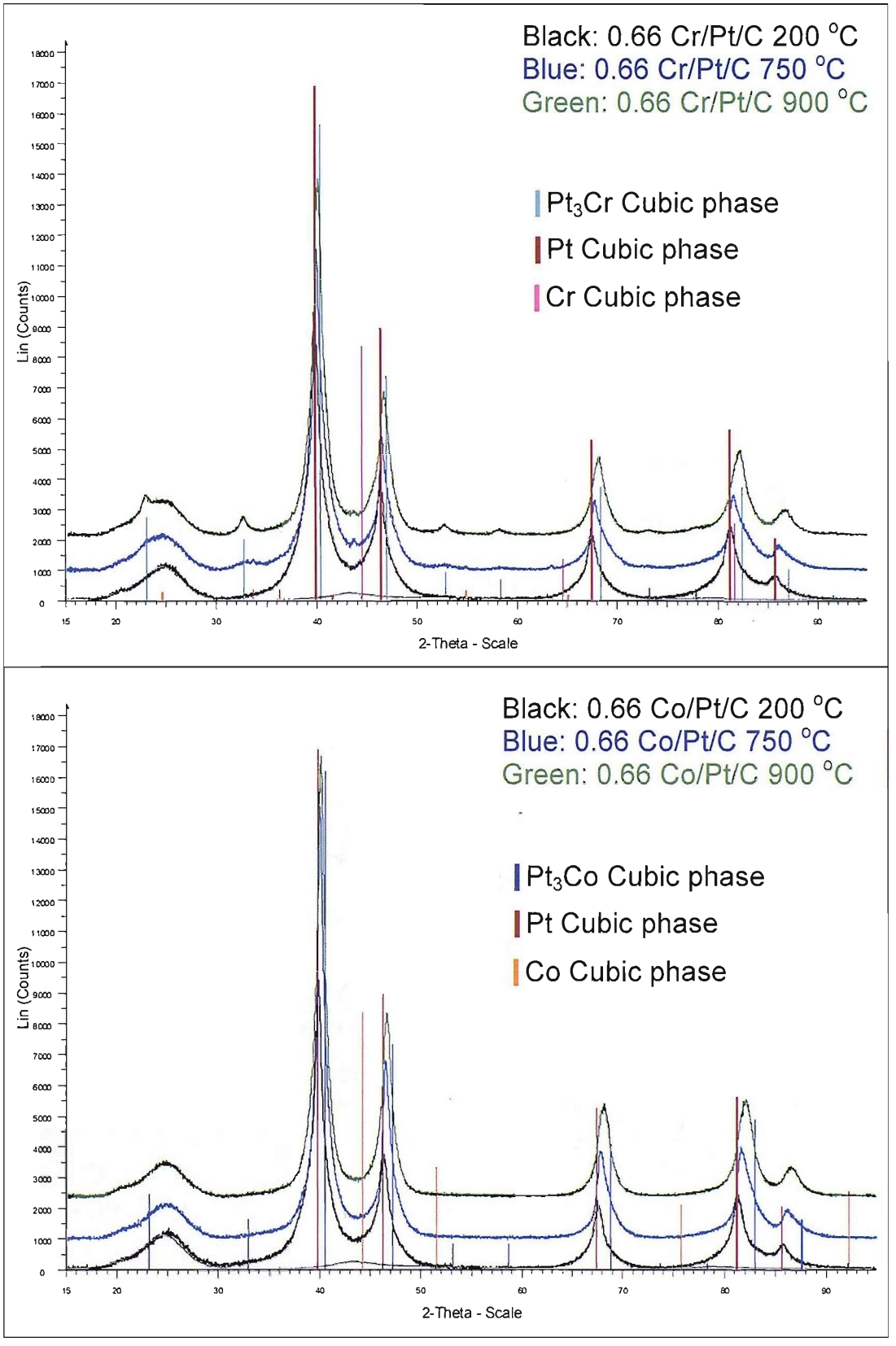

Figure 5 **XRD patterns of (a) Cr/Pt/C and (b) Co/Pt/C at different annealing temperatures. JCPDS reference data are included for a comparison.**

3.3 TEM EDX Analysis

The 0.66 Cr/Pt/C prepared by the $Cr(Ph)_2$ route, 0.66 Co/Pt/C, and Pt/C catalysts were submitted for TEM EDX analysis. TEM micrographs of the 0.66 Cr/Pt/C sample at different magnifications are included (figure 6) as an example of the data generated. For the other catalysts the particle size distributions have been included (figure 7).

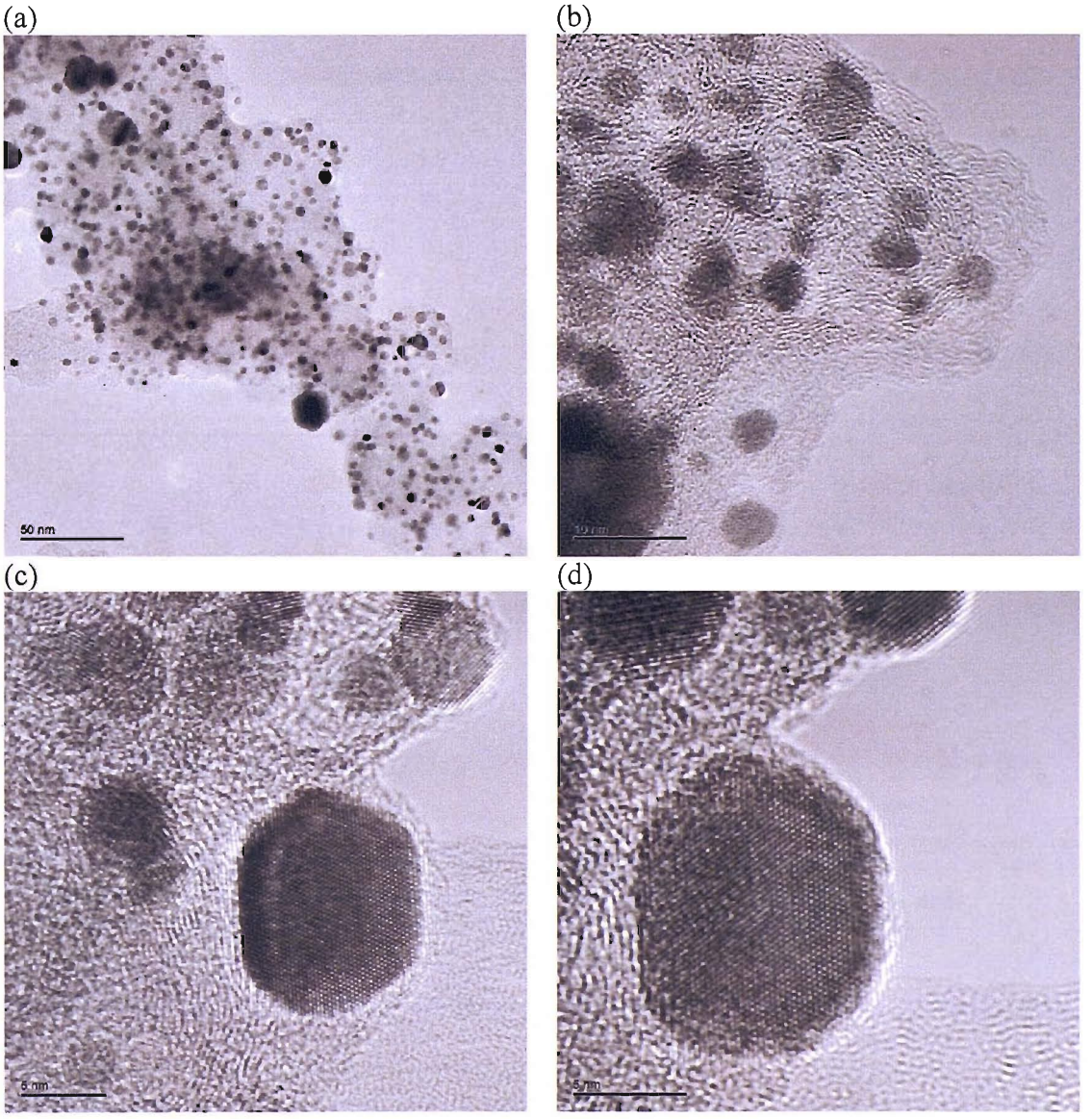

Figure 6 **TEM micrographs of 0.66 Cr/Pt/C 900 °C at magnifications of (a) 50 nm, (b) 10 nm, and (c & d) 5 nm**

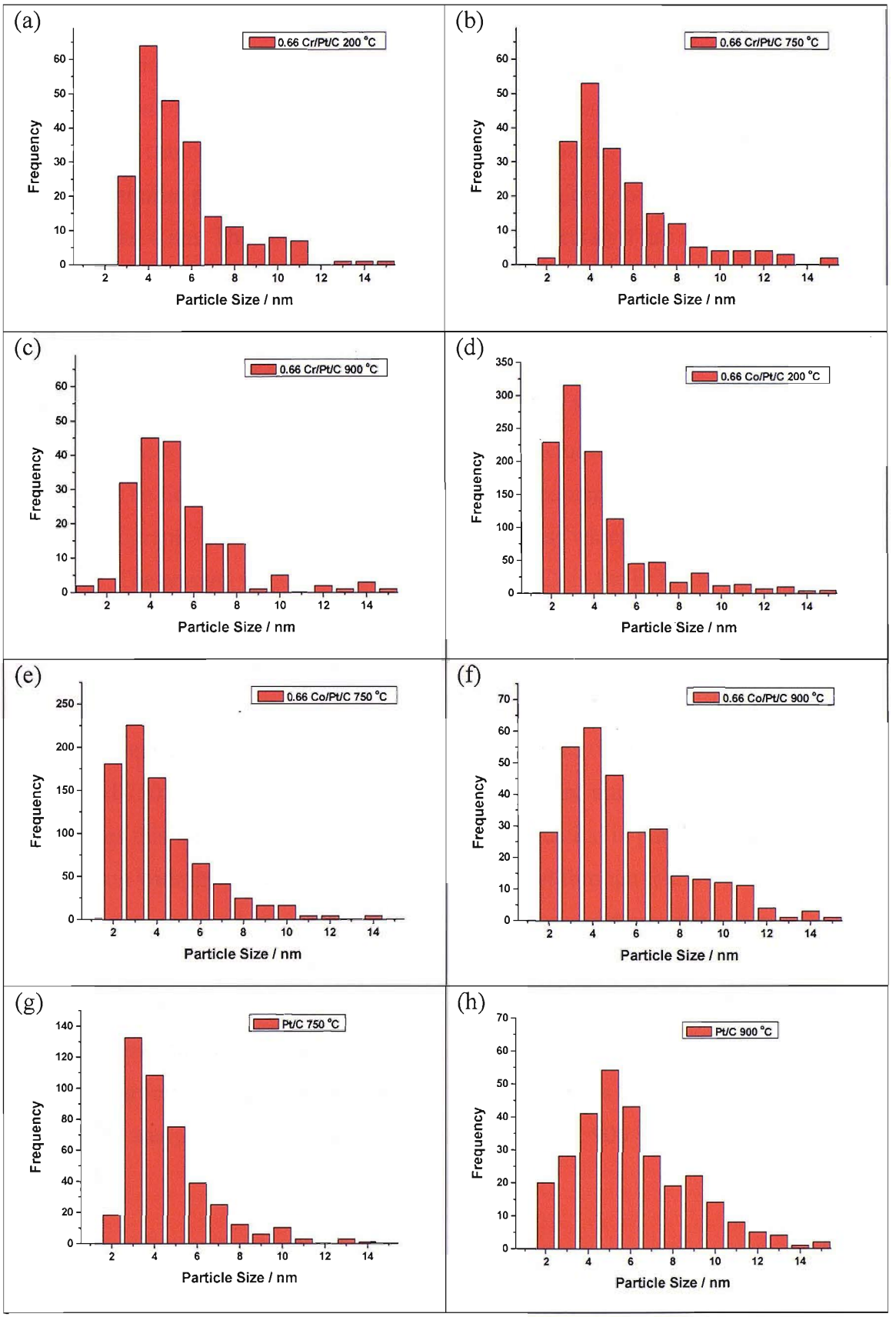

Figure 7 **Particle size distributions for 0.66 Cr/Pt/C (a, b, and c) and 0.66 Co/Pt/C (d, e, and f) annealed at 200, 750 and 900 °C respectively, and Pt/C annealed at 750 and 900 °C (g and h).**

In this report the main application of the TEM technique is to assess the particle size distribution of the different catalysts and to use the EDX function to study the proportion of the metallic components across a range of particles. The 0.66 Cr/Pt/C catalysts prepared by annealing at temperatures of 200 and 750 °C have very similar particle size distributions with the majority of the particles being around 4 nm. The 900 °C annealed 0.66 Cr/Pt/C catalyst has the majority of particles around 5 nm, with many more oversized particles than are present for the other annealing temperatures. EDX analysis for each of the catalysts shows that the Cr and Pt is present in similar proportions across a range of particles and that Cr is not found on the carbon support by itself. The line profile analysis across a particle for the 900 °C annealed catalyst is included to illustrate this in figure 8a. The line profile analysis shows a red line spanning a distance on a TEM micrograph. This line represents the points across which the EDX data is collected. The amount of counts observed for Pt and Cr in the EDX data across the line are in similar proportion at all time. This is good confirmation that the Cr is specifically targeting the Pt sites in the deposition process.

A similar trend is observed for the 0.66 Co/Pt/C catalysts. The catalysts annealed at 200 and 750 °C have similar particle size distributions, although the majority of particles this time are around 3 nm. This slight reduction in particle size in comparison with the Cr modified catalyst is consistent through to the 900 °C annealed sample where the majority of particles are around 4 nm rather than 5 nm. The 900 °C annealed catalyst also has many more oversized particles in comparison with the 200 and 750 °C heat treated samples. The line profile analysis shows that the Co and Pt are present in similar proportions across different particles for each of the annealing temperatures, as illustrated by the line profile analysis across a particle for the 0.66 Co/Pt/C 900 °C catalyst in figure 8b.

The Pt/C samples annealed at 750 and 900 °C have similar particle size distribution as the modified catalysts at the same annealing temperatures. The 750 °C annealed sample has the majority of the particles around 3-4 nm and the 900 °C catalyst has the majority of particles around 5 nm. This shows any

increase in particle size for the modified catalysts may be attributed primarily to the heat treatments and not the deposition of Cr or Co.

(a)

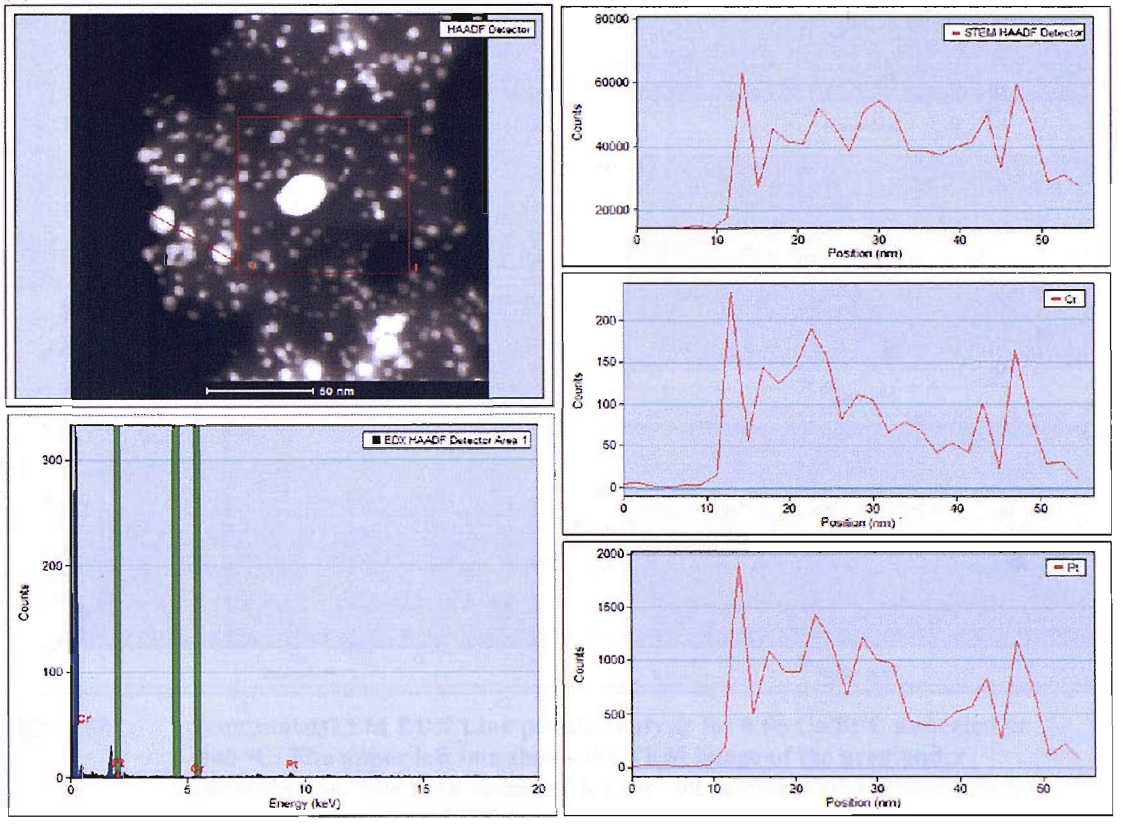

Figure 8a **TEM EDX Line profile analysis for 0.66 Cr/Pt/C annealed at 900 °C. The upper left box shows the TEM image of the area under investigation. The EDX response for the red box labelled 1 is shown below the TEM image. The EDX responses across the red line labelled one are shown on the right hand side and in descending order show total counts, counts from Pt, and counts from Cr respectively.**

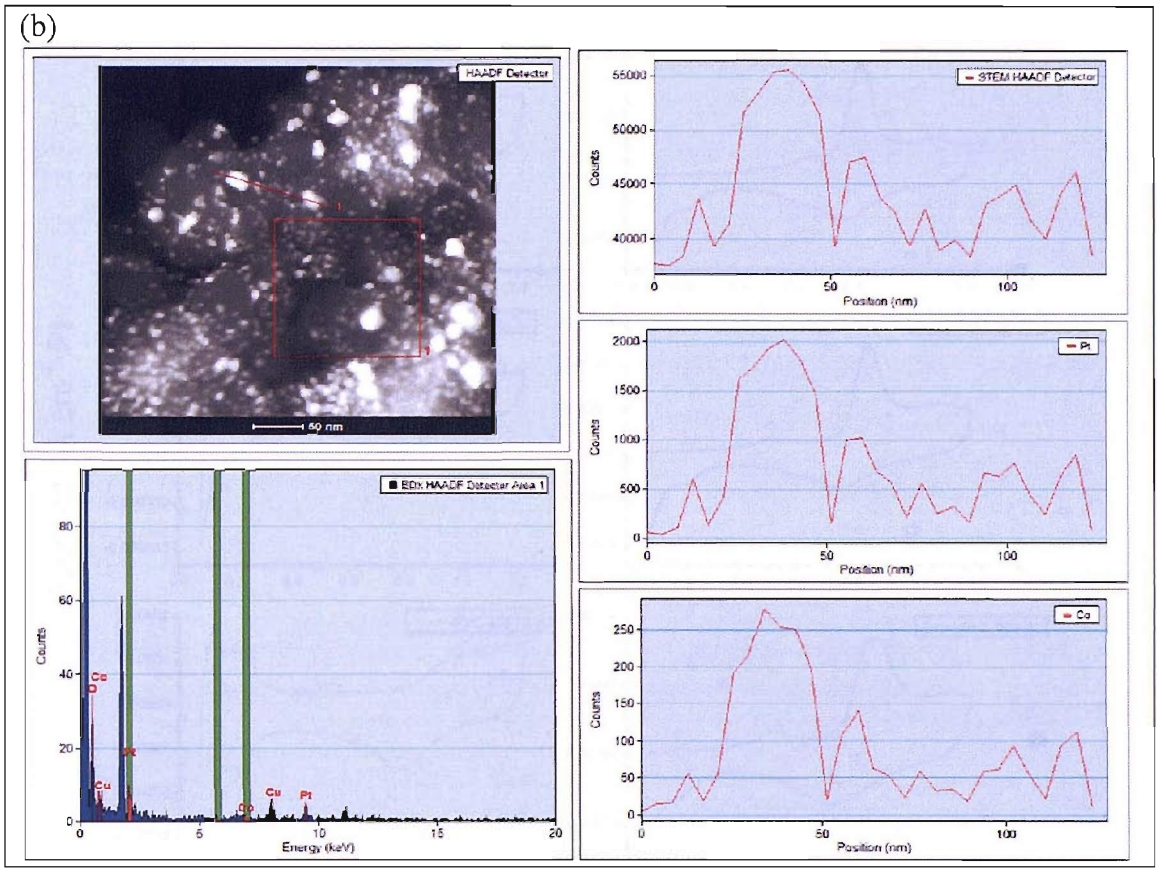

Figure 8b **(continued)TEM EDX Line profile analysis for 0.66 Co/Pt/C annealed at 900 °C. The upper left box shows the TEM image of the area under investigation. The EDX response for the red box labelled 1 is shown below the TEM image. The EDX responses across the red line labelled one are shown on the right hand side and in descending order show total counts, counts from Pt, and counts from Co respectively.**

3.4 Cyclic Voltammetry - Half Cell Studies

Cyclic voltammograms (figures 9-11) and associated parameters (tables 4-6) of Pt/C, 0.66 Cr/Pt/C prepared by the $Cr(Ph)_2$ route, and 0.66 Co/Pt/C at different annealing temperatures are detailed in this section. The cyclic voltammograms have been normalised to the available Pt surface area derived from the area underneath the CO stripping peak. The calculated parameters presented in table 4 include the value for the mass normalised Pt area in $m^2\ g^{-1}$ Pt. This value gives an indication of how the dispersion of the catalysts changes with increasing annealing temperature.

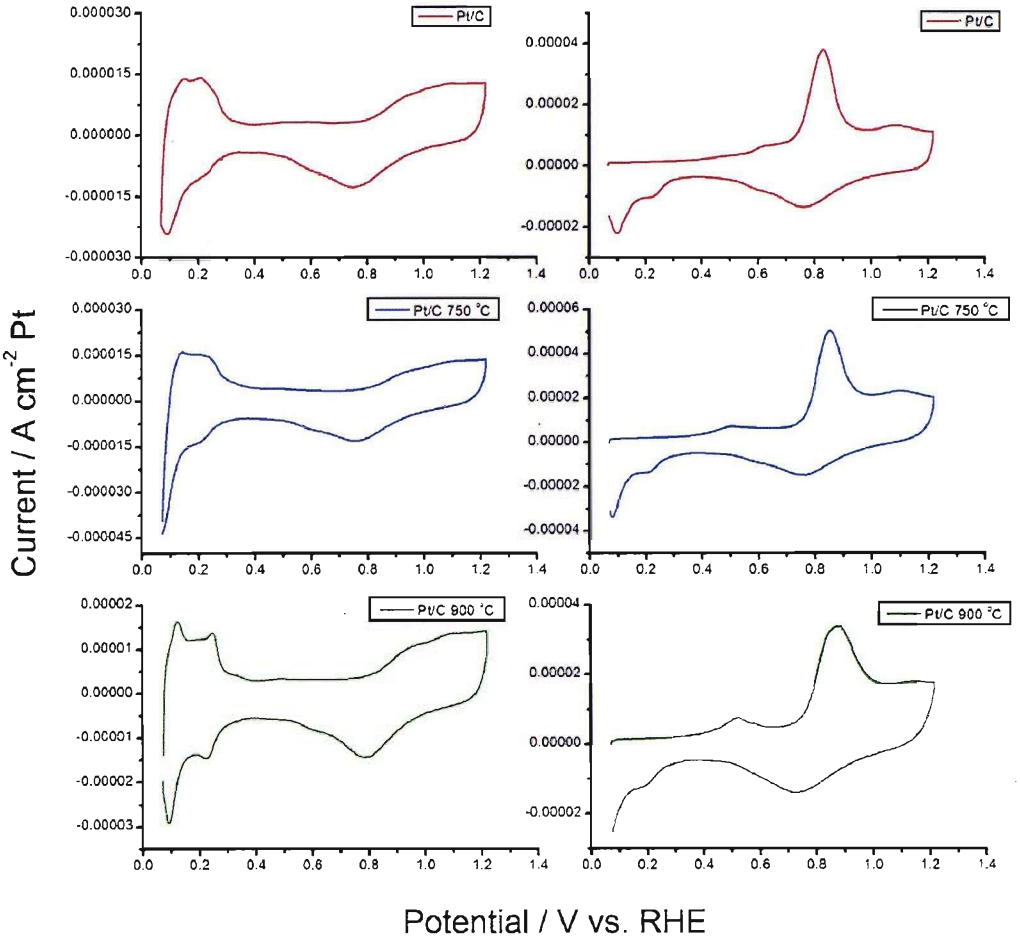

Figure 9 **Cyclic voltammograms (left column) and CO stripping voltammetry (right column) for Pt/C (top) untreated and annealed at 750 °C (middle) and 900 °C (bottom). Carried out in 2.5 M H_2SO_4 with a scan rate of 10 mV s^{-1}, currents normalised to the platinum surface area determined by CO stripping voltammetry.**

Table 4 **Electrochemical parameters taken from CVs in figure 9.**

Sample	Pt loading / mg cm^{-2}	Oxide reduction / V vs. RHE	Pt area / cm^2 Pt	Pt $area_m$ / m^2 Pt g^{-1} Pt
Pt/C	0.349	0.749	349.1	75.8
Pt/C 750 °C	0.310	0.761	177.1	43.3
Pt/C 900 °C	0.327	0.788	132.2	30.7

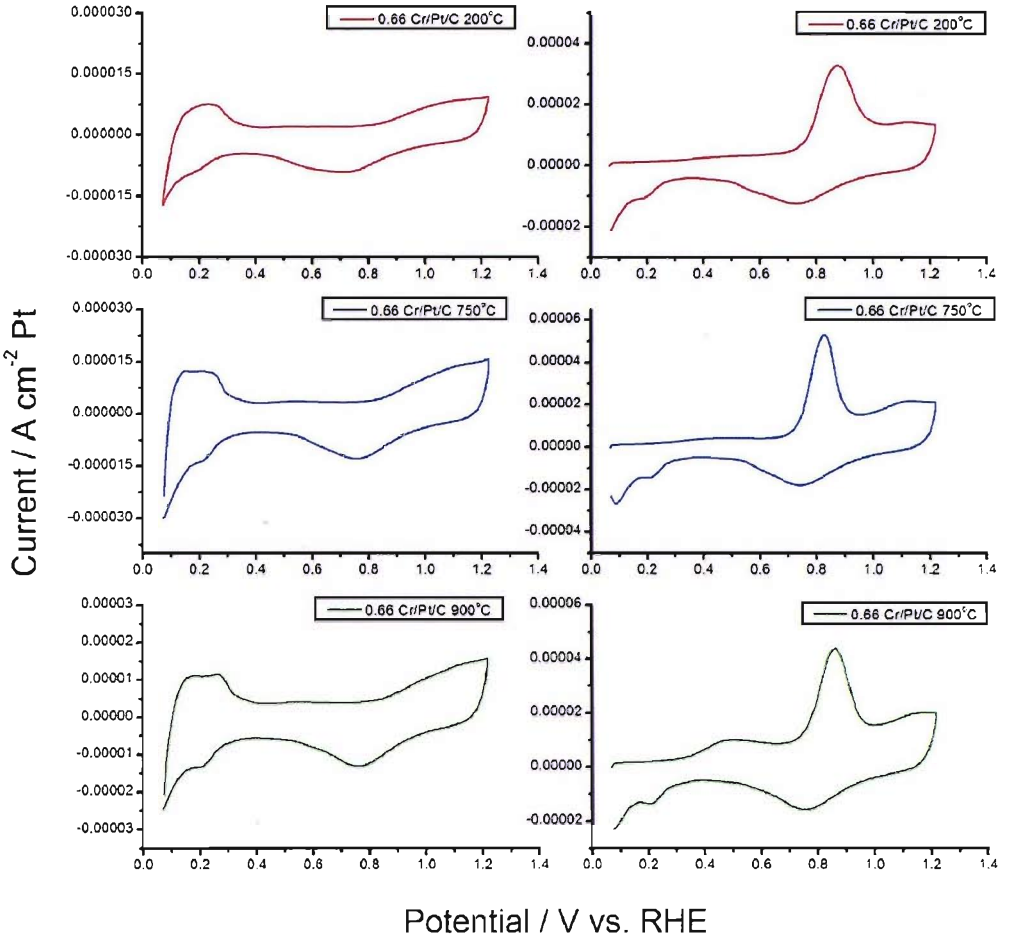

Figure 10 **Cyclic voltammograms (left column) and CO stripping voltammetry (right column) of 0.66 Cr/Pt/C prepared by the $Cr(Ph)_2$ route annealed at 200 °C (top), 750 °C (middle) and 900 °C (bottom). Carried out in 2.5 M H_2SO_4 with a scan rate of 10 mV s^{-1}, currents normalised to the platinum surface area determined by CO stripping voltammetry.**

Table 5 **Electrochemical parameters taken from CVs in figure 10.**

Sample	Pt loading / mg cm^{-2}	Oxide reduction / V vs. RHE	Pt area / cm^2 Pt	Pt $area_m$ / m^2 Pt g^{-1} Pt
0.66 Cr/Pt/C 200 °C	0.362	0.717	319.0	66.8
0.66 Cr/Pt/C 750 °C	0.368	0.759	182.0	37.6
0.66 Cr/Pt/C 900 °C	0.378	0.761	162.4	32.5

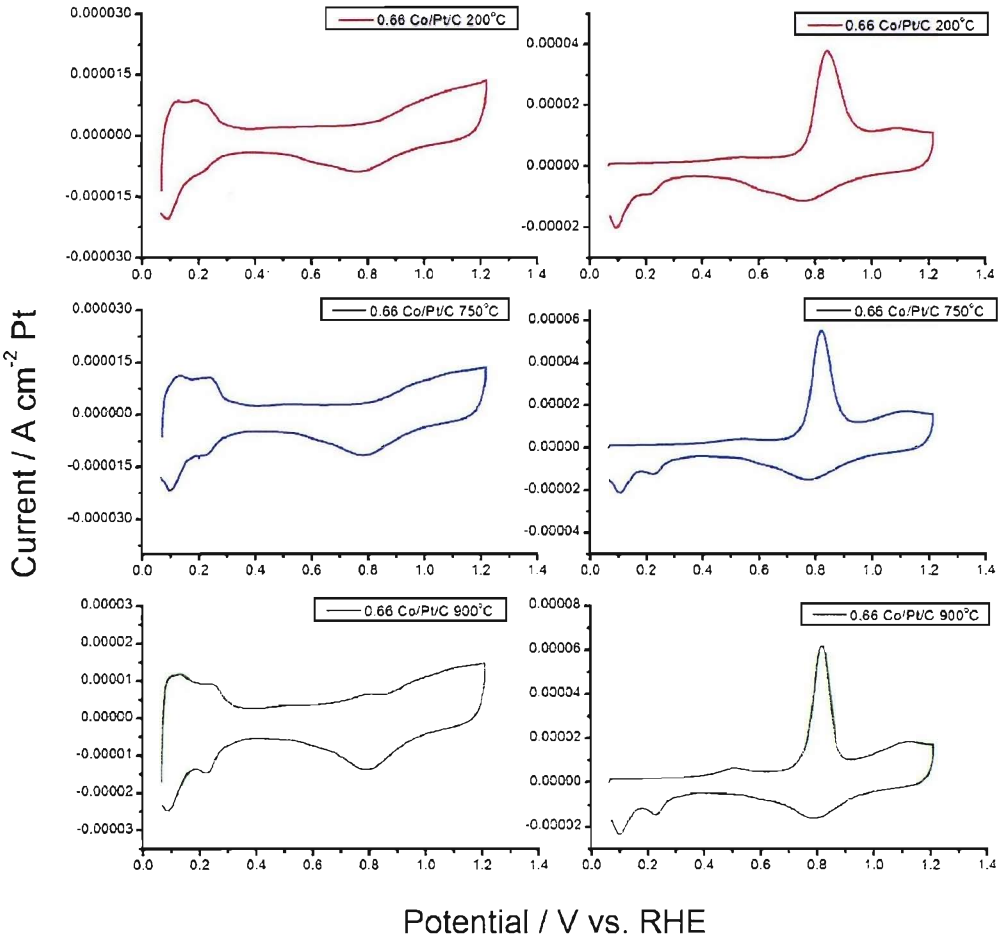

Figure 11 **Cyclic voltammograms (left column) and CO stripping voltammetry (right column) for 0.66 Co/Pt/C annealed at 200 °C (top), 750 °C (middle) and 900 °C (bottom) . Carried out in 2.5 M H_2SO_4 with a scan rate of 10 mV s^{-1}, currents normalised to the platinum surface area determined by CO stripping voltammetry.**

Table 6 **Electrochemical parameters taken from CVs in figure 11.**

Sample	Pt loading / mg cm^{-2}	Oxide reduction / V vs. RHE	Pt area / cm^2 Pt	Pt $area_m$ / m^2 Pt g^{-1} Pt
0.66 Co/Pt/C 200 °C	0.352	0.768	324.8	69.8
0.66 Co/Pt/C 750 °C	0.362	0.784	222.9	46.7
0.66 Co/Pt/C 900 °C	0.391	0.784	168.2	32.6

Assessing the cyclic voltammetry of the Pt/C catalysts several trends can be observed. The hydrogen adsorption /desorption region is a characteristic feature of Pt electrochemistry. The features in this region for the Pt/C catalysts have greater definition on increasing the annealing temperature. The untreated Pt/C catalyst has the smallest particle size of all the Pt/C catalysts. Pt of a very small particle size has very few crystal facets at the surface, giving rise to a lack of distinct adsorption sites. On increasing annealing temperature the particle size increases, yielding extended lattice planes [2]. The study of single Pt crystals has shown that different crystal faces have different hydrogen adsorption / desorption features. In the case of polycrystalline Pt particles, the different crystal faces give rise to two distinct hydrogen adsorption sites. Where the untreated Pt/C catalyst shows a broad hydrogen adsorption/desorption feature, the annealed Pt/C sample at 900 °C shows two well defined peaks. The evidence for growth in crystallite size is replicated in the mass normalised Pt area. The area drops from 75.8 to 30.7 $m^2 g^{-1}$ Pt as the catalyst is annealed to 900 °C.

The hydrogen adsorption / desorption region for the 0.66 Cr/Pt/C catalysts is clearly identifiable, although appears slightly less defined in comparison to the Pt/C catalysts. This may be attributable to the presence of Cr at the surface. In general the electrochemical response for the Cr modified Pt/C catalyst is very similar to that of Pt/C as has been found with PtCr/C alloys previously [6, 32]. A large change has been observed when PtCr/C alloys have been heat treated at 1200 °C [32]. This was explained by the change in ratio of crystal facets at higher annealing temperature as work by Paulus *et al.* has shown [33]. The Cr/Pt/C catalyst prepared by the $Cr(Cp)_2$ route showed very similar features and as such the voltammograms are not included in this section.

A decrease in mass normalised surface area is observed on addition of Cr and Co at the lowest annealing temperature. This could be related to the second metal being present at the surface blocking hydrogen adsorption or that the 200 °C heat treatment could have caused a slight increase in particle size. These mass normalised values should be treated with a certain degree of caution as there are several areas where error can be introduced; the ionomer loading, the compression of the catalyst layer, the amount of catalyst in electrical contact, and

loss of catalyst in the pressing procedure. These are all examples where the calculated mass giving rise to the Pt electrochemical area could be in doubt. As a consequence it is more appropriate to normalise the current by the available Pt surface area as has been done in this section. This is not to say that the measurement of the mass normalised Pt is irrelevant, but that the area determined should be used to identify trends and approximate values. In each of the series of catalysts assessed in this section, the mass normalised Pt area decreases with increasing annealing temperature. The values for mass normalised Pt area show that a drastic drop in area is not observed when the second metal is introduced into the system. Both the modified catalysts presented should ideally have 2/3 of the Pt surface covered with the alloying component. This could mean that the metal being deposited is clustering on deposition or that the second metal is present but not hindering the electrochemical processes occurring at Pt sites. It could also mean that when the secondary metal is exclusively at the surface in a non-alloyed state, it readily dissolves in the electrolytic solution.

The Co/Pt/C catalysts also show very similar hydrogen adsorption/desorption features to those observed for Pt/C, again with two distinct adsorption sites becoming more defined on increasing annealing temperature. The CO stripping voltammograms show a much narrower CO oxidation peak compared to the Pt/C and Cr/Pt/C catalysts, suggesting a change in surface properties. The peak position of the CO oxidation peak varies between 0.83 and 0.87 V vs. RHE for both the Pt/C and Cr/Pt/C catalysts. The position of the CO peak is not dissimilar for the Co/Pt/C catalysts where it ranges from 0.84 to 0.82 V vs. RHE.

3.5 XAS Studies

3.5.1 XANES – 2nd Metal K edge

Analysis of the XANES region of the XAS data allows for information regarding the electronic properties and oxidation state of the metal under investigation to be probed. Figure 12 shows the normalised XANES spectra obtained at the Cr K edge for the prepared Cr/Pt/C catalysts along with reference materials. The data were acquired under atmospheres of H_2 and air, although no discernable differences were apparent, and therefore only data acquired in H_2 are shown.

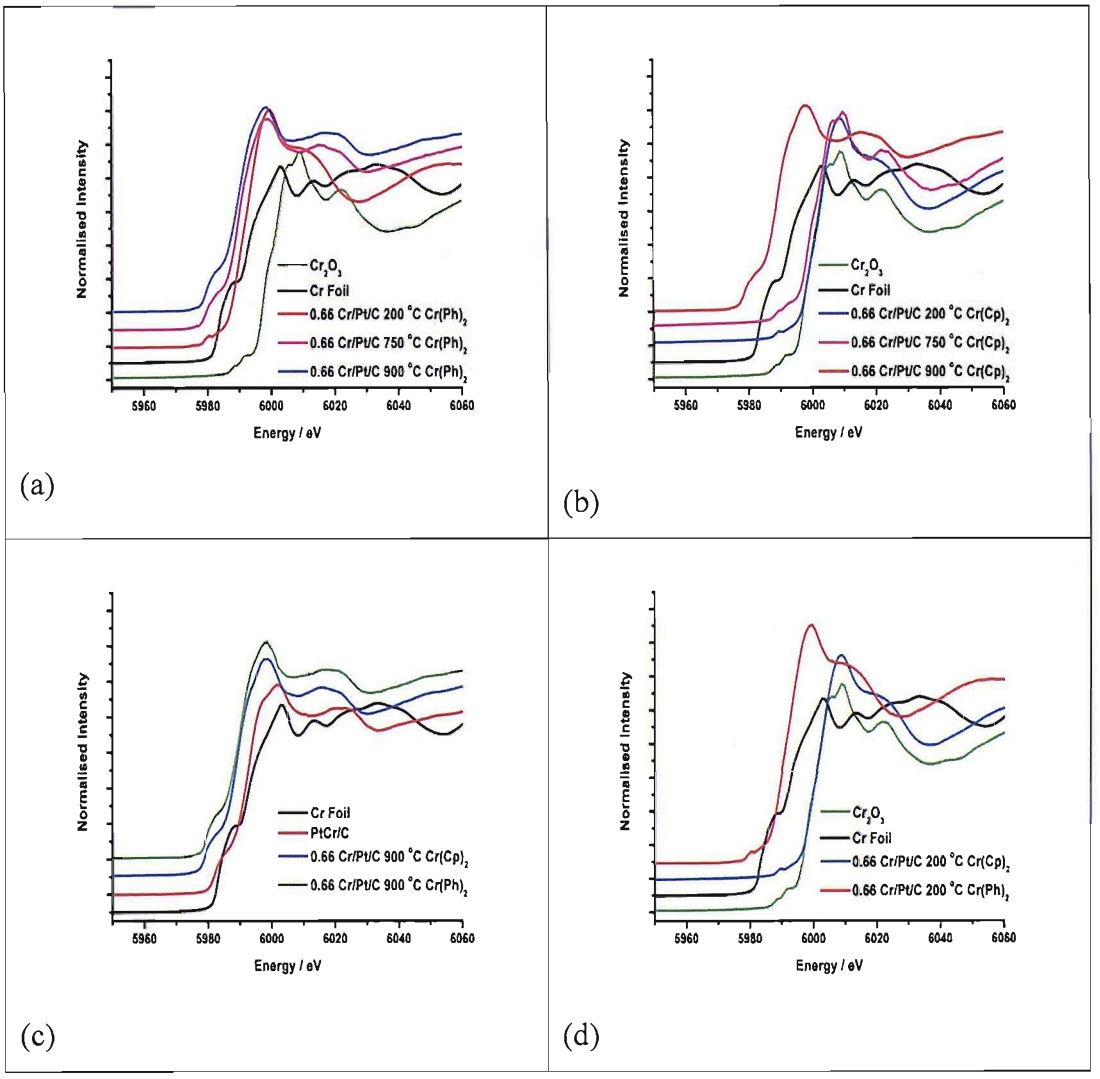

Figure 12 **XANES spectra at the Cr K edge for 0.66 Cr/Pt/C prepared by the (a) $Cr(Ph)_2$ and the (b) $Cr(Cp)_2$ routes at heat treatments of 200, 750, and 900 °C. (c) and (d) show a comparison of the 900 and 200 °C heat treated catalysts respectively. (The comparisons include a Cr foil, Cr_2O_3, and a conventionally prepared PtCr/C alloy catalyst).**

Features in the XANES region can arise due to electronic transitions and this is exemplified by the data obtained at the Cr K edge. A pre-edge feature can be observed at approximately 5980 eV which corresponds to the dipole forbidden 1s → 3d transition. This pre-edge feature is highly sensitive to the coordination geometry of the Cr as the t_2 orbitals have some p-orbital character. It is found that tetrahedrally coordinated Cr species (e.g. CrO_3) exhibit a sharp white line in this pre-edge region [34]. It can be seen that the two preparatory methods give rise to different XANES spectra. The Cr/Pt/C catalyst prepared by the $Cr(Ph)_2$ route at different heat treatments all exhibit an edge position around 5990 eV, similar to that of a Cr foil. In this instance a slight negative shift for the Cr/Pt/C catalysts is observed. Section 1 discussed the enhancement alloying with Cr offers towards Pt based catalysts. One of the reasons proposed was a change in Pt d electron vacancy, with the electrons being transferred to the alloying component. Thus the slight negative shift can be rationalised as charge transfer from the Pt towards the Cr. It has been shown that, for Cr, there is on average an increase in edge position of 1.6 eV per unit change in valency [34]. This suggests that the Cr present in these samples is mostly present in a metallic phase, and the deposition method has successfully targeted the Pt surface sites. However, it is also apparent that the 200 °C heat treated sample is more oxidised than those heated to 750 and 900 °C and is similar in shape to the analogous sample prepared by the chromocene route, although a different oxidation state is observed. Thus it appears that the Cr may be initially present as oxidised adatoms on the Pt surface, becoming more incorporated into a metallic phase as the annealing temperature is increased.

The same trend is not observed for the Cr/Pt/C catalysts prepared by the $Cr(Cp)_2$ route. In this instance, the edge position of the 200 and 750 °C annealed samples is at 5997 eV, the same energy observed for Cr_2O_3. It can also be seen that the 750 °C sample has a near identical XANES spectrum to that obtained for Cr_2O_3. The 900 °C heat treated sample has a XANES spectrum akin to the $Cr(Ph)_2$ prepared Cr/Pt/C samples. This suggests that initially the Cr is present as oxide particles around the Pt. On heating to 750 °C, the Cr_2O_3 phase is formed, and on heating to 900 °C the Cr is driven into the Pt particle. Comparison of both the

900 °C annealed Cr/Pt/C catalysts with a conventionally prepared PtCr/C alloy (figure 12c) shows that the XANES spectra for both are consistent with that of a PtCr alloy.

The Co K edge XANES spectra also exhibit a pre-edge feature as a result of 1s → 3d transitions and are also sensitive on the coordination geometry of the absorber. This sharp feature is present in tetrahedral Co environments but not in octahedral coordination environments [35]. Figure 13 shows the Co K edge XANES spectra for the 0.66 Co/Pt/C samples along with those of the reference materials. The spectra have been acquired in atmospheres of air and H_2, with the spectra being shown in figures 13 and 14 respectively.

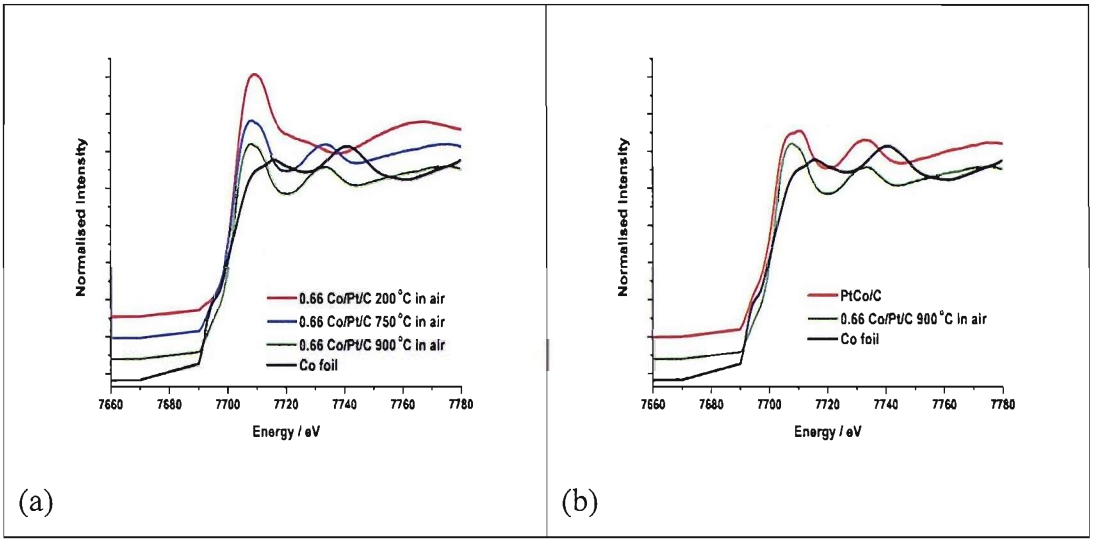

Figure 13 **XANES spectra at the Co K edge for 0.66 Co/Pt/C catalysts (a) at different annealing temperatures and (b) compared to a conventional PtCo/C alloy, acquired in an atmosphere of air.**

The Co/Pt/C catalysts show a similar trend to that of the Cr/Pt/C catalysts prepared by the $Cr(Ph)_2$ route. The edge positions of this series of catalysts are similar to the edge position of the corresponding metal foil. This again suggests that the Co is predominantly in a metal environment and it is assumed that this is a result of association with the Pt particles. The XANES spectra of the 750 and 900 °C annealed catalysts are very similar to each other and very similar to that of a conventionally prepared PtCo/C catalyst as shown in figure 13b. The 200 °C annealed catalyst is still heavily oxidised as shown by the intense white line,

although the XANES do not correlate with that of CoO or Co_3O_4 [35]. When the gaseous environment is changed from air to H_2 there is a substantial change in the XANES spectrum of the 200 °C annealed sample (figure 14a).

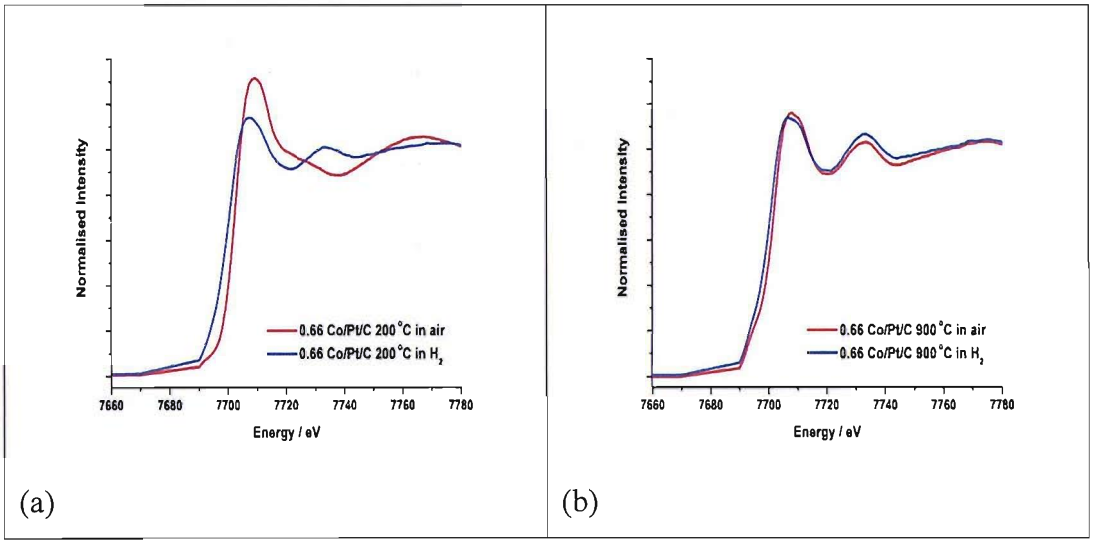

Figure 14 **XANES spectra at the Co K edge for (a) 200 °C and (b) 900 °C 0.66 Co/Pt/C catalysts in atmospheres of air and H_2**

On exposure to H_2, the XANES spectrum of the 200 °C heat treated sample becomes less oxidised and closely resembles the XANES spectra of the 750 and 900 °C heat treated samples. The 900 °C annealed sample retains near identical XANES features in both environments. Overall from the Co K edge XANES spectra, it can be inferred that both the 750 and 900 °C annealed samples are comparable to a conventional alloy and that the 200 °C sample is initially present as a Co oxide on the Pt surface, which becomes incorporated into the Pt particle on exposure to H_2.

3.5.2 XANES – Pt L_2 and L_3 edges

For the Cr/Pt/C catalysts a complete analysis of the Pt L_2 and L_3 edge XANES spectra was performed (figures 15-16) to enable determination of the fractional d-band vacancy.

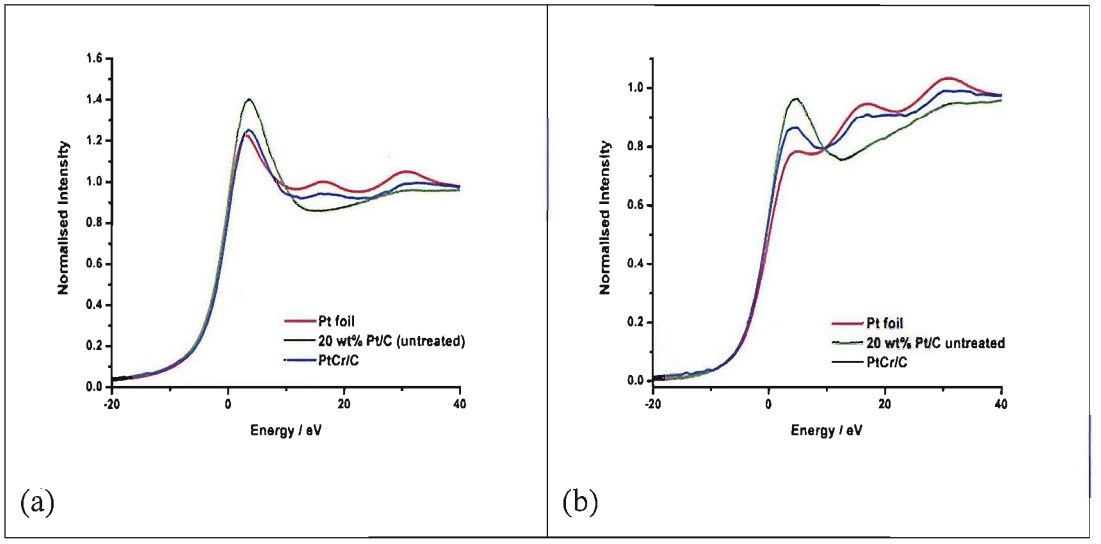

Figure 15 **Pt L_3 (a) and L_2(b) XANES spectra of a Pt foil, Pt/C, and PtCr/C acquired as BN pellets in an atmosphere of air.**

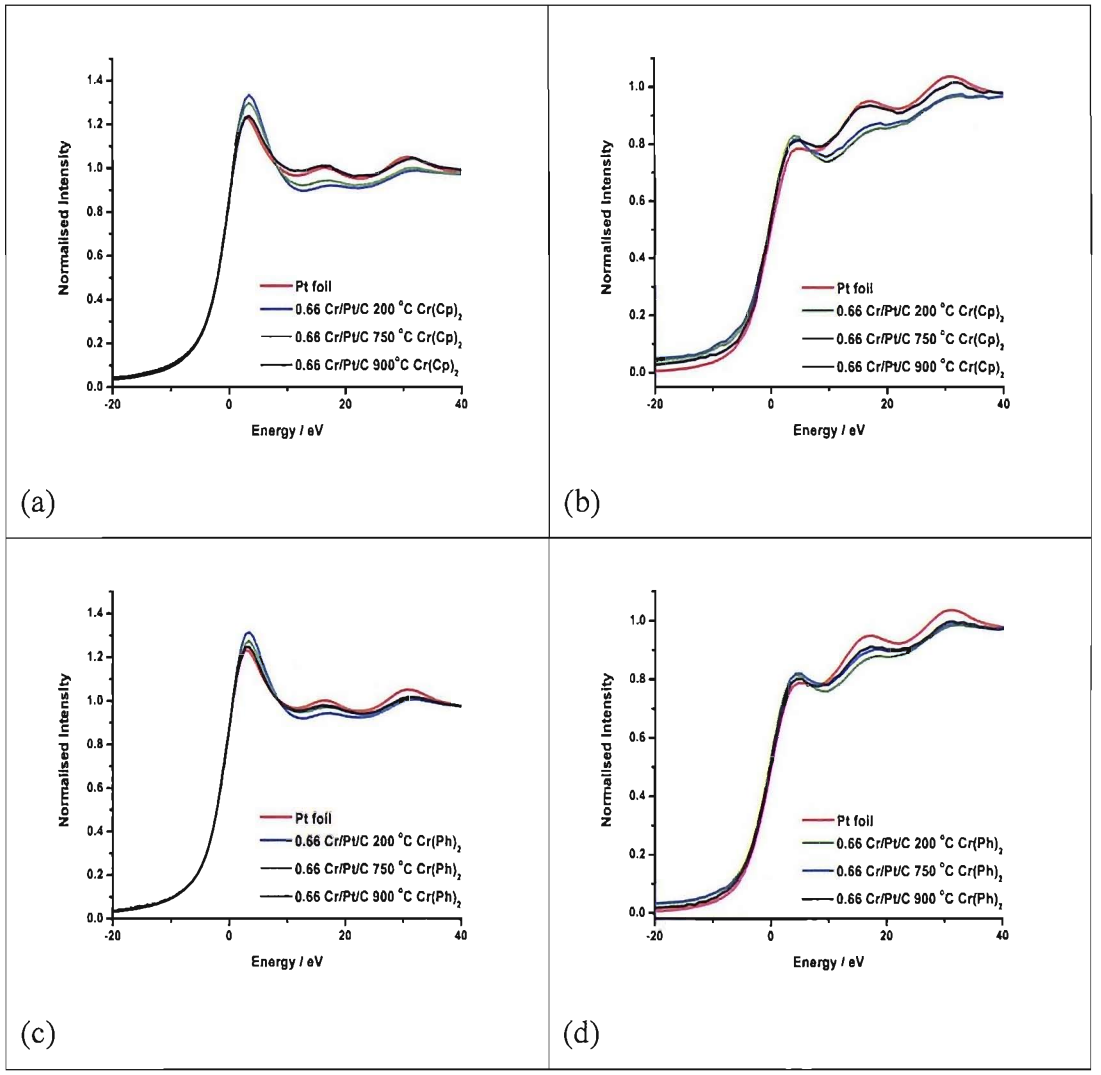

Figure 16 **Pt L_3 and L_2 XANES spectra of the Cr/Pt/C catalysts prepared by the (a & b) $Cr(Cp)_2$ and (c & d) $Cr(Ph)_2$ routes, acquired as BN pellets in an atmosphere of air, a Pt foil is also included for comparison.**

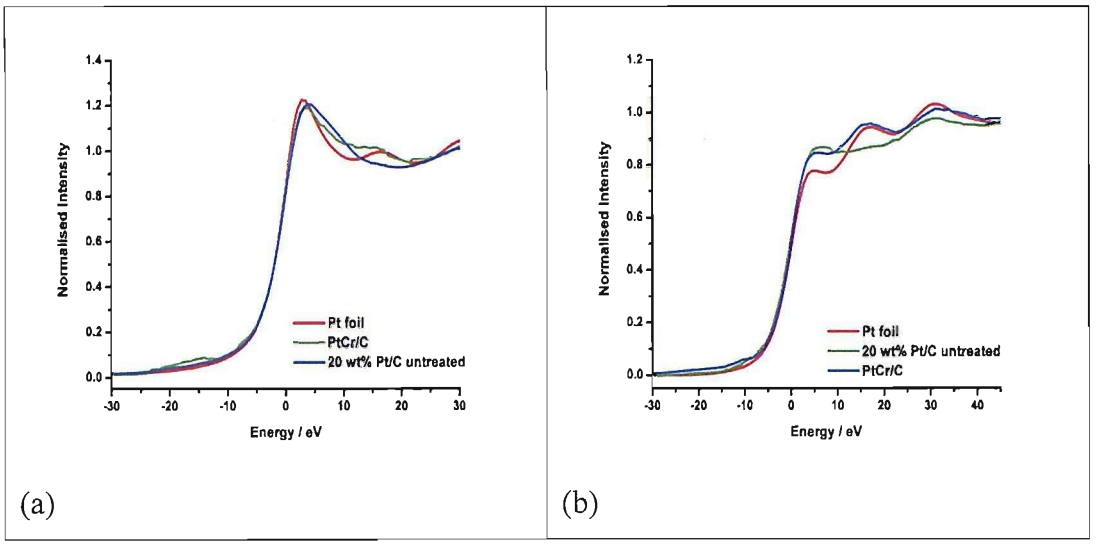

Figure 17 **Pt L_3 (a) and L_2(b) XANES spectra of a Pt foil, Pt/C, and PtCr/C acquired as BN pellets in an atmosphere of H_2.**

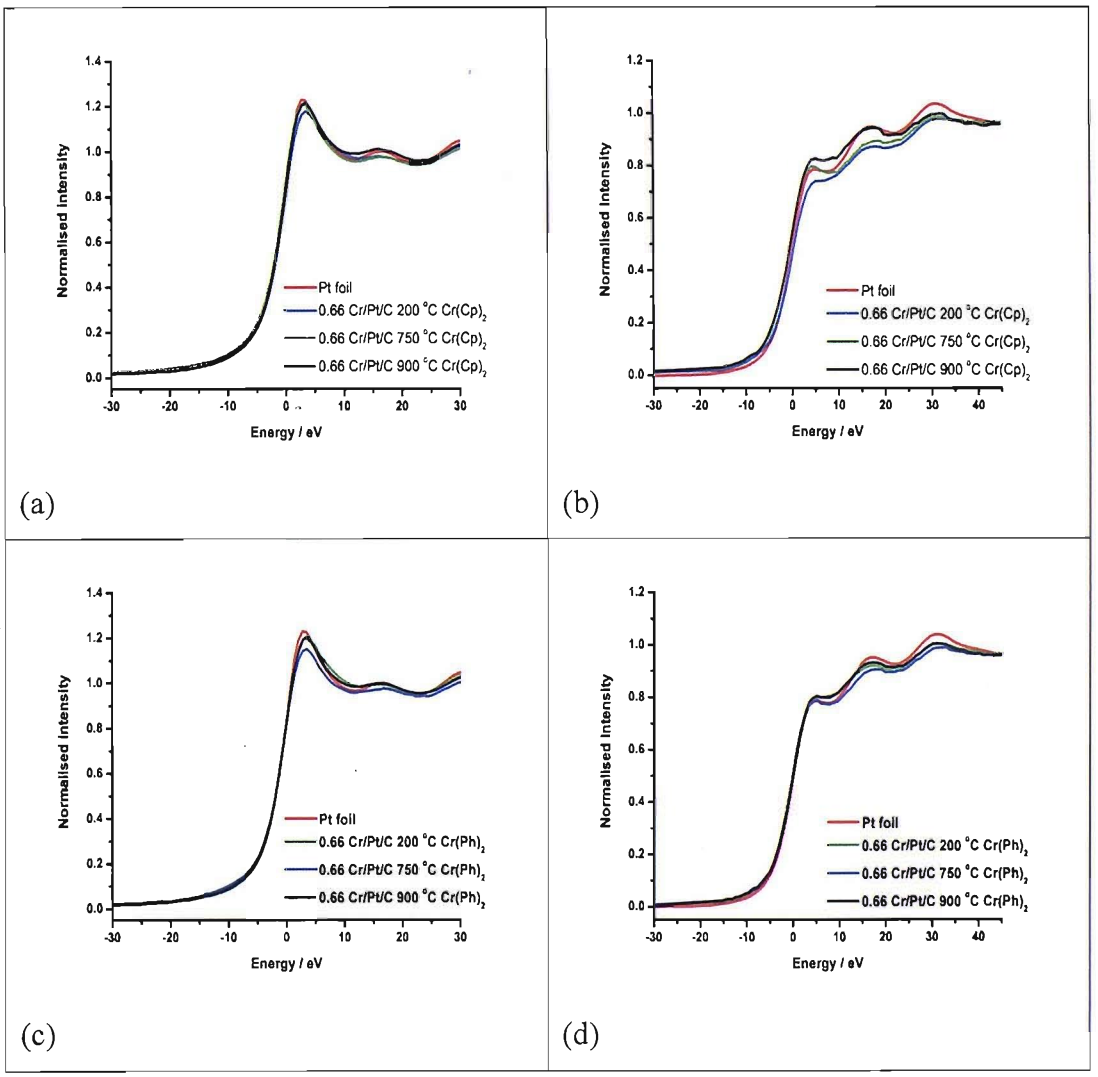

Figure 18 **Pt L_3 and L_2 XANES spectra of the Cr/Pt/C catalysts prepared by the (a & b) $Cr(Cp)_2$ and (c & d) $Cr(Ph)_2$ routes, acquired as BN pellets in an atmosphere of H_2, a Pt foil is also included for comparison.**

For both sets of 0.66 Cr/Pt/C catalysts acquired in air show that the intensity of the white line is a function of the annealing temperature, with the lowest heat treatment resulting in the largest white line. This is exemplified to a greater extent in the more sensitive Pt L_3 edge spectra. As the catalysts are exposed to higher annealing temperatures the particle size increases reducing the amount of surface Pt sites. The intensity of the white line also represents the degree of oxidation of Pt, which is correlated to the proportion of the Pt at the surface. For the 0.66 Cr/Pt/C catalysts prepared by the $Cr(Cp)_2$ route the XANES spectra of the 200 and 750 °C annealed samples have an intense white line indicating that the Pt is highly oxidised. The 900 °C annealed sample has a less intense white line and is close in resemblance to that of a Pt foil. For the 0.66 Cr/Pt/C catalysts prepared by the $Cr(Ph)_2$ route annealed at 750 and 900 °C, the XANES spectra are very similar to a Pt foil, with the 200 °C sample appearing slightly more oxidised. The XANES spectrum of the untreated Pt/C is more distinctive due to the highly oxidised nature of the catalyst and the small Pt particle size, as shown in figure 15. It can also be seen that the XANES spectrum of a conventional PtCr/C catalyst is similar to those prepared using the controlled surface modification procedure. Table 7, shown below, details the values of $(h_J)_{t,s}$ for the catalysts studied in air and H_2.

Table 7 **Pt d-band vacancies for different Pt/C, Cr/Pt/C and PtCr/C catalysts.**

Catalyst	$(h_J)_{t,s}$ air	$(h_J)_{t,s}$ H_2
Untreated 20 wt% Pt/C	0.334	0.345
0.66 Cr/Pt/C 200 °C $Cr(Cp)_2$	0.307	0.276
0.66 Cr/Pt/C 750 °C $Cr(Cp)_2$	0.306	0.306
0.66 Cr/Pt/C 900 °C $Cr(Cp)_2$	0.309	0.313
0.66 Cr/Pt/C 200 °C $Cr(Ph)_2$	0.306	0.296
0.66 Cr/Pt/C 750 °C $Cr(Ph)_2$	0.305	0.282
0.66 Cr/Pt/C 900 °C $Cr(Ph)_2$	0.304	0.301
PtCr/C	0.303	0.333

The calculated values of $(h_J)_{t,s}$ in air indicate that only the untreated Pt/C shows a significant difference. This is most likely due to the small Pt particle size of the catalyst. All the other values can be seen to be comparable to one another within error. The values of $(h_J)_{t,s}$ in H_2 are far more variable, with only the Pt/C and PtCr/C catalysts showing a significant increase in $(h_J)_{t,s}$. The values for the Cr/Pt/C catalysts fluctuate greatly with no obvious explanation for this, and thus must be attributed to the error associated with the measurement. The data acquired in H_2, eliminates the contribution of Pt oxide formation from the XANES spectra, and should be more representative of the electronic properties of the Pt. Mukerjee *et al.* [8] have looked at the fractional band vacancy of different supported Pt alloys including PtCr/C. The experiments were conducted in an *in-situ* electrochemical environment at a potential in the double layer region. Mukerjee found that in this environment a PtCr/C bulk alloy exhibits a $(h_J)_{t,s}$ value of 0.360. This is significantly larger than the value calculated in this study, with the differences in $(h_J)_{t,s}$ being attributable to the different conditions under which the experiments were performed. However, it is worth establishing that there is a large error associated with calculating $(h_J)_{t,s}$, and that the values determined are best used to study trends rather than to be taken as accurate and transferable values. The numerous normalisation processes along with the area calculations bring a significant amount of error into process. Also the Pt L_3 and L_2 edge XANES spectra not only reflect the transitions described but other processes and interactions such as the Pt particle size, as can be seen by the value of $(h_J)_{t,s}$ calculated for Pt/C in this study.

3.5.3 EXAFS – Cr K edge Studies

EXAFS data were collected as BN pellets in atmospheres of H_2 and air. The k^2 weighted EXAFS data along with the associated Fourier transform and the fitting parameters determined for the Cr/Pt/C catalysts are detailed below in figures 19-22 and tables 8-11.

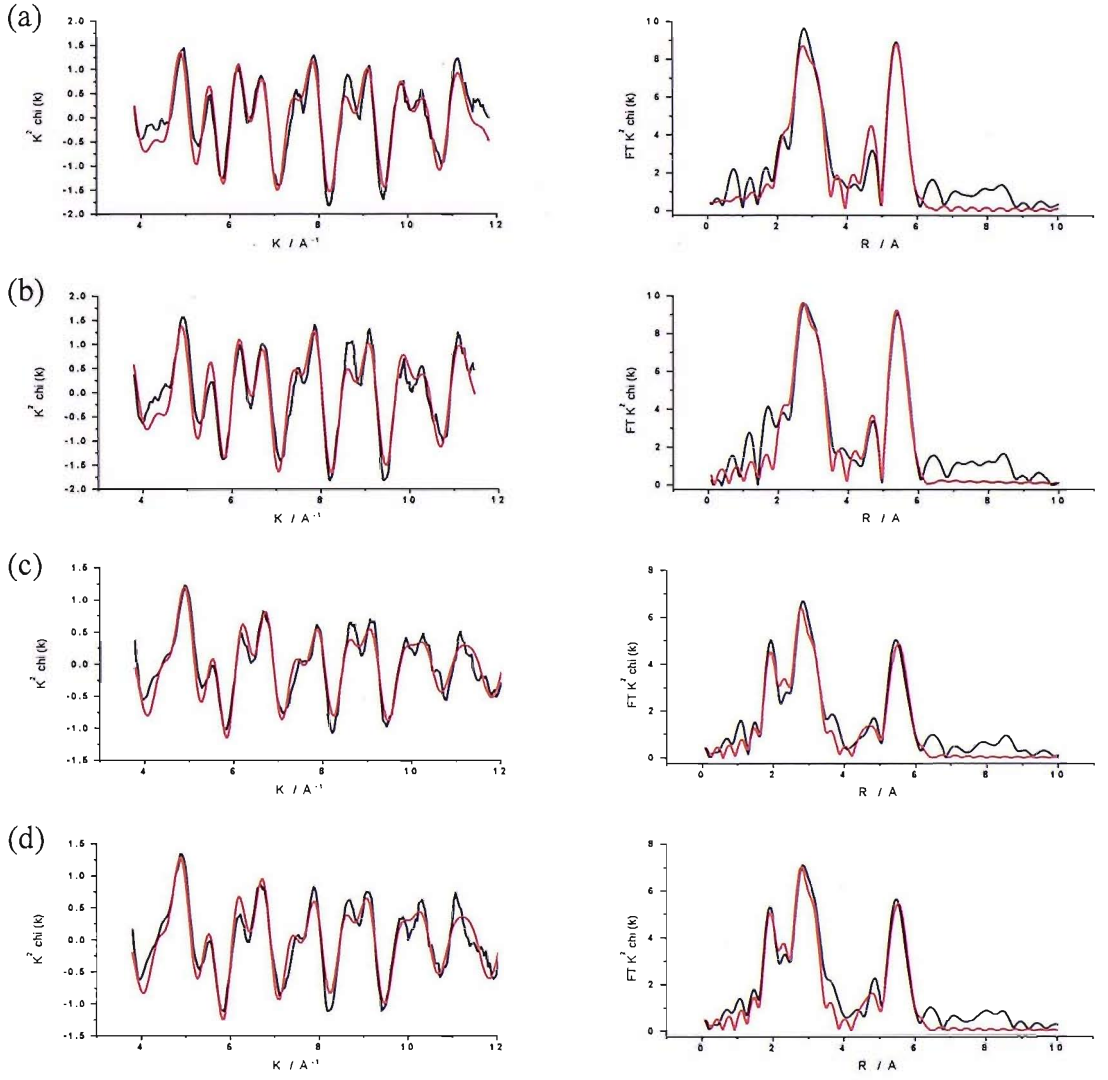

Figure 19 **Cr K edge (left) k^2 weighted experimental data and fit along with (right) the Fourier transform for 40 wt % PtCr (3:1) / C acquired in air and H_2 (a & b), and for 20 wt% PtCr (3:1) / C acquired in air and H_2 (c & d). Data (black line) and fit (red line).**

Table 8 **Structural parameters for PtCr/C catalysts acquired in atmospheres of air and H_2 by fitting the Cr K edge EXAFS data. Un1 refers to unit 1 and designates both scattering processes taking place in the same shell.**

Condition	**PtCr/C - Calculated Parameters (Cr K edge)**					
40 wt % PtCr (3:1) in air	**Shell**	***N***	***R* / Å**	**$2\sigma^2$ / Å^2**	***E_f* / eV**	**R_{exafs} / %**
	Cr-Pt (un1)	6.9 ± 0.6	2.719 ± 0.007	0.011 ± 0.001	- 2.5 ± 0.8	36.1
	Cr-Pt	9.2 ± 2.4	4.76 ± 0.02	0.010 ± 0.002		
	Cr-Pt-Cr (un1)	6.9 ± 0.6	5.48 ± 0.01	0.019 ± 0.002		
40 wt % PtCr (3:1) in H_2	Cr-Pt (un1)	6.8 ± 0.6	2.722 ± 0.008	0.009 ± 0.001	-3.0 ± 0.9	36.6
	Cr-Pt	6.8 ± 2.6	4.76 ± 0.02	0.008 ± 0.003		
	Cr-Pt-Cr (un1)	6.8 ± 0.6	5.49 ± 0.01	0.019 ± 0.002		
20 wt % PtCr (3:1) in air	Cr-O	1.2 ± 0.1	1.99 ± 0.01	0.005 ± 0.002	-3.4 ± 0.7	30.8
	Cr-Pt (un1)	3.9 ± 0.2	2.720 ± 0.005	0.010 ± 0.006		
	Cr-Cr	1.9 ± 0.7	4.79 ± 0.03	0.012 ± 0.006		
	Cr-Pt-Pt (un1)	3.9 ± 0.2	5.50 ± 0.01	0.017 ± 0.002		
20 wt % PtCr (3:1) in air	Cr-O	1.4 ± 0.1	1.99 ± 0.01	0.011 ± 0.006	-3.5 ± 0.8	32.0
	Cr-Pt (un1)	3.7 ± 0.2	2.713 ± 0.005	0.009 ± 0.006		
	Cr-Pt	1.8 ± 0.7	4.70 ± 0.03	0.010 ± 0.006		
	Cr-Pt-Cr (un1)	3.7 ± 0.2	5.50 ± 0.01	0.015 ± 0.002		

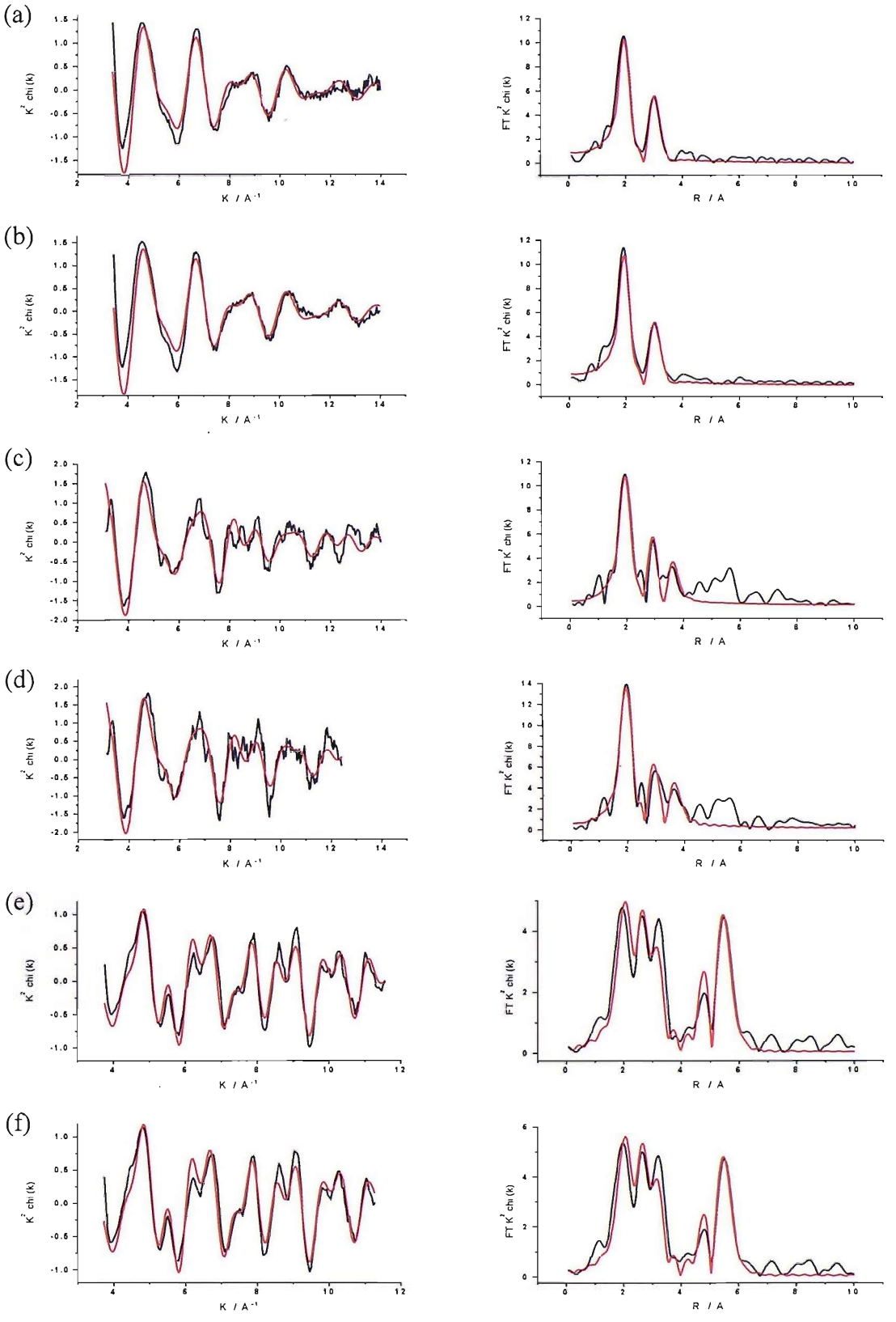

Figure 20 **Cr K edge (left) k^2 weighted experimental data and fit along with (right) the Fourier transform for 0.66 Cr/Pt/C $Cr(Cp)_2$ annealed at 200 °C acquired in air and H_2 (a & b), annealed at 750 °C acquired in air and H_2 (c & d), and annealed at 900 °C acquired in air and H_2 (e & f). Data (black line) and fit (red line).**

Table 9 **Structural parameters for 0.66 Cr/Pt/C $Cr(Cp)_2$ at different annealing temperatures acquired in atmospheres of air and H_2 by fitting the Cr K edge EXAFS data. Un1 refers to unit 1 and designates both scattering processes taking place in the same shell.**

Condition	**0.66 Cr/Pt/C $Cr(Cp)_2$ - Calculated Parameters (Cr K edge)**					
200 °C in air	**Shell**	***N***	***R* / Å**	**$2\sigma^2$ / Å^2**	**E_f / eV**	**R_{exafs} / %**
	Cr-O	3.3 ± 0.2	2.00 ± 0.01	0.007 ± 0.002	- 5.1 ± 1.0	38.5
	Cr-Cr	2.0 ± 0.3	3.00 ± 0.01	0.012 ± 0.003		
200 °C in H_2	Cr-O	3.4 ± 0.2	1.95 ± 0.01	0.006 ± 0.002	-4.2 ± 1.0	38.6
	Cr-Cr	1.9 ± 0.3	3.00 ± 0.02	0.012 ± 0.003		
750 °C in air	Cr-O	3.6 ± 0.2	2.00 ± 0.01	0.009 ± 0.002	-3.3 ± 0.9	42.5
	Cr-Cr	1.6 ± 0.3	2.93 ± 0.02	0.010 ± 0.003		
	Cr-Cr	1.5 ± 0.6	3.69 ± 0.03	0.004 ± 0.003		
750 °C in H_2	Cr-O	3.8 ± 0.3	1.99 ± 0.02	0.006 ± 0.002	-2.6 ± 1.2	43.5
	Cr-Cr	1.7 ± 0.4	2.94 ± 0.02	0.010 ± 0.004		
	Cr-Cr	1.9 ± 0.8	3.68 ± 0.03	0.004 ± 0.003		
900 °C in air	Cr-O	1.6 ± 0.2	2.02 ± 0.01	0.009 ± 0.003	-6.2 ± 1.0	34.4
	Cr-Pt (un1)	3.3 ± 0.3	2.714 ± 0.008	0.012 ± 0.001		
	Cr-Pt	5.4 ± 1.4	4.77 ± 0.02	0.010 ± 0.002		
	Cr-Pt-Cr (un1)	3.3 ± 0.3	5.49 ± 0.02	0.020 ± 0.003		
900 °C in H_2	Cr-O	1.7 ± 0.2	2.02 ± 0.01	0.008 ± 0.002	-4.4 ± 1.0	31.6
	Cr-Pt (un1)	3.7 ± 0.3	2.706 ± 0.008	0.012 ± 0.001		
	Cr-Pt	5.5 ± 1.5	4.77 ± 0.02	0.011 ± 0.003		
	Cr-Pt-Cr (un1)	3.7 ± 0.3	5.48 ± 0.02	0.018 ± 0.002		

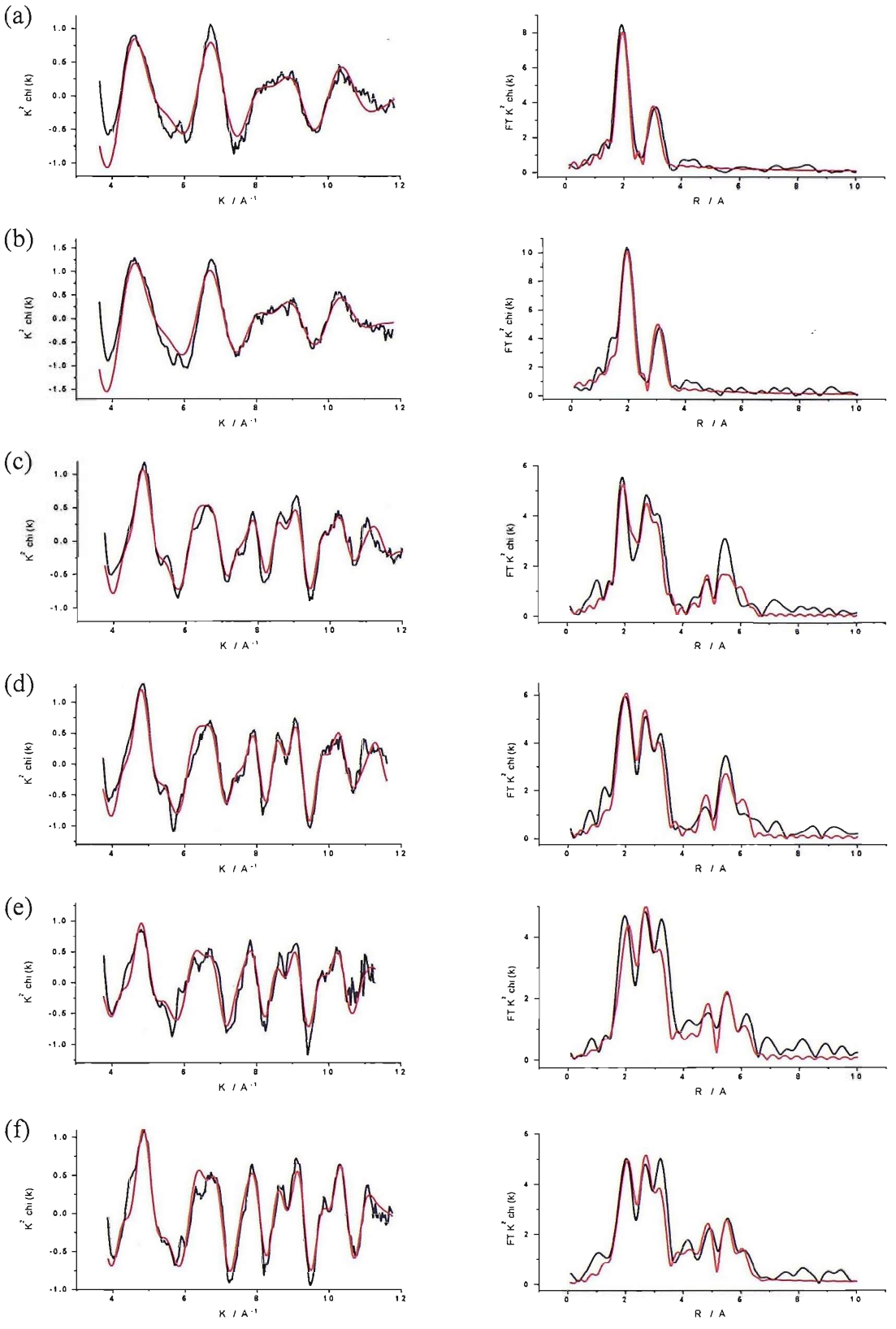

Figure 21 **Cr K edge (left) k^2 weighted experimental data and fit along with (right) the Fourier transform for 0.66 Cr/Pt/C $Cr(Ph)_2$ annealed at 200 °C acquired in air and H_2 (a & b), annealed at 750 °C acquired in air and H_2 (c & d), and annealed at 900 °C acquired in air and H_2 (e & f). Data (black line) and fit (red line).**

Table 10 **Structural parameters for 0.66 Cr/Pt/C $Cr(Ph)_2$ acquired in atmospheres of air and H_2 by fitting the Cr K edge EXAFS data. Un1 refers to unit 1 and designates both scattering processes taking place in the same shell.**

Condition	**0.66 Cr/Pt/C $Cr(Ph)_2$ - Calculated Parameters (Cr K edge)**					
200 °C in air	**Shell**	***N***	***R* / Å**	**$2\sigma^2$ / Å^2**	**E_f / eV**	**R_{exafs} / %**
	Cr-O	2.1 ± 0.2	1.99 ± 0.02	0.003 ± 0.001	- 1.2 ± 2.0	36.7
	Cr-Cr	1.3 ± 0.3	2.97 ± 0.02	0.011 ± 0.004		
200 °C in H_2	Cr-O	2.8 ± 0.3	1.99 ± 0.02	0.004 ± 0.002	-3.7 ± 1.9	36.7
	Cr-Cr	1.5 ± 0.4	2.98 ± 0.02	0.009 ± 0.003		
750 °C in air	Cr-O	1.7 ± 0.1	2.00 ± 0.01	0.008 ± 0.002	-4.8 ± 1.7	32.6
	Cr-Pt (un1)	3.1 ± 0.2	2.716 ± 0.006	0.012 ± 0.001		
	Cr-Pt	3.7 ± 1.0	4.77 ± 0.02	0.012 ± 0.003		
	Cr-Pt-Pt (un1)	3.1 ± 0.2	5.56 ± 0.02	0.016 ± 0.003		
750 °C in H_2	Cr-O	1.9 ± 0.1	2.00 ± 0.01	0.007 ± 0.002	-5.4 ± 1.1	30.2
	Cr-Pt (un1)	3.2 ± 0.3	2.714 ± 0.008	0.010 ± 0.001		
	Cr-Pt	4.2 ± 1.1	4.75 ± 0.02	0.010 ± 0.003		
	Cr-Pt-Pt (un1)	3.2 ± 0.3	5.57 ± 0.02	0.010 ± 0.003		
900 °C in air	Cr-O	1.3 ± 0.2	2.02 ± 0.02	0.009 ± 0.003	-3.5 ± 1.5	38.5
	Cr-Pt (un1)	3.4 ± 0.3	2.718 ± 0.007	0.011 ± 0.001		
	Cr-Pt	1.4 ± 1.0	3.95 ± 0.02	0.014 ± 0.009		
	Cr-Pt	3.7 ± 1.1	4.77 ± 0.01	0.008 ± 0.003		
	Cr-Pt-Pt (un1)	3.4 ± 0.3	5.56 ± 0.01	0.013 ± 0.004		
900 °C in H_2	Cr-O	1.5 ± 0.1	2.00 ± 0.01	0.006 ± 0.002	-3.5 ± 0.9	25.1
	Cr-Pt (un1)	3.6 ± 0.3	2.718 ± 0.007	0.010 ± 0.001		
	Cr-Pt	4.0 ± 0.5	3.95 ± 0.01	0.004 ± 0.001		
	Cr-Pt	2.2 ± 0.5	4.70 ± 0.02	0.012 ± 0.003		
	Cr-Pt-Pt (un1)	3.6 ± 0.3	5.55 ± 0.01	0.015 ± 0.003		

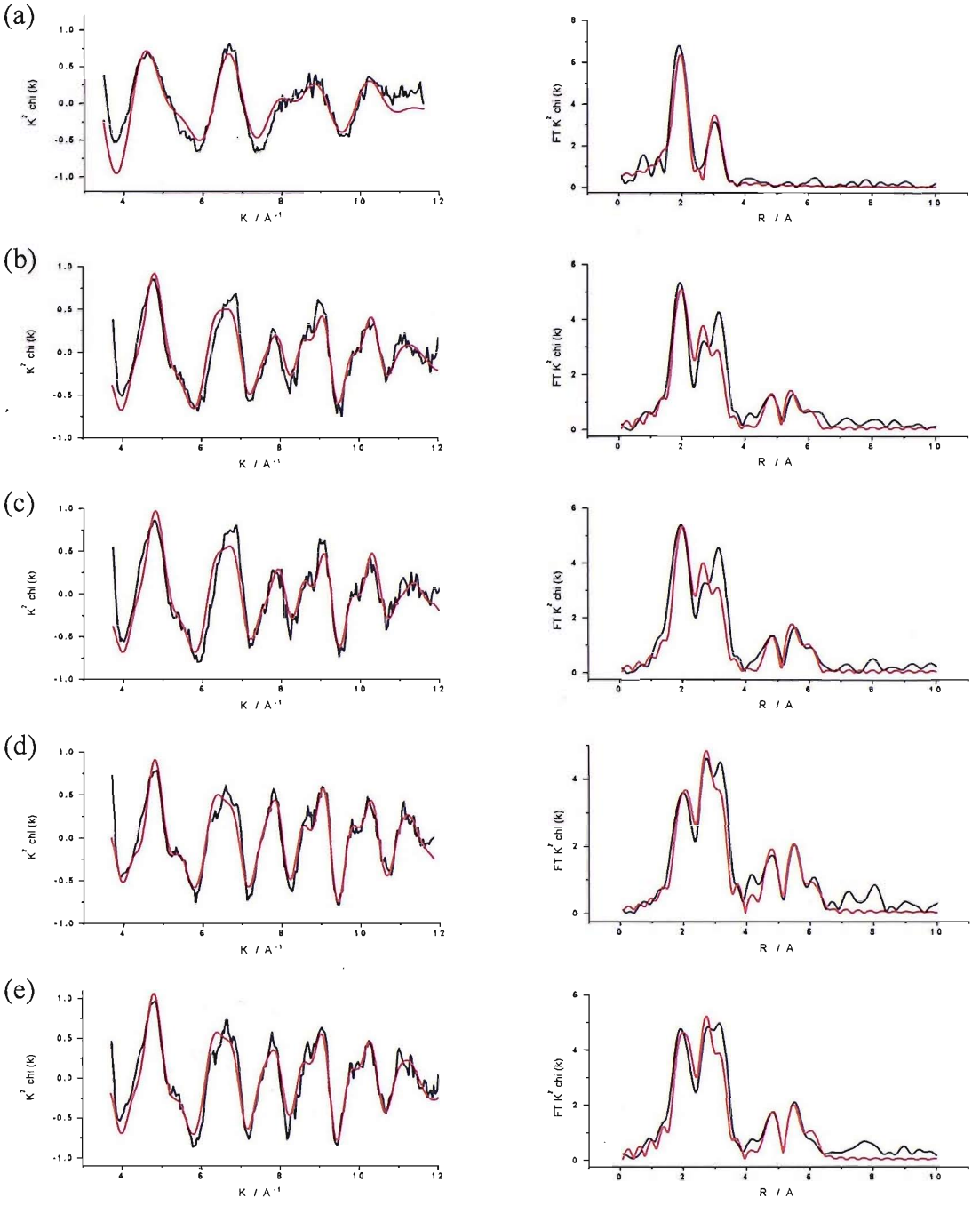

Figure 22 **Cr K edge (left) k^2 weighted experimental data and fit along with (right) the Fourier transform for 0.166 Cr/Pt/C $Cr(Ph)_2$ annealed at 200 °C acquired in air (a), annealed at 750 °C acquired in air and H_2 (b & c), and annealed at 900 °C acquired in air and H_2 (d &e). Data (black line) and fit (red line).**

Table 11 **Structural parameters for 0.166 Cr/Pt/C $Cr(Ph)_2$ at different annealing temperatures acquired in atmospheres of air and H_2 by fitting the Cr K edge EXAFS data. Un1 refers to unit 1 and designates both scattering processes taking place in the same shell.**

Condition	**0.166 Cr/Pt/C $Cr(Ph)_2$ - Calculated Parameters (Cr K edge)**					
200 °C in air	**Shell**	***N***	***R* / Å**	**$2\sigma^2$ / Å^2**	**E_f / eV**	**R_{exafs} / %**
	Cr-O	1.7 ± 0.2	2.00 ± 0.02	0.004 ± 0.001	- 4.5 ± 1.8	45.7
	Cr-Cr	1.1 ± 0.3	3.00 ± 0.02	0.008 ± 0.004		
750 °C in air	Cr-O	1.5 ± 0.2	1.98 ± 0.02	0.006 ± 0.002	-2.0 ± 1.7	37.6
	Cr-Pt (un1)	2.5 ± 0.3	2.69 ± 0.01	0.012 ± 0.001		
	Cr-Pt	2.7 ± 1.1	4.76 ± 0.03	0.009 ± 0.004		
	Cr-Pt-Pt (un1)	2.5 ± 0.3	5.53 ± 0.03	0.014 ± 0.005		
750 °C in H_2	Cr-O	1.7 ± 0.3	1.99 ± 0.02	0.007 ± 0.002	-4.6 ± 1.9	40.3
	Cr-Pt (un1)	2.7 ± 0.3	2.69 ± 0.01	0.012 ± 0.002		
	Cr-Pt	2.5 ± 1.2	4.76 ± 0.03	0.007 ± 0.004		
	Cr-Pt-Pt (un1)	1.7 ± 0.3	5.53 ± 0.03	0.010 ± 0.004		
900 °C in air	Cr-O	1.1 ± 0.1	2.00 ± 0.02	0.007 ± 0.003	-5.1 ± 1.0	31.5
	Cr-Pt (un1)	3.2 ± 0.2	2.708 ± 0.007	0.011 ± 0.001		
	Cr-Pt	5.0 ± 1.0	4.76 ± 0.02	0.011 ± 0.002		
	Cr-Pt-Pt (un1)	3.2 ± 0.2	5.55 ± 0.02	0.016 ± 0.003		
900 °C in H_2	Cr-O	1.5 ± 0.2	2.00 ± 0.01	0.008 ± 0.002	-5.8 ± 1.1	31.5
	Cr-Pt (un1)	3.5 ± 0.3	2.710 ± 0.007	0.011 ± 0.001		
	Cr-Pt	4.6 ± 1.0	4.77 ± 0.02	0.011 ± 0.003		
	Cr-Pt-Pt (un1)	3.5 ± 0.3	5.55 ± 0.02	0.015 ± 0.003		

The fitting parameters of the 20 wt % and 40 wt % 3:1 PtCr/C are substantially different from each other. The 40 wt % 3:1 PtCr/C is prepared by a route thought to yield a well alloyed catalyst, and the fitting parameters agree with this assumption. There are no Cr-O interactions in the 1st shell, and there is a significantly larger 1st shell Cr-Pt coordination number compared to the 20 wt% PtCr/C. It can also be argued that these effects are due to the larger particle size of the 40 wt% catalyst. The larger the particle size, the greater the ratio of bulk Cr to surface Cr, assuming a homogeneous distribution. The greater fraction of Cr in the bulk averages out any surface Cr-O present, and contributes to the average increase in Cr-Pt coordination number. As EXAFS is an averaging technique it is hard in this case to prove which scenario is correct. It can also be seen that there is little difference in the EXAFS data acquired in air and hydrogen, and this trend is observed throughout the series of Cr/Pt/C catalysts. This shows that the mild conditions of $H_2(g)$ at room temperature are not sufficient to reduce the surface Cr-O species.

EXAFS data of 0.66 Cr/Pt/C prepared by the $Cr(Cp)_2$ route show no signs of alloying until the catalyst is annealed at 900 °C. The EXAFS data for the 200 °C annealed catalyst exhibits the majority of its oscillatory amplitude in the low *k* space region, with very few oscillations being present over the whole *k* space range. This suggests that the Cr is mostly in an environment surrounded by low *Z* neighbours, without any long range order. Additional heating to 750 °C gives a much different EXAFS spectrum, where the oscillatory amplitude is more evenly distributed, although still at its highest in low *k* space. There are more oscillations over the range, but the EXAFS fitting parameters generated only show Cr-Cr, and Cr-O interactions. When the chi plot of the 750 °C annealed sample is compared to that of Cr_2O_3 (figure 23a), only small differences are observed. Thus it is suggested that the 750 °C heat treatment is forming Cr_2O_3 which is a more stable oxide phase. Cr_2O_3 is the most stable oxide of chromium and is readily formed above 250 °C. [36] By 900 °C a PtCr alloy has been formed, as is shown by the presence of Cr-Pt contributions at around 2.7 and 4.7 Å. There is also a multiple scattering contribution to the spectrum of the type Cr-Pt-Cr, which is also found in the fitting parameters of the conventional PtCr/C catalysts.

The interpretation of the EXAFS for the 0.66 Cr/Pt/C catalyst series prepared by the $Cr(Cp)_2$ route cannot be extended to that prepared using the $Cr(Ph)_2$ precursor. In this instance, the 200 °C annealed sample is in general agreement with the previous analysis, although there is a significant reduction in the Cr-O coordination number, from 3.3 ± 0.2 to 2.1 ± 0.2. This correlates with the Cr-K edge XANES analysis which suggests that the catalyst is in a much less oxidised environment than for the equivalent catalyst prepared using the $Cr(Cp)_2$ route. The EXAFS data for the 750 °C annealed samples (figure 23b) are different and indicate that an alloy is formed at the lower temperature when the $Cr(Ph)_2$ precursor is used.

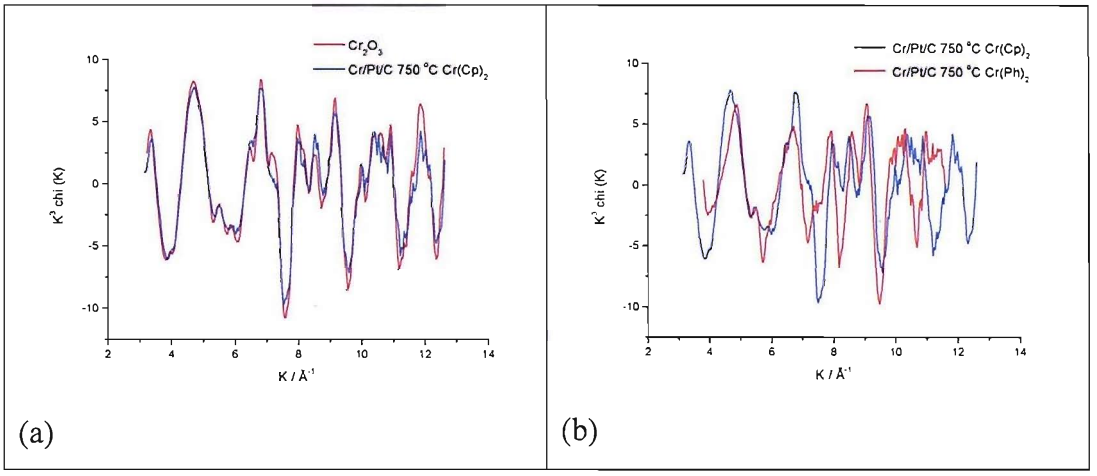

Figure 23 **Experimental k^3 chi plot of 0.66 Cr/Pt/C 750 °C $Cr(Cp)_2$ compared with (a) Cr_2O_3 and (b) 0.66 Cr/Pt/C 750 °C $Cr(Ph)_2$**

The comparison of the chi plots has been k^3 weighted to give emphasis to high Z neighbours, which will magnify any differences which occur from Cr-Pt interactions. Where the 0.66 Cr/Pt/C prepared by the $Cr(Cp)_2$ route resembles Cr_2O_3 the chi plot of the 0.66 Cr/Pt/C prepared by the $Cr(Ph)_2$ is markedly different. The fitting parameters confirm that an alloy has been formed at a lower temperature as Cr-Pt shells are present around 2.7 and 4.7 Å. The same can be seen for the 0.66 Cr/Pt/C $Cr(Ph)_2$ catalyst annealed at 900 °C. For the 0.66 Cr/Pt/C catalyst annealed at 750 °C prepared by the $Cr(Ph)_2$ route a fit incorporating a multiple scattering process of the type Cr-Pt-Pt rather than Cr-Pt-Cr improves the quality of the EXAFS fit. This infers that the $Cr(Ph)_2$ route of preparation yields a catalyst with very well distributed Cr.

The fitting parameters of the 0.66 Cr/Pt/C $Cr(Ph)_2$ 750 and 900 °C catalysts are in close agreement with each other and the 20 wt % PtCr/C and the 900 °C annealed 0.66 Cr/Pt/C prepared by the $Cr(Cp)_2$ route. The 0.66 monolayer Cr/Pt/C catalysts also have approximately a 3:1 Pt:Cr atomic ratio, so upon alloying similar values would be predicted. Although similar fitting parameters are generated, this does not confirm that the catalysts possess the same structure. As EXAFS is an averaging technique similar materials can possess different structures but still give rise to the same average local structure.

Looking at the values for the 900 °C $Cr(Ph)_2$ prepared catalyst, the 1st shell coordination numbers for the Cr-O and Cr-Pt contributions are 1.5 ± 0.1 and 3.6 ± 0.3, respectively. The R_{exafs} value can be improved by fitting a Cr-Cr shell at ~ 2.95 Å. If this shell is included in the fit, the value for $2\sigma^2$ calculated has a larger associated error than the value itself; this contribution has been excluded from the final fitting parameters. The 1st shell Cr-O coordination number of 1.5 ± 0.1 suggests that there is a disproportionately large amount of Cr at the surface of the catalyst or that there are separate Cr oxide particles. The TEM EDX line profile analysis shows that the Cr is targeting the Pt sites, so it is unlikely that Cr is being deposited onto the support and forming Cr oxide particles. Also the XRD analysis shows the presence of a single PtCr phase. Thus, the EXAFS results are interpreted as indicating that there is some segregation of Cr towards the surface of the particle. The data from the 0.166 Cr/Pt/C prepared by the $Cr(Ph)_2$ route (figure 23 and table 11) was very similar to that of the 0.66 Cr/Pt/C prepared by the same method. As there are not any Cr-Cr or Cr-Pt-Cr shells included in the fit for the 0.66 Cr/Pt/C catalyst, reducing the Cr content should not affect the local structure around the Cr.

3.5.4 EXAFS – Pt L_3 edge Studies of Cr Modified Catalysts

EXAFS data were collected as BN pellets in H_2 and air. The k^2 weighted EXAFS data along with the Fourier transforms and the fitting parameters determined for the Cr/Pt/C and Pt/C catalysts are detailed in figures 24-27 and tables 12-15.

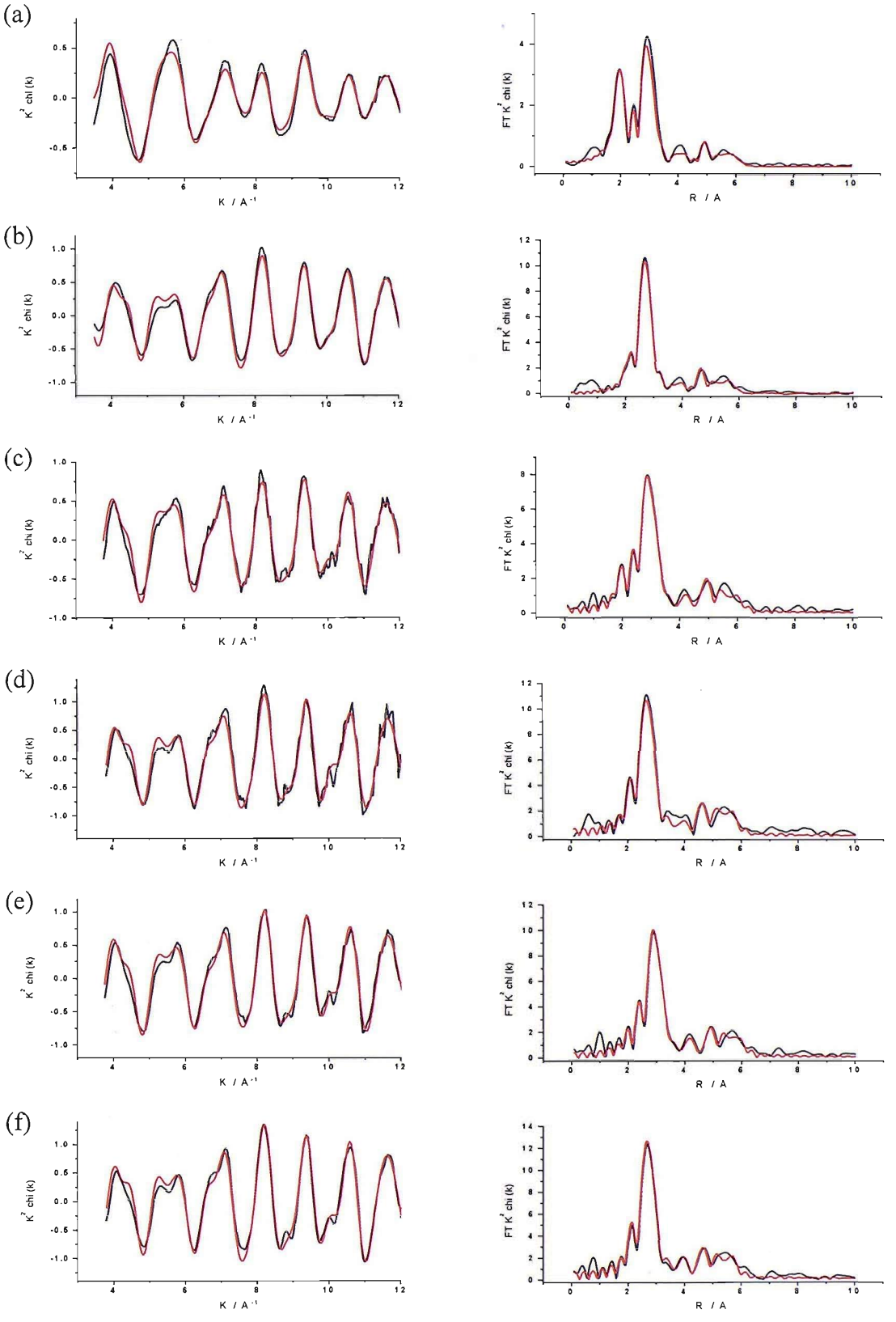

Figure 24 **Pt L_3 edge (left) k^2 weighted experimental data and fit along with (right) the Fourier transform for 20 wt % Pt/C acquired in air and H_2 (a & b), annealed at 750 °C acquired in air and H_2 (c & d), and annealed at 900 °C acquired in air and H_2 (e & f). Data (black line) and fit (red line).**

Table 12 **Structural parameters for Pt/C catalysts acquired in atmospheres of air and H_2 by fitting the Pt L_3 edge EXAFS data. Un1 refers to unit 1 and designates both scattering processes taking place in the same shell.**

Condition	**20 wt% Pt/C - Calculated Parameters (Pt L_3 edge)**					
In air	**Shell**	***N***	***R* / Å**	**$2\sigma^2$ / Å^2**	**E_f / eV**	**R_{exafs} / %**
	Pt-O	1.5 ± 0.1	2.021 ± 0.009	0.009 ± 0.001	- 14.6	22.4
	Pt-Pt(un1)	3.0 ± 0.2	2.758 ± 0.004	0.012 ± 0.000	± 0.8	
	Pt-Pt	2.0 ± 0.4	3.86 ± 0.01	0.021 ± 0.005		
	Pt-Pt	3.3 ± 0.7	4.81 ± 0.01	0.015 ± 0.003		
	Pt-Pt-Pt (un1)	3.0 ± 0.2	5.54 ± 0.01	0.020 ± 0.004		
In H_2	Pt-Pt(un1)	7.3 ± 0.2	2.758 ± 0.002	0.011 ± 0.000	-11.5	16.7
	Pt-Pt	2.0 ± 0.5	3.91 ± 0.01	0.013 ± 0.002	± 0.6	
	Pt-Pt	5.1 ± 0.9	4.794 ± 0.008	0.012 ± 0.001		
	Pt-Pt-Pt (un1)	7.3 ± 0.2	5.533 ± 0.006	0.027 ± 0.003		
750 °C in air	Pt-O	0.8 ± 0.2	2.03 ± 0.02	0.009 ± 0.003	-14.1	20.5
	Pt-Pt(un1)	6.4 ± 0.3	2.767 ± 0.004	0.011 ± 0.000	± 0.7	
	Pt-Pt	2.1 ± 0.7	3.92 ± 0.02	0.013 ± 0.003		
	Pt-Pt	7.0 ± 1.2	4.824 ± 0.009	0.012 ± 0.001		
	Pt-Pt-Pt (un1)	6.4 ± 0.3	5.560 ± 0.008	0.022 ± 0.003		
750 °C in H_2	Pt-Pt(un1)	8.6 ± 0.4	2.762 ± 0.004	0.011 ± 0.000	-5.41	27.0
	Pt-Pt	2.2 ± 0.8	3.87 ± 0.02	0.011 ± 0.004	± 1.1	
	Pt-Pt	7.8 ± 1.4	4.78 ± 0.01	0.010 ± 0.002		
	Pt-Pt-Pt (un1)	8.6 ± 0.4	5.54 ± 0.02	0.018 ± 0.003		

Table 12... **(continued) Structural parameters for Pt/C catalysts acquired in atmospheres of air and H_2 by fitting the Pt L_3 edge EXAFS data. Un1 refers to unit 1 and designates both scattering processes taking place in the same shell.**

900 °C in air	Pt-O	0.5 ± 0.2	2.02 ± 0.04	0.009 ± 0.007	-11.79 ± 0.61	21.7
	Pt-Pt(un1)	7.7 ± 0.3	2.759 ± 0.002	0.011 ± 0.000		
	Pt-Pt	2.5 ± 0.7	3.90 ± 0.02	0.011 ± 0.003		
	Pt-Pt	6.8 ± 1.4	4.80 ± 0.01	0.010 ± 0.001		
	Pt-Pt-Pt (un1)	7.7 ± 0.3	5.538 ± 0.006	0.019 ± 0.002		
900 °C in H_2	Pt-Pt(un1)	9.9 ± 0.4	2.765 ± 0.003	0.011 ± 0.000	-11.98 ± 0.58	18.7
	Pt-Pt	3.3 ± 0.8	3.91 ± 0.01	0.011 ± 0.002		
	Pt-Pt	9.0 ± 1.5	4.810 ± 0.009	0.010 ± 0.001		
	Pt-Pt-Pt (un1)	9.9 ± 0.4	5.549 ± 0.007	0.019 ± 0.002		

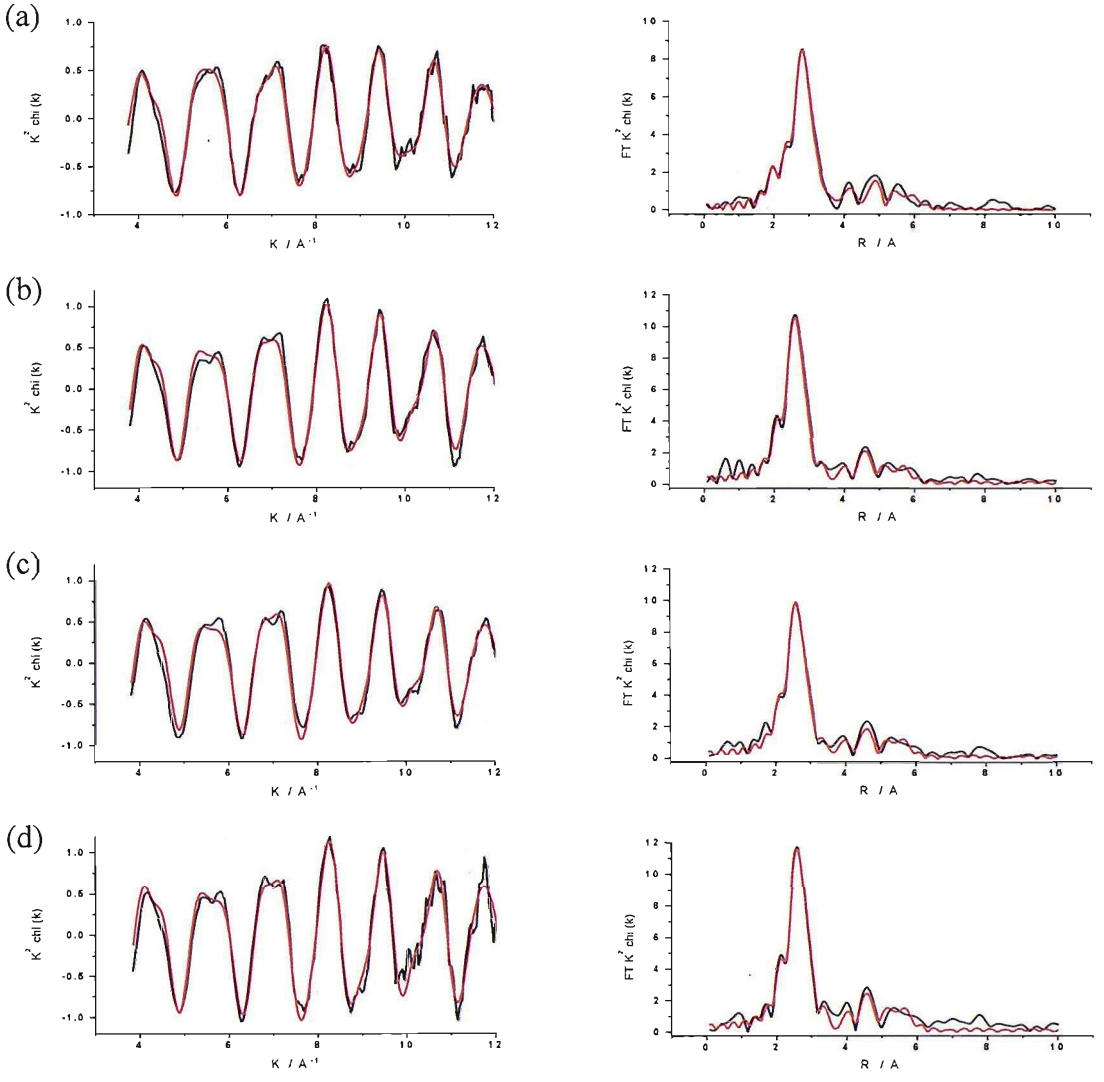

Figure 25 **Pt L_3 edge (left) k^2 weighted experimental data and fit along with (right) the Fourier transform for 0.66 Cr/Pt/C $Cr(Ph)_2$ annealed at 750 °C acquired in air and H_2 (a & b), annealed at 900 °C acquired in air and H_2 (c & d). Data (black line) and fit (red line).**

Table 13 **Structural parameters for 0.66 Cr/Pt/C $Cr(Ph)_2$ at different annealing temperatures acquired in atmospheres of air and H_2 by fitting the Pt L_3 edge EXAFS data. Un1 refers to unit 1 and designates both scattering processes taking place in the same shell.**

Condition	**0.66 Cr/Pt/C $Cr(Ph)_2$ - Calculated Parameters (Pt L_3 edge)**					
750 °C in air	**Shell**	***N***	***R* / Å**	**$2\sigma^2$ / $Å^2$**	***E_f* / eV**	**R_{exafs} / %**
	Pt-O	0.7 ± 0.2	2.05 ± 0.02	0.011 ± 0.004	-13.5 ± 0.9	18.7
	Pt-Pt(un1)	5.3 ± 0.3	2.748 ± 0.004	0.012 ± 0.000		
	Pt-Cr	1.0 ± 0.2	2.72 ± 0.02	0.009 ± 0.002		
	Pt-Pt	1.7 ± 0.6	3.89 ± 0.02	0.010 ± 0.002		
	Pt-Pt	6.2 ± 1.1	4.79 ± 0.01	0.015 ± 0.002		
	Pt-Pt-Pt (un1)	5.3 ± 0.3	5.51 ± 0.01	0.023 ± 0.003		
750 °C in H_2	Pt-Pt(un1)	7.2 ± 0.5	2.747 ± 0.004	0.012 ± 0.000	-11.8 ± 0.8	21.5
	Pt-Cr	1.1 ± 0.3	2.73 ± 0.02	0.011 ± 0.003		
	Pt-Pt	2.3 ± 0.8	3.87 ± 0.02	0.015 ± 0.004		
	Pt-Pt	8.4 ± 1.5	4.77 ± 0.01	0.014 ± 0.002		
	Pt-Pt-Pt (un1)	7.2 ± 0.5	5.50 ± 0.01	0.024 ± 0.004		
900 °C in air	Pt-Pt(un1)	6.5 ± 0.4	2.740 ± 0.004	0.012 ± 0.000	-11.1 ± 0.8	19.7
	Pt-Cr	1.1 ± 0.2	2.70 ± 0.02	0.010 ± 0.002		
	Pt-Pt	1.9 ± 0.7	3.86 ± 0.02	0.012 ± 0.003		
	Pt-Pt	7.3 ± 1.2	4.76± 0.01	0.014 ± 0.002		
	Pt-Pt-Pt (un1)	6.5 ± 0.4	5.472 ± 0.009	0.021 ± 0.003		
900 °C in H_2	Pt-Pt(un1)	7.7 ± 0.5	2.745 ± 0.004	0.011 ± 0.000	-11.5 ± 0.8	23.3
	Pt-Cr	1.2 ± 0.3	2.72 ± 0.02	0.011 ± 0.003		
	Pt-Pt	2.2 ± 0.9	3.87 ± 0.02	0.015 ± 0.005		
	Pt-Pt	9.1 ± 1.5	4.75 ± 0.01	0.013 ± 0.002		
	Pt-Pt-Pt (un1)	7.7 ± 0.5	5.48 ± 0.01	0.020 ± 0.003		

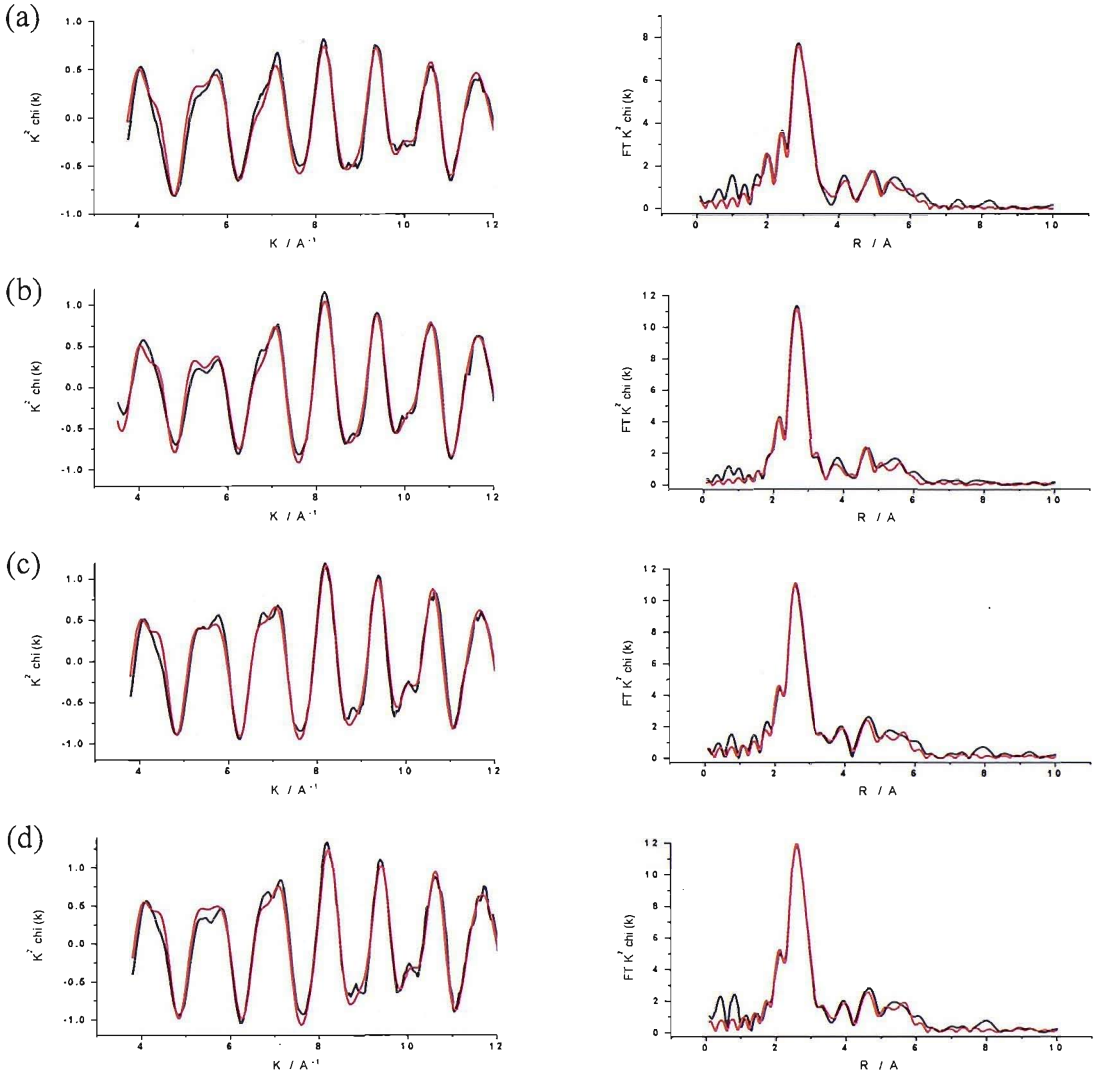

Figure 26 **Pt L_3 edge (left) k^2 weighted experimental data and fit along with (right) the Fourier transform for 0.66 Cr/Pt/C $Cr(Cp)_2$ annealed at 750 °C acquired in air and H_2 (a & b), annealed at 900 °C acquired in air and H_2 (c & d). Data (black line) and fit (red line).**

Table 14 **Structural parameters for 0.66 Cr/Pt/C $Cr(Ph)_2$ at different annealing temperatures acquired in atmospheres of air and H_2 by fitting the Pt L_3 edge EXAFS data. Un1 refers to unit 1 and designates both scattering processes taking place in the same shell.**

Condition	**0.66 Cr/Pt/C $Cr(Cp)_2$ - Calculated Parameters (Pt L_3 edge)**					
750 °C in air	**Shell**	***N***	***R* / Å**	**$2\sigma^2$ / $Å^2$**	**E_f / eV**	**R_{exafs} / %**
	Pt-O	0.8 ± 0.2	2.01 ± 0.02	0.008 ± 0.003	-12.5 ± 0.7	20.3
	Pt-Pt(un1)	6.4 ± 0.3	2.757 ± 0.004	0.012 ± 0.000		
	Pt-Pt	1.7 ± 0.7	3.92 ± 0.02	0.008 ± 0.002		
	Pt-Pt	6.9 ± 1.2	4.82 ± 0.01	0.013 ± 0.002		
	Pt-Pt-Pt (un1)	6.4 ± 0.3	5.560 ± 0.009	0.023 ± 0.003		
750 °C in H_2	Pt-Pt(un1)	8.4 ± 0.2	2.756 ± 0.002	0.011 ± 0.000	-12.8 ± 0.4	15.3
	Pt-Pt	2.3 ± 0.5	3.90 ± 0.01	0.013 ± 0.002		
	Pt-Pt	7.1 ± 0.8	4.793 ± 0.006	0.012 ± 0.001		
	Pt-Pt-Pt (un1)	8.4 ± 0.2	5.54 ± 0.01	0.025 ± 0.002		
900 °C in air	Pt-Pt(un1)	7.8 ± 0.4	2.755 ± 0.003	0.011 ± 0.000	-12.1 ± 0.7	16.1
	Pt-Cr	0.9 ± 0.2	2.72 ± 0.02	0.011 ± 0.002		
	Pt-Pt	3.3 ± 0.7	3.89 ± 0.02	0.011 ± 0.001		
	Pt-Pt	9.6 ± 1.2	4.80 ± 0.01	0.013 ± 0.001		
	Pt-Pt-Pt (un1)	7.8 ± 0.4	5.520 ± 0.008	0.019 ± 0.002		
900 °C in H_2	Pt-Pt(un1)	8.5 ± 0.5	2.749 ± 0.003	0.011 ± 0.000	-12.9 ± 0.7	19.0
	Pt-Cr	0.8 ± 0.3	2.72 ± 0.02	0.016 ± 0.004		
	Pt-Pt	2.2 ± 0.9	3.89 ± 0.02	0.010 ± 0.002		
	Pt-Pt	9.1 ± 1.5	4.79 ± 0.01	0.013 ± 0.002		
	Pt-Pt-Pt (un1)	8.5 ± 0.5	5.533 ± 0.007	0.018 ± 0.002		

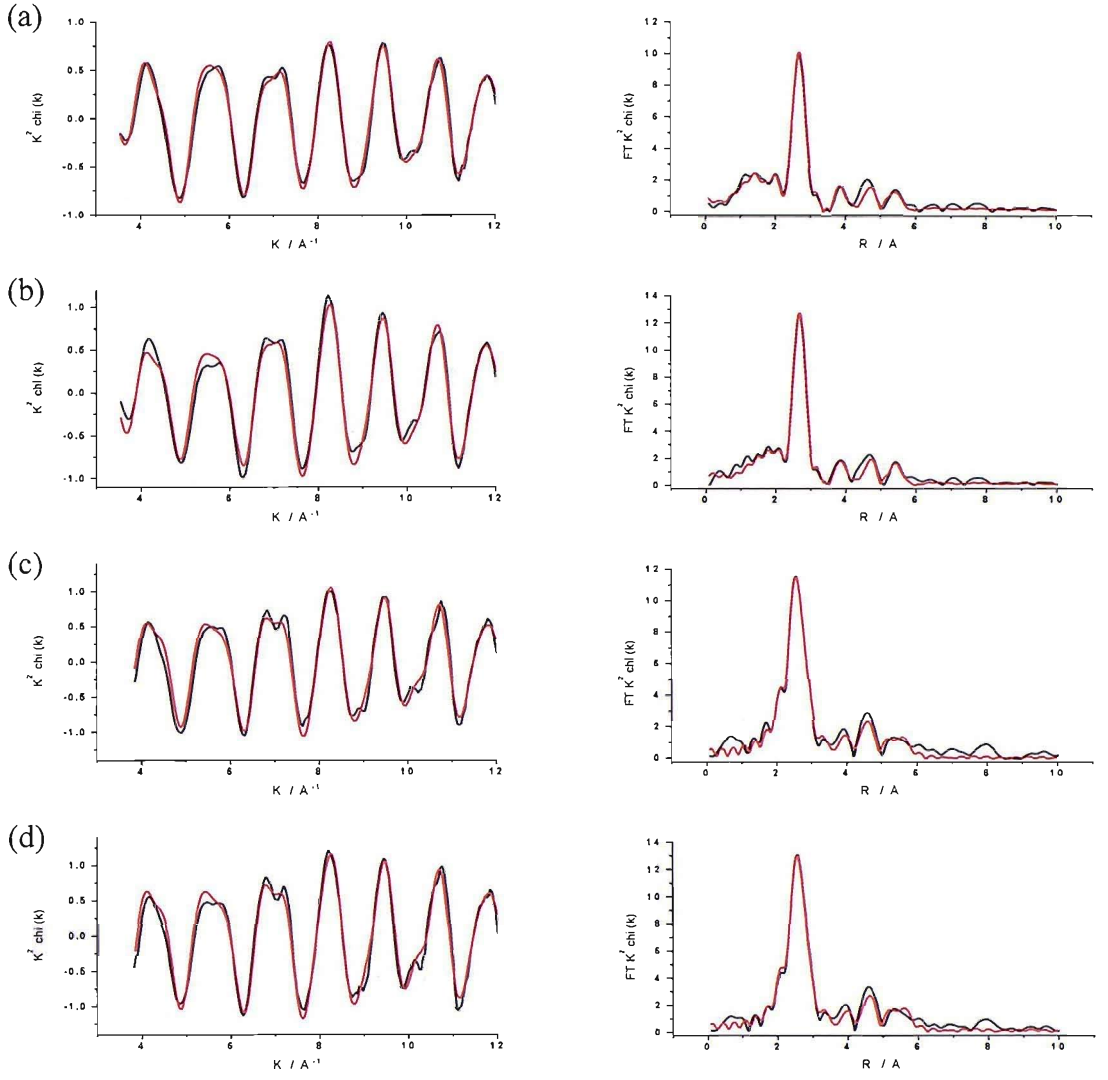

Figure 27 **Pt L_3 edge (left) k^2 weighted experimental data and fit along with (right) the Fourier transform for 40wt % PtCr (3:1) / C acquired in air and H_2 (a & b), and for 20 wt% PtCr (3:1) / C acquired in air and H_2 (c & d). Data (black line) and fit (red line).**

Table 15 **Structural parameters for PtCr/C catalysts acquired in atmospheres of air and H_2 by fitting the Pt L_3 edge EXAFS data. Un1 refers to unit 1 and designates both scattering processes taking place in the same shell.**

Condition	PtCr/C - Calculated Parameters (Pt L_3 edge)					
40 wt % PtCr (3:1) in air	**Shell**	***N***	***R* / Å**	**$2\sigma^2$ / Å^2**	**E_f / eV**	**R_{exafs} / %**
	Pt-Pt(un1)	7.0 ± 04	2.735 ± 0.004	0.011 ± 0.000	-11.1 ± 0.7	19.8
	Pt-Cr	1.5 ± 0.2	2.72 ± 0.01	0.011 ± 0.002		
	Pt-Pt	2.4 ± 0.7	3.87 ± 0.02	0.012 ± 0.003		
	Pt-Pt	8.7 ± 1.3	4.751 ± 0.009	0.014 ± 0.002		
	Pt-Pt-Pt (un1)	7.0 ± 0.4	5.46 ± 0.01	0.019 ± 0.003		
40 wt % PtCr (3:1) in H_2	Pt-Pt(un1)	7.8 ± 0.4	2.740 ± 0.004	0.012 ± 0.000	-11.4 ± 0.7	19.2
	Pt-Cr	1.7 ± 0.3	2.73 ± 0.01	0.010 ± 0.002		
	Pt-Pt	2.9 ± 0.8	3.87 ± 0.02	0.014 ± 0.003		
	Pt-Pt	9.6 ± 1.3	4.761 ± 0.009	0.013 ± 0.002		
	Pt-Pt-Pt (un1)	7.8 ± 0.4	5.473 ± 0.009	0.018 ± 0.002		
20 wt % PtCr (3:1) in air	Pt-O	0.7 ± 0.1	2.00 ± 0.02	0.011 ± 0.002	-13.5 ± 0.7	12.6
	Pt-Pt(un1)	5.8 ± 0.3	2.733 ± 0.003	0.012 ± 0.000		
	Pt-Cr	1.0 ± 0.2	2.71 ± 0.01	0.010 ± 0.001		
	Pt-Pt	2.3 ± 0.5	3.86 ± 0.01	0.014 ± 0.002		
	Pt-Pt	5.6 ± 1.0	4.762 ± 0.009	0.014 ± 0.001		
	Pt-Pt-Pt (un1)	5.8 ± 0.3	5.482 ± 0.007	0.025 ± 0.002		
20 wt % PtCr (3:1) in H_2	Pt-Pt(un1)	6.0 ± 0.0	2.736 ± 0.003	0.010 ± 0.000	-13.2 ± 0.7	17.4
	Pt-Cr	1.0 ± 0.2	2.72 ± 0.02	0.006 ± 0.001		
	Pt-Pt	2.3 ± 0.7	3.87 ± 0.02	0.012 ± 0.002		
	Pt-Pt	5.8 ± 1.2	4.76 ± 0.01	0.012 ± 0.001		
	Pt-Pt-Pt (un1)	6.0 ± 0.0	5.471 ± 0.008	0.021 ± 0.003		

The Pt L_3 edge data supports that at the Cr K edge, which shows that the Cr/Pt/C catalyst prepared via the $Cr(Ph)_2$ route forms a PtCr alloy phase at a lower annealing temperature than the $Cr(Cp)_2$ route. One of the proposed explanations for the enhancement Pt alloys show towards the ORR is a contraction of the Pt-Pt interatomic spacing. Upon alloying the lattice spacing between Pt neighbours decreases, supposedly producing a more energetically favourable adsorption site for the O_2 molecule. The following discussion of Pt-Pt 1st shell distances is based on the data acquired in H_2 only as more of the Pt is incorporated into the bulk of the particle as the surface oxides have been reduced. As can be seen in table 12 there is a slight increase in Pt-Pt distance on increasing the annealing temperature for the Pt/C catalysts. The distance increases from 2.758 Å to 2.762 Å to 2.765 Å for the untreated 20 wt % Pt/C catalyst when it is heat treated at 750 °C and then 900 °C. This increase is within the error, ± 0.003 Å, of the fitting and therefore can not be treated as significant. However, the trend is of interest. The Cr/Pt/C series of catalysts prepared by the $Cr(Cp)_2$ route show a notable Pt-Pt contraction when the catalyst is annealed at 900 °C corresponding to the formation of an alloy. A Pt-Pt distance of 2.749 ± 0.003 Å is observed compared to the distance of 2.765 ± 0.004 Å for the Pt/C annealed at the same temperature.

The 0.66 Cr/Pt/C catalysts prepared by the $Cr(Ph)_2$ route shows a Pt-Pt contraction at annealing temperatures of 750 and 900 °C. The 750 °C annealed sample displays a Pt-Pt distance of 2.747 ± 0.004 Å, with the 900 °C annealed sample having a similar distance of 2.745 ± 0.004 Å. The conventionally prepared PtCr/C alloys show a slightly more pronounced Pt-Pt contraction suggesting that these catalysts are better alloyed than the Cr modified Pt/C catalysts. The 20 wt % 3:1 PtCr/C catalyst has a 1st shell Pt-Pt distance of 2.736 ± 0.003 Å, with the 40 wt % 3:1 PtCr/C catalyst having a Pt-Pt distance of 2.740 ± 0.004 Å. For both the 900 °C annealed Cr/Pt/C catalysts there are no Pt-O 1st shell neighbours when the EXAFS are acquired in air. This would be expected in an atmosphere of H_2 as the surface Pt-O species are reduced. The 900 °C annealed Pt/C in air has 0.5 ± 0.2 Pt-O neighbours. Any slight reduction in Pt-O neighbours will lead to the error value becoming too large to fit the Pt-O contribution with confidence. The Cr K edge data suggests that there is a disproportionate amount of Cr at the surface. Assuming that this is the case then

a large drop in Pt-O neighbours would be expected as is the case in the Pt L_3 edge EXAFS data.

The growth of the catalyst particles on increasing annealing temperature is mirrored by an increase in total 1st shell metal neighbours as larger particles have a greater ratio of bulk to surface atoms. As the extent of oxide formation in air may depend on the preparation method, only the data for the samples acquired in an atmosphere of H_2 will be considered. For the Pt/C samples the 1st shell metal coordination increases from 7.3 (as prepared) to 8.6 to 9.9 as the heat treatment temperature is increased from 750 °C to 900 °C. For the $Cr(Ph)_2$ prepared 0.66 Cr/Pt/C catalyst, the corresponding increase in 1st shell metal coordination is 8.3 to 8.9 and for the $Cr(Cp)_2$ prepared 0.66 Cr/Pt/C catalysts, from 8.4 to 9.3 for the 750 and 900 °C annealed catalysts respectively. It can be seen that the numbers of 1st shell metal neighbours for the alloys is less than that for the Pt/C standards at the equivalent heat treatments. This is interpreted as the incorporation of Cr into the particles affecting the packing of the atoms and hence the coordination around each atom changes. The 40 wt % PtCr/C catalyst has a much larger particle size but only has a 1st shell metal coordination of 9.5.

The EXAFS of the 0.166 Cr/Pt/C prepared by the $Cr(Ph)_2$ route was also acquired but not included in this chapter. For each heat treatment it was not possible to fit any Pt-Cr coordination shells to the data. For the 0.66 Cr/Pt/C catalyst prepared by the same method there are 1.2 ± 0.3 Pt-Cr neighbours. If the amount of Cr is reduced by a factor of 4, a coordination number of 0.3 Pt-Cr neighbours is predicted. Such a low coordination number is very hard to fit from the Pt perspective with any accuracy.

3.5.5 EXAFS – Pt L_3 and Co K edge Studies of Co Modified Catalysts

EXAFS data were collected as BN pellets in atmospheres of H_2 and air. The k^2 weighted EXAFS data along with the associated Fourier transform and the fitting parameters determined for the Co/Pt/C catalysts are detailed below in figures 28-29 and tables 16-17.

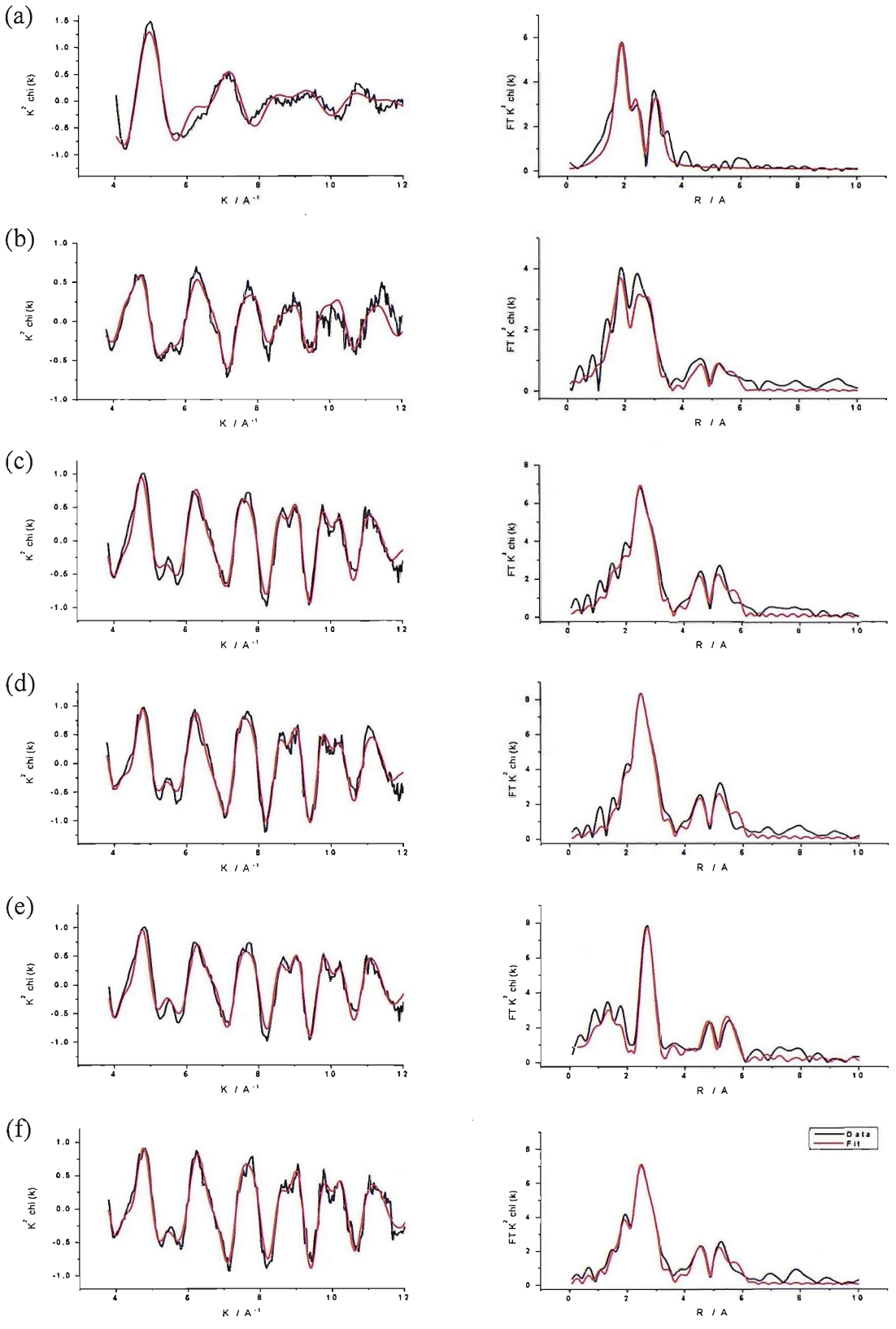

Figure 28 **Co K edge(left) k^2 weighted experimental data and fit along with (right) the Fourier transform for 0.66 Co/Pt/C annealed at 200 °C acquired in air and H_2 (a & b), annealed at 750 °C acquired in air and H_2 (c & d), and annealed at 900 °C acquired in air and H_2 (e & f). Data (black line) and fit (red line).**

Table 16 **Structural parameters for 0.66 Co/Pt/C at different annealing temperatures acquired in atmospheres of air and H_2 by fitting the Co K edge EXAFS data. Un1 refers to unit 1 and designates both scattering processes taking place in the same shell.**

Condition	**0.66 Co/Pt/C - Calculated Parameters (Co K edge)**					
200 °C in air	**Shell**	***N***	***R* / Å**	**$2\sigma^2$ / Å^2**	***E_f* / eV**	**R_{exafs} / %**
	Co-O	2.4 ± 0.2	1.84 ± 0.02	0.011 ± 0.002	16.3 ± 2.2	42.3
	Co-Co	0.6 ± 0.2	2.45 ± 0.02	0.014 ± 0.005		
	Co-Co	1.6 ± 0.3	3.14 ± 0.02	0.016 ± 0.004		
200 °C in H_2	Co-O	1.4 ± 0.1	2.04 ± 0.02	0.011 ± 0.003	-5.2 ± 1.6	34.9
	Co-Pt(un1)	2.6 ± 0.2	2.685 ± 0.009	0.013 ± 0.001		
	Co-Pt	2.3 ± 0.9	4.75 ± 0.03	0.014 ± 0.006		
	Co-Pt-Pt (un1)	2.6 ± 0.2	5.50 ± 0.02	0.017 ± 0.005		
750 °C in air	Co-O	1.0 ± 0.1	2.00 ± 0.02	0.016 ± 0.005	-4.0 ± 1.0	25.7
	Co-Pt(un1)	3.9 ± 0.3	2.707 ± 0.005	0.011 ± 0.001		
	Co-Co	0.5 ± 0.2	2.64 ± 0.02	0.011 ± 0.004		
	Co-Pt	5.9 ± 0.9	4.74 ± 0.01	0.010 ± 0.002		
	Co-Pt-Pt (un1)	3.9 ± 0.3	5.51 ± 0.01	0.010 ± 0.002		
750 °C in H_2	Co-O	0.8 ± 0.2	2.06 ± 0.02	0.015 ± 0.008	-5.1 ± 0.92	26.6
	Co-Pt(un1)	4.6 ± 0.4	2.713 ± 0.006	0.012 ± 0.001		
	Co-Co	0.7 ± 0.2	2.63 ± 0.02	0.011 ± 0.004		
	Co-Pt	6.8 ± 1.1	4.74 ± 0.01	0.011 ± 0.002		
	Co-Pt-Pt (un1)	4.6 ± 0.4	5.52 ± 0.01	0.013 ± 0.002		
900 °C in air	Co-O	0.9 ± 0.2	2.04 ± 0.02	0.016 ± 0.007	-4.5 ± 0.9	25.2
	Co-Pt(un1)	4.0 ± 0.3	2.715 ± 0.006	0.012 ± 0.001		
	Co-Co	0.7 ± 0.2	2.65 ± 0.02	0.008 ± 0.003		
	Co-Pt	6.6 ± 1.0	4.76 ± 0.01	0.012 ± 0.002		
	Co-Pt-Pt (un1)	4.0 ± 0.3	5.53 ± 0.01	0.015 ± 0.002		

Table 16... **(continued)Structural parameters for 0.66 Co/Pt/C at different annealing temperatures acquired in atmospheres of air and H_2 by fitting the Co K edge EXAFS data. Un1 refers to unit 1 and designates both scattering processes taking place in the same shell.**

900 °C in H_2	Co-O	1.1 ± 0.2	2.04 ± 0.01	0.013 ± 0.004	-5.2 ± 0.8	22.3
	Co-Pt(un1)	4.0 ± 0.3	2.708 ± 0.005	0.012 ± 0.001		
	Co-Co	0.5 ± 0.2	2.64 ± 0.02	0.009 ± 0.004		
	Co-Pt	6.4 ± 0.9	4.76 ± 0.01	0.012 ± 0.002		
	Co-Pt-Pt (un1)	4.0 ± 0.3	5.53 ± 0.01	0.016 ± 0.002		

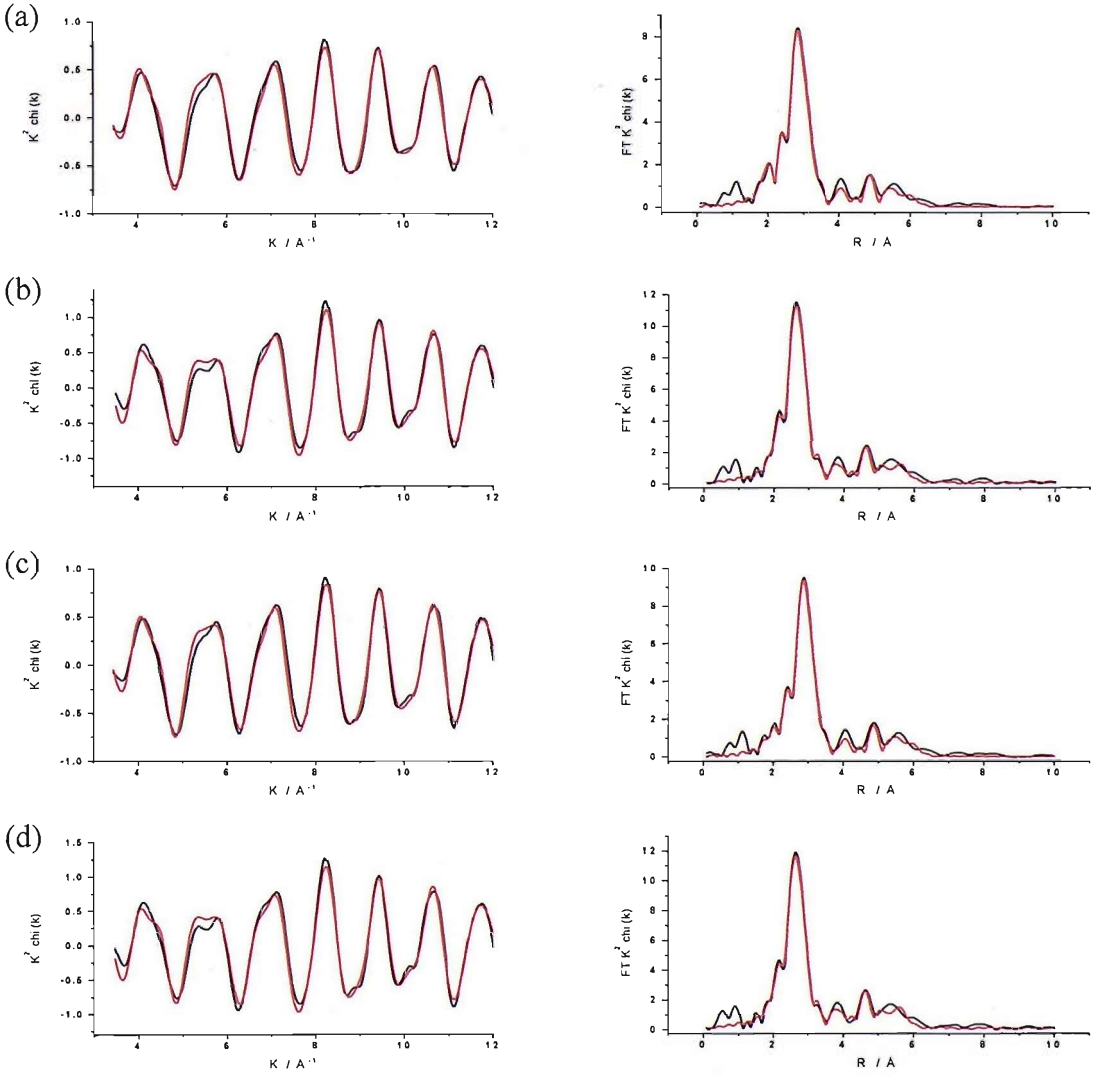

Figure 29 **Pt L_3 edge (left) k^2 weighted experimental data and fit along with (right) the Fourier transform for 0.66 Co/Pt/C annealed at 750 °C acquired in air and H_2 (a & b), annealed at 900 °C acquired in air and H_2 (c & d). Data (black line) and fit (red line).**

Table 17 **Structural parameters for 0.66 Co/Pt/C at different annealing temperatures acquired in atmospheres of air and H_2 by fitting the Pt L_3 edge EXAFS data. Un1 refers to unit 1 and designates both scattering processes taking place in the same shell.**

Condition	0.66 Co/Pt/C - Calculated Parameters (Pt L_3 edge)					
750 °C in air	**Shell**	***N***	***R* / Å**	**$2\sigma^2$ / Å^2**	***E_f* / eV**	**R_{exafs} / %**
	Pt-O	0.7 ± 0.1	2.00 ± 0.02	0.008 ± 0.002	-13.1 ± 0.7	15.2
	Pt-Pt(un1)	5.5 ± 0.3	2.739 ± 0.003	0.011 ± 0.000		
	Pt-Co	0.5 ± 0.2	2.67 ± 0.02	0.010 ± 0.002		
	Pt-Pt	1.2 ± 0.5	3.87 ± 0.02	0.011 ± 0.002		
	Pt-Pt	4.0 ± 1.0	4.79 ± 0.01	0.012 ± 0.002		
	Pt-Pt-Pt (un1)	5.5 ± 0.3	5.515 ± 0.008	0.026 ± 0.003		
750 °C in H_2	Pt-Pt(un1)	7.7 ± 0.4	2.744 ± 0.003	0.011 ± 0.000	-12.1 ± 0.7	17.2
	Pt-Co	0.7 ± 0.2	2.69 ± 0.02	0.010 ± 0.002		
	Pt-Pt	1.9 ± 0.7	3.89 ± 0.02	0.011 ± 0.002		
	Pt-Pt	5.9 ± 1.3	4.78 ± 0.01	0.011 ± 0.001		
	Pt-Pt-Pt (un1)	7.7 ± 0.4	5.505 ± 0.007	0.023 ± 0.003		
900 °C in air	Pt-O	0.6 ± 0.1	2.01 ± 0.02	0.018 ± 0.006	-14.2 ± 0.6	15.5
	Pt-Pt(un1)	5.9 ± 0.0	2.740 ± 0.003	0.011 ± 0.000		
	Pt-Co	0.5 ± 0.1	2.70 ± 0.02	0.008 ± 0.002		
	Pt-Pt	1.1 ± 0.5	3.87 ± 0.02	0.010 ± 0.003		
	Pt-Pt	4.4 ± 1.0	4.78 ± 0.01	0.012 ± 0.001		
	Pt-Pt-Pt (un1)	5.9 ± 0.0	5.521 ± 0.008	0.023 ± 0.003		
900 °C in H_2	Pt-Pt(un1)	7.7 ± 0.4	2.745 ± 0.003	0.011 ± 0.000	-12.4 ± 0.7	17.8
	Pt-Co	0.8 ± 0.2	2.70 ± 0.02	0.010 ± 0.002		
	Pt-Pt	2.0 ± 0.7	3.89 ± 0.02	0.011 ± 0.002		
	Pt-Pt	7.0 ± 1.3	4.779 ± 0.009	0.012 ± 0.001		
	Pt-Pt-Pt (un1)	7.7 ± 0.4	5.511 ± 0.007	0.022 ± 0.002		

One of the most notable differences between the EXAFS of the Cr/Pt/C samples and the Co/Pt/C samples is the ability to fit Co-Pt neighbours at the Co K edge for the 200 °C annealed sample when acquired in H_2. Assuming the modification procedure proceeds by the same pathway in both instances this shows that Co is more mobile than Cr and is able to alloy with Pt at lower temperatures. Thus it was expected that when annealing temperatures of 750 and 900 °C were employed well alloyed materials would be produced. For the 750 °C and 900 °C annealed samples looking from the Co K edge perspective there are Co-Pt coordination shells around 2.7 and 4.7 Å and a Co-Pt-Pt contribution at around 5.5 Å. In the Pt L_3 edge data a Pt-Co shell can also be fitted around 2.7 Å. These alloys also show the same lattice contraction and have a distance of around 2.745 Å. For the EXAFS of the 200 °C annealed Co/Pt/C catalysts at the Co K edge acquired in air the Co-O bond distance is 1.84 Å, which is remarkably small for Co-O and corresponds to the Co-O bond distance for the unstable Co (IV) oxidation state. Although this value seems peculiar the R_{exafs} value is dramatically increased if the Co-O bond distance is set to 2 Å.

There are other differences which can be observed in the EXAFS data. From the Co K edge it can be seen that there are Co-Co neighbours in the fits of the data for both the 750 and 900 °C annealed samples. When looking at the Cr samples it was not possible to fit any Cr-Cr interactions. This indicates that there is more Co clustered into the same regions than is the case with the Cr/Pt/C samples. Also from the Pt L_3 edge it can be seen that there are less Pt-Co neighbours than there were Pt-Cr neighbours. Taking the 900 °C annealed sample in air as an example, there are 0.5 ± 0.2 Pt-Co neighbours opposed to 1.2 ± 0.2 for the equivalent Pt-Cr sample. For the same sample there are also more Pt-O neighbours in the Co case than the Cr, 0.6 ± 0.1 compared to none. All these factors combined, suggest that there could be some segregation of Pt towards the surface of the particle for the Co/Pt/C alloys. Thus more Pt-O neighbours are observed and the bulk has a higher proportion of Co, so a reduced number of Co-Co neighbours are seen.

3.6 Catalytic Activity Towards the ORR

The slow kinetics observed for Pt based catalysts towards the ORR make it a difficult catalytic process to assess. Initial studies used a similar half cell set-up to that described in chapter 2, section 3.2.2, with the ability to flow different gases to the back of the electrode surface. Oxygen reduction polarisation curves from this set-up offered very poor reproducibility. Water produced from the ORR accumulates in the catalyst layer and the pores of the carbon paper backing, thereby, affecting the mass transport of O_2 to the catalyst surface. Using an RDE assembly overcomes the problems of flooding of the catalyst layer and enables control over the rate of mass transport.

3.6.1 ORR Testing Using the RDE

Cyclic voltammograms were acquired between 1.0 V and 0.05 V vs. RHE with a scan rate of 2 mV s^{-1} whilst flowing O_2(g) over the surface of the previously O_2 saturated electrolyte for rotation rates of 900, 1600, 2500, and 3600 RPM. In between measurements, the electrolyte was purged with O_2(g) whilst rotating the electrode at 1000 RPM. Different rotation rates were employed to check that the relationship between the limiting current and the rotation rate as described by the Levich equation, was shown to be upheld (figure 30). The value for I_k was extracted from the data (as detailed in chapter 2, section 3.3) and used to create Tafel plots by plotting Potential against Log [I_k].

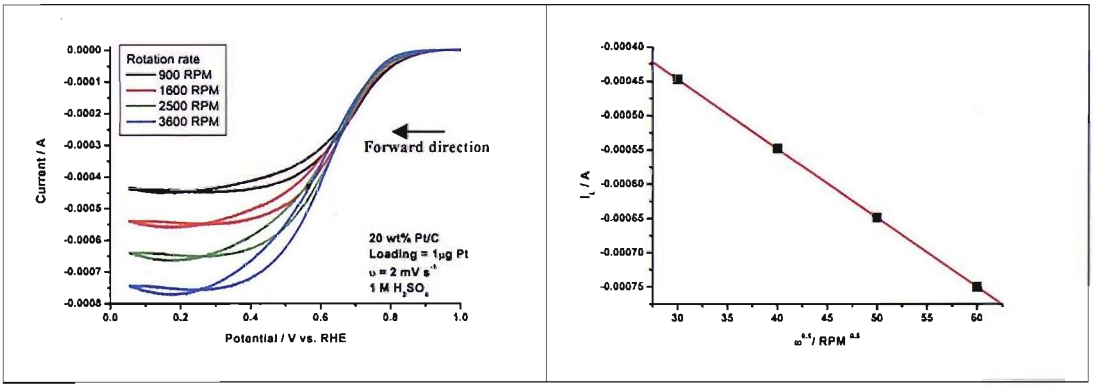

Figure 30 **(left) Cyclic voltammograms of 20 wt % Pt/C from 1.0 to 0.05 V in 1 M H_2SO_4 with a scan rate of 2 mV s^{-1} at different rotation rates. (right) The limiting currents at each rotation rate plotted against $\omega^{0.5}$. The line of best fit is also included, with the straight line indicating good mass transport control.**

The forward scan of the CVs acquired at 2500 RPM was used in each case to assess the performance of the catalysts. The data were normalised by the available Pt surface area, calculated using the CO area. Whilst preparing the thin

catalyst layer, it became apparent that the appearance of the catalyst layer varied greatly. The small volume of dilute catalyst solution deposited onto the electrode surface gives rise to a large amount of uncertainty in the amount of catalyst deposited. Thus it was deemed that there was too much error in calculating the mass of Pt added to the electrode surface and as such mass normalised data was considered to unreliable.

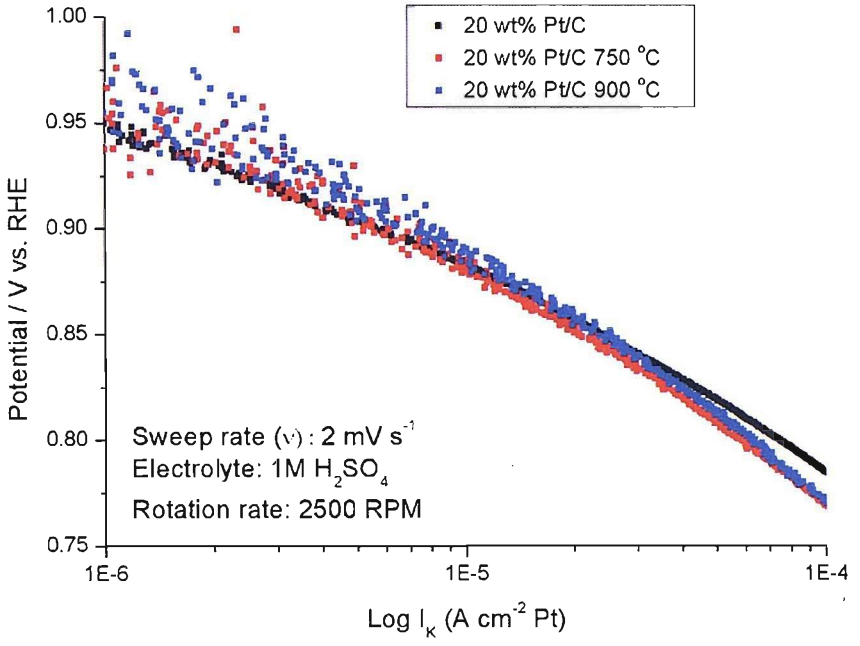

Figure 31 **Oxygen reduction Tafel plots for 20 wt% Pt/C, untreated and annealed at 750 °C and 900 °C.**

Figure 31 shows the Tafel plots for the Pt/C samples annealed at different temperatures. The most notable difference between the Tafel slopes is the noise observed for the heat treated samples at the higher potentials. At these potentials there are smaller currents passed and as a consequence the background noise has a greater effect. One reason for the smaller currents is the decrease in Pt area as a result of the heat treatments. Due to the large noise levels it is hard to comment on the performance for the different Pt/C catalysts at the higher potentials. By 0.90 V vs. RHE the noise is much reduced and it can be seen that the catalysts all exhibit a similar performances. The 900 °C annealed sample has a slightly larger specific activity of 7.8 μA cm^{-2} Pt compared to 5.6 μA cm^{-2} Pt for the untreated Pt/C at 0.90 V vs. RHE. This agrees well with work by Kinoshita [2], who showed a correlation between increase in Pt particle size and specific activity

towards the ORR.

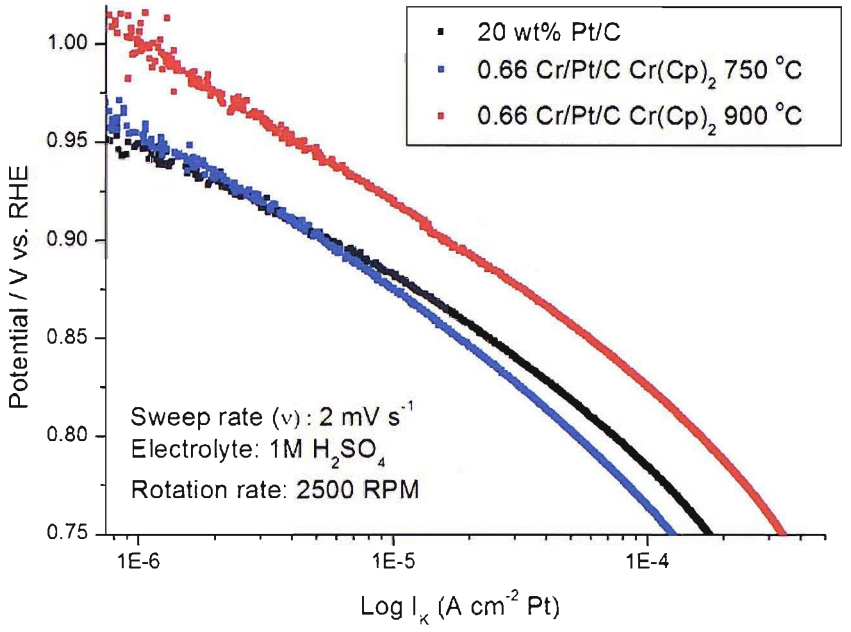

Figure 32 **Oxygen reduction Tafel plots for 20 wt% Pt/C, and 0.66 Cr/Pt/C prepared by the $Cr(Cp)_2$ route annealed at 750 and 900 °C.**

Figures 32 and 33 show the ORR Tafel plots for the 0.66 Cr/Pt/C catalysts prepared by the $Cr(Cp)_2$ and $Cr(Ph)_2$ routes, respectively. Data for the untreated 20 wt % Pt/C catalyst is included for comparison. The differences in the physical characteristics of the 0.66 Cr/Pt/C catalysts prepared by the two preparatory routes have been identified using XRD, TEM, and XAS and can now be correlated to the catalytic activity towards the ORR. The $Cr(Cp)_2$ prepared series of catalysts showed no signs of alloying until they were annealed at 900 °C. In this series of catalysts only the 900 °C annealed catalyst shows an enhancement towards the ORR compared to the Pt/C substrate catalyst as evidenced by figure 32. The Tafel plots of 750 °C annealed sample and Pt/C almost have near identical specific activities at 0.90 V of 5.3 and 5.6 $\mu A\ cm^{-2}$ Pt, respectively, showing that there is no performance advantage for this catalyst.

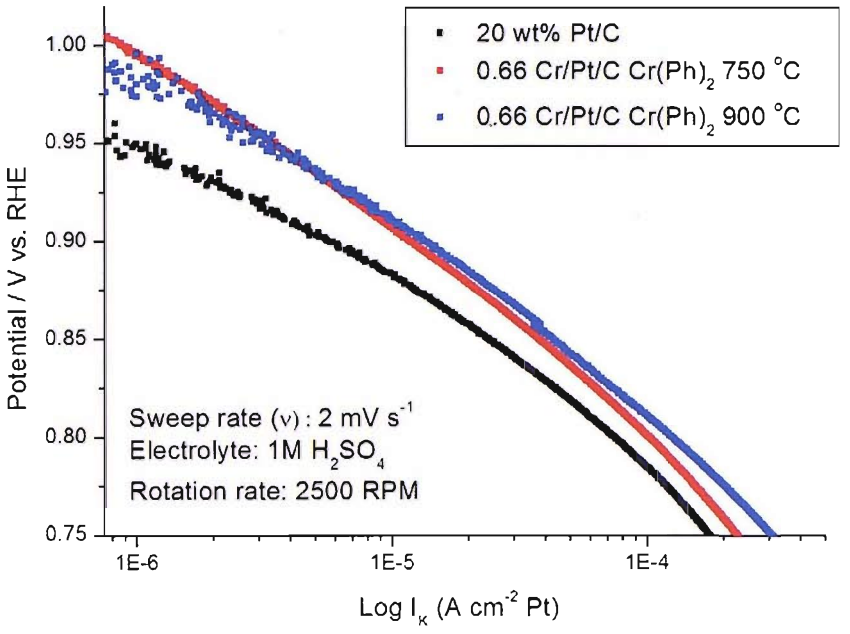

Figure 33 **Oxygen reduction Tafel plots for 20 wt% Pt/C, and 0.66 Cr/Pt/C prepared by the $Cr(Ph)_2$ route annealed at 750 and 900 °C.**

The 0.66 Cr/Pt/C catalysts prepared by the $Cr(Ph)_2$ route were shown to form a PtCr alloy phase by 750 °C. This difference in structure is mirrored in the performance of the catalysts towards the ORR (figure 33) as the 0.66 Cr/Pt/C catalysts annealed at 750 and 900 °C prepared by the $Cr(Ph)_2$ route show a significant enhancement and have specific activities at 0.90 V vs. RHE of 11.8 and 13.2 μA cm^{-2} Pt respectively. This 2 to 3 fold enhancement is typical for Pt_3Cr alloys [7]. The XRD data show that the 750 °C annealed sample can not simply be described as a Pt_3Cr alloy, as there are also Pt and Cr_2O_3 crystalline phases present in the sample. Whereas the XRD data shows that the 900 °C annealed sample has only the Pt_3Cr phase present. It is of interest then that these samples possess the same enhancement. One way to envisage the 750 °C annealed sample is of a surface consisting of some Cr_2O_3 and Pt_3Cr with the core being crystalline Pt. At 900 °C more of the Cr is driven into the bulk of the particle. It can be concluded from this study that it is the Pt_3Cr alloy phase which offers increased activity towards the ORR. The presence of unalloyed Cr at the surface does not aid the performance of the catalysts towards the ORR. It appears that the 900 °C annealed sample prepared by the $Cr(Cp)_2$ route is slightly more active than that prepared by the $Cr(Ph)_2$ route. Repeat measurements were taken

in all cases, and although there was in general a good agreement between the measurements, there were occasional differences. The small difference in activity observed between the two 900 °C annealed samples is therefore, within the confidence limit of the measurement.

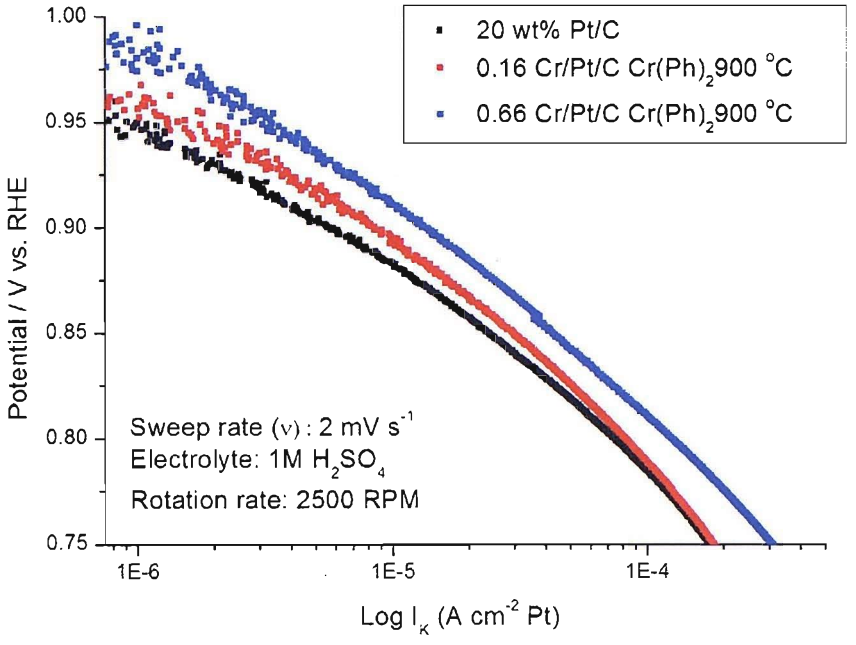

Figure 34 **Oxygen reduction Tafel plots for 20 wt% Pt/C, and 0.166 and 0.66 Cr/Pt/C prepared by the $Cr(Ph)_2$ route annealed at 900 °C.**

The effect of Cr loading can be seen by comparing the 0.66 and 0.166 Cr/Pt/C catalysts prepared by the $Cr(Ph)_2$ route (figure 34). The Tafel plots show that the 0.166 monolayer catalyst has a slight enhancement towards the ORR compared to Pt/C, of 8.1 μA cm^{-2} Pt compared to 5.6 μA cm^{-2} Pt at 0.90 V. However, the catalyst is not as active as the 0.66 monolayer catalyst. In this case increasing the Cr fraction increases the performance of the catalyst towards the ORR. A much larger study would be needed to truly assess how the Cr content affects the performance towards the ORR. Initial work by Qian [29] assessed the performance of a range of Cr/Pt/C catalysts prepared by the $Cr(Cp)_2$ route. The 0.66 monolayer catalyst was found to be the most active and hence was chosen as the fraction which was extensively studied in this work. Qian found that the catalysts annealed at 750 °C gave the best enhancement, whilst in this report they were found to offer no enhancement towards the ORR compared to Pt alone. Qian's testing was carried out in a flooded half cell environment, and it can only

be assumed that the deficiencies of such a testing method, highlighted earlier, have led to the discrepancy.

If it is the presence of the Pt_3Cr phase which offers the increased performance then it would appear there would be little advantage in adding any more Cr than the stoichiometry demands, which is approximately equal to the 0.66 monolayer catalyst. Comparing the Cr/Pt/C catalysts to the conventionally prepared 20 wt % and 40 wt % PtCr(3:1)/C (figure 35) it can be seen that the 20 wt % PtCr(3:1) offers a similar performance to the Cr/Pt/C catalyst annealed at 900 °C of 13.1 $\mu A\ cm^{-2}$ Pt at 0.90 V vs. RHE. The 40 wt% PtCr (3:1)/C catalyst has a greater performance than the other alloys so far studied in this work and has a specific activity of 19.2 $\mu A\ cm^{-2}$ Pt at 0.90 V vs. RHE. The EXAFS of the 20 wt% PtCr(3:1)/C has shown that the local structure around both alloying elements is similar to those in the Cr/Pt/C systems annealed at 900 °C. As the catalysts are similar in structure then it follows that the performance should also be similar. The 40 wt% PtCr(3:1)/C may have increased performance because of the greater degree of alloying that this system is believed to possess, but, as with the EXAFS analysis, the reason for the differences observed could also be to do with the increased particle size of this catalyst. In terms of the cost of the catalyst in a fuel cell, the mass activity will be important. Unfortunately the errors associated with loading the catalyst on the RDE make such a comparison impossible.

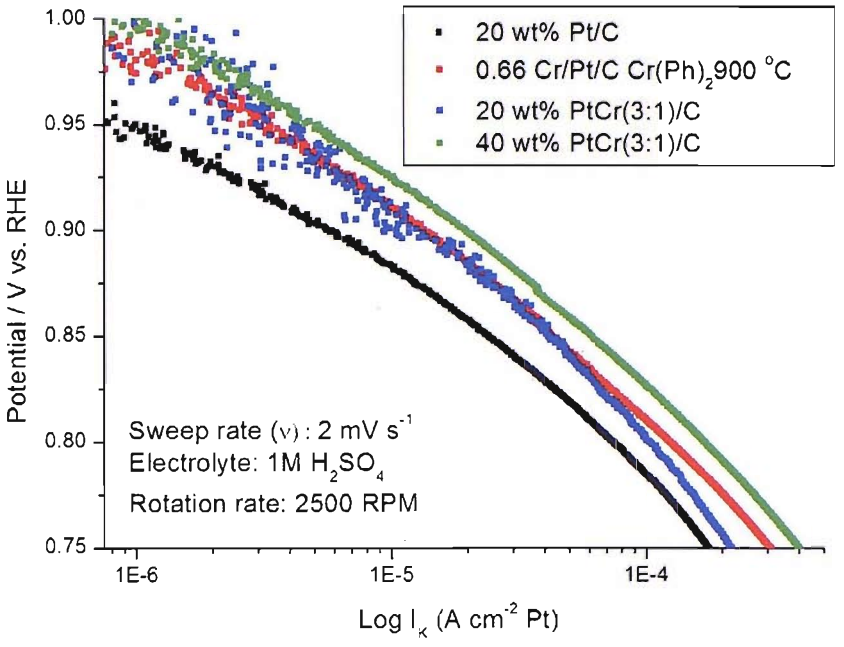

Figure 35 **Oxygen reduction Tafel plots for 20 wt% Pt/C, 0.66 Cr/Pt/C prepared by the $Cr(Ph)_2$ route annealed at 900 °C, 20 wt % PtCr(3:1)/C, and 40 wt % PtCr(3:1)/C.**

The testing of the 0.66 Co/Pt/C (figure 36) gives similar trends to the Cr/Pt/C systems. By the annealing temperature of 750 °C, a Pt_3Co alloy has been formed as shown by the XRD data. So like the Cr/Pt/C catalyst prepared by the $Cr(Ph)_2$ route, the 750 and 900 °C annealed samples both show the same level of enhancement towards the ORR of 12.8 and 13.0 μA cm^{-2} Pt respectively. The as prepared (no additional annealing temperature) Co/Pt/C shows a slight improvement in performance over Pt/C of 7.7 μA cm^{-2} Pt. This is in agreement with the EXAFS data which shows that Co-Pt interactions are present (when the sample was acquired in an atmosphere of H_2). Neither the EXAFS nor XRD show any signs of extensive alloying, so a large enhancement would not be expected.

The equivalent 40 wt % PtCo (3:1)/C catalyst has a performance advantage compared to that of the Co/Pt/C with a specific activity of 20 μA cm^{-2} Pt. As mentioned before the much larger particle size of the 40 wt% catalyst may be responsible for this increase in specific activity. The EXAFS of this 40 wt % PtCo(3:1)/C catalyst have been acquired and showed signs of a large amount of

Co being at the surface, as there are a large number of Co-O neighbours in the Co K edge EXAFS data. Thus, there is nothing to suggest that this increase in performance can be related to a greater degree of alloying.

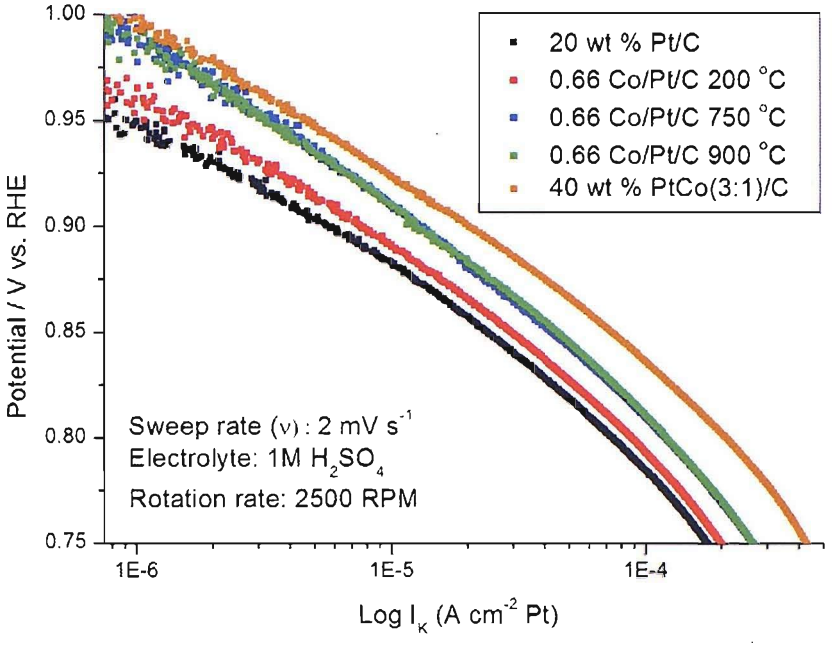

Figure 36 **Oxygen reduction Tafel plots for 20 wt% Pt/C, 0.66 Co/Pt/C route annealed at 200 °C, 750 °C and 900 °C, and 40 wt % PtCo(3:1)/C.**

The table below summarises the performance of the catalysts assessed towards the ORR (table 18). The Pt/C catalysts annealed at different temperatures all have Tafel slopes of 60 mV decade^{-1}, which are consistent with the value reported for the ORR on Pt in this potential region [37]. The gradient of the Tafel slope reflects the reaction mechanism. Thus the results for the other catalysts where Tafel slopes between 70 to 90 mV decade^{-1} are reported may indicate that the ORR is proceeding through another reaction mechanism.

Table 18 **Electrochemical parameters derived from the RDE measurements.**

Catalyst	Specific activity I_k at 0.9 V / μA cm^{-2} Pt	Tafel Slope / mV $decade^{-1}$
Pt/C	5.6	63.2
Pt/C 750 °C	6.2	63.5
Pt/C 900 °C	7.8	60.1
0.66 Cr/Pt/C $Cr(Cp)_2$ 750 °C	5.3	79.6
0.66 Cr/Pt/C $Cr(Cp)_2$ 900 °C	16.7	85.9
0.66 Cr/Pt/C $Cr(Ph)_2$ 750 °C	11.8	93.4
0.66 Cr/Pt/C $Cr(Ph)_2$ 900 °C	13.2	82.3
0.17 Cr/Pt/C $Cr(Ph)_2$ 900 °C	8.1	69.3
20 wt % PtCr(3:1)/C	13.1	73.4
40 wt % PtCr(3:1)/C	19.2	84.4
0.66 Co/Pt/C 200 °C	7.7	71.4
0.66 Co/Pt/C 750 °C	12.8	86.8
0.66 Co/Pt/C 900 °C	13.0	84.3
40 wt % PtCo(3:1)/C	20.0	78.2

4. Conclusions

From the results gathered in this chapter, several observations can be made regarding the success of the controlled surface modification procedure. For the catalysts made using the $Co(Cp)_2$ and $Cr(Ph)_2$ precursors the characterisation tends to suggest that the secondary metal is deposited solely on the Pt particles and is finely dispersed. Further thermal treatment can then be employed to incorporate the additional metal into the bulk of the particle. For the $Cr(Cp)_2$ system the picture is not as straight forward. The precursor is inherently unstable in the presence of air and moisture and as a consequence is added to the reduced Pt surface as a suspension, rather than dissolved in solution. The characterisation presented herein implies that rather than forming a well dispersed Cr layer on the Pt surface, it forms Cr or Cr oxide clusters as it is deposited. These clusters are suitably large that on annealing at 750 °C, a distinct Cr_2O_3 phase is formed. For the $Cr(Ph)_2$ precursor at the same temperature there is evidence of a Pt_3Cr phase. However, the data for the $Cr(Cp)_2$ precursor catalysts suggest that these clusters are still targeting the Pt sites and if the heat treatment is large enough, then the Cr can be driven into the bulk of the particle.

The aim of this work was to prepare these model systems and relate their structural properties to their performance towards the ORR. The results reported here show that a PtCr or PtCo alloy phase is needed to provide an enhancement towards the reduction of oxygen. When the Pt_3M phase is present, the specific activity of the catalyst is 2 to 3 times more than that of a conventional Pt/C catalyst. When the secondary metal is present at the surface of the catalysts but not part of an alloy phase then no enhancement towards the ORR was observed. The formation of an alloy phase is also linked to a reduction of Pt-Pt bond distance and as a consequence the electronic properties of the catalysts. This is in contradiction to recent work presented by Koffi *et al.* [11] In their work a series of non-alloyed Pt-Cr/C catalysts have been prepared and an enhancement towards the ORR is reported. They report the absence of an alloy phase as a reduction in lattice parameter on increasing Cr content was not observed. However, the report makes no mention of any annealing temperature used in the

preparation of the catalysts, and no XAS data were obtained. As illustrated in this chapter the XRD data only gives a picture of the extended structure of the catalyst and does not offer as much detail as EXAFS in assessing the local structure of the catalysts. The characterisation of the catalysts reported in this section is more thorough and provides a more detailed picture of the system under study. As a consequence it is felt that the link between catalyst structure and activity reported here is more reliable.

5. References

1. Yeager, E., Journal of Molecular Catalysis, 1986. **38**: p. 5.
2. Kinoshita, K., J. Electrochem. Soc., 1990. **137**(3): p. 845.
3. Markovic, N.M., H.A. Gasteiger, and P.N. Ross, J. Electrochem. Soc., 1997. **144**(5): p. 1591.
4. Jalan, V. and E.J. Taylor, J. Electrochem. Soc., 1983. **130**(11): p. 2299.
5. Glass, J.T., G.L. Cahen, G.E. Stoner, and E.J. Taylor, J. Electrochem. Soc., 1987. **134**(1): p. 58.
6. Paffett, M.T., J.G. Beery, and S. Gottesfeld, J. Electrochem. Soc., 1988. **135**(6): p. 1431.
7. Mukerjee, S. and S. Srinivasan, J. Electroanal. Chem., 1993. **357**: p. 201.
8. Mukerjee, S., S. Srinivasan, M.P. Soriaga, and J. McBreen, J. Electrochem. Soc., 1995. **142**(5): p. 1409.
9. Yang, H., N. Alonso-Vante, J.M. Leger, and C. Lamy, J. Phys. Chem. B, 2004. **108**(6): p. 1938.
10. Yang, H., N. Alonso-Vante, C. Lamy, and D.L. Akins, J. Electrochem. Soc., 2005. **152**(4): p. A704.
11. Koffi, R.C., C. Coutanceau, and E. Garnier, Electrochim. Acta, 2005. **50**: p. 4117.
12. Toda, T., H. Igarashi, H. Uchida, and M. Watanabe, J. Electrochem. Soc., 1999. **146**(10): p. 3750.
13. Toda, T., H. Igarashi, and M. Watanabe, J. Electroanal. Chem., 1999. **460**(1-2): p. 258.
14. Antolini, E., J.R.C. Salgado, M.J. Giz, and E.R. Gonzalez, International Journal of Hydrogen Energy, 2005. **30**: p. 1213.
15. Murthi, V.S., R.C. Urian, and S. Mukerjee, J. Phys. Chem. B, 2004. **108**(30): p. 11011.
16. Roques, R.M. and A.B. Anderson, J. Electrochem. Soc., 2004. **151**(3): p. E85.
17. Stamenkovic, V.R., B.S. Mun, K.J.J. Mayrhofer, P.N. Ross, and N.M. Markovic, J. Am. Chem. Soc., 2006. **128**(27): p. 8813.

18. Stamenkovic, V., T.J. Schmidt, P.N. Ross, and N.M. Markovic, J. Phys. Chem. B, 2002. **106**(46): p. 11970.
19. Stamenkovic, V., T.J. Schmidt, P.N. Ross, and N.M. Markovic, J. Electroanal. Chem., 2003. **554**: p. 191.
20. Christensen, P.A., A. Hamnett, J. Munk, and G.L. Troughton, J. Electroanal. Chem., 1994. **370**(1-2): p. 251.
21. Arico, A.S., A.K. Shukla, H. Kim, S. Park, M. Min, and V. Antonucci, Appl. Surf. Sci., 2001. **172**(1-2): p. 33.
22. Crabb, E.M., M.K. Ravikumar, D. Thompsett, M. Hurford, A. Rose, and A.E. Russell, Phys. Chem. Chem. Phys., 2004. **6**(8): p. 1792.
23. Crabb, E.M., M.K. Ravikumar, Y. Qian, A.E. Russell, S. Maniguet, J. Yao, D. Thompsett, M. Hurford, and S.C. Ball, Electrochem. Solid State Lett., 2002. **5**(1): p. A5.
24. Crabb, E.M. and M.K. Ravikumar, Electrochim. Acta, 2001. **46**(7): p. 1033.
25. Crabb, E.M., R. Marshall, and D. Thompsett, J. Electrochem. Soc., 2000. **147**(12): p. 4440.
26. Crabb, E.M. and R. Marshall, Appl. Catal. A-Gen., 2001. **217**(1-2): p. 41.
27. Russell, A.E. and A. Rose, Chem. Rev., 2004. **104**(10): p. 4613.
28. Sasaki, K., Y. Mo, J.X. Wang, M. Balasubramanian, F. Uribe, J. McBreen, and R.R. Adzic, Electrochim. Acta, 2003. **48**(25-26): p. 3841.
29. Qian, Y., Preparation of Platinum based bimetallic catalysts for the oxygen reduction reaction for PEM fuel cells, PhD Thesis, 2004, The Open University
30. Mansour, A.N., J.W. Cook, and D.E. Sayers, J. Phys. Chem., 1984. **88**(11): p. 2330.
31. Brown, M., E.A. Stern, and R.E. Peierls, Phys. Rev. B, 1977. **15**(2): p. 738.
32. Wiltshire, R.J.K., Extending in situ XAS of PEM Fuel Cells to more Realistic Conditions, PhD Thesis, 2005, University of Southampton
33. Paulus, U.A., A. Wokaun, G.G. Scherer, T.J. Schmidt, V. Stamenkovic, V. Radmilovic, N.M. Markovic, and P.N. Ross, J. Phys. Chem. B, 2002. **106**(16): p. 4181.

34. Panterlouris, A., H. Modrow, and M. Pantelouris, Chemical Physics, 2004. **300**: p. 13.

35. Moen, A. and D.G. Nicholson, Chem. Mat., 1997. **9**: p. 1241.

36. Greenwood, N.N. and A. Earnshaw, *Chemistry of the Elements*. First ed. 1984: Pergamon Press.

37. Gattrell, M. and B. MacDougall, *Reaction mechanisms of the O_2 reduction/evolution reaction*, in *Handbook of Fuel Cells - Fundamentals, Technology, and Applications*. 2003.

Chapter Four: Pt and Pd Surface Modified Catalysts for the Oxygen Reduction Reaction.

1 Introduction

Chapter 3 dealt with the problems surrounding the ORR for Pt based cathodes in PEMFCs, focussing on the use of Pt alloyed with first row transition metals as improved ORR catalysts. Due to the prohibitive economics governing the use of Pt it is also desirable to reduce the Pt loading required, whilst also increasing the activity of catalyst towards the ORR. A target of 0.44 A mg^{-1} Pt (at 0.9 V vs. RHE) has been set as an economically viable target for Pt based catalysts towards the ORR with conventional PtCo/C catalysts only achieving 0.28 A mg^{-1} Pt [1].

One method of reducing the Pt loading and to retain / enhance the catalytic properties is the preparation of Pt surface modified supported metal nanoparticles. The desired aim is to have nanoparticles with a surface composed solely of Pt, and a core composed of another metal which has less economic constraints. Adzic *et al.* [2] initially looked at Pt deposited on Ru for hydrogen oxidation, and Pt, Pd, and Ag, deposited onto Au/C for the ORR. The PtRu material was prepared by a spontaneous deposition route involving the immersion of a Ru single crystal in a Pt ion containing solution [3]. The M/Au/C catalyst was prepared by the redox replacement of a previously deposited Cu underpotential deposition (upd) adlayer on Au. The Cu upd adlayer undergoes a spontaneous irreversible redox process, where the Cu is oxidised by the more noble metal cations, which are reduced and simultaneously deposited [4].

Conventionally, PtPd alloy catalysts have been prepared by surface redox reactions [5] or organometallic routes [6]. The surface redox process involves the modification of a supported monometallic Pd catalyst prepared by impregnation. The monometallic Pd catalyst can then directly reduce a solution of a Pt salt

added as the Pt^{2+}/Pt couple has a higher electrochemical potential than the Pd^{2+}/Pd couple. These bimetallic catalysts are then annealed at 400 °C to form a conventional alloy. The organometallic route [6] involves the co-impregnation of a support using a co-dissolved mixture of $Pt(acac)_2$ and $Pd(acac)_2$, eventually ending in an annealing step of 500 °C.

Adzic and co-workers also applied the same Cu upd displacement method to prepare Pt/Pd(111) and Pt/Pd/C [7]. These catalysts offered improved kinetic performance for the ORR compared to a Pt (111) surface and a Pt/C catalyst, respectively. The Pt/Pd/C catalysts prepared were shown the have a mass activity 5 to 8 times higher and a specific activity 2 times higher than conventional Pt/C catalysts. The observed specific activity enhancement was attributed to a decrease in the formation of Pt-OH groups at the surface, which act to block the reactive sites for the ORR to proceed through. The kinetic improvement offered by the Pt/Pd(111) catalyst shows that not only can the Pt loading be decreased by placing the Pt solely at the surface but the inherent activity of the catalyst can also be improved. The affect of different substrates was then studied [8] to see if the catalytic activity could be enhanced further. Ru(0001), Ir(111), Rh(111), Au(111), Pt(111), and Pd(111) were all studied as substrates for a Pt monolayer with only Pt_{ML}/Pd(111) offering improved kinetics over the Pt (111) surface. The activity of the Pt monolayer catalyst on the different substrates exhibits a volcano type behaviour with respect to the position of the d band centre. A large value for d band centre correlates to the catalyst binding intermediates more strongly and enhances the kinetics of dissociation reactions producing these adsorbates. A surface with a lower d band centre conversely binds these adsorbates more weakly and thus acts to facilitate the formation of bonds between these adsorbates more readily. An intermediate value for the d band centre is therefore required and hence explains the volcano type behaviour exhibited. Further work on these Pt modified substrates [9] including XANES studies carried out in an *in-situ* electrochemical cell at potentials around 1.15 V vs. RHE showed that there was reduced –OH adsorption at these potentials. The study also showed that additional work was required to increase the durability of the catalysts.

The link between OH adsorption and ORR performance was studied further by preparing ternary systems where the Pd(111) surface was modified with a monolayer consisting of $Pt_{0.8}M_{0.2}$ where M was Au, Pt, Pd, Rh, Ru, Ir, Re, and Os [10]. A linear correlation is reported between the kinetic current at 0.8 V vs. RHE and the OH-OH / OH-O repulsion energy calculated between OH adsorbed on Pt and OH adsorbed on M. As OH binds more strongly to the M component the repulsion between this and neighbouring OH adsorbed on Pt increases. Thus, this tertiary system acts to reduce the overall OH coverage on Pt. The use of metals such as Ir, Re, and Os were most successful in promoting the ORR with only Au having a negative influence. This negative effect can be rationalised by the very weak binding interaction between OH and Au. The $Pt_{0.8}Ir_{0.2\ ML}$/Pd(111) catalyst has an observed current density around 3 times larger than Pt/Pd(111), and a Pt mass specific activity 21 times larger than a 10 wt % Pt/C catalyst.

The inverse system of Pd on the surface of Pt has also received attention as an active oxygen reduction catalyst [11-14]. Ross *et al.* [12] prepared epitaxial thin films of Pd on a Pt(111) crystal. The pseudomorphic monolayer of Pd produced had a two fold decrease in the performance towards the ORR, compared to Pt(111) alone, with the decrease being even more pronounced in the presence of a specifically adsorbing anion such as bisulfate. Similar catalysts were then studied by Markovic *et al.* [14] in both acidic and alkaline environments. The same reduction in performance was noted for experiments conducted in perchloric acid. However, when the experiment was performed in 0.1M KOH a three fold improvement was noted for a single monolayer of Pd on the Pt (111) crystal. The performance strongly depended on the Pd loading at the Pt surface, with a partial monolayer coverage resulting in only a slight enhancement and a reduction in activity noted for an increased monolayer coverage of 1.5.

Adzic *et al.* [11] have used their same Cu displacement method to prepare Pd films on different substrates e.g. Pt (111), Rh (111), Au (111) The same volcano type behaviour for ORR performance with respect to d band centre was found. The studies were performed in 0.1 M perchloric acid with the most active

catalyst being the Pd / Pt(111) system although it failed to achieve the same activity of the Pt(111) single crystal substrate.

Xu and Zhao [15] have looked at increasing the utilisation of Pt by decorating Au nanoparticles with small amounts of Pt. The catalysts prepared had extremely high utilisation, in some cases mass normalised areas in excess of 230 $m^2 g^{-1}$ Pt were reported. Despite this increase in utilisation the overall catalytic activity has a maximum value of 0.16 A mg^{-1} Pt, which is less than that observed for the conventionally prepared PtCo/C catalysts [1].

Elsewhere, Adzic *et al.* [16] have used their Cu displacement procedure to produce a monolayer of Pt on $AuNi_{10}$, $PdCo_5$, and $PtCo_5$ cores. The core particles are first subjected to high annealing temperatures (up to 850 °C) where the results of DFT calculations predict that the noble metal components should segregate towards the surface [17]. The Cu displacement method, was then used to add a monolayer of Pt to the surface. The mass activity enhancements noted so far have been reported on the basis of the Pt content with the total noble metal loading still remaining high. The preparation of such systems, reduce the noble metal loading, with the $Pt/PtCo_5/C$ catalyst having a noble metal mass activity 5 times greater than that of a conventional Pt/C catalyst.

There is also a drive to produce entirely Pt free catalysts for the ORR. PdCo alloy catalysts have been shown to be very active towards the ORR [11, 18] and are reported to exhibit the same noble metal mass specific activity as Pt, in some instances. At the time of writing, the Johnson Matthey Base price for Pt was 1173 $/oz compared to 336 $/oz for Pd [19]. If a Pd based catalyst can achieve the same noble metal mass specific activity as Pt it represents a 3 to 4 times reduction in cost. The estimated amounts of Pt and Pd in the Earth's crust vary but are around 0.01 and 0.015 ppm respectively [20]. Due to the limited resources of precious metal catalysts and their high cost it is desirable to prepare active non-precious metal catalysts for the ORR. One of the major issues regarding the use of non-precious metal catalysts is their stability [1]. It is not in the scope of this thesis to carry out a comprehensive review of all the

non-precious metal catalysts studied, but one recent example of an interesting system is a cobalt-polypyrrole-carbon catalyst. The catalyst exhibits promising activity towards the ORR and good long term stability [21].

In the study reported in this chapter the controlled surface modification procedure developed by Crabb *et al.* [22-26] and detailed in chapter 2, section 2, is to be used to prepare Pt/C catalysts modified with Pd and Pd/C catalysts modified with Pt. For future reference the catalytic systems will be denoted as Pd/Pt/C and Pt/Pd/C, respectively. It is believed that the controlled surface modification procedure offers advantages in comparison to the Cu electrochemical displacement method. The controlled surface modification procedure does not introduce Cu into the system and offers greater control in the deposition. The Pt/Pd/C and Pd/Pt/C catalysts have been characterised using electrochemistry, XRD, ICP-AES, TEM EDX and EXAFS techniques. The most promising catalysts have been tested for their performance towards the ORR.

2 Experimental Details

2.1 Catalyst Preparation

Pd/Pt/C and Pt/Pd//C catalysts were prepared as detailed in chapter 2, section 2.2. Modifications were made to a 20 wt % Pt/C (XC-72R) catalyst and an 18.8 wt % Pd/C (XC-72R) with calculated dispersions of 0.48 and 0.45, respectively. The organometallic precursors used for the controlled surface modification were $Pt(acac)_2$ and $Pd(acac)_2$. Table 1 below gives details of the catalysts prepared.

Table 1 **Details of catalysts prepared**

Catalyst	Equivalent monolayers	Precursor	Heat treatment / °C	Initial colour of solution	End colour of filtrate
Pd/Pt/C	0.5	$Pd(acac)_2$	200	Yellow	colourless
Pd/Pt/C	1.0	$Pd(acac)_2$	200	Yellow	colourless
Pd/Pt/C	1.5	$Pd(acac)_2$	200	Yellow	colourless
Pt/Pd/C	0.5	$Pt(acac)_2$	200	Yellow	colourless
Pt/Pd/C	1	$Pt(acac)_2$	200	Yellow	colourless
Pt/Pd/C	1.5	$Pt(acac)_2$	200	Yellow	colourless

Control reactions were also carried out on the carbon support to indicate whether the precursor would solely target the supported metal. No reaction between $Pt(acac)_2$ and the carbon support was observed. However, the $Pd(acac)_2$ was found to react with all the surfaces present in the reactor vessel, the glassware, the magnetic stirrer, and the carbon support. However, this deposition onto the other surfaces was not observed when Pt/C was used for the reactions. Thus, it is likely that the Pt offers a preferential reactive site and thus the reaction still solely takes place at the metal surface. The characterisation of the catalysts using EXAFS enabled confirmation of whether the Pd is present at the Pt surface or on the carbon support.

2.2 Electrochemical Characterisation

2.2.1 Cyclic Voltammetry

The electrochemical properties of the catalysts were characterised using the standard 3 electrode half cell detailed in chapter 2, section 3.2.2, with button electrodes prepared according to chapter 2, section 3.2.1. The button electrodes prepared used an overall metal loading (Pt and Pd) of 0.35 mg cm^{-2} M.

2.2.2 Oxygen Reduction Testing

The performance of the catalysts towards the ORR was assessed in the mini cell as described in chapter 2 section 3.4. The mini cell was used in preference to the

RDE for testing the electrocatalysts, as it is a more accurate method for determining mass activities, and is more representative of the ultimate fuel cell performance of a catalyst.

2.3 XAS Studies

2.3.1 Pt L_3 and Pd K edge Investigations

Pt L_3 and Pd K edge XAS spectra were acquired on station 16.5 at the SRS, Daresbury Laboratory. Station 16.5 is on a 6T Wiggler line, and utilises a double crystal Si(220) monochromator to acquire EXAFS in the range of 7 KeV to 40 KeV. EXAFS of the catalyst material were acquired in transmission mode where possible otherwise, using fluorescence mode with a liquid nitrogen cooled 30 element Ge solid state detector. EXAFS of metal foils and oxide standards were also acquired in transmission mode. All catalysts were prepared as BN pellets for XAS measurements.

2.4 XRD, TEM, and ICP-AES Analysis

All samples were submitted to Johnson Matthey Technology Centre, Sonning Common, where the analyses were performed.

The XRD analysis used a Bruker AXS D-500 diffractometer with a 40 position sample changer, a Ni filtered Cu K_α X-ray source, a scan range of 15 to 95° 2θ with a 0.02° step size, and a scan rate of 0.25° 2θ per minute.

Powder samples for TEM EDX were crushed between two glass slides and samples positioned onto a lacey carbon coated copper 'finder' grid with the aid of a micro manipulator. The samples were examined in a Tecnai F20 Transmission Electron Microscope. Both bright field and high resolution electron microscopy modes were used.

3 Results and Discussion

3.1 ICP-AES Analysis

Elemental analysis of the prepared catalysts was carried out using ICP-AES. The experimental values along with the theoretically calculated values are detailed in table 2.

Table 2 Elemental analysis of prepared Pd/Pt/C and Pt/Pd/C catalysts

Sample	Wt % Pt Theoretical	Wt % Pt Experimental	Wt % Pd Theoretical	Wt % Pd Experimental
0.5 Pd/Pt/C	19.1	19.1	2.5	2.5
1.0 Pd/Pt/C	18.0	19.4	5.0	4.9
1.5 Pd/Pt/C	17.2	18.5	7.3	6.5
0.5 Pt/Pd/C	7.6	7.0	17.4	17.3
1.0 Pt/Pd/C	14.2	13.6	16.5	16.3
1.5 Pt/Pd/C	19.9	18.3	15.0	15.0

The ICP-AES results for the Pt/Pd/C catalysts are in good agreement with the theoretical values suggesting that the entirety of the secondary metal introduced in the form of the organometallic precursor was deposited onto the catalyst. The Pt content of the Pd/Pt/C catalysts are generally higher than expected; the Pt content increases to 19.4 wt % for the 1.0 Pd/Pt/C catalyst compared to a value of 19.1 wt % for the 0.5 Pd/Pt/C. This discrepancy can only be explained by errors in the testing procedure. All the analyses are performed in triplicate which should negate any differences that arise due to any heterogeneity in the systems.

3.2 XRD Analysis

The XRD patterns of the Pd/Pt/C catalysts can all be interpreted in the same way and are shown in figure 1a. The diffraction patterns indicate that the sample is mainly composed of a poorly crystalline cubic platinum phase, supported on XC-72R. There is no evidence to suggest the presence of either a PtPd or Pd crystal phase. However, there is some evidence of the presence of an amorphous

phase as there is a broadening of the characteristic platinum peak, giving rise to a non-Gaussian crystallite size distribution. As there is a non-Gaussian distribution, two different Gaussian particle size distributions were fitted to the data, and are shown in table 3. Although there is not any evidence of PtPd alloy formation, the data is not necessarily inconsistent with a monolayer of Pd present on the surface of Pt. The XRD only looks at the long range order of materials and thus with the majority of Pt being in the interior of the particle the Pd monolayer may not be observed. The EXAFS analysis presented in section 3.5 gives a more accurate assessment of the structure of the catalyst materials.

Table 3 **Lattice parameters and particle size for Pd/Pt/C catalysts determined using XRD.**

Catalyst	Crystallite size /nm		Lattice parameter / Å	
	Distribution 1	Distribution 2	Distribution 1	Distribution 2
0.5 Pd/Pt/C	2.3	10.3	3.93	3.93
1.0 Pd/Pt/C	2.4	9.3	3.93	3.92
1.5 Pd/Pt/C	2.5	9.9	3.93	3.92

The Pt/Pd/C XRD patterns (figure 1b) can also be interpreted in the same way as each other. The catalysts are composed entirely of a poorly crystalline platinum palladium alloy phase, supported on carbon. There is no evidence to suggest any other crystalline phases are present. The XRD data confirms that there is a higher degree of alloying for the Pt/Pd/C catalysts compared to the Pd/Pt/C catalysts. Thus, it can be inferred that the Pt is not found exclusively at the surface. The calculated parameters for the Pt/Pd/C catalysts are presented in table 4.

Table 4 **Lattice parameters and particle size for Pt/Pd/C catalysts determined using XRD.**

Catalyst	Lattice parameter / Å	Particle size / nm
0.5 Pt/Pd/C	3.91	2.0
1.0 Pt/Pd/C	3.91	2.5
1.5 Pt/Pd/C	3.91	2.5

(a)

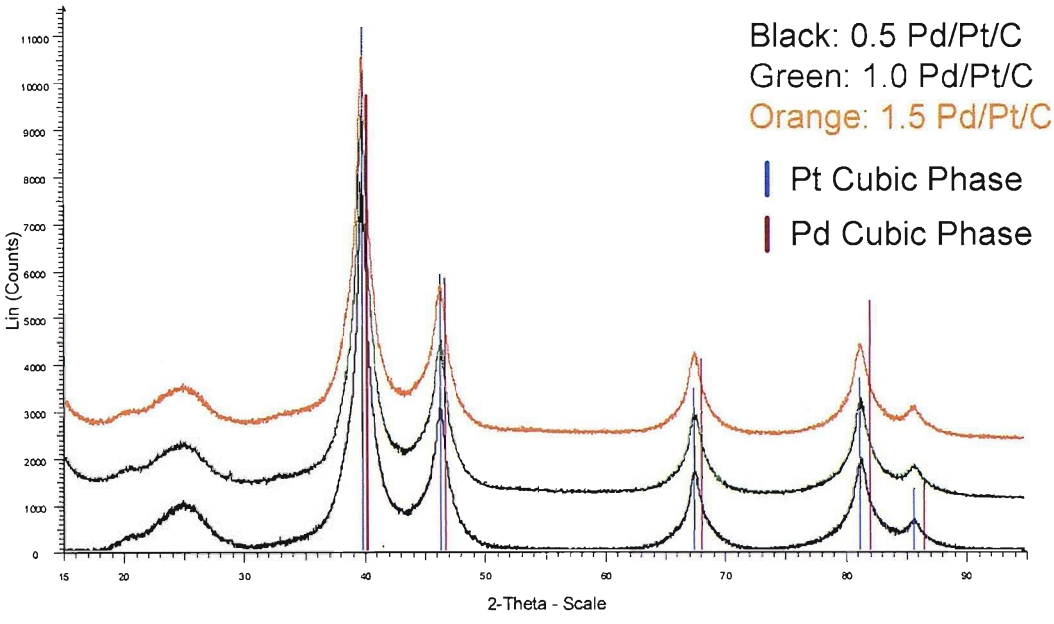

(b)

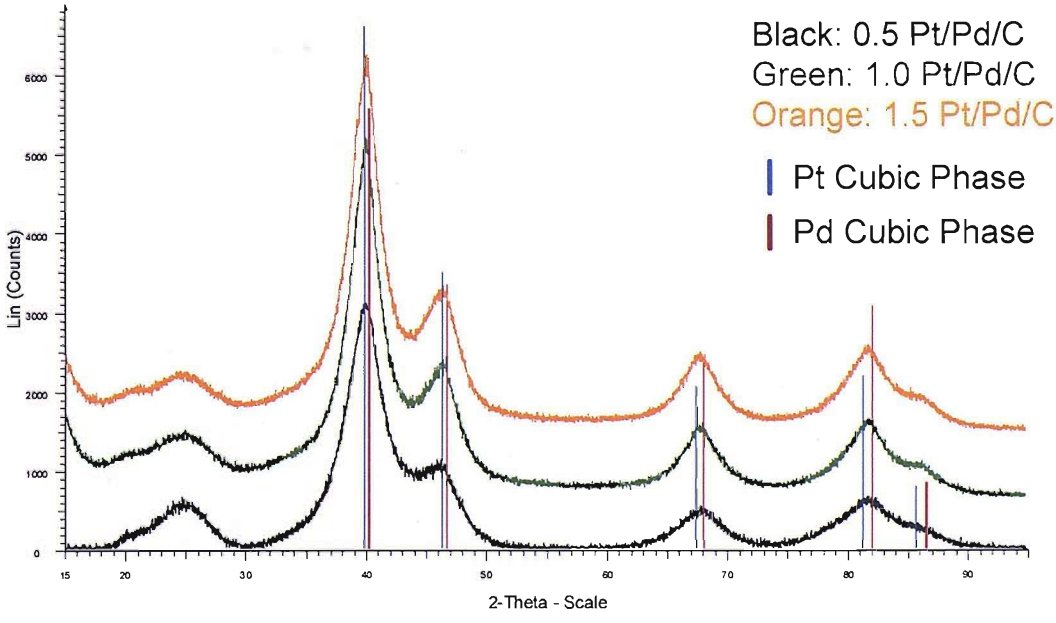

Figure 1 **XRD patterns of (a) Pd/Pt/C and (b) Pt/Pd/C catalysts. JCPDS reference data are included for comparison.**

3.3 TEM EDX Analysis

Particle size distributions and TEM micrographs of the Pd/Pt/C and Pt/Pd/C catalysts are shown below in figures 2 and 3, respectively.

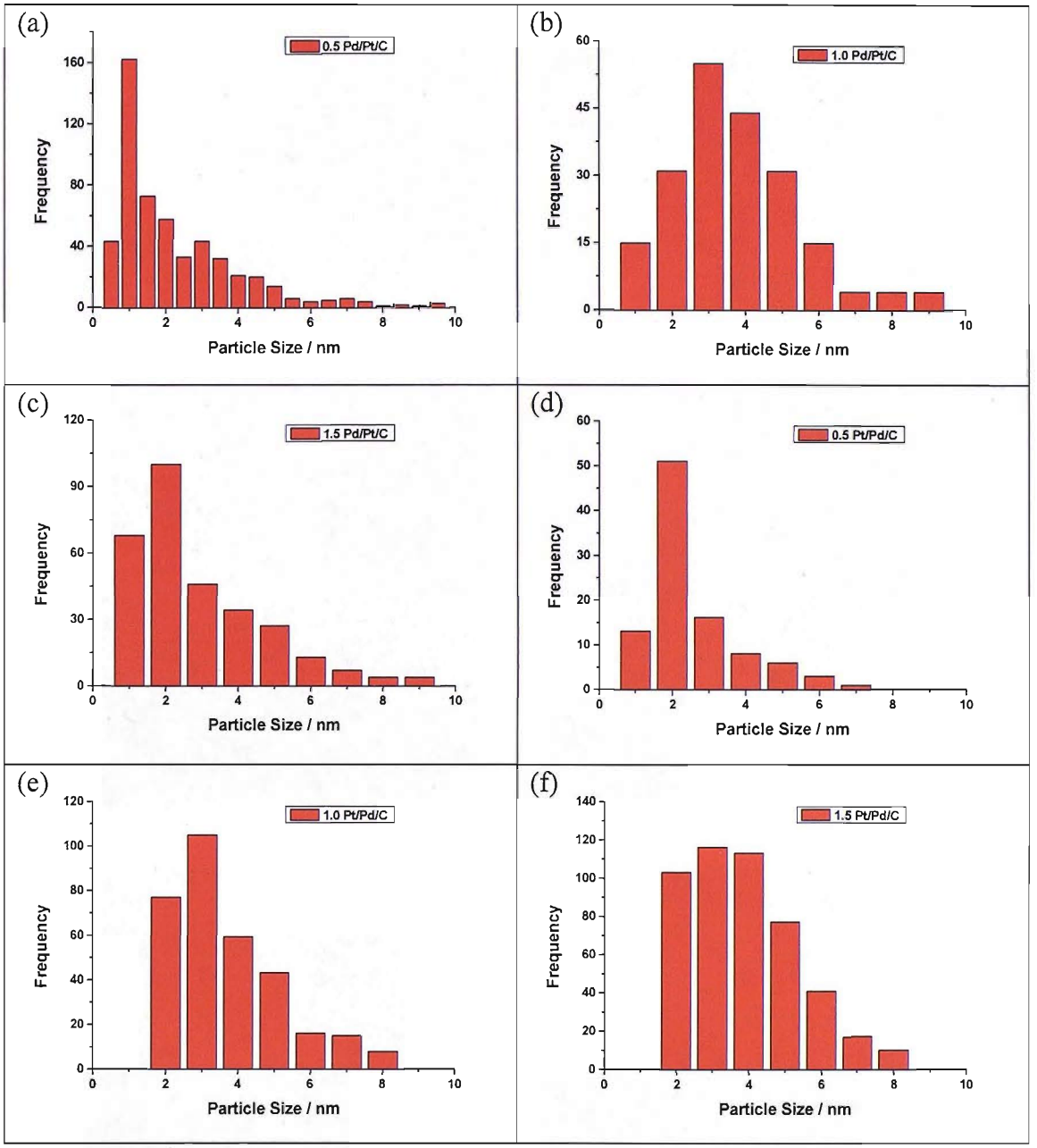

Figure 2 **Particle size distributions of (a-c) 0.5, 1.0 and 1.5 Pd/Pt/C and (d-f) 0.5, 1.0, and 1.5 Pt/Pd/C catalysts.**

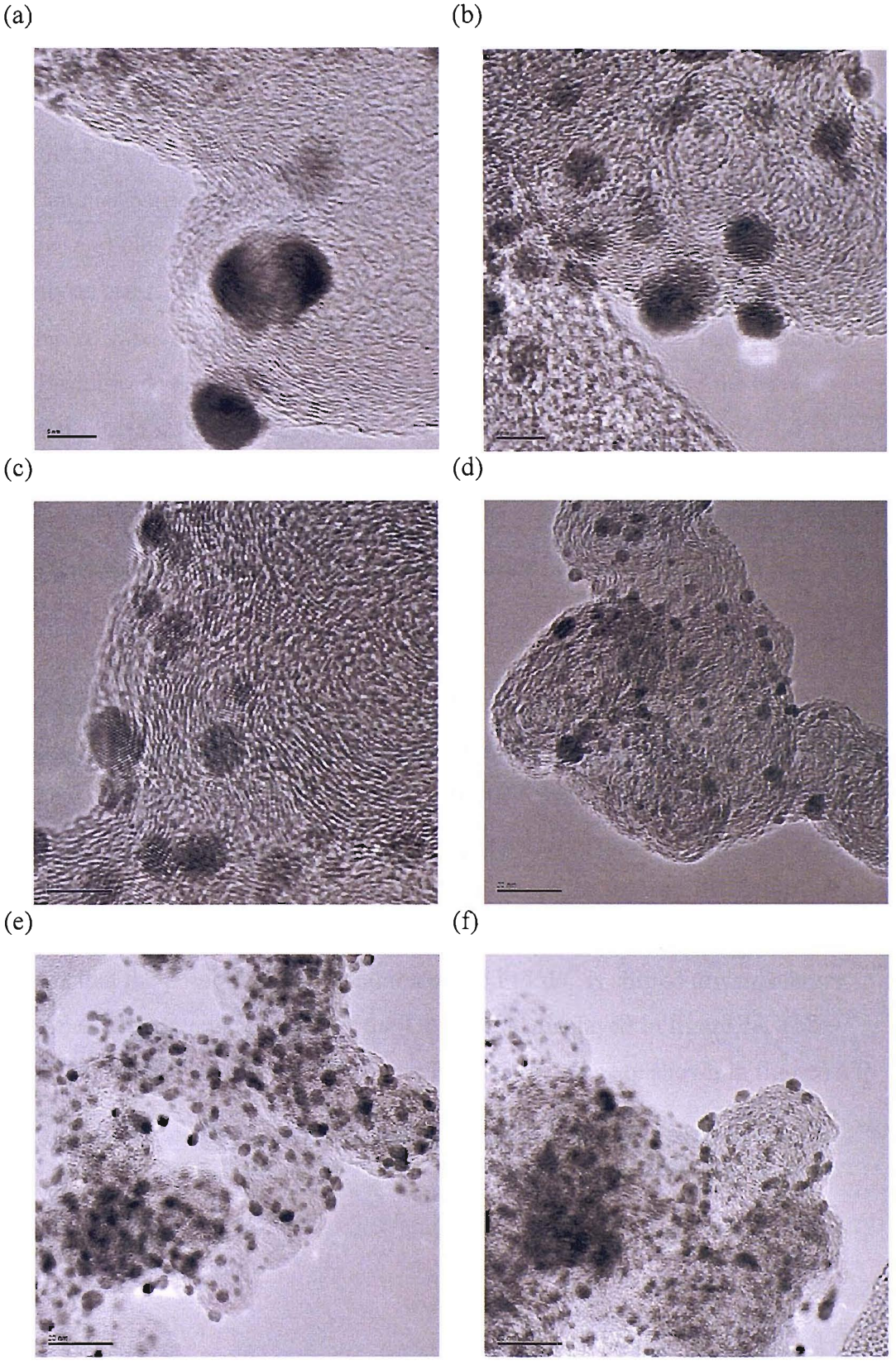

Figure 3 **TEM micrographs of (a-c) 0.5, 1, and 1.5 Pd/Pt/C the scale bar on each micrograph is 5 nm, and (d-f) 0.5, 1, and 1.5 Pt/Pd/C the scale bar on each micrograph is 20 nm.**

In this report the main application of the TEM technique is to assess the particle size distribution of the different catalysts and to use the EDX function to study the proportion of the metallic components across a range of particles. The TEM micrographs of the Pd/Pt/C samples gave evidence of small (1-1.5 nm) and large particles (10-15 nm). The particle size estimations performed are biased towards the smaller particles as the areas chosen for the analysis had very few of the larger particles in view. The average particle size of the 0.5, 1, and 1.5 Pd/Pt/C catalysts are 2.1, 3.2, and 2.5 nm, respectively. The increase in particle size observed when the monolayer fraction is increased from 0.5 to 1 is in agreement with additional amounts of Pd being deposited onto the surface of the Pt. The particle size for the 1.5 Pd/Pt/C catalyst is smaller in comparison to the 1.0 Pd/Pt/C. This result is not in agreement with the modification procedure. This discrepancy could be associated with statistical error in the particle size determination, or as a result of the larger particles being excluded from the analysis.

The average particle size of the 0.5, 1, and 1.5 Pt/Pd/C catalysts are 2.0, 3.3, and 3.4 nm, respectively. An increase in particle size is observed with increasing Pt content, in agreement with the desired controlled surface modification. Again the 1.5 monolayer catalyst has a smaller average particle size than would be expected in comparison to the increase observed for the 0.5 and 1 Pt/Pd/C catalysts. Although only a small particle size increase is observed, figure 2f shows that the particle size distribution of 1.5 Pt/Pd/C is shifted towards larger particles in comparison to that of the 1.0 Pt/Pd/C displayed in figure 2e. The TEM EDX analyses of the Pd/Pt/C and Pt/Pd/C samples are shown in figures 4 to 9.

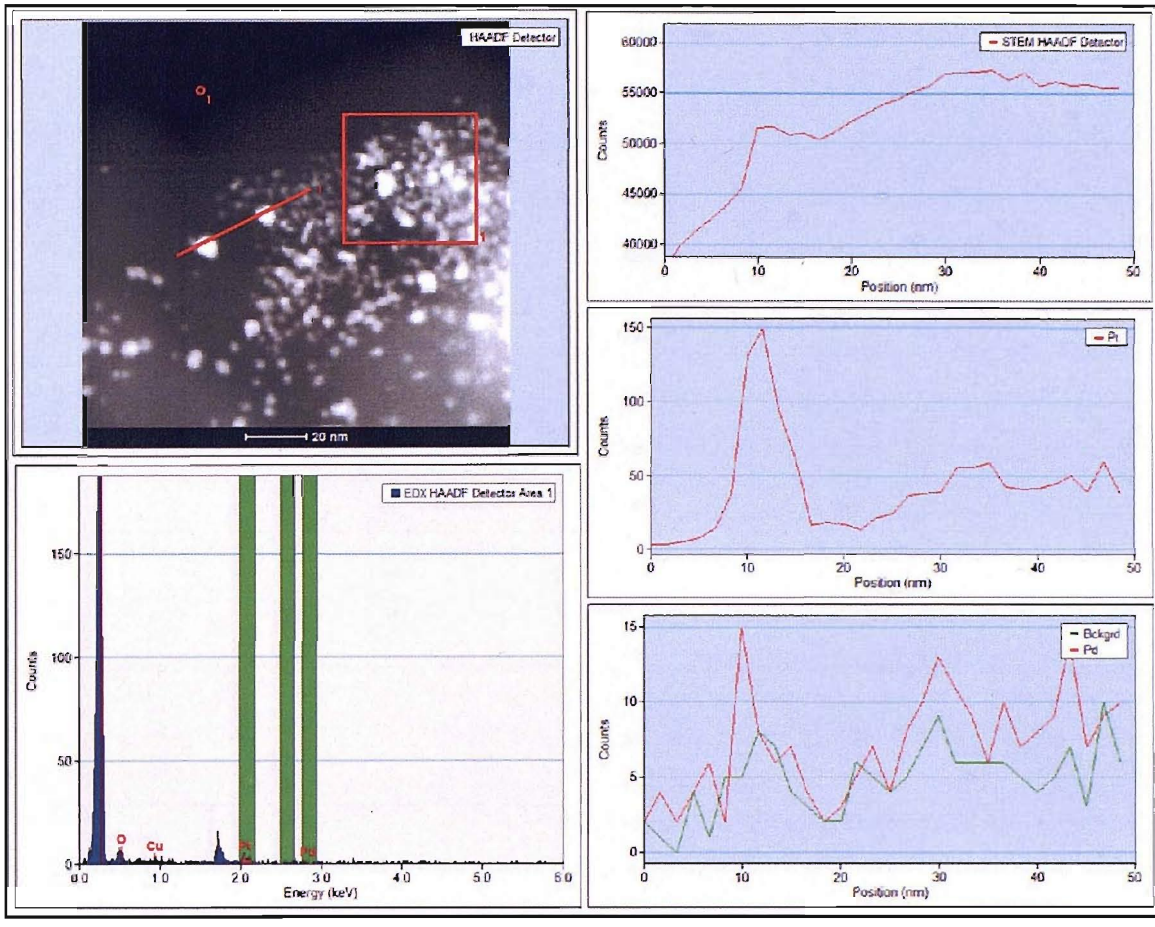

Figure 4 **TEM EDX Line profile analysis for 0.5 Pd/Pt/C. The upper left box shows the TEM image of the area under investigation. The EDX response for the red box labelled 1 is shown below the TEM image. The EDX response across the red line labelled one are shown on the right hand side and in descending order show total counts, counts from Pt, and counts from Pd (the counts for the background alone are included for comparison).**

The TEM EDX line profile data (figure 4) for the 0.5 Pd/Pt/C catalyst primarily show that the Pt and Pd are found in the same areas. The data needs to be treated with a certain amount of caution as the intensity that arises due to Pd is of a similar level as the background counts. The TEM line profiles show that the Pt and Pd distributions do not follow each other across the particle, with the intensity if the Pd line scan being localised at the centre of a mainly Pt composed particle. This could indicate a localised Pd coating or a central nucleation site.

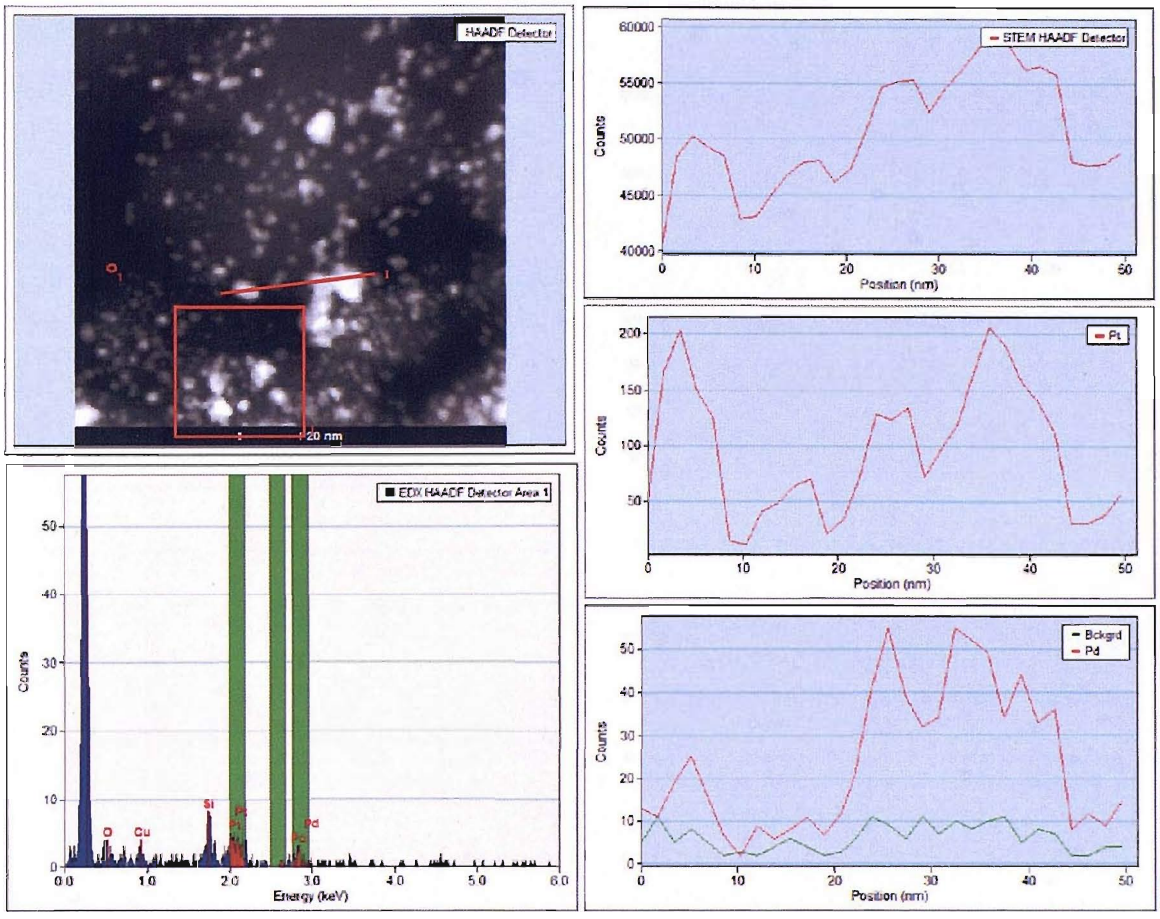

Figure 5 **TEM EDX Line profile analysis for 1.0 Pd/Pt/C. The upper left box shows the TEM image of the area under investigation. The EDX response for the red box labelled 1 is shown below the TEM image. The EDX response across the red line labelled one are shown on the right hand side and in descending order show total counts, counts from Pt, and counts from Pd (the counts for the background alone are included for comparison).**

The TEM EDX line profiles (figure 5) for the 1.0 Pd/Pt/C catalyst primarily show that the Pt and Pd are found in the same areas across different particles. Unlike the 0.5 Pd/Pt/C catalyst the counts arising from Pd are far larger than the background counts. The TEM line profiles show that the Pt and Pd distributions do not follow each other across the particle. In this instance there is evidence of a wider Pd distribution, this could be interpreted as Pd being present predominantly at the exterior of the particle.

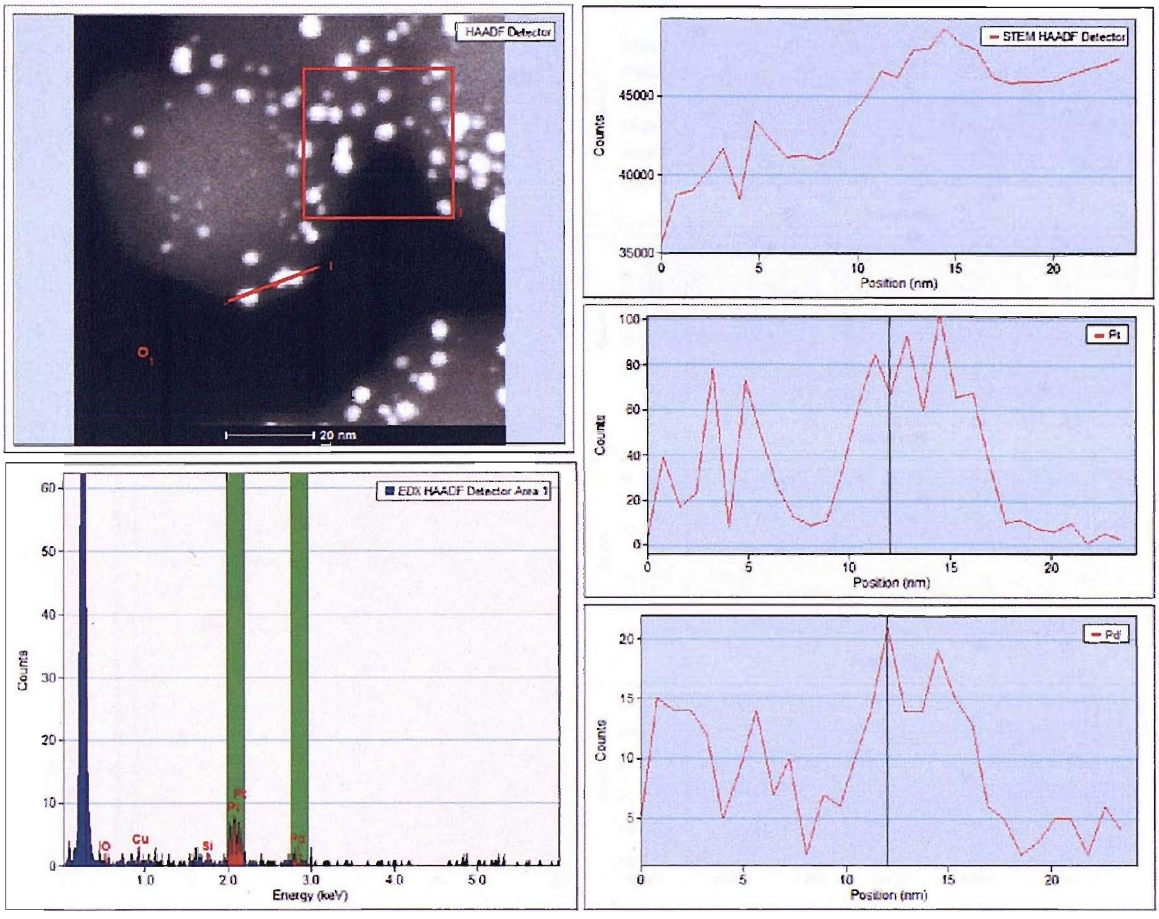

Figure 6 **TEM EDX Line profile analysis for 1.5 Pd/Pt/C. The upper left box shows the TEM image of the area under investigation. The EDX response for the red box labelled 1 is shown below the TEM image. The EDX response across the red line labelled one are shown on the right hand side and in descending order show total counts, counts from Pt, and counts from Pd.**

The TEM EDX line profiles (figure 6) for the 1.5 Pd/Pt/C catalyst primarily show that the Pt and Pd are found in the same areas, and is consistent with the interpretation for the 1 Pd/Pt/C catalyst, showing evidence of a wider Pd distribution, and thus that Pd is enriched on the exterior of the particle. The TEM EDX line profile analysis for the Pd/Pt/C samples supports the presence of Pd at the surface of a Pt particle, inferring that the controlled surface modification procedure has been successful.

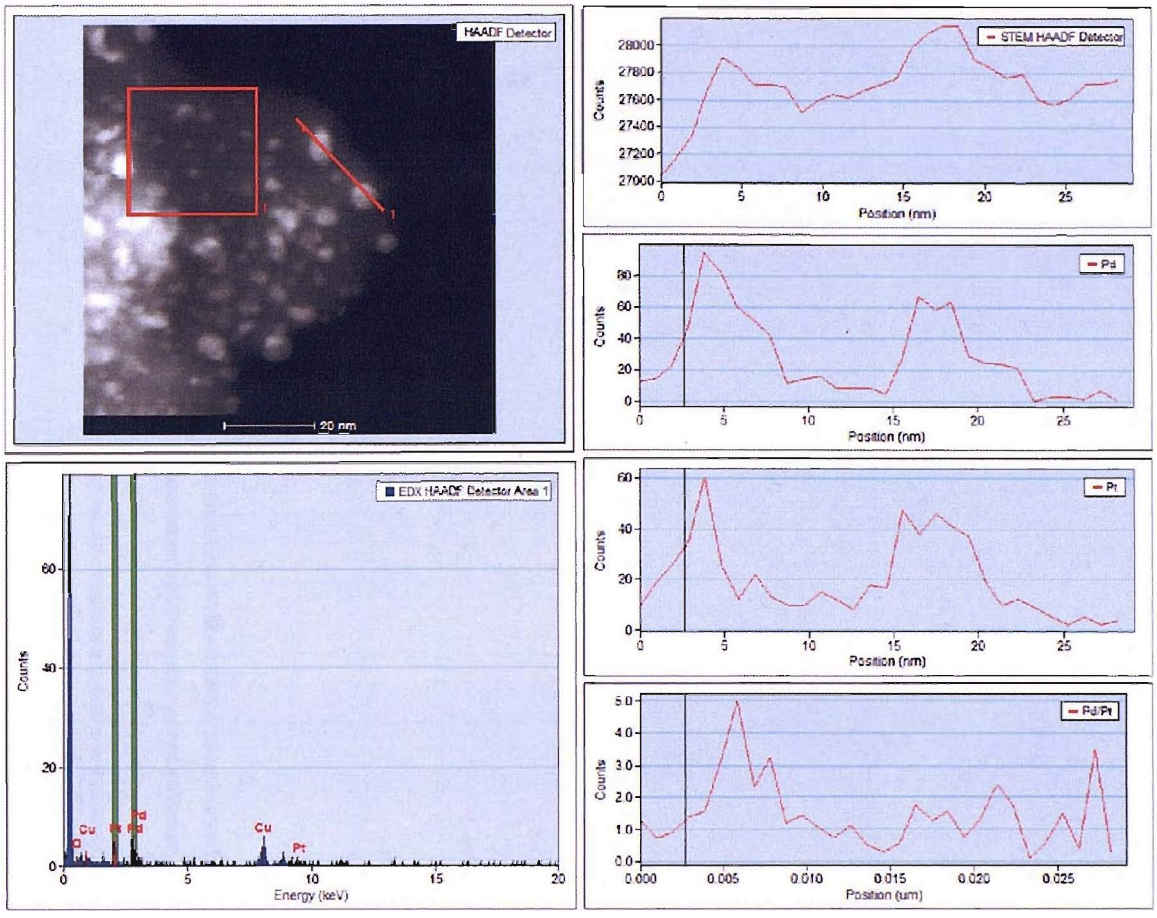

Figure 7 **TEM EDX Line profile analysis for 0.5 Pt/Pd/C. The upper left box shows the TEM image of the area under investigation. The EDX response for the red box labelled 1 is shown below the TEM image. The EDX response across the red line labelled one are shown on the right hand side and in descending order show total counts, counts from Pd, counts from Pt, and the ratio of Pd to Pt counts.**

The TEM EDX line profiles (figure 7) for the 0.5 Pt/Pd/C catalyst primarily show that the Pt and Pd are found in the same areas across different particles. The TEM line profiles show that the Pt and Pd distributions do not follow each other across the particle. However, it is not possible to establish whether there is any Pt enrichment on the exterior of the particle.

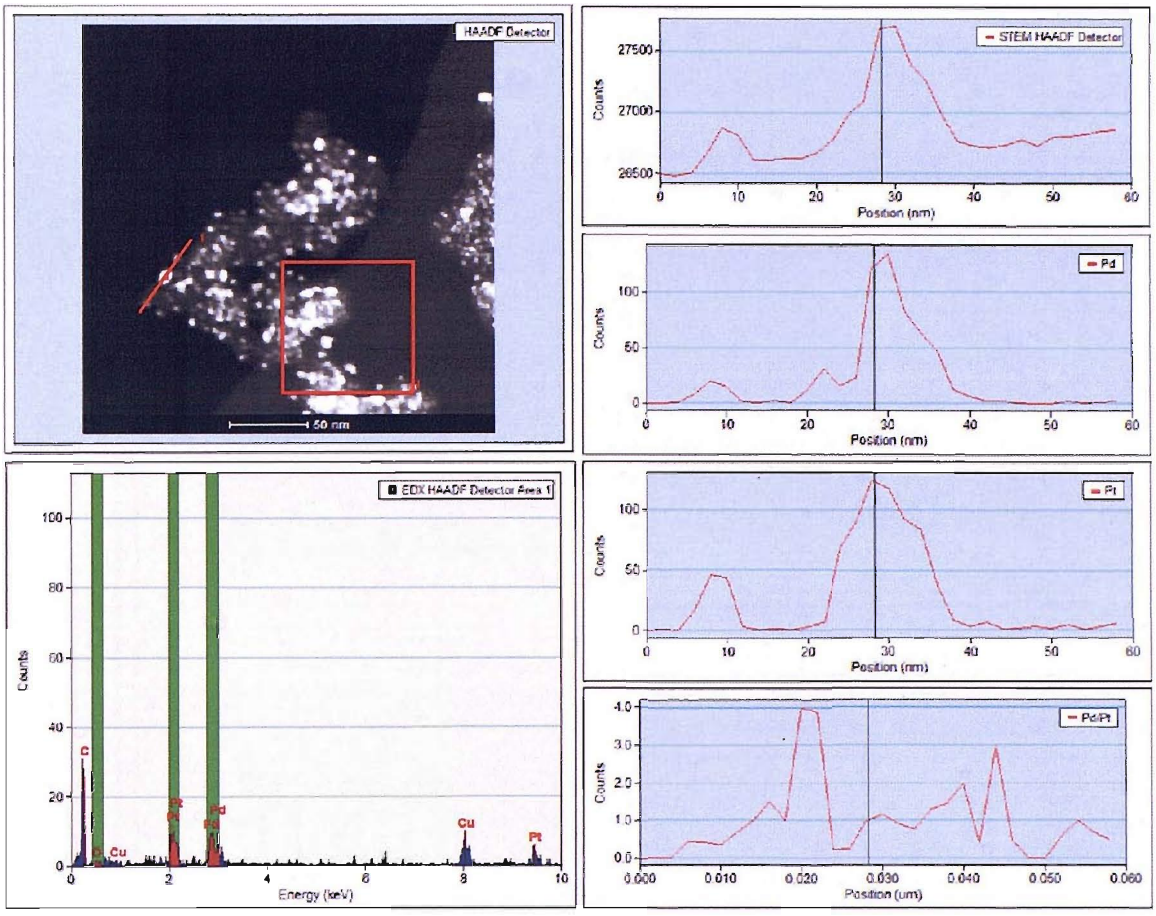

Figure 8 **TEM EDX Line profile analysis for 1.0 Pt/Pd/C. The upper left box shows the TEM image of the area under investigation. The EDX response for the red box labelled 1 is shown below the TEM image. The EDX response across the red line labelled one are shown on the right hand side and in descending order show total counts, counts from Pd, counts from Pt, and the ratio of Pd to Pt counts.**

The TEM EDX line profiles (figure 8) for the 1 Pt/Pd/C catalyst primarily show that the Pt and Pd are found in the same areas across different particles. There is sufficient broadening of the Pt distribution with respect to the Pd distribution such that it can be inferred that there are increased levels of Pt on the exterior of the particle. It can also be seen that there are small fragments of Pd on the support just outside the particle. The evidence of Pd in isolation may be as a result of small Pd particles not being as active towards the controlled surface modification procedure, or due to small clusters of Pd breaking off the main Pd particle during the reaction.

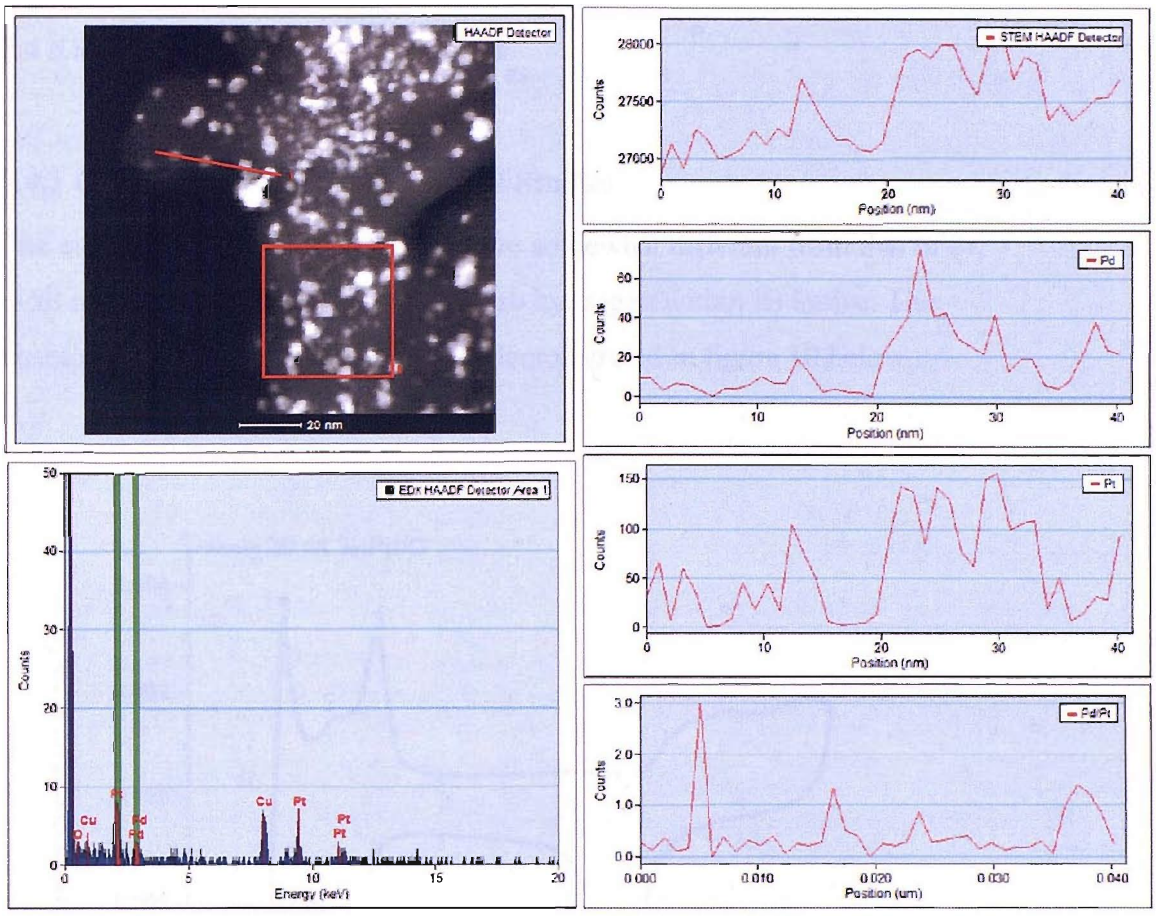

Figure 9 **TEM EDX Line profile analysis for 1.5 Pt/Pd/C. The upper left box shows the TEM image of the area under investigation. The EDX response for the red box labelled 1 is shown below the TEM image. The EDX response across the red line labelled one are shown on the right hand side and in descending order show total counts, counts from Pd, counts from Pt, and the ratio of Pd to Pt counts.**

The TEM EDX data for the 1.5 Pt/Pd/C catalyst (figure 9) can be interpreted in the same way as the 1 Pt/Pd/C catalyst. Again there is evidence of a broader Pt distribution, suggesting Pt is present at the surface of the Pd particle, and also evidence of small Pd particles found in isolation on the support. As with the Pd/Pt/C samples, the TEM EDX data are consistent with a successful controlled surface modification, showing evidence of the secondary metal being present on the exterior of the particle.

3.4 Electrochemical Characterisation

3.4.1 Cyclic Voltammetry – Half Cell Studies

The electrochemical properties of Pd are somewhat different from that of Pt, most notably Pd has the ability to absorb hydrogen within its lattice. The characteristics of Pd voltammetry are demonstrated in figure 10 below.

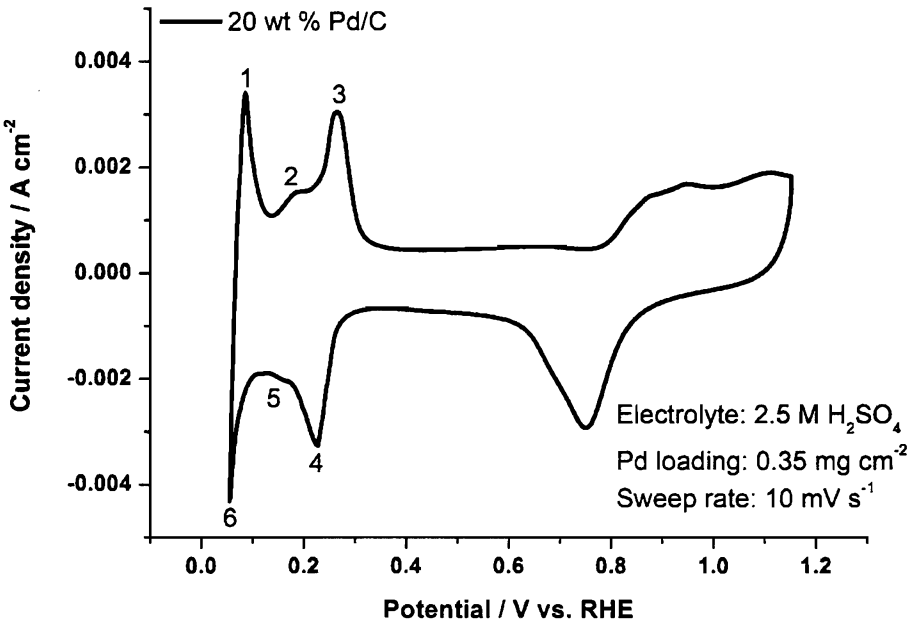

Figure 10 **CV of 20 wt % Pd/C highlighting the hydride features. Peak (1) oxidation of β - hydride phase (2) oxidation of α - hydride phase (3) removal of adsorbed hydrogen (4) adsorption of hydrogen (5) formation of α - hydride phase (6) formation of β - hydride phase**

Although there are differences in the oxide region of the voltammogram the key differences are in the hydrogen region and these processes have been labelled in figure 10. Peaks 4 and 3 labelled above correspond to the formation and removal of adsorbed hydrogen on the Pd surface, respectively. When hydrogen is absorbed into the Pd lattice two hydride phases are formed, an α phase and a β phase. The formation and removal of the α hydride phase correspond to the peaks labelled 5 and 2, respectively. The α hydride phase represents only a small contribution to the currents observed, as it is only stable up to H / Pd ratios of

0.05 [27, 28]. The predominant amount of hydrogen is absorbed into the β phase, the formation and removal of which are denoted as peaks 6 and 1, in figure 10. It should be noted that the Pd/C used for the modification with Pt was different from that shown above, which had a much larger particle size.

Voltammetric investigations of both the unmodified Pt/C and Pd/C used in this section along with the Pt/Pd/C and Pd/Pt/C are detailed in figures 11-13, with the key determined parameters reported in tables 5-7.

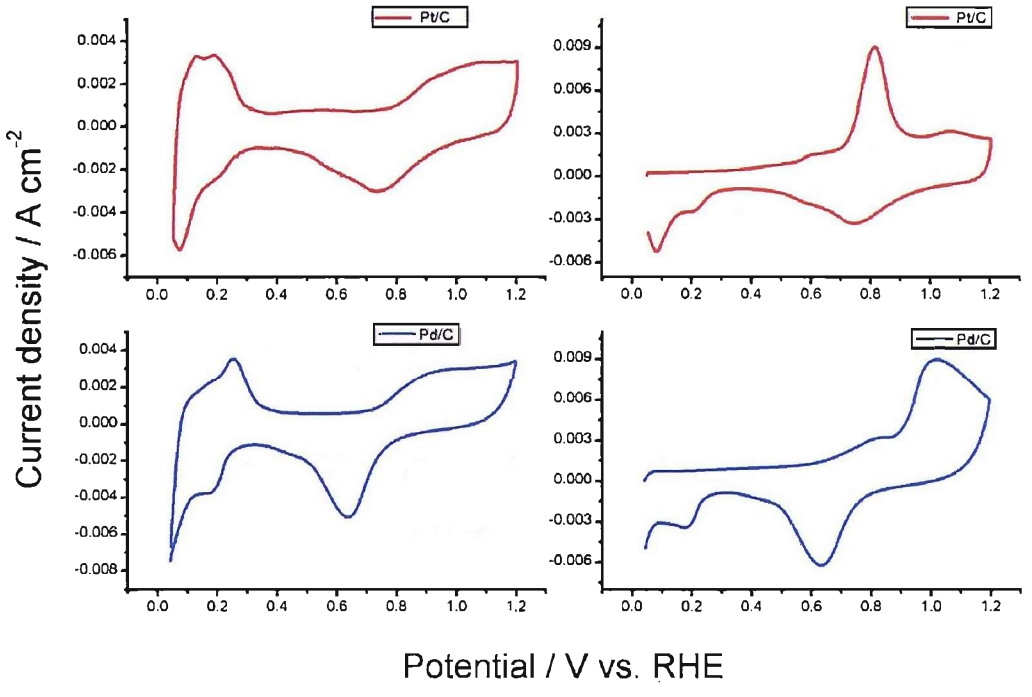

Figure 11 **Cyclic voltammograms (left column) and CO stripping voltammetry (right column) for 20 wt % Pt/C (red) and 18.8 wt % Pd/C (blue). Carried out in 2.5 M H_2SO_4 with a scan rate of 10 mV s^{-1}.**

Table 5 **Electrochemical parameters taken from CVs in figure 11.**

Sample	M loading / mg cm^{-2}	Oxide reduction / V vs. RHE	CO oxidation / V vs. RHE
20 wt % Pt/C	0.349	0.749	0.821
18.8 wt % Pd/C	0.334	0.632	1.014

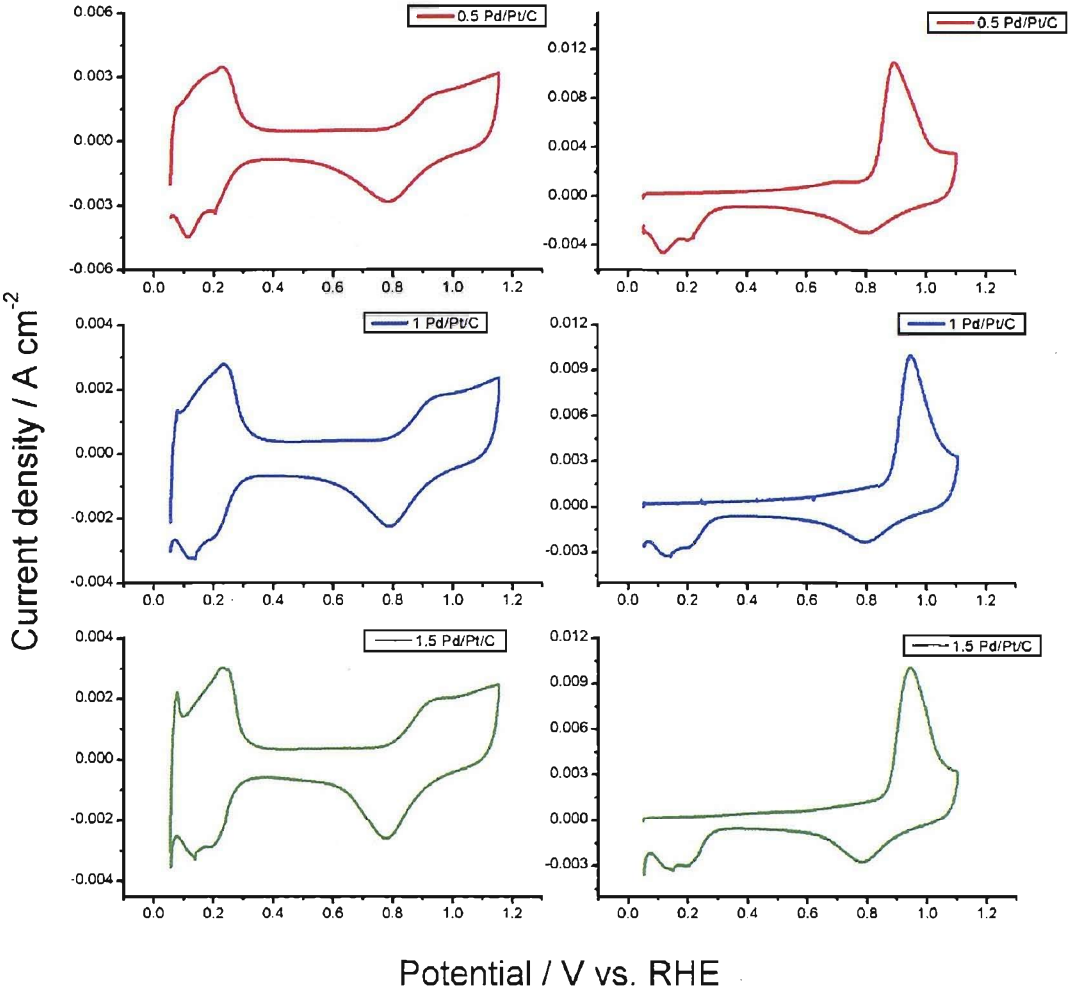

Figure 12 **Cyclic voltammograms (left column) and CO stripping voltammetry (right column) for 0.5 (red), 1 (blue), and 1.5 (green) Pd/Pt/C. Carried out in 2.5 M H_2SO_4 with a scan rate of 10 mV s^{-1}.**

Table 6 **Electrochemical parameters taken from CVs in figure 12.**

Sample	M loading / mg cm^{-2}	Oxide reduction* / V vs. RHE	CO oxidation / V vs. RHE
0.5 Pd/Pt/C	0.480	0.787	0.894
1.0 Pd/Pt/C	0.482	0.783	0.945
1.5 Pd/Pt/C	0.496	0.771	0.942

*the upper potential limit used was 1.15 V vs. RHE, opposed to 1.20 V vs. RHE used in the other measurements.

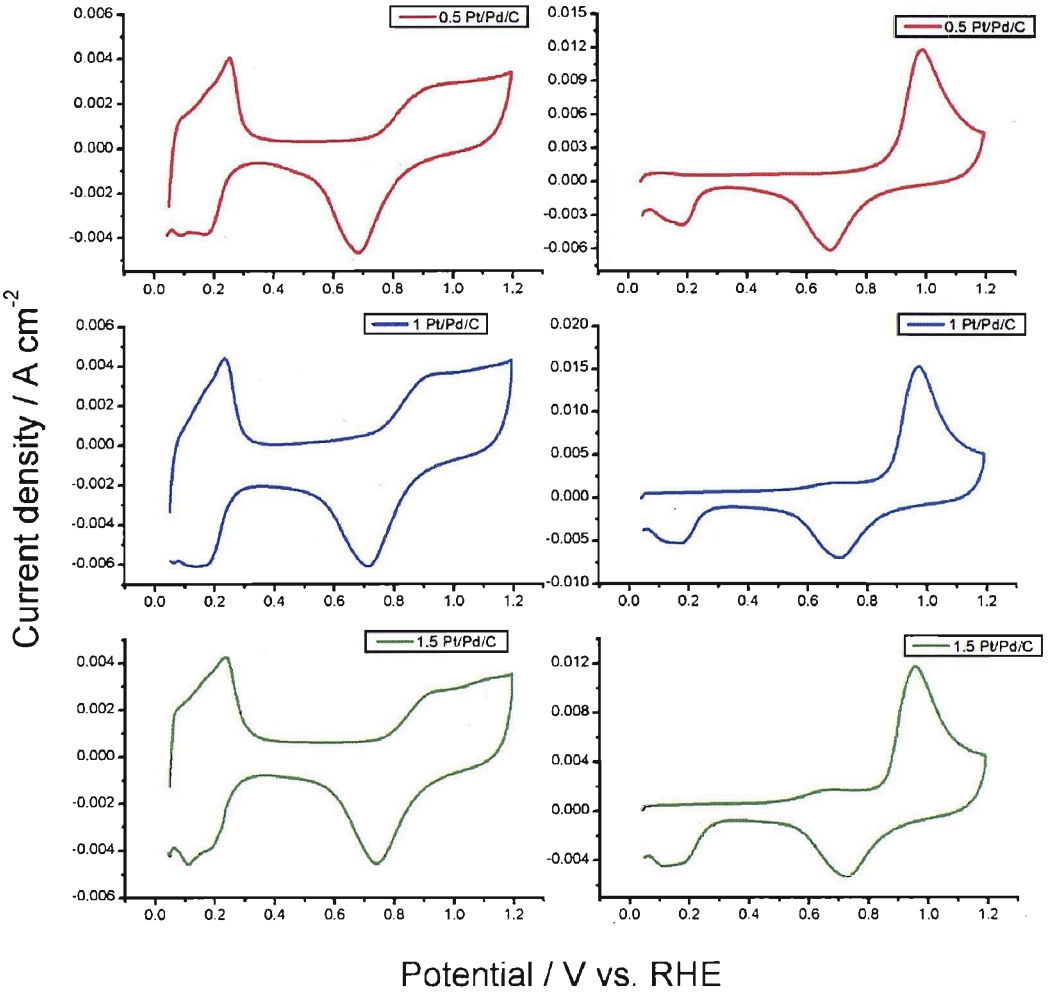

Figure 13 **Cyclic voltammograms (left column) and CO stripping voltammetry (right column) for 0.5 (red), 1 (blue), and 1.5 (green) Pt/Pd/C. Carried out in 2.5 M H_2SO_4 with a scan rate of 10 mV s^{-1}.**

Table 7 **Electrochemical parameters taken from CVs in figure 13.**

Sample	M loading / mg cm^{-2}	Oxide reduction / V vs. RHE	CO oxidation / V vs. RHE
0.5 Pt/Pd/C	0.323	0.680	0.990
1.0 Pt/Pd/C	0.359	0.711	0.972
1.5 Pt/Pd/C	0.401	0.734	0.954

The Pd/C used for the modification has a different voltammetric response compared to the other Pd/C voltammogram described in figure 10. These differences are attributable to the relative particle sizes of the supported Pd/C catalysts. The Pd/C voltammogram shown in figure 10 has a much larger Pd particle size and thus more defined Pd crystal facets which give rise to the distinct Pd features observed. The electro-oxidation of CO on Pd surfaces is less favoured than on Pt surfaces, as observed by the potential of the CO oxidation peak which is 0.82 V vs. RHE for Pt and 1.01 V vs. RHE for Pd.

The voltammograms obtained for the Pd/Pt/C catalysts show strong Pd characteristics as demonstrated by a variety of features. The removal of adsorbed hydrogen occurs around 0.24 V vs. RHE, and this peak becomes more prominent as the fraction of Pd is increased at the catalyst surface. The peak at 0.15 V vs. RHE for Pt/C associated with the removal of weakly adsorbed hydrogen appears to be minimal for all of the Pd/Pt/C catalysts, with the appearance of any shoulder in this region diminishing with increasing levels of Pd. The 1 and 1.5 Pd/Pt/C catalysts also exhibit a pair of peaks around 0.07 V vs. RHE. The shape and symmetry of these peaks suggest that they could be the result of Pd hydride formation and removal. As the Pd monolayer fraction increases the position of the oxide reduction peak shifts to more negative potentials. These values cannot be compared directly to the Pt/C and Pd/C monometallic catalysts as less time is spent in the oxide region as the potential was only cycled to an upper limit of 1.15 V vs. RHE for the Pd/Pt/C catalysts. However, this trend still shows that the characteristics of the oxide peak are becoming more Pd like in nature as the potential is shifting to lower values. Also the shape of the oxide removal peak is more defined and pronounced in comparison to the standard Pt/C peak which is much broader. The potential of the CO oxidation peak is shifted to more positive potentials for the Pd/Pt/C catalysts compared to Pt/C. The 0.5 Pd/Pt/C catalyst exhibits the smallest increase in CO oxidation potential, with the 1 and 1.5 Pd/Pt/C catalysts having a similar CO oxidation potential around 0.945 V vs. RHE. The increase in CO oxidation potential is another indicative feature of Pd characteristics. From the similarity of the CO oxidation peak potential for the 1 and 1.5 Pd/Pt/C catalysts it can be inferred, that by the addition of 1 monolayer

of Pd the surface is completely saturated with Pd as the additional Pd coverage does not result in a shift to more positive potentials.

The voltammograms obtained for the Pt/Pd/C catalysts similarly show signs of increased character of the modifying metal, compared to Pd/C. The peak associated with the removal of weakly adsorbed hydrogen on Pt appears as a shoulder at more positive potentials than the large Pd hydrogen adsorption peak, for all the Pt/Pd/C catalysts. The charge associated with this peak increases with Pt coverage. A peak at 0.11 V vs. RHE in the reverse sweep can be seen for the 1.5 Pt/Pd/C catalyst and is associated with the formation of weakly adsorbed hydrogen on Pt. In both systems any sign of the strongly bound hydrogen on Pt is masked by the large hydrogen adsorption / desorption features associated with Pd. The oxide removal peak also shifts to more positive potentials as the Pt loading is increased. The peak associated with the removal of oxide is 0.734 V vs. RHE for the 1.5 Pt/Pd/C catalyst which is close in comparison to that of Pt/C, occurring at 0.749 V vs. RHE. The position of the CO oxidation peak decreases from 0.99 V → 0.97 V → 0.95 V vs. RHE as the monolayer fraction of Pt is increased from 0.5, to 1, and then to 1.5, also indicating increased Pt character. Unlike the Pd/Pt/C catalysts the 1 and 1.5 Pt/Pd/C catalysts do not have the same performance for the electrooxidation of CO. These characteristics combined with the strong hydrogen adsorption / desorption regions associated with Pd indicate that the surface is a mixture of both Pt and Pd. The control reactions show that the Pt is targeting the Pd sites and not the support, so this observation could be a result of Pt clustering, Pd segregating to the surface, or Pt targeting only a proportion of the Pd particles.

An important feature associated with Pd electrochemistry is the dissolution that occurs at positive potentials. The dissolution of Pd in PdPt alloys has been studied previously [29] and it was shown that the dissolution of Pd occurs initially at a slow rate at 1.0 V vs. RHE. However, when the upper potential limit is increased to 1.5 V vs. RHE it took only 50 scans at 50 mV s^{-1} to yield an electrochemical profile of a pure Pt surface. A change in surface properties as a result of cycling was also observed in these studies (figure 14).

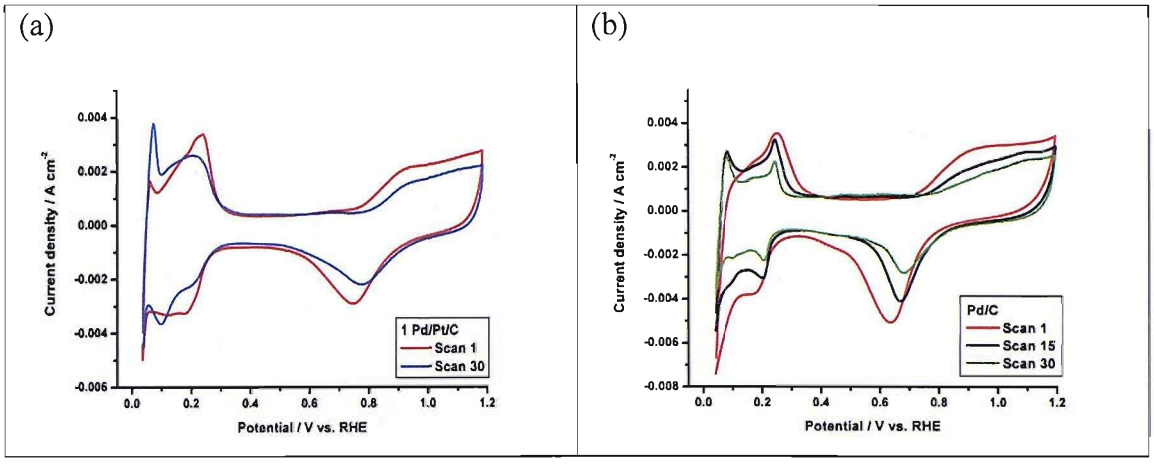

Figure 14 **Cyclic voltammetry studies of (a) 1 Pd/Pt/C and (b) 18.8 wt % Pd/C supplied by Johnson Matthey. Scans were taken at a sweep rate of 10 mV s^{-1} in 2.5 M H_2SO_4. The metal loading was 0.35 mg cm^{-2}.**

The cyclic voltammograms of 1 Pd/Pt/C show that after cycling between the potential limits of 0.05 and 1.2 V vs. RHE the surface becomes more Pt like in character indicating that the surface composition has changed. The dominant hydrogen adsorption / desorption characteristics of Pd disappear, and the two peaks associated with adsorption of weakly and strongly bound hydrogen on Pt are present. However, there is also an increase in the peaks associated with the formation and removal of the Pd-hydride phase. The change in surface properties can therefore not simply be described solely by a dissolution process. A reduction of surface area and increased definition of the Pd hydride features are also apparent in the voltammograms of Pd/C catalyst on cycling. The initial voltammogram of Pd/C show that the voltammetric features associated with Pd are broad. As the electrode is cycled between the potential limits the area under the hydrogen region diminishes and the peaks become more defined. This could be as a result of either dissolution or particle sintering at high potentials. This poor stability of Pd makes it an unsuitable choice of electrocatalyst for fuel cell applications, regardless of its activity towards the catalytic processes. It is important that the Pt/Pd/C catalysts show increased stability under these conditions if they are to be useful. The same cycling experiment was used to assess the stability of the 1.5 Pt/Pd/C catalyst and is shown in figure 15.

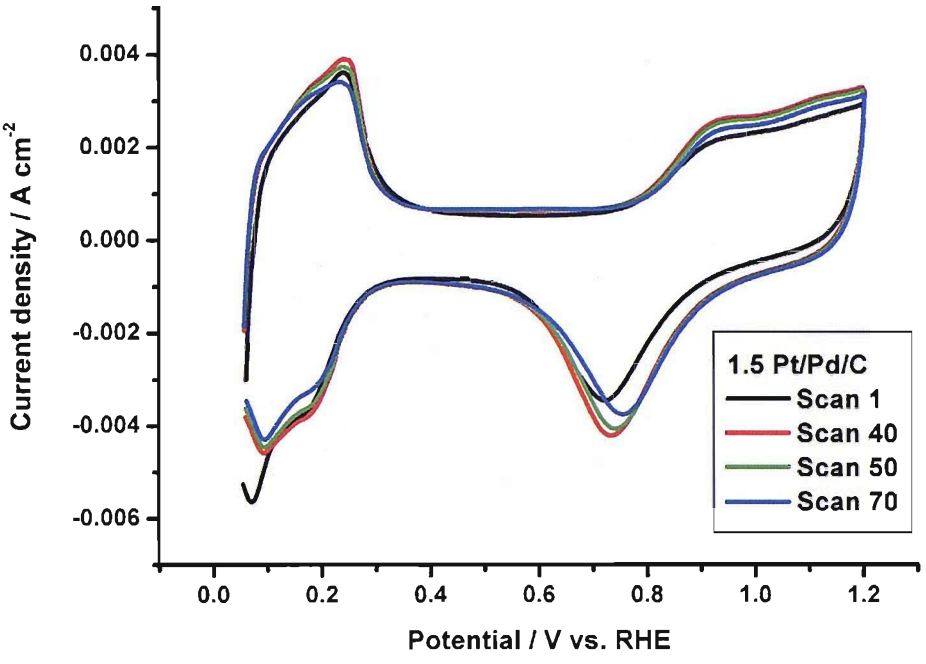

Figure 15 **Cyclic voltammetry studies of 1.5 Pt/Pd/C carried out with a sweep rate of 10 mV s^{-1} in 2.5 M H_2SO_4, the metal loading was 0.35 mg cm^{-2}.**

The cyclic voltammograms of the 1.5 Pt/Pd/C catalyst show that the surface is stabilised by the modification with Pt. There are some signs of a change in surface structure with cycling, as there is a decrease in the charge associated with the Pd hydride adsorption / desorption characteristics. It should be noted that the 1.5 Pt/Pd/C electrode has been subjected to 70 cycles in comparison to the 30 for the analysis of the Pd/C catalyst, demonstrating the enhanced stability of the modified catalysts.

3.4.2 Hydride Storage Properties

The extent of hydride formation of the Pd and 0.5 Pt/Pd/C catalysts was investigated by holding the electrode at a potential in the region of the β - hydride formation (but not in the hydrogen evolution region) until the current associated with this process had decayed to zero. Linear sweep voltammograms were then obtained over the hydride range and the experiments repeated for a range of sweep rates. Figure 16 shows the hydride storage voltammograms of Pd/C and the 0.5 Pt/Pd/C catalysts.

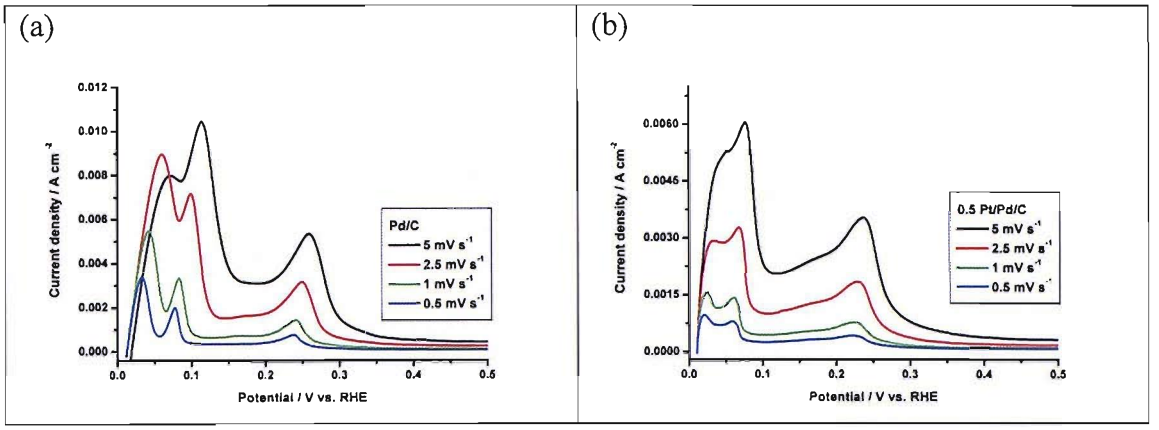

Figure 16 **Linear sweep voltammograms of (a) Pd/C and (b) 0.5 Pt/Pd/C. The metal loading was 0.35 mg cm^{-2}, the initial holding potential was 0.01 V vs. RHE, and the electrolyte was 2.5 M H_2SO_4.**

Work by Bartlett *et al.* [27, 28] on nano-architectured Pd films showed two distinct well resolved peaks for a similar experiment. Peaks around 0.05 V vs. RHE, corresponding to the oxidation of the β - hydride phase, and another around 0.2 V vs. RHE for the removal of adsorbed hydrogen, were found. Additional work by Rose *et al.* carried out on Pd/C detailed two broad peaks overlapping in the range from 0.05 to 0.4 V vs. RHE when a sweep rate of 10 mV s^{-1} was used. The data presented in figure 16 show that as the sweep rate is decreased it is possible to identify two peaks between 0.01 and 0.15 V vs. RHE, as well as the peak for removal of adsorbed hydrogen around 0.25 V vs. RHE. Work by Rose *et al.* [30, 31], looked at the extent of hydrogen storage within the Pd lattice using *in-situ* XAS and electrochemical methods. They found that the electrochemical methods suggested a larger amount of stored hydrogen compared to the XAS studies, and attributed this to adsorbed hydrogen, hydrogen which has spilled over onto the carbon support, or hydrogen trapped in the porous electrode structure. The secondary peak in the β - hydride phase region between 0.05 and 0.15 V vs. RHE is not noted in the other studies, and could be a result of hydrogen trapped in the porous electrode structure or on the carbon support. However, if either of these peaks were due to oxidation of stored hydrogen in the pores or on the support it would be expected to be small compared to the large amount of hydrogen that can be stored within the Pd lattice. Qualitatively, it can be seen that both the peaks in the β - hydride phase

region are of similar area, suggesting that this is not the case. At these potentials the Pd surface sites should have a layer of adsorbed hydrogen present, as the oxidation of adsorbed hydrogen occurs at higher potentials. Thus, it is valid to assume that any hydrogen oxidised at these potentials correlates to hydrogen trapped in the lattice. A more detailed figure of the voltammogram with slowest sweep rate for the Pd/C catalyst is shown below in figure 17.

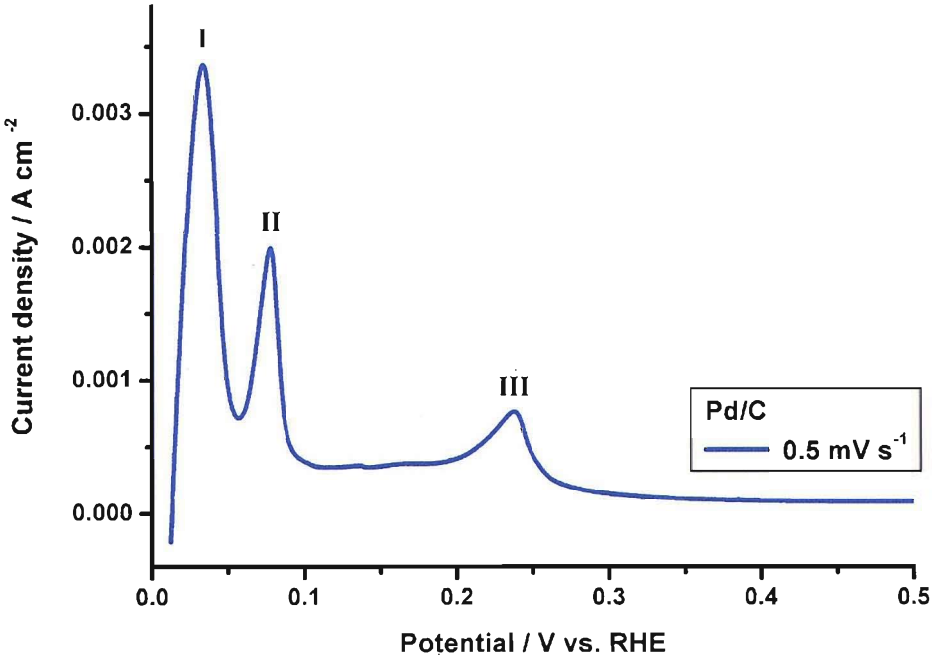

Figure 17 **Linear sweep voltammogram of Pd/C. The metal loading was 0.35 mg cm^{-2}, the initial holding potential was 0.01 V vs. RHE, and the electrolyte was 2.5 M H_2SO_4**

The ratio of peaks I and II detailed in figure 17 change with sweep rate. As the sweep rate is decreased the area of peak I becomes greater than peak II, and the separation between the two peaks increases. The changes observed in the peak ratio may be due to the relative kinetics of the processes. The oxidation giving rise to peak I may be sufficiently slow that at fast scan rates, the process occurring has not reached completion by the time process II begins. Thus, at fast scan rates the area peak II is greater than that of peak I.

It can also be seen that there are differences between the voltammograms observed for Pd/C and 0.5 Pt/Pd/C. However, it has proved difficult to acquire consistent data for different Pt/Pd/C samples and therefore any firm conclusions cannot be drawn.

3.5 EXAFS Analysis

EXAFS data were collected as BN pellets in atmospheres of air and H_2. The k^2 weighted EXAFS data along with the associated Fourier transform and the fitting parameters determined for the Pd/Pt/C catalysts are detailed below in figures 18 and 19 and tables 8 and 9.

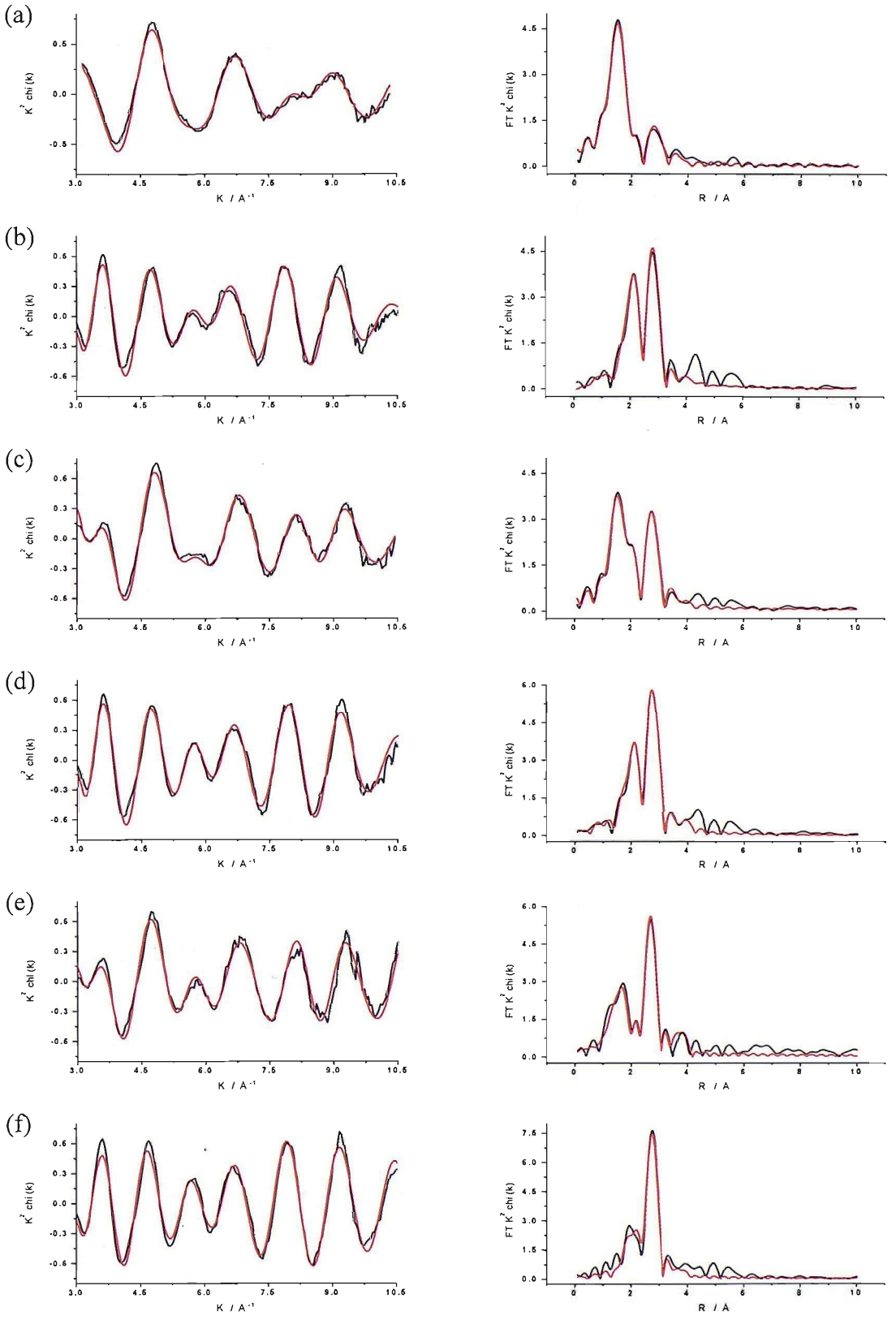

Figure 18 **Pd K edge (left) k^2 weighted experimental data and fit along with (right) the Fourier transform for 0.5 Pd/Pt/C acquired in air and H_2 (a & b), 1 Pd/Pt/C acquired in air and H_2 (c & d), and 1.5 Pd/Pt/C acquired in air and H_2 (e & f). Data (black line) and fit (red line).**

Table 8 **Structural parameters for Pd/Pt/C catalysts acquired in atmospheres of air and H_2 obtained by fitting the Pd K edge EXAFS data.**

Condition	**Pd/Pt/C - Calculated Parameters (Pd K edge)**					
0.5 Pd/Pt/C	**Shell**	***N***	***R* / Å**	**$2\sigma^2$ / $Å^2$**	***E_f* / eV**	**R_{exafs} / %**
In air	Pd-O	1.5 ± 0.0	2.003 ± 0.005	0.004 ± 0.001	- 1.0	17.3
	Pd-Pt	1.2 ± 0.2	2.751 ± 0.001	0.012 ± 0.005	± 0.7	
	Pd-Pd	0.7 ± 0.1	2.742 ± 0.007	0.009 ± 0.003		
	Pd-Pd	0.7 ± 0.3	3.92 ± 0.03	0.023 ± 0.003		
0.5 Pd/Pt/C	Pd-Pt	3.4 ± 0.2	2.770 ± 0.001	0.009 ± 0.002	-0.6	24.7
In H_2	Pd-Pd	2.0 ± 0.2	2.762 ± 0.007	0.009 ± 0.001	± 0.4	
	Pd-Pd	1.3 ± 0.6	3.85 ± 0.02	0.028 ± 0.012		
1 Pd/Pt/C	Pd-O	1.0 ± 0.1	1.980 ± 0.007	0.004 ± 0.001	-3.0	22.0
In air	Pd-Pt	2.3 ± 0.2	2.714 ± 0.009	0.013 ± 0.001	± 0.6	
	Pd-Pd	1.7 ± 0.1	2.707 ± 0.008	0.011 ± 0.001		
	Pd-Pd	0.9 ± 0.3	3.85 ± 0.02	0.017 ± 0.007		
1 Pd/Pt/C	Pd-Pt	3.0 ± 0.3	2.764 ± 0.009	0.012 ± 0.002	-0.1	20.4
In H_2	Pd-Pd	3.0 ± 0.2	2.765 ± 0.008	0.012 ± 0.002	± 0.4	
	Pd-Pd	1.5 ± 0.5	3.90 ± 0.02	0.021 ± 0.006		
1.5 Pd/Pt/C	Pd-O	0.8 ± 0.1	2.00 ± 0.05	0.004 ± 0.002	-0.6	25.6
In air	Pd-Pt	1.1 ± 0.4	2.749 ± 0.009	0.023 ± 0.011	± 0.6	
	Pd-Pd	2.7 ± 0.1	2.747 ± 0.005	0.012 ± 0.001		
	Pd-Pd	1.1 ± 0.3	3.90 ± 0.02	0.021 ± 0.006		
1.5 Pd/Pt/C	Pd-Pt	2.0 ± 0.2	2.77 ± 0.01	0.009 ± 0.002	-0.1 ±	23.1
In H_2	Pd-Pd	3.6 ± 0.2	2.783 ± 0.005	0.009 ± 0.001	0.4	
	Pd-Pd	0.6 ± 0.6	3.93 ± 0.03	0.018 ± 0.012		

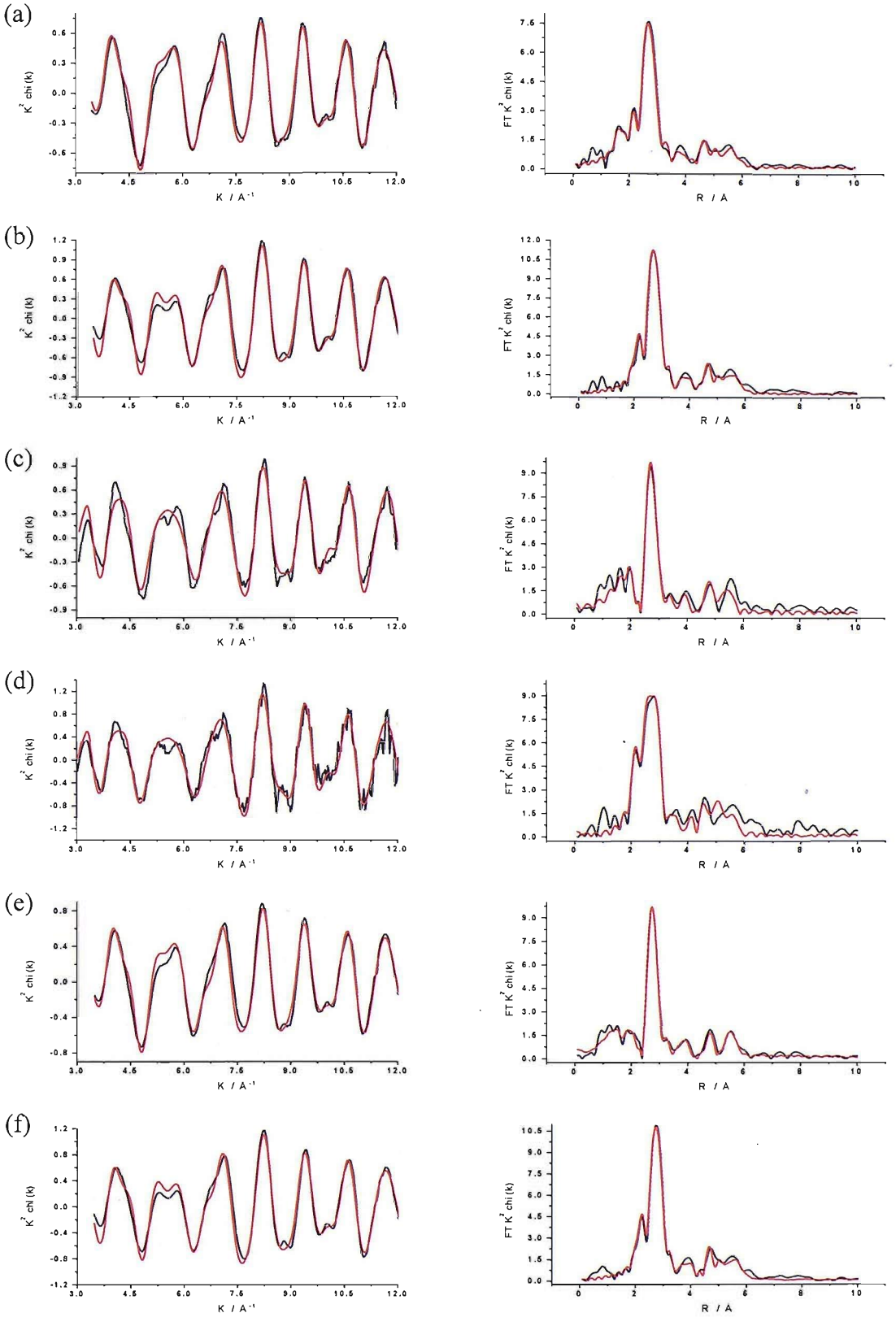

Figure 19 **Pt L_3 edge (left) k^2 weighted experimental data and fit along with (right) the Fourier transform for 0.5 Pd/Pt/C acquired in air and H_2 (a & b), 1 Pd/Pt/C acquired in air and H_2 (c & d), and 1.5 Pd/Pt/C acquired in air and H_2 (e & f). Data (black line) and fit (red line)**

Table 9 **Structural parameters for Pd/Pt/C catalysts acquired in atmospheres of air and H_2 obtained by fitting the Pt L_3 edge EXAFS data.**

Condition	Pd/Pt/C - Calculated Parameters (Pt L_3 edge)					
0.5 Pd/Pt/C	**Shell**	***N***	***R* / Å**	**$2\sigma^2$ / Å^2**	***E_f* / eV**	**R_{exafs} / %**
In air	Pt-O	1.1 ± 0.1	2.00 ± 0.01	0.014 ± 0.002	- 13.4	16.3
	Pt-Pt (un1)	5.7 ± 0.2	2.754 ± 0.003	0.011 ± 0.000	± 0.6	
	Pt-Pt	2.0 ± 0.5	3.90 ± 0.01	0.014 ± 0.002		
	Pt-Pt	4.1 ± 0.9	4.79 ± 0.01	0.010 ± 0.001		
	Pt-Pt-Pt (un1)	5.7 ± 0.2	5.522 ± 0.007	0.021 ± 0.002		
0.5 Pd/Pt/C	Pt-Pt (un1)	8.6 ± 0.4	2.757 ± 0.003	0.011 ± 0.000	-12.9	17.7
In H_2	Pt-Pd	0.7 ± 0.2	2.74 ± 0.02	0.014 ± 0.004	± 0.6	
	Pt-Pt	2.4 ± 0.8	3.90 ± 0.02	0.011 ± 0.002		
	Pt-Pt	6.7 ± 1.4	4.79 ± 0.01	0.012 ± 0.001		
	Pt-Pt-Pt (un1)	8.6 ± 0.4	5.548 ± 0.006	0.023 ± 0.002		
1 Pd/Pt/C	Pt-Pt (un1)	7.3 ± 0.3	2.750 ± 0.003	0.011 ± 0.001	-9.3	27.6
In air	Pt-Pd	0.5 ± 0.2	2.70 ± 0.02	0.011 ± 0.004	± 0.5	
	Pt-Pt	2.4 ± 0.8	3.88 ± 0.02	0.010 ± 0.003		
	Pt-Pt	6.7 ± 1.4	4.78 ± 0.01	0.009 ± 0.002		
	Pt-Pt-Pt (un1)	8.6 ± 0.4	5.43 ± 0.01	0.012 ± 0.002		
1 Pd/Pt/C	Pt-Pt (un1)	8.2 ± 0.5	2.761 ± 0.005	0.010 ± 0.001	-12.7	33.9
In H_2	Pt-Pd	0.5 ± 0.2	2.74 ± 0.03	0.006 ± 0.002	± 0.7	
	Pt-Pt	2.5 ± 1.3	3.89 ± 0.03	0.014 ± 0.006		
	Pt-Pt	6.7 ± 1.1	4.78 ± 0.02	0.010 ± 0.002		
	Pt-Pt-Pt (un1)	8.2 ± 0.5	5.45 ± 0.02	0.011 ± 0.003		

Table 9... **(continued) Structural parameters for Pd/Pt/C catalysts acquired in atmospheres of air and H_2 obtained by fitting the Pt L_3 edge EXAFS data.**

1.5 Pd/Pt/C In air	Pt-Pt (unl)	6.5 ± 0.2	2.757 ± 0.002	0.011 ± 0.001	-13.7 ± 0.5	17.6
	Pt-Pd	0.3 ± 0.1	2.73 ± 0.03	0.011 ± 0.005		
	Pt-Pt	2.2 ± 0.4	3.90 ± 0.01	0.012 ± 0.002		
	Pt-Pt	2.8 ± 0.4	4.798 ± 0.007	0.008 ± 0.001		
	Pt-Pt-Pt (unl)	6.5 ± 0.2	5.55 ± 0.01	0.022 ± 0.002		
1.5 Pd/Pt/C In H_2	Pt-Pt (unl)	8.3 ± 0.4	2.759 ± 0.003	0.011 ± 0.000	-12.2 ± 0.6	16.7
	Pt-Pd	0.6 ± 0.3	2.76 ± 0.03	0.008 ± 0.002		
	Pt-Pt	3.0 ± 0.8	3.91 ± 0.01	0.014 ± 0.002		
	Pt-Pt	4.6 ± 1.4	4.80 ± 0.01	0.009 ± 0.001		
	Pt-Pt-Pt (unl)	8.3 ± 0.4	5.541 ± 0.006	0.023 ± 0.002		

The Pd K edge data confirm the presence of 1st shell Pd-Pt neighbours at ~ 2.74 Å, and this is the primary indication of the success of the controlled surface modification. The Pd K edge data are also consistent with the Pd being present at the surface of the particle, as the data in air show the presence of Pd-O neighbours. As the monolayer fraction of Pd is increased from 0.5 through to 1.5 the number of Pd-O 1st shell neighbours decreases from 1.5 to 1.0 to 0.8. Assuming that the Pd is evenly distributed on the Pt surface, as the monolayer fraction of Pd is increased the available amount of Pd surface decreases and thus a reduction in the average Pd-O contribution is expected. Although this trend is consistent with the idea of an even monolayer on Pt, it is also in agreement with Pd clustering on the Pt surface as it is deposited. Figure 20 illustrates how the models of clustering and an evenly deposited Pd monolayer can both reduce the average Pd surface area, and thus the number of Pd-O neighbours.

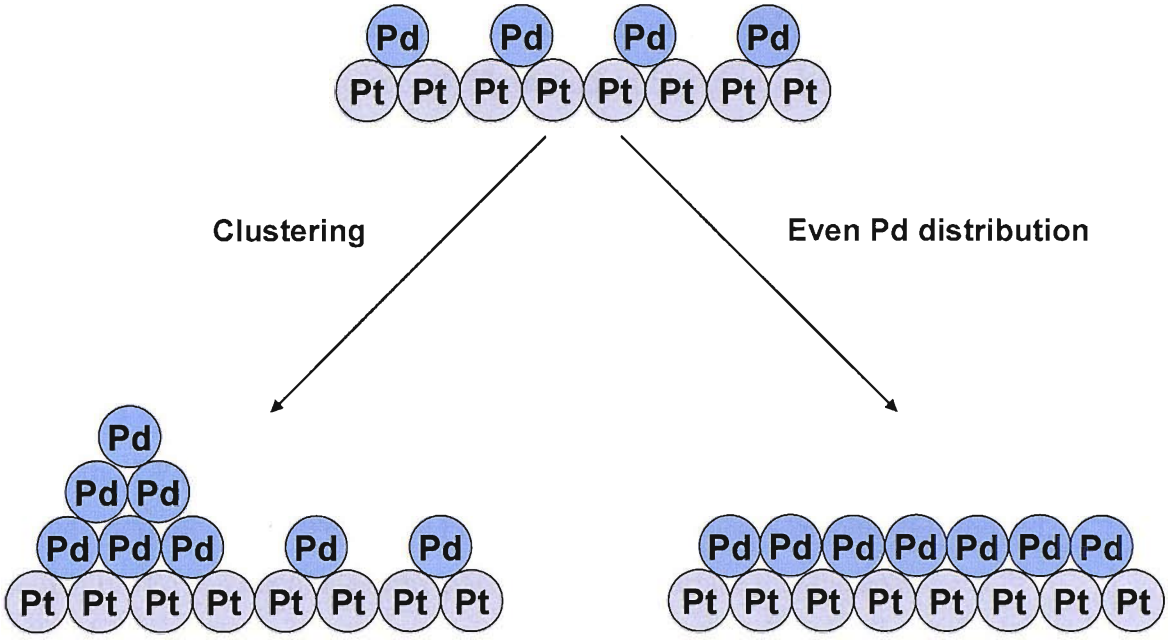

Figure 20 **Schematic diagram to illustrate how Pd can cluster on a Pt surface or form an evenly distributed monolayer**

The metal neighbour contributions were assessed by examining the data obtained in H_2 as this facilitated removal of the oxide and more accurately represents the maximum number of metal neighbours possible. As the monolayer fraction of Pd is increased the number of Pd-Pd neighbours increases from 2.0 to 3.0 to 3.6. These values are consistent with Pd being evenly distributed on the Pt surface and Pd clustering as it is deposited. The amount of Pd-Pt interactions decreases from 3.4 to 3.0 to 2.0 for the 0.5,1, and 1.5 Pd/Pt/C catalysts, respectively. Within the error estimates the 0.5 and 1 Pd/Pt/C catalysts have the same number of Pd-Pt contributions, which is consistent with the model of Pd evenly distributed over the Pt surface. As the Pd loading is increased above the monolayer level the amount of Pd-Pt neighbours decreases. The addition of Pd in excess of a monolayer results in Pd atoms with no immediate Pt neighbours and the average Pd-Pt coordination number therefore decreases. The data agree with the model that Pd is being deposited evenly over the Pt surface and not with Pd clustering. A much reduced number of Pd-Pt interactions would be expected if the Pd was clustering as it was deposited.

The contraction of the Pd-Pt distance provides evidence that the Pd forms a pseudomorphic monolayer on the Pt surface. Only the bond distances for the data

obtained in air will be considered due to the formation of Pd-hydride phases which may occur in the presence of H_2, which will be discussed below. For the 0.5 and 1.5 Pd/Pt/C catalysts in air the Pt-Pd bond distances are 2.751 and 2.749 Å, respectively. The 1 Pd/Pt/C displays a radial contraction from ~ 2.75 to 2.71 Å. Renouprez *et al.* [32] have looked at the EXAFS of Pd-Pt aggregates and also demonstrated a 0.04 Å contraction for a thin film of Pd on Pt. Another confirmation of this is the contraction of the Pd-Pd distance, which is 2.742 and 2.747 Å for the 0.5 and 1.5 Pd/Pt/C catalysts, respectively, but decreases to 2.707 Å for the 1 Pd/Pt/C catalyst in air. These contractions are confirmation of the pseudomorphic monolayer as the Pd-Pd and Pd-Pt distances become constrained, so that the Pd can adopt the same positions on the surface that the analogous Pt atoms in the next layer would occupy.

When the data was acquired in H_2 the Pd-Pd and Pd-Pt distances show a considerable increase which can be attributed to the absorption of hydrogen into the Pt lattice. Looking at the Pd-Pd distance the value increases from 2.742 → 2.762 Å, 2.707 → 2.765 Å, and 2.747 → 2.783 Å for the 0.5, 1, and 1.5 Pd/Pt/C catalysts, respectively. A near identical increase is mirrored for the Pd-Pt distance. Rose *et al.* [30, 31] looked at the Pd-Pd distance in an *in-situ* electrochemical environment and noted that the Pd-Pd distance increases from 2.73 to 2.82 Å when the Pd lattice is saturated with H_2.

The Pt L_3 edge data are also in agreement with the Pd being deposited solely onto the Pt surface. This is illustrated by the small contribution of Pt-Pd neighbours in the first shell. As the Pd is exclusively at the surface, the Pt in the interior of the particle has no Pd neighbours and, thus, the average number of Pt-Pd interactions is minimal. For the 0.5 Pd/Pt/C catalyst the average contribution is sufficiently small that Pt-Pd neighbours cannot be detected when the EXAFS was collected in an atmosphere of air. However, this is not the case for the EXAFS data of the 0.5 Pt/Pd/C catalyst acquired in an atmosphere of H_2 as 0.7 Pt-Pd neighbours are reported. When the environment was switched from air to H_2 the surface oxide species are reduced and the Pd at the surface can become incorporated into the particle and there are more Pt-Pd interactions. Within the

error limits the number of Pt-Pd neighbours does not vary for the 0.5, 1, and 1.5 Pd/Pt/C catalysts. The number of Pt-Pd neighbours in H_2 for the 0.5, 1, and 1.5 Pd/Pt/C catalysts are 0.7, 0.5, and 0.6 respectively. These small coordination numbers are much less than the Pd-Pt coordination number seen from the Pd K edge, which supports the theory that the Pd is found on the exterior of the particle.

After the addition of 1 monolayer of Pd to the Pt surface it is no longer possible to fit any Pt-O contributions (in air) at the Pt L_3 edge, which is confirmation that the Pd is completely saturating the Pt surface. The Pt-Pd bond distance also changes on switching the gas environment from air to hydrogen. For the 1 and 1.5 Pd/Pt/C catalysts the Pt-Pd distance increases from 2.697 → 2.742 Å, and 2.730 → 2.760 Å respectively. Unlike data collected at the Pd edge, the errors associated with this bond distance are much larger, and thus the distances are not significantly different. It is therefore not possible to confirm that the Pt-Pd distance is increasing on exposure to hydrogen.

EXAFS data, along with the associated Fourier transform and the fitting parameters determined for the Pt/Pd/C catalysts, are detailed below in figures 21 and 22 and tables 10 and 11.

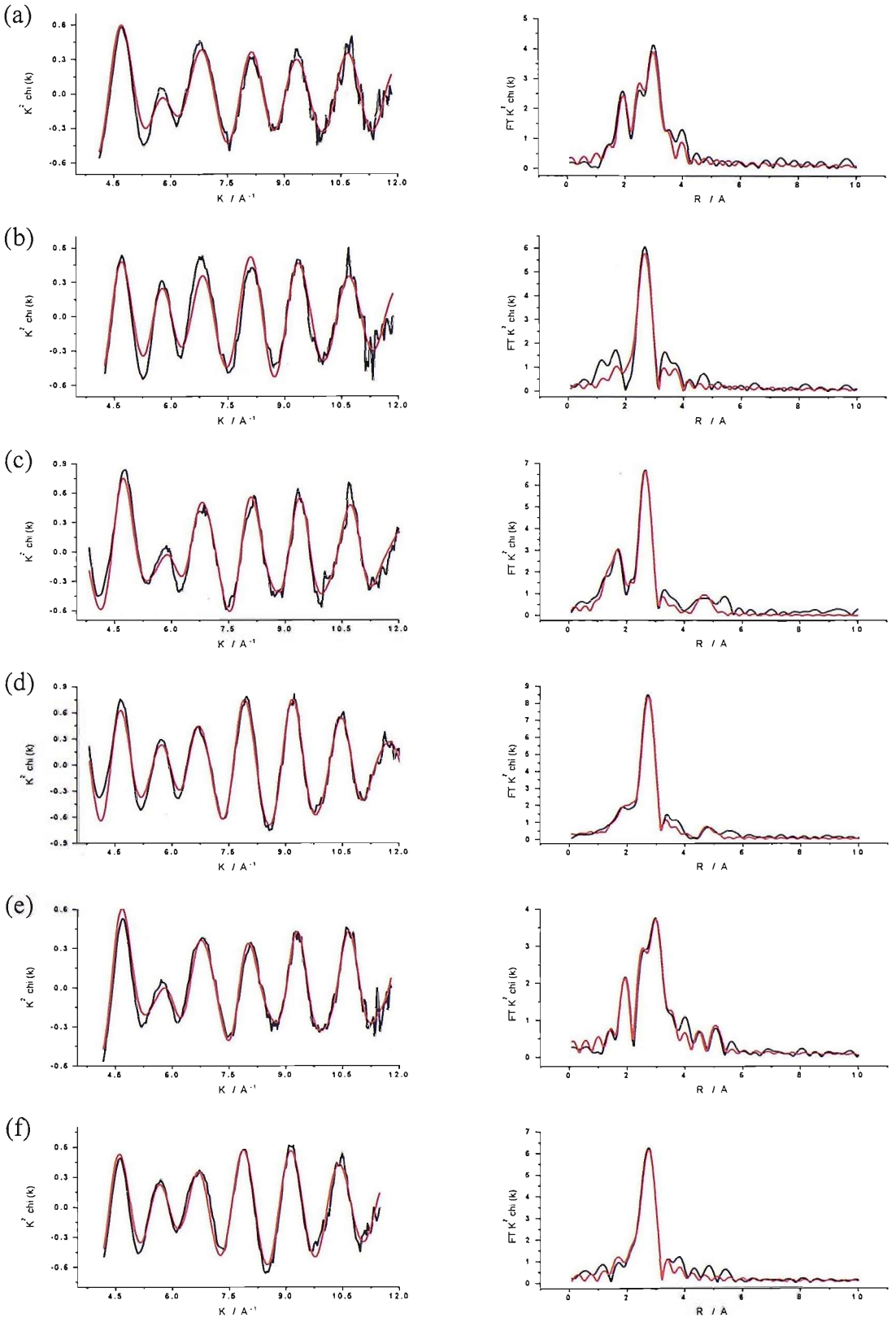

Figure 21 **Pd K edge (left) k^2 weighted experimental data and fit along with (right) the Fourier transform for 0.5 Pt/Pd/C acquired in air and H_2 (a & b), 1 Pt/Pd/C acquired in air and H_2 (c & d), and 1.5 Pt/Pd/C acquired in air and H_2 (e & f). Data (black line) and fit (red line).**

Table 10 **Structural parameters for Pt/Pd/C catalysts acquired in atmospheres of air and H_2 obtained by fitting the Pd K edge EXAFS data.**

Condition	**Pt/Pd/C - Calculated Parameters (Pd K edge)**					
0.5 Pt/Pd/C	**Shell**	***N***	***R* / Å**	**$2\sigma^2$ / $Å^2$**	**E_f / eV**	**R_{exafs} / %**
In air	Pd-O	1.1 ± 0.1	2.03 ± 0.01	0.009 ± 0.002	- 1.5	27.1
	Pd-Pd	2.3 ± 0.1	2.737 ± 0.007	0.012 ± 0.001	± 0.9	
	Pd-Pt	0.4 ± 0.2	2.76 ± 0.05	0.015 ± 0.007		
	Pd-Pd	0.5 ± 0.3	3.87 ± 0.04	0.014 ± 0.009		
0.5 Pt/Pd/C	Pd-Pd	3.5 ± 0.4	2.732 ± 0.009	0.012 ± 0.001	-2.2 ±	32.2
In H_2	Pd-Pt	0.7 ± 0.2	2.73 ± 0.04	0.013 ± 0.008	1.1	
	Pd-Pd	0.7 ± 0.3	3.85 ± 0.09	0.016 ± 0.010		
1 Pt/Pd/C	Pd-O	1.0 ± 0.1	2.02 ± 0.01	0.009 ± 0.003	-1.0	26.6
In air	Pd-Pd	2.8 ± 0.2	2.726 ± 0.007	0.011 ± 0.001	± 0.9	
	Pd-Pt	1.0 ± 0.1	2.70 ± 0.02	0.008 ± 0.004		
	Pd-Pd	2.0 ± 0.7	4.76 ± 0.02	0.010 ± 0.003		
1 Pt/Pd/C	Pd-Pd	3.8 ± 0.2	2.783 ± 0.005	0.011 ± 0.001	-0.5	19.9
In H_2	Pd-Pt	1.4 ± 0.1	2.76 ± 0.02	0.006 ± 0.002	± 0.6	
	Pd-Pd	1.4 ± 0.7	4.85 ± 0.03	0.010 ± 0.004		
1.5 Pt/Pd/C	Pd-O	0.7 ± 0.1	2.01 ± 0.01	0.005 ± 0.002	-4.7	22.6
In air	Pd-Pd	2.4 ± 0.1	2.747 ± 0.006	0.011 ± 0.001	± 0.6	
	Pd-Pt	0.6 ± 0.2	2.78 ± 0.03	0.009 ± 0.004		
	Pd-Pd	1.7 ± 0.5	4.80 ± 0.02	0.010 ± 0.003		
1.5 Pt/Pd/C	Pd-Pd	3.4 ± 0.2	2.792 ± 0.006	0.011 ± 0.001	-5.8 ±	23.5
In H_2	Pd-Pt	1.2 ± 0.3	2.79 ± 0.02	0.009 ± 0.004	0.7	

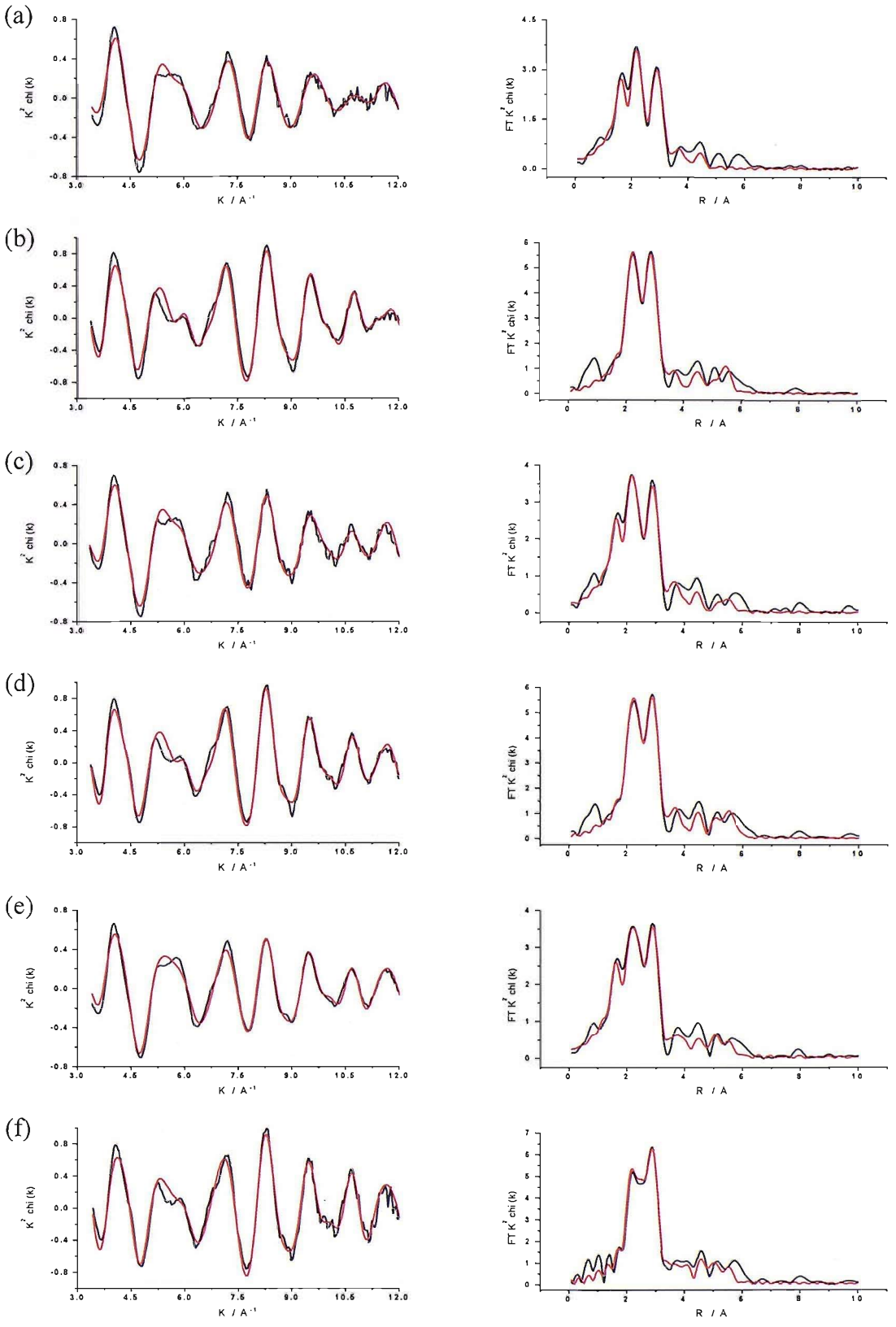

Figure 22 **Pt L_3 edge (left) k^2 weighted experimental data and fit along with (right) the Fourier transform for 0.5 Pt/Pd/C acquired in air and H_2 (a & b), 1 Pt/Pd/C acquired in air and H_2 (c & d), and 1.5 Pt/Pd/C acquired in air and H_2 (e & f). Data (black line) and fit (red line).**

Table 11 **Structural parameters for Pt/Pd/C catalysts acquired in atmospheres of air and H_2 obtained by fitting the Pt L_3 edge EXAFS data.**

Condition	Pt/Pd/C - Calculated Parameters (Pt L_3 edge)					
0.5 Pt/Pd/C	**Shell**	***N***	***R* / Å**	**$2\sigma^2$ / Å^2**	***E_f* / eV**	***R_{exafs}* / %**
In air	Pt-O	0.8 ± 0.1	1.99 ± 0.01	0.011 ± 0.003	- 9.8	24.0
	Pt-Pt	3.6 ± 0.2	2.741 ± 0.006	0.012 ± 0.001	± 0.6	
	Pt-Pd	1.9 ± 0.1	2.726 ± 0.007	0.011 ± 0.001		
	Pt-Pt	1.4 ± 0.4	3.88 ± 0.02	0.013 ± 0.004		
	Pt-Pd	0.7 ± 0.3	4.47 ± 0.03	0.014 ± 0.008		
0.5 Pt/Pd/C	Pt-Pt	5.1 ± 0.2	2.755 ± 0.005	0.011 ± 0.001	-9.8	20.1
In H_2	Pt-Pd	2.9 ± 0.2	2.758 ± 0.005	0.011 ± 0.001	± 0.5	
	Pt-Pt	2.1 ± 0.5	3.89 ± 0.01	0.011 ± 0.003		
	Pt-Pd	1.5 ± 0.4	4.50 ± 0.02	0.013 ± 0.004		
	Pt-Pd	3.1 ± 0.7	5.48 ± 0.01	0.010 ± 0.002		
1 Pt/Pd/C	Pt-O	0.7 ± 0.1	1.98 ± 0.01	0.012 ± 0.003	-10.1	22.7
In air	Pt-Pt	4.2 ± 0.2	2.747 ± 0.006	0.012 ± 0.001	± 0.6	
	Pt-Pd	1.6 ± 0.1	2.736 ± 0.007	0.012 ± 0.001		
	Pt-Pt	1.8 ± 0.4	3.90 ± 0.01	0.013 ± 0.003		
	Pt-Pd	0.9 ± 0.3	4.50 ± 0.02	0.015 ± 0.006		
	Pt-Pt	2.3 ± 0.9	5.43 ± 0.02	0.014 ± 0.006		
1 Pt/Pd/C	Pt-Pt	5.7 ± 0.2	2.759 ± 0.005	0.011 ± 0.001	-10.0	20.0
In H_2	Pt-Pd	2.6 ± 0.2	2.762 ± 0.006	0.011 ± 0.001	± 0.5	
	Pt-Pt	2.6 ± 0.5	3.90 ± 0.01	0.012 ± 0.002		
	Pt-Pd	1.7 ± 1.4	4.51 ± 0.01	0.013 ± 0.004		
	Pt-Pt	4.6 ± 1.9	5.44 ± 0.03	0.012 ± 0.007		
	Pt-Pd	2.6 ± 1.3	5.46 ± 0.03	0.009 ± 0.006		

Table 11... **(continued) Structural parameters for Pt/Pd/C catalysts acquired in atmospheres of air and H_2 by fitting the Pt L_3 edge EXAFS data.**

1.5 Pt/Pd/C In air	Pt-O	0.8 ± 0.1	1.99 ± 0.01	0.011 ± 0.002	-10.3 ± 0.5	17.1
	Pt-Pt	4.4 ± 0.2	2.747 ± 0.005	0.012 ± 0.001		
	Pt-Pd	1.4 ± 0.1	2.737 ± 0.007	0.012 ± 0.001		
	Pt-Pt	1.3 ± 0.3	3.89 ± 0.01	0.013 ± 0.003		
	Pt-Pt	2.2 ± 0.5	4.75 ± 0.01	0.012 ± 0.003		
	Pt-Pt	3.0 ± 0.7	5.40 ± 0.01	0.013 ± 0.004		
1.5 Pt/Pd/C In H_2	Pt-Pt	6.5 ± 0.3	2.756 ± 0.004	0.011 ± 0.001	-10.2 ± 0.5	23.7
	Pt-Pd	2.0 ± 0.2	2.76 ± 0.03	0.011 ± 0.001		
	Pt-Pt	2.0 ± 0.5	3.89 ± 0.01	0.011 ± 0.003		
	Pt-Pt	3.8 ± 0.9	4.76 ± 0.01	0.012 ± 0.003		
	Pt-Pt	4.8 ± 1.2	5.40 ± 0.01	0.013 ± 0.003		

Analysis of the 1st shell coordination numbers allows several conclusions to be drawn. The Pd-K edge analysis of the Pt/Pd/C samples in air demonstrates that it is possible to fit a Pd-O coordination shell for each of the catalysts. This shows that there are still Pd sites at the surface as suggested by the CO stripping voltammetry. The Pt L_3 edge analysis shows that all the Pt/Pd/C samples also have contributions resulting from Pt-O interactions. Thus, the surface has a mixed composition of both Pt and Pd, which is in agreement with the CVs and TEM EDX data. The average number of Pd-O neighbours decreases from 1.1 to 1.0 to 0.7 for the 0.5, 1, and 1.5 Pt/Pd/C catalysts, respectively. When taking into account the error in these values there is only a marginal difference observed and it is hard to confirm that increasing the Pt loading decreases the available Pd surface sites. This could be due to agglomeration of Pt on the surface. After Pt is deposited onto the surface of the catalyst, it represents an alternative reaction site. Subsequent Pt atoms could be deposited around these alternative Pt sites creating Pt clusters. However, this model of the deposition process does not agree with the number of Pt-O neighbours. The 0.5, 1, and 1.5 Pt/Pd/C catalysts have 0.8, 0.7, and 0.8 Pt-O neighbours, respectively. It would be expected that the average Pt-O contribution would decrease, with increasing the Pt loading, if

the Pt was clustering on deposition. Looking at the fitting parameters of the 1 Pt/Pd/C sample in H_2, at the Pt L_3 edge there are 2.6 1st shell Pd neighbours, and at the Pd K edge there are 1.4 1st shell Pt neighbours. If there were any Pt agglomeration on the surface of the Pd/C catalyst then there should be limited amounts of Pt-Pd and Pd-Pt interactions, which is not the case. The TEM EDX data have shown there are small unmodified particles of Pd, which will give rise to a Pd-O contribution. As EXAFS is an averaging technique it makes it difficult to accurately describe the local structure of the catalysts for such a complex arrangement as is apparent for the Pt/Pd/C catalysts.

The Pt L_3 edge data show that the 1st shell has a greater proportion of Pt neighbours than Pd with the inverse also being found for the Pd K edge. This shows that the catalyst is not a PtPd solid solution, and there are regions rich in Pt and regions rich in Pd. Norskov et al [17] have reported that in a PtPd system where Pd is the host Pt has a positive segregation energy, and prefers to be in the interior of the host. For a system where Pt is the host and Pd is the impurity there is no segregation energy driver for the Pd to stay at the surface or in the interior. These segregation properties could explain the coordination numbers being observed. The Pt may react at the surface and then move towards the interior, leaving behind a surface with a mixture of Pt and Pd. The segregation energy towards the centre is only small so it is expected that some Pt remains at the surface. Underneath this surface there will be a layer predominately consisting of Pt, and a core predominantly consisting of Pd. This theory is in agreement with the 1st shell coordination numbers observed. Subsequent shells have been fitted, and the error values generated are reasonable. However, in reality either Pt or Pd could have been fitted in some of these additional shells, so it is hard to use these values to deduce the structural composition of the catalysts.

The EXAFS data suggest that the presence of Pt may affect the hydride storage properties of the Pt/Pd/C catalysts. For the 0.5 Pt/Pd/C catalyst the Pd-Pd distance does not increase on exposure to hydrogen, the value changes from 2.737 to 2.732 Å, which taking into account the error limits can be assumed to be the same value. The 1 and 1.5 Pt/Pd/C catalysts have a Pd-Pd distances which

increase from 2.726 to 2.783 Å, and 2.747 to 2.792 Å on exposure to hydrogen, respectively. This increase in Pd-Pd distance suggests that the presence of Pt aids the storage of hydrogen in the Pd lattice as increased levels of Pt correlate to an increased Pd-Pd distance.

3.6 Mini Cell Testing

One of the objectives of depositing Pt onto a Pd core is to reduce the required Pt loading whilst retaining the same activity of the catalyst. It is imperative in this situation to be able to present the data as mass activities. The deficiencies of the RDE method in accurately predicting the loading placed on the electrode surface leads to large errors in the estimation of mass activities. Thus, the mini cell testing environment has been chosen as it offers a more accurate means of mass activity determination. The Pd/Pt/C catalysts have not been assessed towards the ORR due to the instability encountered on cycling, highlighted in section 3.4. The Pt/Pd/C catalysts have been tested according to the procedure described in chapter 2, section 3.4.

The mini cell was operated under high reactant stoichiometries with flows of H_2 and O_2 of 60 cm^3 min^{-1} for the anode and cathode, respectively. The catalyst loading used was 0.4 mg M cm^{-2} (M = Pt and Pd) for both the anode and cathode. In each case the anode was a 40 wt % Pt/C standard. The cathode loading was set relative to the entire metal contribution rather than just Pt to reduce thickness effects. Current interrupt measurements were performed to take into account the effects of cell resistance. The potentials reported in the polarisation curves and Tafel plots are the iR corrected values. Figures 23 to 26 show the polarisation curves and the associated Tafel plots for the Pt/Pd/C catalysts normalised to the available metal area (as discussed in chapter 2, section 3.2.4) and the mass of Pt. Table 12 details the electrochemical properties of the Pt/Pd/C catalysts.

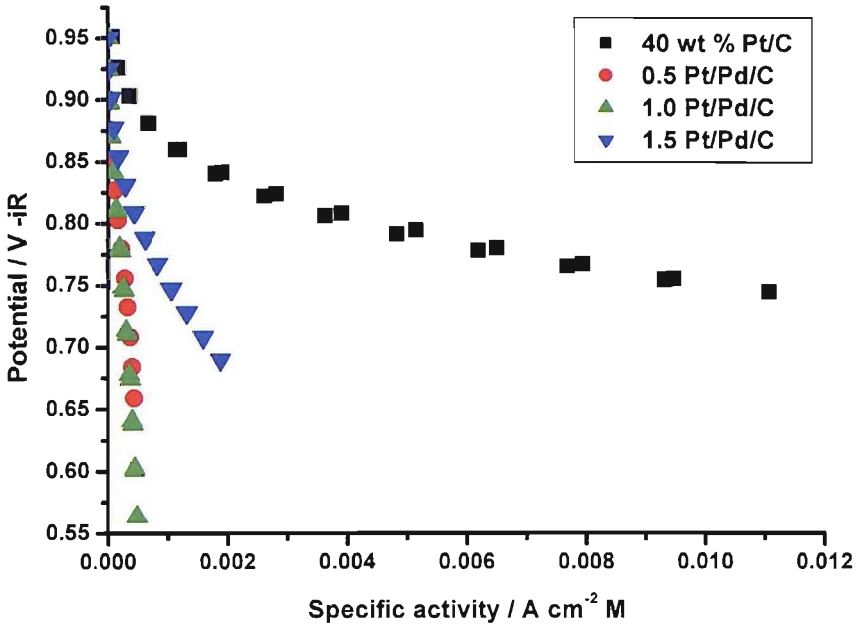

Figure 23 iR corrected polarisation curves for the Pt/Pd/C catalysts. The current has been normalised to the available metal area. A 40 wt% Pt/C standard has been included for comparison.

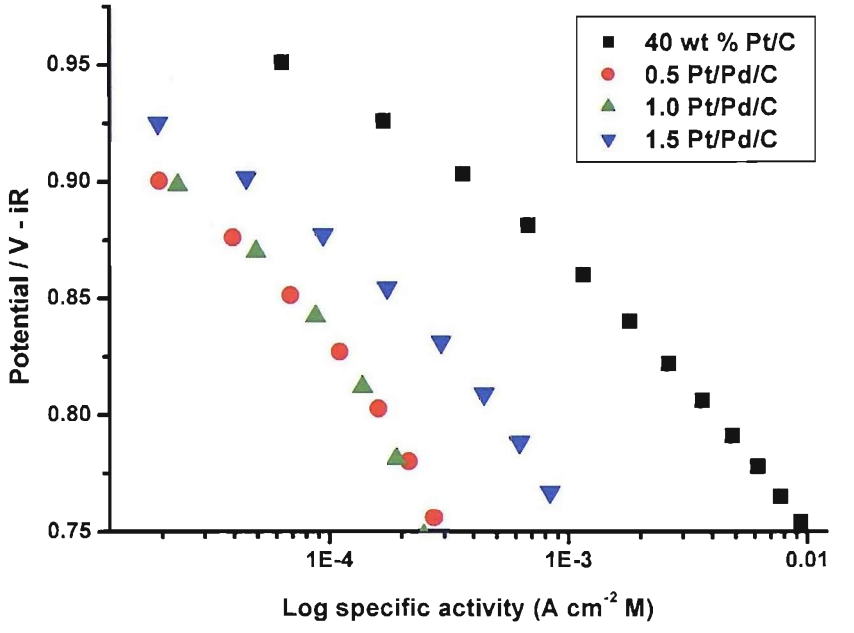

Figure 24 iR corrected Tafel plots for the Pt/Pd/C catalysts, corresponding to the data in figure 23. The current has been normalised to the available metal area. A 40 wt% Pt/C standard has been included for comparison.

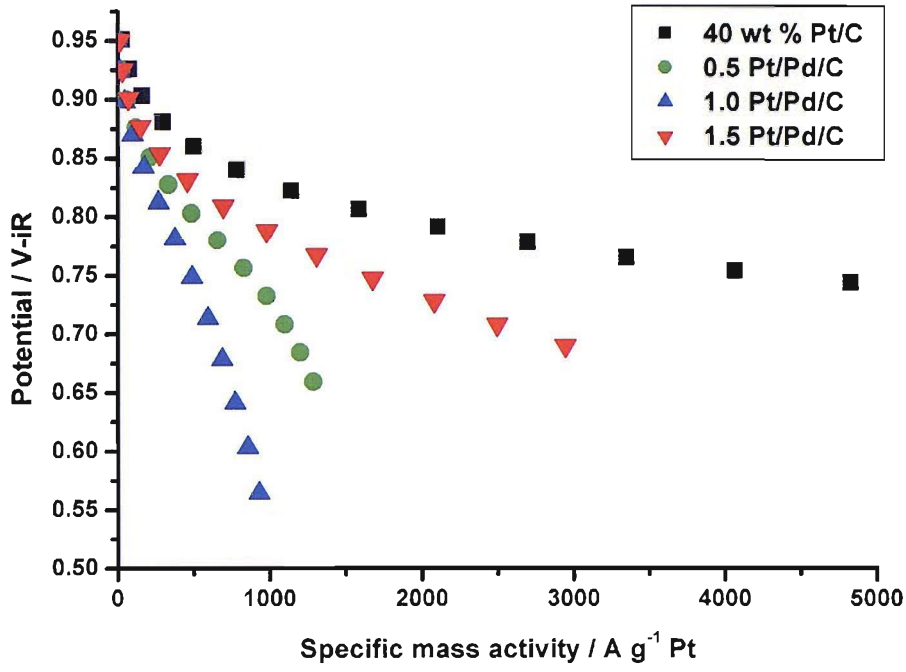

Figure 25 iR corrected polarisation curves for the Pt/Pd/C catalysts. The current has been normalised to the mass of Pt. A 40 wt% Pt/C standard has been included for comparison.

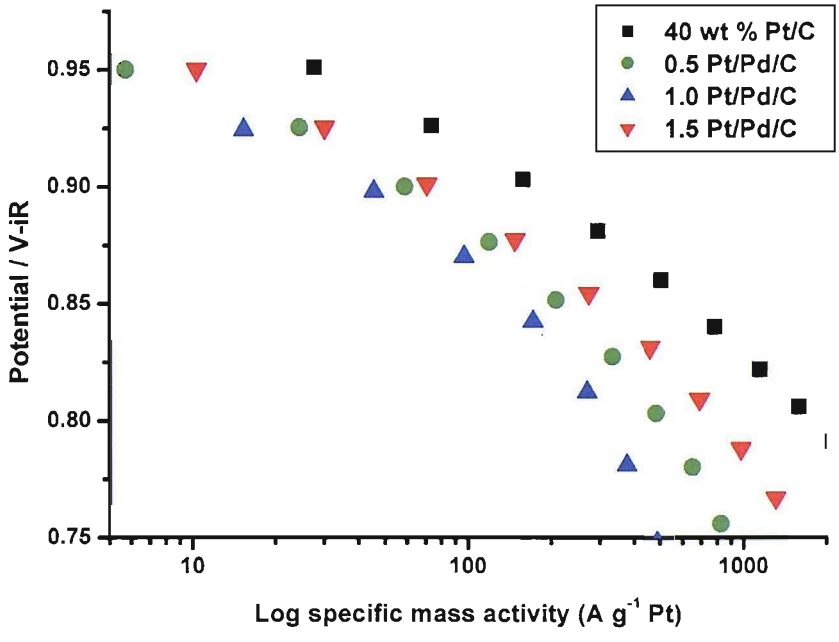

Figure 26 iR corrected Tafel plots for the Pt/Pd/C catalysts. Corresponding to the data in figure 24. The current has been normalised to the mass of Pt. A 40 wt% Pt/C standard has been included for comparison.

Table 12 **Electrochemical and electrokinetic properties of Pt/Pd/C catalysts, the parameters of the 40 wt % Pt/C standard is included to facilitate a comparison.**

Catalyst	M loading / mg cm^{-2}	O.C. / V vs. SHE	Specific activity at 0.9 V / $\mu A\ cm^{-2}$ M	Mass activity at 0.9 V / mA g^{-1} Pt	Tafel Slope / mV $decade^{-1}$
40 wt% Pt/C	0.40	0.972	393	175	72
0.5 Pt/Pd/C	0.42	0.949	19	58	62
1.0 Pt/Pd/C	0.40	0.936	21	41	77
1.5 Pt/Pd/C	0.41	0.966	46	72	67

The specific activities of the Pt/Pd/C catalysts are considerably smaller than those of the 40 wt % Pt/C standard. The 1.5 Pt/Pd/C catalyst is the most active of the series and has a specific activity of 46 $\mu A\ cm^{-2}$ M, compared to 393 $\mu A\ cm^{-2}$ M for the 40 wt % Pt/C standard. The TEM EDX analysis has shown the presence of unmodified Pd particles, with the EXAFS and cyclic voltammetry investigations also identifying that the surface of the catalysts consists of both Pt and Pd. Thus, the normalised surface takes into account both the Pt and Pd surface area. Pd has a much poorer performance towards the ORR than Pt and as this contribution is taken into consideration for the specific activity determination, a much reduced specific activity is expected. The specific activities of the Pt/Pd/C catalysts show that the 1.5 Pt/Pd/C catalyst is considerably more active than the 0.5 and 1 Pt/Pd/C catalysts, which have specific activities of 19 and 21 $\mu A\ cm^{-2}$ M, respectively. The EXAFS and cyclic voltammetry investigations suggest that the average surface bears close resemblance to the 1 Pt/Pd/C catalyst, so the difference in specific activity is unlikely to be an effect of decreased Pd at the surface. The TEM EDX data confirms that there are some unmodified small Pd particles. If these small particles remain unmodified throughout the series of Pt/Pd/C catalysts the average surface composition may appear the same. The increased activity of the 1.5 Pt/Pd/C catalyst may be associated with the formation of Pd particles with a

complete overlayer of Pt, which benefit from the increased intrinsic performance of these systems as reported in the literature [7, 10].

The specific mass activities of the Pt/Pd/C catalysts are also less than the standard 40 wt% Pt/C catalyst. The 1.5 Pt/Pd/C catalyst is again the most active from the series and has a specific mass activity of 72 mA g^{-1} Pt compared to 175 mA g^{-1} Pt for the 40 wt % Pt/C standard. These mass activities are normalised to the Pt loading and this negates any contribution towards the ORR from the Pd present in the catalyst. This may explain why the 0.5 Pt/Pd/C catalysts has a greater mass activity than the 1 Pt/Pd/C catalyst of 58 mA g^{-1} Pt compared to 41 mA g^{-1} Pt. It is also reasonable to assume that the differences observed between these two catalysts are comparable to the error associated with the experiment. The small Pt mass activities reported are disappointing as large enhancements for Pt monolayers on Pd have been reported [7, 10]. The particle size of the catalysts may contribute towards this. Kinoshita has shown [33] that particles below 3 nm do not have the required number of Pt 100 and 111 facets and have a considerable drop in performance. The particle size distribution of all the Pt/Pd/C catalysts (figure 2) have a significant amount of particles around the 2 nm mark and these may contribute to the small mass activities observed. The small particle size of the Pd catalyst also means that that the proportion of bulk to surface Pd is reasonably small, with relatively large amount of Pt required for a complete monolayer coverage. Thus, the Pt loading is not significantly reduced, with the 1.5 Pt/Pd/C catalyst consisting of 18.3 wt % Pt. It is proposed that a true Pt mass advantage would be achieved if the modifications were performed on a much larger Pd core.

5 Conclusions

The results presented in this chapter suggest that the controlled surface modification procedure has successfully been employed to prepare Pd/C and Pt/C catalysts modified with Pt and Pd, respectively. For the Pd/Pt/C catalysts the XRD analysis shows no signs of PdPt alloy formation, whereas the TEM EDX, EXAFS, and cyclic voltammetry investigations suggest that the surface is rich in Pd. The EXAFS analysis unambiguously confirms that the Pd is exclusively at the surface. Despite the success of the preparation method the cyclic voltammograms illustrated that the Pd/Pt/C catalysts were unstable in the electrochemical environment. The surface properties of the catalyst changed, most likely as a result of dissolution of Pd. However, the cyclic voltammograms also show evidence of Pd-hydride formation after the surface loses its Pd characteristics. It appears that the change in characteristics that are observed cannot solely be explained by the dissolution of surface Pd and the situation is far more complex. Regardless of the origin of the instability observed, it was decided that as the surface properties changed so readily it would be hard to accurately relate the structure to the activity of the catalyst and as such the catalysts were not tested towards the ORR in the mini cell. Also, with regards to improved specific Pt mass activities, the results indicate that there would be little promise in the Pd/Pt/C system.

The results suggest that the controlled surface modification procedure has been successful for the Pt/Pd/C catalysts. The TEM EDX analysis shows that the Pt is found on the exterior of the particle with small particles of Pd appearing in isolation on the support. This is in agreement with the cyclic voltammograms and EXAFS analysis, which show that the surface is a mixture of both Pt and Pd. The EXAFS analysis highlights that the local structures around Pt and Pd are Pt and Pd rich, respectively. This evidence is consistent with there being some Pt and Pd segregation. The XRD analysis shows that each Pt/Pd/C catalyst is formed entirely of poorly crystalline PtPd cubic phase. The XRD analysis failed to show any evidence of PtPd phase formation for the Pd/Pt/C catalyst, which is consistent with the Pd being exclusively at the surface and the majority of the

sample being bulk Pt. The XRD data therefore suggests that there is an improved mixing of the Pt and Pd in the Pt/Pd/C system compared to that of Pd/Pt/C. The EXAFS and cyclic voltammograms are consistent with a catalyst structure which has a surface consisting of a mixture of Pt and Pd, a Pt rich underlayer, and a Pd rich core. Therefore it is not possible to confirm with any certainty the structure of the Pt/Pd/C catalysts.

The specific and mass activities of the Pt/Pd/C catalysts towards the ORR were found to be very poor compared to the 40 wt % Pt/C standard. As the surface is a mixture of both Pt and Pd, it was expected that the specific activity observed would be reduced in comparison to the Pt standard. The poor mass activities observed can be attributed to the small particle size of the Pd/C catalyst, requiring a large amount of Pt to be added to the surface. It is believed that improved mass activities would be observed if larger Pd particles were used for the controlled surface modification procedure.

6 References

1. Gasteiger, H.A., S.S. Kocha, B. Sompalli, and F.T. Wagner, Appl. Catal. B-Environ., 2005. **56**(1-2): p. 9.
2. Sasaki, K., Y. Mo, J.X. Wang, M. Balasubramanian, F. Uribe, J. McBreen, and R.R. Adzic, Electrochim. Acta, 2003. **48**(25-26): p. 3841.
3. Brankovic, S.R., J. McBreen, and R.R. Adzic, Surf. Sci., 2001. **479**(1-3): p. L363.
4. Brankovic, S.R., J.X. Wang, and R.R. Adzic, Surf. Sci., 2001. **474**(1-3): p. L173.
5. Micheaud, C., P. Marecot, M. Guerin, and J. Barbier, Appl. Catal. A-Gen., 1998. **171**: p. 229.
6. Dossi, C., A. Pozzi, S. Recchia, A. Fusi, R. Psaro, and V. Dal Santo, J. Mol. Catal. A-Chem., 2003. **204**: p. 465.
7. Zhang, J., Y. Mo, M.B. Vukmirovic, R. Klie, K. Sasaki, and R.R. Adzic, J. Phys. Chem. B, 2004. **108**(30): p. 10955.
8. Zhang, J., M.B. Vukmirovic, Y. Xu, M. Mavrikakis, and R.R. Adzic, Angew. Chem. Int. Ed., 2005. **44**: p. 2132.
9. Zhang, J., M.B. Vukmirovic, K. Sasaki, F. Uribe, and R.R. Adzic, Journal of the Serbian Chemical Society, 2005. **70**(3): p. 513.
10. Zhang, J.L., M.B. Vukmirovic, K. Sasaki, A.U. Nilekar, M. Mavrikakis, and R.R. Adzic, J. Am. Chem. Soc., 2005. **127**(36): p. 12480.
11. Shao, M.H., T. Huang, P. Liu, J. Zhang, K. Sasaki, M.B. Vukmirovic, and R.R. Adzic, Langmuir, 2006. **22**(25): p. 10409.
12. Climent, V., N.M. Markovic, and P.N. Ross, J. Phys. Chem. B, 2000. **104**(14): p. 3116.
13. Arenz, M., V. Stamenkovic, P.N. Ross, and N.M. Markovic, Surf. Sci., 2004. **573**(1): p. 57.
14. Arenz, M., T.J. Schmidt, K. Wandelt, P.N. Ross, and N.M. Markovic, J. Phys. Chem. B, 2003. **107**(36): p. 9813.
15. Zhao, D. and B.Q. Xu, Phys. Chem. Chem. Phys., 2006. **8**(43): p. 5106.
16. Zhang, J., F.H.B. Lima, M.H. Shao, K. Sasaki, J.X. Wang, J. Hanson, and R.R. Adzic, J. Phys. Chem. B, 2005. **109**(48): p. 22701.

17. Christoffersen, E., P. Liu, A. Ruban, H.L. Skriver, and J.K. Norskov, J. Catal., 2001. **199**(1): p. 123.
18. Savadogo, O., K. Lee, H. Oishi, S. Mitsushima, N. Kamiya, and K.I. Ota, Electrochem. Commun., 2004. **6**: p. 105.
19. Anon. www.platinum.matthey.com. [website] 2007 30th January 2007 [cited.
20. Greenwood, N.N. and A. Earnshaw, Chemistry of the Elements. First ed. 1984: Pergamon Press.
21. Bashyam, R. and P. Zelenay, Nature, 2006. **443**(7107): p. 63.
22. Crabb, E.M., M.K. Ravikumar, D. Thompsett, M. Hurford, A. Rose, and A.E. Russell, Phys. Chem. Chem. Phys., 2004. **6**(8): p. 1792.
23. Crabb, E.M., M.K. Ravikumar, Y. Qian, A.E. Russell, S. Maniguet, J. Yao, D. Thompsett, M. Hurford, and S.C. Ball, Electrochem. Solid State Lett., 2002. **5**(1): p. A5.
24. Crabb, E.M. and M.K. Ravikumar, Electrochim. Acta, 2001. **46**(7): p. 1033.
25. Crabb, E.M., R. Marshall, and D. Thompsett, J. Electrochem. Soc., 2000. **147**(12): p. 4440.
26. Crabb, E.M. and R. Marshall, Appl. Catal. A-Gen., 2001. **217**(1-2): p. 41.
27. Bartlett, P.N. and J. Marwan, Phys. Chem. Chem. Phys., 2004. **6**(11): p. 2895.
28. Bartlett, P.N., B. Gollas, S. Guerin, and J. Marwan, Phys. Chem. Chem. Phys., 2002. **4**(15): p. 3835.
29. Solla-Gullon, J., V. Montiel, A. Aldaz, and J. Clavilier, Electrochem. Commun., 2002. **4**(9): p. 716.
30. Rose, A., Structural Effects in Fuel Cell Electrocatalysts, PhD Thesis, 2004, University of Southampton
31. Rose, A., O. South, I. Harvey, S. Diaz-Moreno, J.R. Owen, and A.E. Russell, Phys. Chem. Chem. Phys., 2005. **7**(2): p. 366.
32. Renouprez, A., J.L. Rousset, A.M. Cadrot, Y. Soldo, and L. Stievano, J. Alloy. Compd., 2001. **328**(1-2): p. 50.
33. Kinoshita, K., J. Electrochem. Soc., 1990. **137**(3): p. 845.

Chapter Five: CeO_x Modified Pt/Al_2O_3 Catalysts

1 Introduction

Decreasing the level of CO found in PEMFC H_2 fuel streams derived from reformed hydrocarbons is a major challenge. Levels of CO as low as 10 ppm act as a poison towards Pt based catalysts used within the fuel cell. One of the ways to reduce the amount of CO in the fuel stream is by a cleanup process utilising the water gas shift (WGS) reaction:

$$CO + H_2O \leftrightarrows CO_2 + H_2 \qquad \Delta H^o_{298} = -41.1 \text{ kJ mol}^{-1} \qquad \textbf{Equation 1}$$

At present a multi-stage cleanup process involving preferential oxidation (PROX), low temperature WGS (LTS), and high temperature WGS (HTS) are employed to achieve levels of CO less than 10 ppm. LTS and HTS steps are used in conjunction as the exothermic nature of the WGS reaction leads to an 80 fold increase in the equilibrium constant when the temperature is reduced from 600 to 200 °C [1]. A typical set-up exploits the kinetics of the process by employing an initial HTS step, in turn helping to decrease the required catalyst load. Subsequently, the gas stream is cooled before entering the LTS stage where the favourable thermodynamics are then exploited. The combination of HTS and LTS steps can reduce CO levels to less than 2000 ppm [2]. The PROX reaction refers to the preferential oxidation of CO in H_2 rich environments and is used after the WGS steps to achieve high CO conversion to CO_2. The PROX catalysts need to be able to achieve a reduction of CO levels to less than 10 ppm [2] without any excessive oxidation of hydrogen to water.

Conventionally, Fe/Cr and Cu/Zn catalysts are used for the HTS and LTS processes, respectively [1-3]. These catalysts are not suitable for use in conjunction with fuel cell applications for several reasons. The catalysts need to

be activated before operation to control the reduction of surface oxides to produce the catalytic active states. The exothermic nature of the reduction means the activation in a reducing gas must be carried out with a slow heating rate. This is impractical in areas in which low temperature fuel cells are expected to be employed, such as the automotive sector. For such an application, the sintering of the catalysts that would be encountered for a rapid activation step, would lead to poor mechanical stability as a result of start-up / shut down cycles [1, 2, 4]. When in operation, the active reduced surface of the catalyst is pyrophoric. If the catalyst is exposed to air as a result of an accident, an exothermic reaction resulting in temperatures in excess of 650 °C would be typical [2].

Ceria supported metal catalysts are known to promote the WGS reaction. Early mechanistic work regarding the promotion was carried out by Shido and Iwasawa [5, 6]. They proposed that bridging –OH groups on the surface of the ceria support react with CO to form bidentate formates. These bidentate formates then decompose in the presence of water to yield H_2 and CO_2 (figure 1). It was suggested that the role of the promoter metal was to aid the reduction of surface CeO_2 sites to form the active bridging –OH groups.

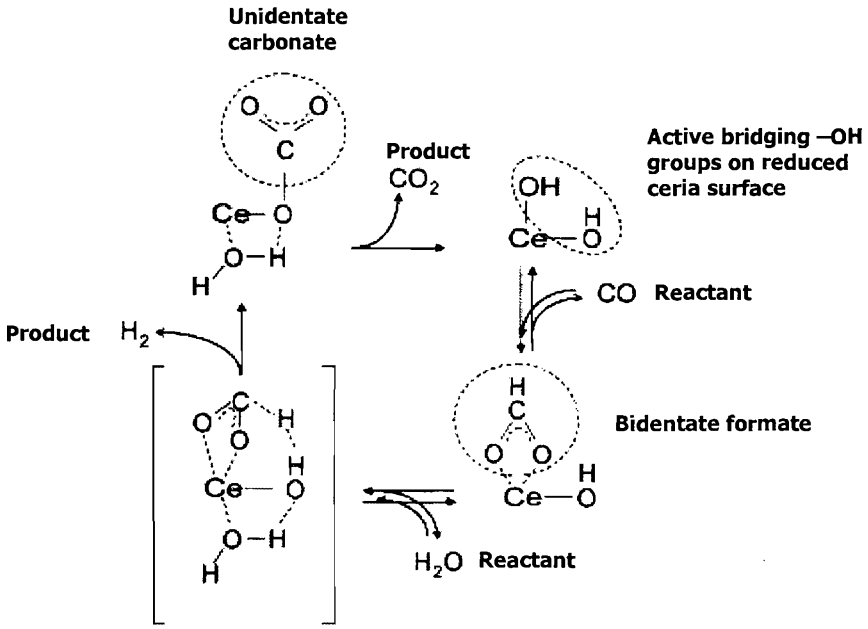

Figure 1 **Schematic diagram for the WGS reaction proceeding through the surface formate mechanism. The cycle begins with the formation of the active bridging –OH groups [7].**

The exact mechanism by which the promoter aids the formation of bridging –OH groups is unclear. One possibility is that the removal of surface oxygen by H_2 or CO is followed by dissociative adsorption of water. Another possibility is that the H_2 is dissociated directly over the promoter metal, with hydrogen spilling over onto the ceria surface leading to the formation of the bridging –OH groups.

Another mechanism based on a surface redox process has also been put forward as a possible pathway for the WGS reaction on ceria supported precious metal catalysts. The surface redox mechanism proceeds as described in equations 2 to 4 and figure 2:

$$Pt + CO \rightarrow Pt\text{-}CO \qquad \textbf{Equation 2}$$

$$Pt\text{-}CO + 2CeO_2 \rightarrow Ce_2O_3 + CO_2 + Pt \qquad \textbf{Equation 3}$$

$$Ce_2O_3 + H_2O \rightarrow 2CeO_2 + H_2 \qquad \textbf{Equation 4}$$

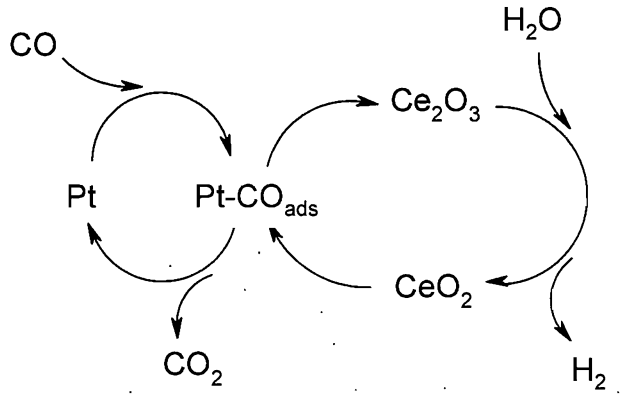

Figure 2 **Schematic diagram illustrating the principles of the surface redox process. The process starts with the formation of $Pt\text{-}CO_{ads}$, a ceria redox process occurs with CeO_2 converting to Ce_2O_3, and CO_2 expelled as a product. The Ce_2O_3 can then be oxidised by water, and the CeO_2 surface is reformed as well as yielding H_2 as a by product.**

Jacobs *et al.* have put forward the case for the formate mechanism as shown in figure 1 [7-16]. They used *in-situ* DRIFTS measurements to confirm the presence of bridging –OH and surface formate groups adsorbed on ceria [7-9, 17]. *In situ* XANES studies of Pt/CeO_2 in a 23% H_2 / He gas mix at elevated temperatures confirmed the formation of Ce (III) species [7, 9]. Only a small change in overall Ce valency was observed, as the XANES technique provides the per-atom average oxidation state of the ceria at the surface and in the bulk. The XANES showed no evidence of ceria re-oxidation by water in a H_2 rich environment as predicted by the surface redox process. Further XANES studies, again carried out in a 23% H_2/He environment at elevated temperatures, showed a correlation between the Pt loading and the reducibility of the Pt/CeO_2 catalysts [13]. As the Pt loading was increased the catalysts exhibited more Ce (III) character indicating that the metal promoter is linked to the formation of Ce (III) species. Kinetic isotope studies [10-12] were conducted on Pt/ceria using H_2O and D_2O. The thermal decomposition of D-formate was slower than that of H-formate, and this step was linked to the reaction rate of the WGS reaction. Thus the decomposition of H-formate was proposed to be the rate limiting step for the WGS reaction on Pt/ceria catalysts.

The redox mechanism (equations 2 to 4 and figure 2) proposes that CO adsorbs on the surface of reduced metal sites and reacts with oxygen from ceria to form CO_2. Work by Gorte *et al.* has strongly supported the surface redox mechanism [18-20]. Studies of a Pd/ceria catalyst carried out in a pulse reactor, where the catalyst was initially oxidised in water, and then subsequently exposed to pulses of CO and H_2O gas at 723 K, have been used to study the reaction mechanism [19]. The composition of the exit gas stream was followed by mass spectrometry. The pulse experiments showed that an initial pulse of CO was followed by the formation of CO_2 and H_2, with a secondary pulse of CO yielding no additional products. A subsequent H_2O pulse resulted in a release of CO_2 and H_2. This release of CO_2 on pulsing with H_2O is in agreement with the redox mechanism as it implies that H_2O reoxidises the Ce surface, allowing for the further decomposition of adsorbed Pt-CO species. Investigations into the reaction order

with respect to CO and H_2 were also investigated and a zero order dependency with respect to CO and a first order dependency with respect to H_2O were found [20]. The zero reaction order with respect to CO is to be expected for strong CO adsorption on precious metal catalysts.

There is much debate regarding both mechanisms with a lot of conflicting evidence being reported. DRIFTS work by Hilaire *et al.* [18] reports the presence of carbonate species on the ceria surface that are removed by the reoxidation of water. This has been challenged as it is claimed that is unclear whether bands in this region of the IR spectrum correlate to formates or carbonates and that other bands present elsewhere in the spectrum can be used to clarify the situation [8]. It is claimed that the zero reaction order for CO could equally relate to the saturation of ceria by either the carbonates or formates at the high CO/H_2O ratios utilised [7]. At high H_2O/CO ratios the reaction orders change and the process becomes first order with respect to CO and zero order with respect to H_2O [21]. These reaction orders could then apply to the formate mechanism where the zero order observed for water relates to the ceria surface being saturated with bridging –OH groups. The formate mechanism has been challenged as it is suggested that formates have minimal thermal stability and that maximum reaction rates should be found at lower temperatures than those observed [19]. The pulse response temporal analysis of products technique has been used to show that for the reverse WGS reaction the formate mechanism dominates [22]. This was shown as the conversion of CO_2 to CO was maximised when CO_2 and H_2 were pulsed sequentially with a minimal time lag. As both reactants are needed at the same time to achieve a maximum conversion this finding is in agreement with the formate mechanism. What is clear is that the mechanism for the WGS reaction is highly contested and that further research is required to clarify the situation.

Typical catalysts for the PROX reaction include a precious metal component (e.g. Pt, Au, Rh) on an oxide support (ceria, alumina, titania) [23-26]. In most cases the role of the metal is to adsorb CO with the oxide promoter binding and dissociating the O_2 molecule [2]. This process is mirrored in the reaction orders with respect to CO for different catalysts. The near saturation of Pt with CO

under reaction conditions leads to a negative reaction order, whereas Au catalysts have an upper adsorption limit of CO around $\theta_{CO} = 0.2$, so a positive reaction order is observed [24].

One of the problems with the Pt/CeO_2 system is the deactivation of the catalyst over time. This deactivation has been linked to carbon deposits on the ceria surface and poor mechanical stability as a result of sintering [27, 28]. Consequently ceria supported precious metal catalysts are doped with other metal oxides to help prevent sintering and also to promote the reduction of Ce(IV) to Ce(III) species [4, 29-31] .

In this study, the controlled surface modification procedure developed by Crabb *et al.* [32] and detailed in chapter 2, section 2, was used to prepare Pt/Al_2O_3 catalysts modified with Ce. It is expected that the Ce will be present at the surface in oxide form. Thus, the catalysts prepared are denoted as $CeO_x/Pt/Al_2O_3$. The objective of preparing these catalysts was to investigate how the presence of CeO_x at the surface of Pt/Al_2O_3 influences the performance of the catalyst towards the WGS reaction. Ideally, the aim was to exploit the catalytic properties of the Pt/CeO_2 system whilst utilising the advantageous properties of a more stable Al_2O_3 support. The performance of the catalysts towards the oxidation of CO was also assessed. The reaction order with respect to CO was studied to assess the impact of having CeO_x species present at the surface.

The characterisation techniques used to probe the physical structure of the catalysts were XANES, CO chemisorption and TEM EDX analysis.

The EXAFS technique was not used as EXAFS analysis of the $CeO_x/Pt/Al_2O_3$ samples proved to be very problematic. The low levels of Ce present in the samples, coupled with the high degree of background absorption attributable to the alumina support at this energy range, gives rise to a low signal to noise ratio. The noise levels could be reduced to a suitable level by acquiring approximately 20 scans. With one scan taking 40 min, this meant that very few samples could be assessed in the allotted beamtime. The position of the Ce L_2 edge also restricts

the acquisition of EXAFS beyond 10 $Å^{-1}$ in *k* space. In addition to these data acquisition issues, Ce L_3 edge EXAFS analysis is inherently difficult due to the final state mixed valence behaviour and intense multi-electron excitations. The multi-electron excitations are responsible for the presence of strong resonant like features superimposed on the EXAFS signal at ~ 120 eV beyond the absorption edge. Fonda *et al.* [33] have developed a model to help improve the theoretical prediction of Ce L_3 edge EXAFS spectra. The model involves the simultaneous use of two different phase shifted EXAFS signals, and was shown to be a necessity in predicting the EXAFS signal. This model is not available using the Daresbury suite of software, so accurate analysis of the data acquired is not possible. EXAFS of the Ce K edge could not be acquired due to the high photon energy required > 40 KeV.

2 Experimental Details

2.1 Catalyst Preparation

$CeO_x/Pt/Al_2O_3$ catalysts were prepared as detailed in chapter 2, section 2.2. The alumina supported catalysts were dried at 110 °C overnight and calcined in air for an hour at 350 °C before use. The first reduction step of the $Pt\text{-}Al_2O_3$ in the reactor was carried out at 350 °C, instead of 200 °C for the carbon supported catalysts. Modifications were made to a 4 wt % Pt/ $\gamma\text{-}Al_2O_3$ catalyst with a calculated dispersion of 0.26. $Ce(acac)_3{\cdot}H_2O$ was used as the precursor. The reaction was first performed on a 20 wt % Pt/C catalyst as it was readily available and to give an indication of the success of the reaction. The table below (table 1) gives details of the catalysts prepared.

Control reactions were carried out to investigate whether the precursor was specifically targeting Pt sites and not the carbon or alumina support. These studies found that there was some reaction between $Ce(acac)_3{\cdot}H_2O$ and the alumina support, as evidenced by a change in colour of the filtrate, which was

initially orange but turned colourless after the end of the reaction. The control reaction between $Ce(acac)_3 \cdot H_2O$ and the carbon support found that no Ce deposition occurred.

Pt/CeO_2 was supplied by Johnson Matthey to facilitate a comparison with the surface modified catalysts

Table 1 Details of catalysts prepared using the $Ce(acac)_3 \cdot H_2O$ precursor

Catalyst	Equivalent monolayers	Initial colour of solution	End colour of filtrate
$CeO_x/Pt/C$	1	Orange	colourless
$CeO_x/Pt/Al_2O_3$	0.5	Orange	colourless
$CeO_x/Pt/Al_2O_3$	1	Orange	colourless
$CeO_x/Pt/Al_2O_3$	2	Orange	colourless
$CeO_x/Pt/Al_2O_3$	4	Orange	colourless
$CeO_x/Pt/Al_2O_3$	8	Brown-Orange	Light-Orange

2.2 XAS Studies

2.2.1 Ce L_3 edge Investigations

Ce L_3 edge XAS spectra were acquired on station 7.1 at the SRS, Daresbury Laboratory. Station 7.1 utilises a double crystal Si(111) monochromator for EXAFS in the range of 4 keV to 10 keV. EXAFS of the catalyst materials were acquired in Fluorescence mode using a liquid nitrogen cooled 9 element Ge solid state detector. EXAFS of metal foils and oxide standards were acquired in transmission mode. All catalysts were prepared as BN pellets for XAS measurements. The different gas environments used in the measurements were air, H_2 and CO.

2.3 WGS and CO Oxidation testing

WGS and CO oxidation measurements were carried out using the rig described in chapter 2, section 7.1, and the testing procedures detailed in sections 7.1 and 7.2. The mole fractions of CO investigated were 0.167, 0.25, 0.33, 0.5, and 0.67.

2.4 TEM, CO Chemisorption and ICP-AES Analysis

All samples were submitted to Johnson Matthey Technology Centre, Sonning Common, where the analyses were performed.

Powder samples for TEM EDX were crushed between two glass slides and samples positioned onto a lacey carbon coated copper 'finder' grid with the aid of a micro manipulator. The samples were examined in a Tecnai F20 Transmission Electron Microscope. Both bright field and high resolution electron microscopy modes were used.

3 Results and Discussion

3.1 ICP-AES Analysis

Elemental analyses of the prepared catalysts were carried out using ICP-AES. The experimental values, along with the theoretically calculated values, are shown below in table 2.

Table 2 Elemental analysis of prepared $CeO_x/Pt/Al_2O_3$ catalysts

Sample	Wt % Pt Theoretical	Wt % Pt Experimental	Wt % M_2 Theoretical	Wt % M_2 Experimental
$0.5CeO_x/Pt/Al_2O_3$	3.99	3.67	0.37	0.33
$1\ CeO_x/Pt/Al_2O_3$	3.97	3.67	0.74	0.70
$2\ CeO_x/Pt/Al_2O_3$	3.94	3.60	1.47	1.30
$4\ CeO_x/Pt/Al_2O_3$	3.88	3.56	2.90	2.33
$8\ CeO_x/Pt/Al_2O_3$	3.77	3.40	5.64	4.29

In general, the ICP-AES results are in good agreement with the theoretical values, confirming that all the secondary metal is deposited onto the Pt/Al_2O_3. The large amounts of CeO_x deposited indicate that it is unlikely that the CeO_x is present at the Pt surface alone. The control reaction with Al_2O_3 confirmed that the procedure was also successful in the absence of Pt. However, this is not the case with carbon. It is believed that this is caused by greater reducibility of the Al_2O_3 support in comparison to carbon or the presence of other deposition sites on the support. The large amount of CeO_x being deposited can be rationalised by the CeO_x targeting both Pt and Al_2O_3 sites or by the CeO_x preferentially targeting Pt sites before migrating onto the support.

3.2 TEM EDX Analysis

Selected TEM micrographs and EDX analysis for the 0.5, 1, 2, and 4 $CeO_x/Pt/Al_2O_3$ samples are shown in figures 3 to 7. SEM EDX maps are also shown for 0.5 and 4 $CeO_x/Pt/Al_2O_3$ in figures 8 and 9.

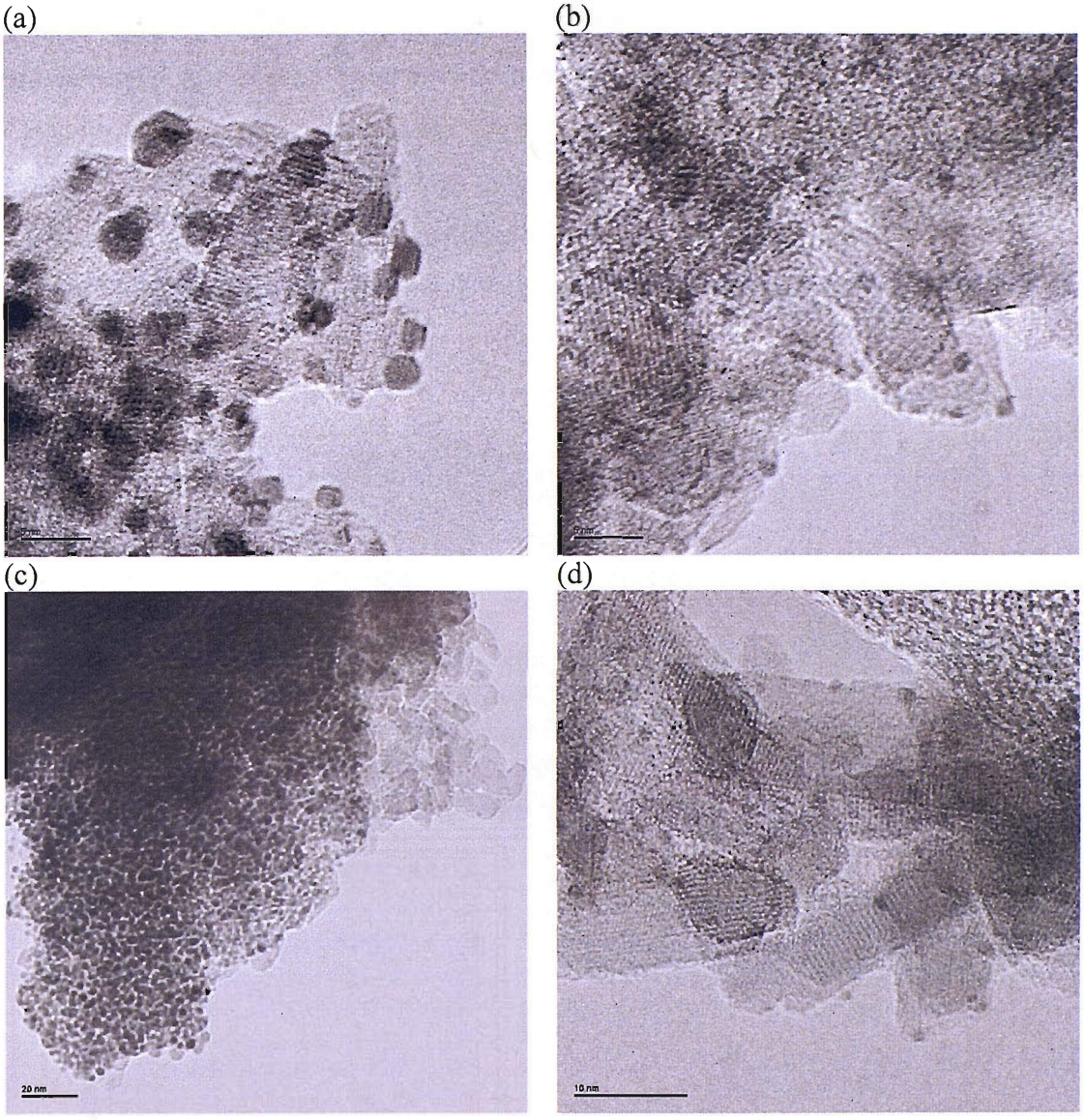

Figure 3 **TEM micrographs of (a) 0.5, (b)1, (c) 2, and (d) 4 $CeO_x/Pt/Al_2O_3$. The scale bars for figures, a,b,c, and d are 5, 5, 10 and 20 nm, respectively.**

The TEM micrographs confirm the presence of small Pt particles supported on alumina. In some cases the supported particles were found in isolation on the alumina support as is the case with figures 3a, 3b, and 3d but in some instances dense agglomerations were found as illustrated in figure 3c. Figure 3a also shows that some of the particles found were faceted. Due to the small size of the Pt particles (~1-2 nm), particle size analyses were not performed. However, a

significant particle size was not observed on addition of even 4 monolayer equivalents of CeO_x, as evidenced by the TEM micrographs.

EDX analysis in the TEM instrument was used in an attempt to confirm the co-locality of Pt and Ce on the Al_2O_3 support. However, the method is not very sensitive to components present at concentrations below 1 wt %; the 0.5 $CeO_x/Pt/Al_2O_3$ sample consisted of 0.35 wt % Ce. Thus, the analysis is not expected to be very accurate and was only used as a rough screening method. In addition, the small size of the Pt particles (1 to 2 nm particles) does not facilitate the accurate use of line scans across a single particle, as was possible for the larger carbon supported Pt catalysts in chapters 3 and 4.

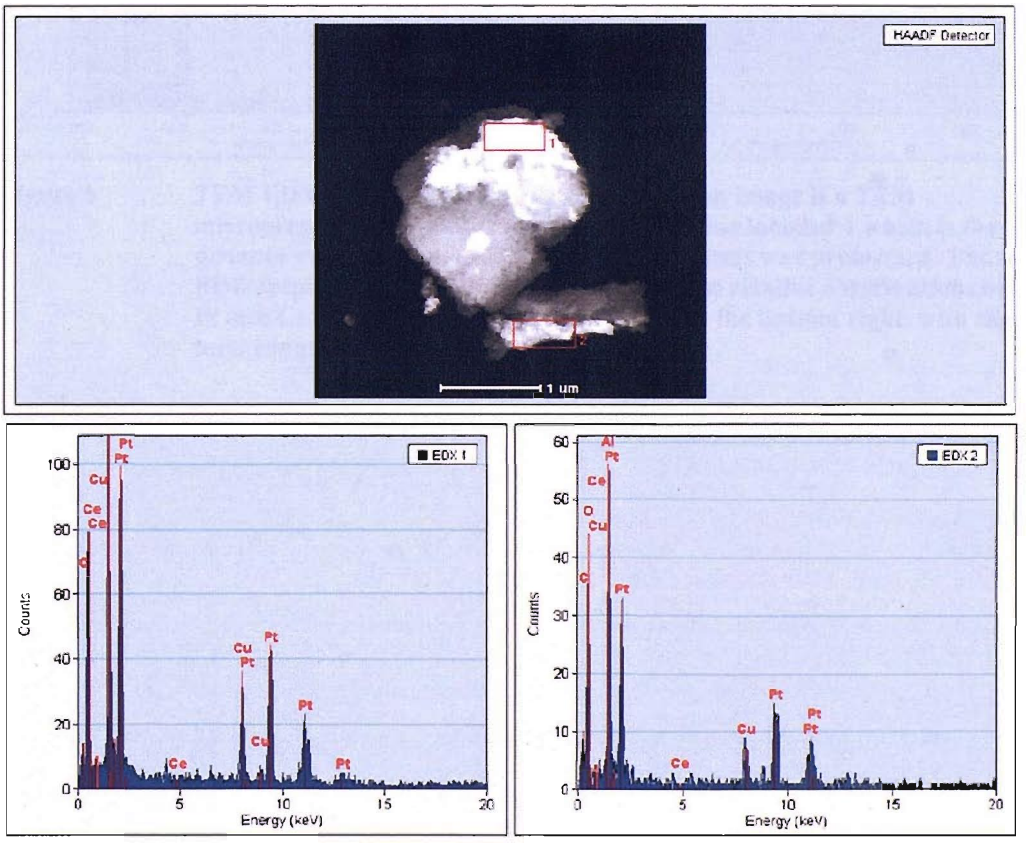

Figure 4 **TEM EDX studies of 0.5 $CeO_x/Pt/Al_2O_3$. The top image is a TEM micrograph of the catalyst with two areas highlighted for the EDX analysis. The EDX profiles for the red boxes labelled 1 and 2 are shown in the bottom left and right, respectively.**

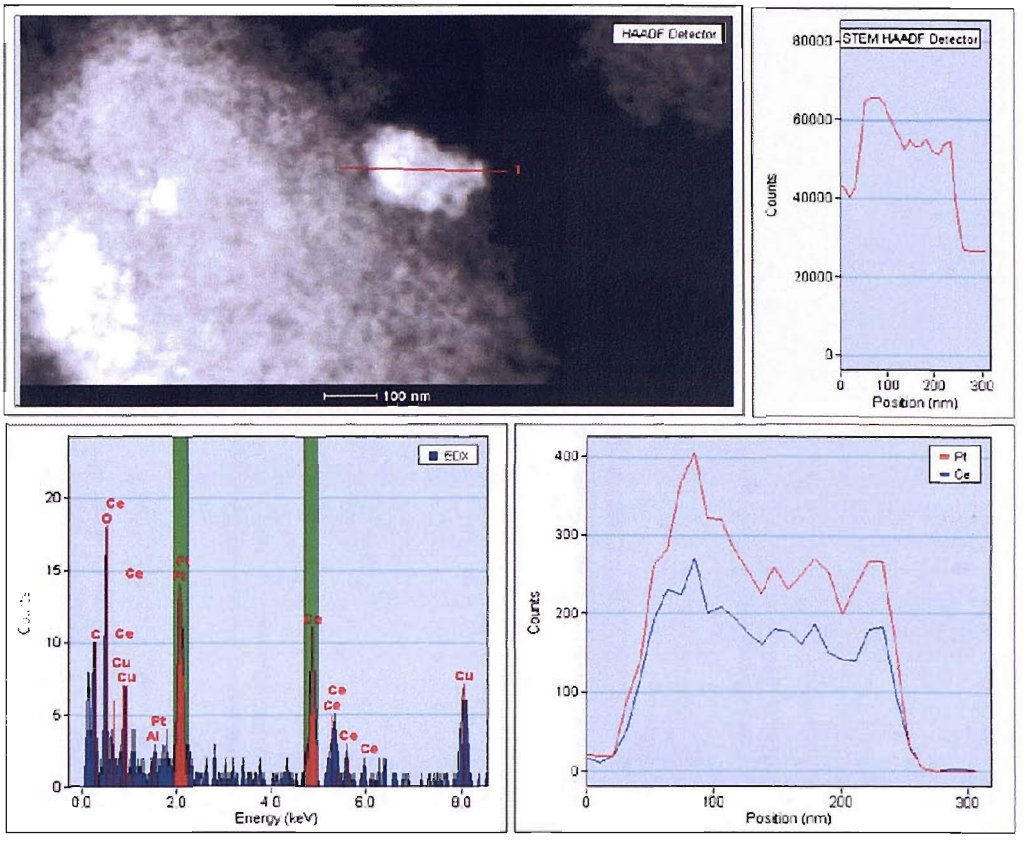

Figure 5 **TEM EDX studies of 1 $CeO_x/Pt/Al_2O_3$. The top image is a TEM micrograph of the catalyst identifying a red line labelled 1 which is the distance over which the EDX line profile analysis was performed. The total EDX response is shown in the bottom left. The relative contributions of the Pt and Ce counts across the line are shown in the bottom right, with the total counts shown in the top right.**

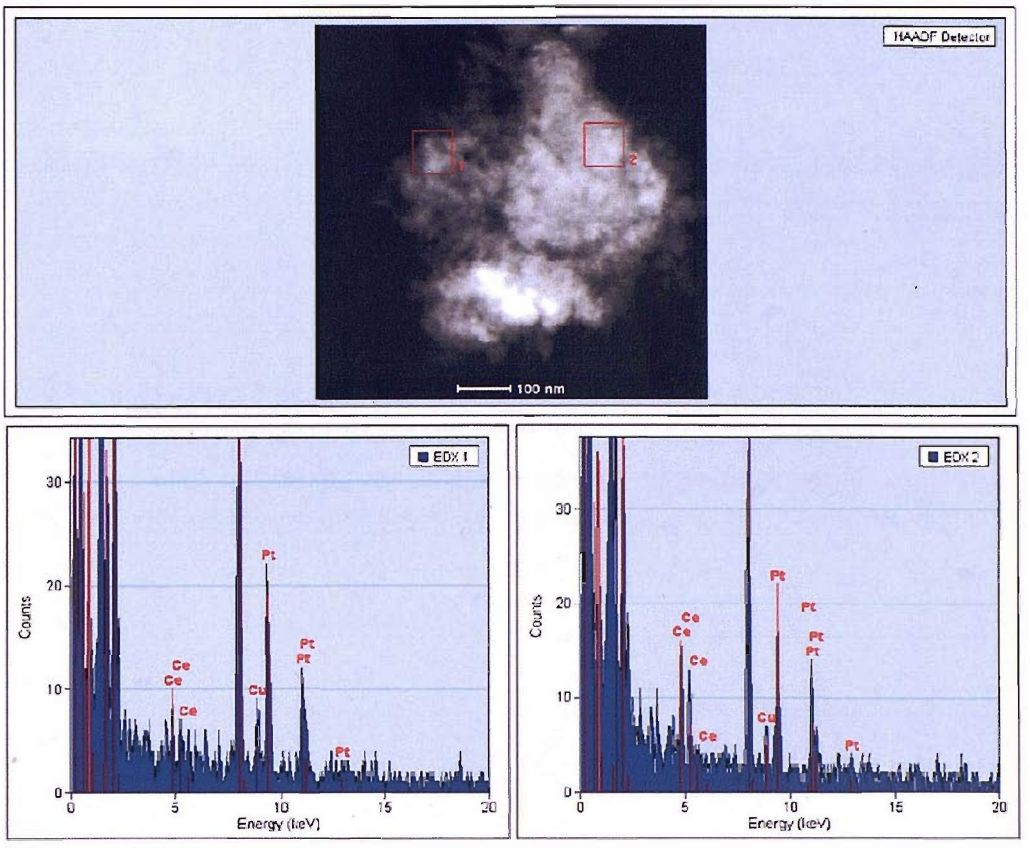

Figure 6 **TEM EDX studies of 2 $CeO_x/Pt/Al_2O_3$. The top image is a TEM micrograph of the catalyst with two areas highlighted for the EDX analysis. The EDX profiles for the red boxes labelled 1 and 2 are shown in the bottom left and right, respectively.**

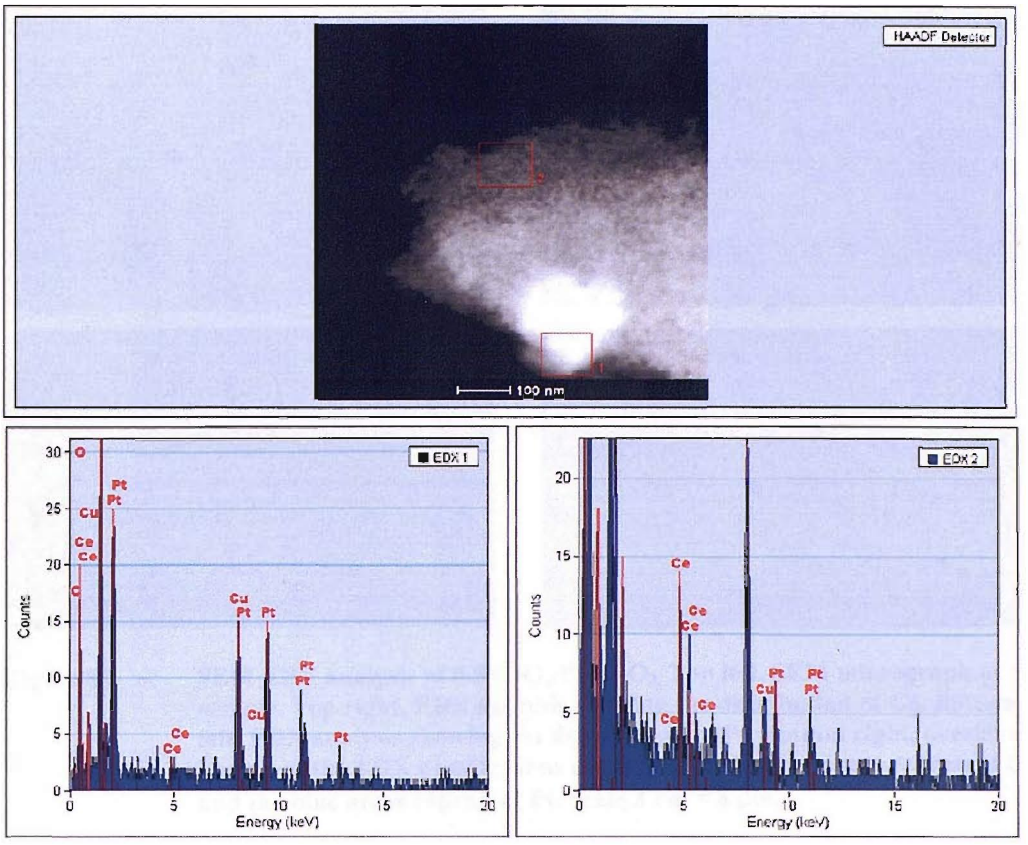

Figure 7 **TEM EDX studies of 4 $CeO_x/Pt/Al_2O_3$. The top image is a TEM micrograph of the catalyst with two areas highlighted for the EDX analysis. The EDX profiles for the red boxes labelled 1 and 2 are shown in the bottom left and right, respectively.**

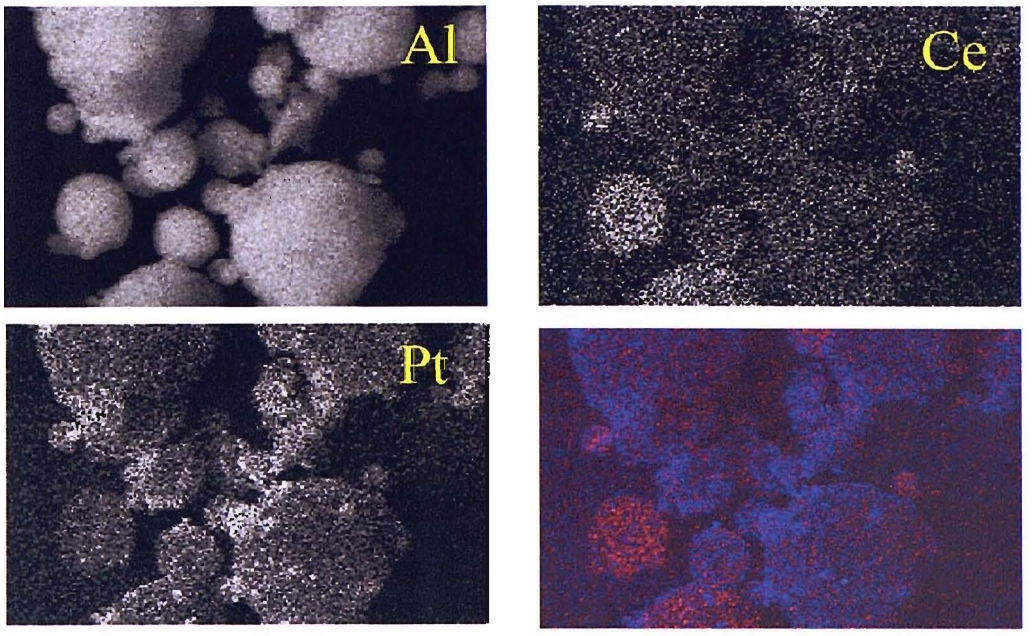

Figure 8 **SEM EDX analysis of 0.5 $CeO_x/Pt/Al_2O_3$. Top left, SEM micrograph of the sample. Top right, EDX analysis showing the distribution of Ce. Bottom left, EDX analysis showing the distribution of Pt. Bottom right, overlayed images of the EDX distributions of Ce and Pt. The red areas represent Ce and the blue areas represent Pt. Scale 1 cm = 8 μm.**

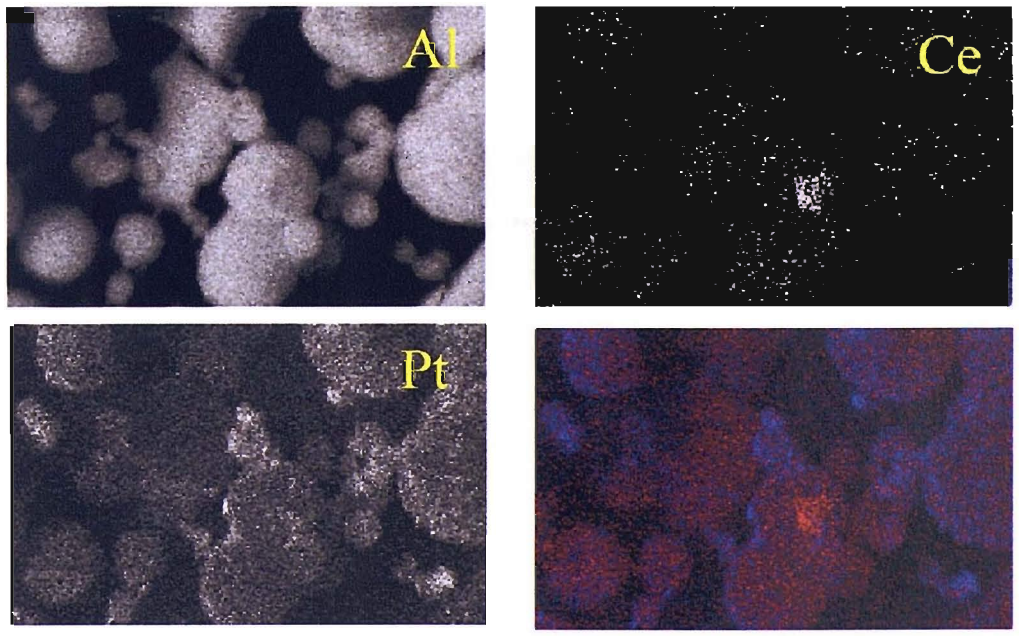

Figure 9 **SEM EDX analysis of 4 $CeO_x/Pt/Al_2O_3$. Top left, SEM micrograph of the sample. Top right, EDX analysis showing the distribution of Ce. Bottom left, EDX analysis showing the distribution of Pt. Bottom right, overlayed images of the EDX distributions of Ce and Pt. The red areas represent Ce and the blue areas represent Pt. Scale 1 cm = 8 μm.**

The EDX analysis is not conclusive in confirming the co-locality of the different components of the catalyst. The TEM EDX analysis of 0.5 $CeO_x/Pt/Al_2O_3$ (figure 4) shows that the EDX response from the areas probed confirmed the presence of Pt in isolation, with no Ce detected in either of the areas. Conversely, the SEM EDX map (figure 8) shows that the Ce is present and localised in specific areas that overlap well with the areas of dispersed Pt. The SEM EDX map of 4 $CeO_x/Pt/Al_2O_3$ (figure 9) also confirmed the presence of Ce in localised areas, although in this instance, the Ce was more readily detected. The TEM EDX analysis for the 1, 2, and 4 $CeO_x/Pt/Al_2O_3$ (figures 5 to 7) show that in some places the Ce is found in the presence and others in the absence of Pt. The EDX data that are shown in figures 5 to 7 show the regions where Ce and Pt are found along side one another. The TEM EDX line profile analysis of 1 $CeO_x/Pt/Al_2O_3$ (figure 5) identifies an area where Ce and Pt are found together and in similar proportions across a particle.

3.3 CO Chemisorption

CO chemisorption was used as a means to assess blocking of the surface of Pt particles by the deposition of CeO_x, which may be observed as a decrease of the apparent dispersion of the catalysts. It was assumed that Co only adsorbed on the Pt sites and not the CeO_x. The dispersion measurements for the $CeO_x/Pt/Al_2O_3$ catalyst are detailed below in table 3.

Table 3 **Pt dispersion values for $CeO_x/Pt/Al_2O_3$ catalysts determined using CO chemisorption.**

Catalyst	Pt dispersion / %
4 wt% Pt/Al_2O_3	26
0.5 $CeO_x/Pt/Al_2O_3$	28.4
1 $CeO_x/Pt/Al_2O_3$	29.5
2 $CeO_x/Pt/Al_2O_3$	27.0
4 $CeO_x/Pt/Al_2O_3$	25.7

A slight decrease in the apparent dispersion is observed as the amount of Ce was increased, with the exception of the 1 $CeO_x/Pt/Al_2O_3$. However, the magnitude of the change is within the error of the experiment, approximately ± 2 %. Thus, assuming CO is only adsorbed on Pt, the chemisorption measurements indicate that the CeO_x is located on the Al_2O_3 support and is not blocking the surface of the Pt particles. However, these measurements do not provide any indication of the mechanism of the deposition of the CeO_x; i.e. whether the $Ce(acac)_3 \cdot H_2O$ precursor reacted first at the Pt sites and then spilled over on to the Al_2O_3 support or if it was deposited directly onto the support.

3.4 XANES Analysis

All XANES spectra were normalised as detailed in section 4.1.4. The III and IV oxidation states of Ce give rise to very different Ce L_3 edge XANES spectra. The XANES spectrum (figure 10) of CeO_2 (Ce IV) shows two distinct peaks b_2 and c, with two shoulders a and b_1 also visible. The weak shoulder a is attributed as transitions towards the Ce 6s states or as impurities (hydroxyl groups etc.) in the system [34-37]. There is still some debate about the nature of peak b_1, although peak b_2 has been attributed to transitions to the final state Ce $[2p^5 4f^1 5d^1]$ O $[2p^5]$ and the final state configuration of peak c has been widely reported as transitions to Ce $[2p^5 4f^0 5d^1]$ O $[2p^6]$ [34-37].

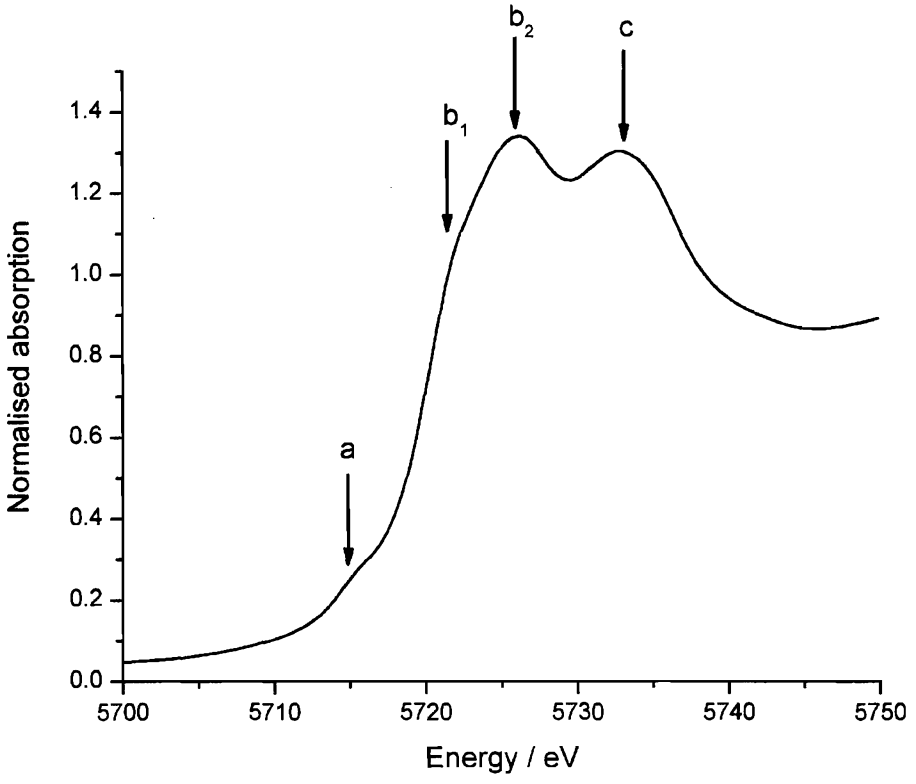

Figure 10 **Ce L_3 edge XANES spectrum of CeO_2 in air.**

The XANES spectrum (figure 11) of the Ce L_3 edge of $Ce(NO_3)_6$ (Ce III) has starkly different characteristic from the spectrum of CeO_2. Ce (III) marks the occupation of the *4f* energy levels and thus certain transitions become less favoured. There is one observable peak b_0 and this is due to transitions to the final state Ce $[2p^5 4f^1 5d^1]$ O $[2p^6]$. These differences in XANES characteristics for the (III) and (IV) oxidation states of Ce at the Ce L_3 edge, make comparison of XANES an appropriate technique for probing the reducibility of Ce under different conditions. In this study only a qualitative assessment of the Ce oxidation state is employed, although there are procedures for a quantitative determination [34].

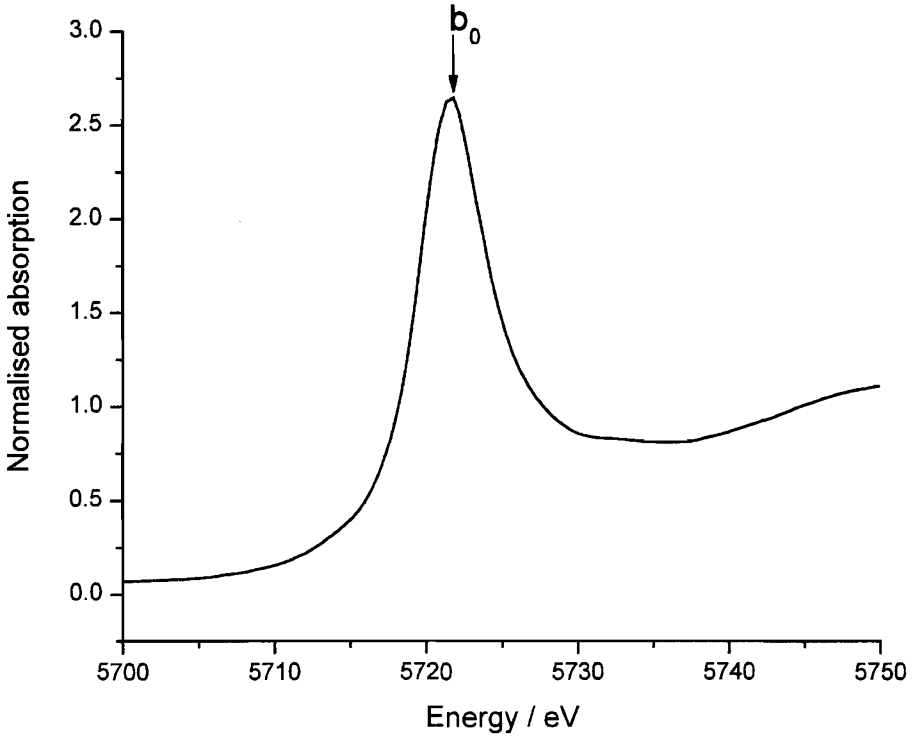

Figure 11 **Ce L_3 edge XANES spectrum of $Ce(NO_3)_6$ in air.**

The XANES spectra of the CeO_x modified Pt/Al_2O_3 catalysts are reported in figure 12 with those of the control and CeO_x modified Pt/C catalysts. They were initially acquired in a sequential order of gas treatment of air, H_2, and CO, without any purging phases in between. The experiments were repeated changing the order of the gas treatments and purging the gas treatment cell with $N_2(g)$ after exposure to each of the different gases. In each instance, the XANES spectra had the same appearance as reported in figure 12. The appearance of the XANES spectra of the $CeO_x/Pt/Al_2O_3$ catalysts with relation to the Ce standards illustrated in figures 10 and 11 have been used to perform a qualitative assessment of the oxidation state of Ce.

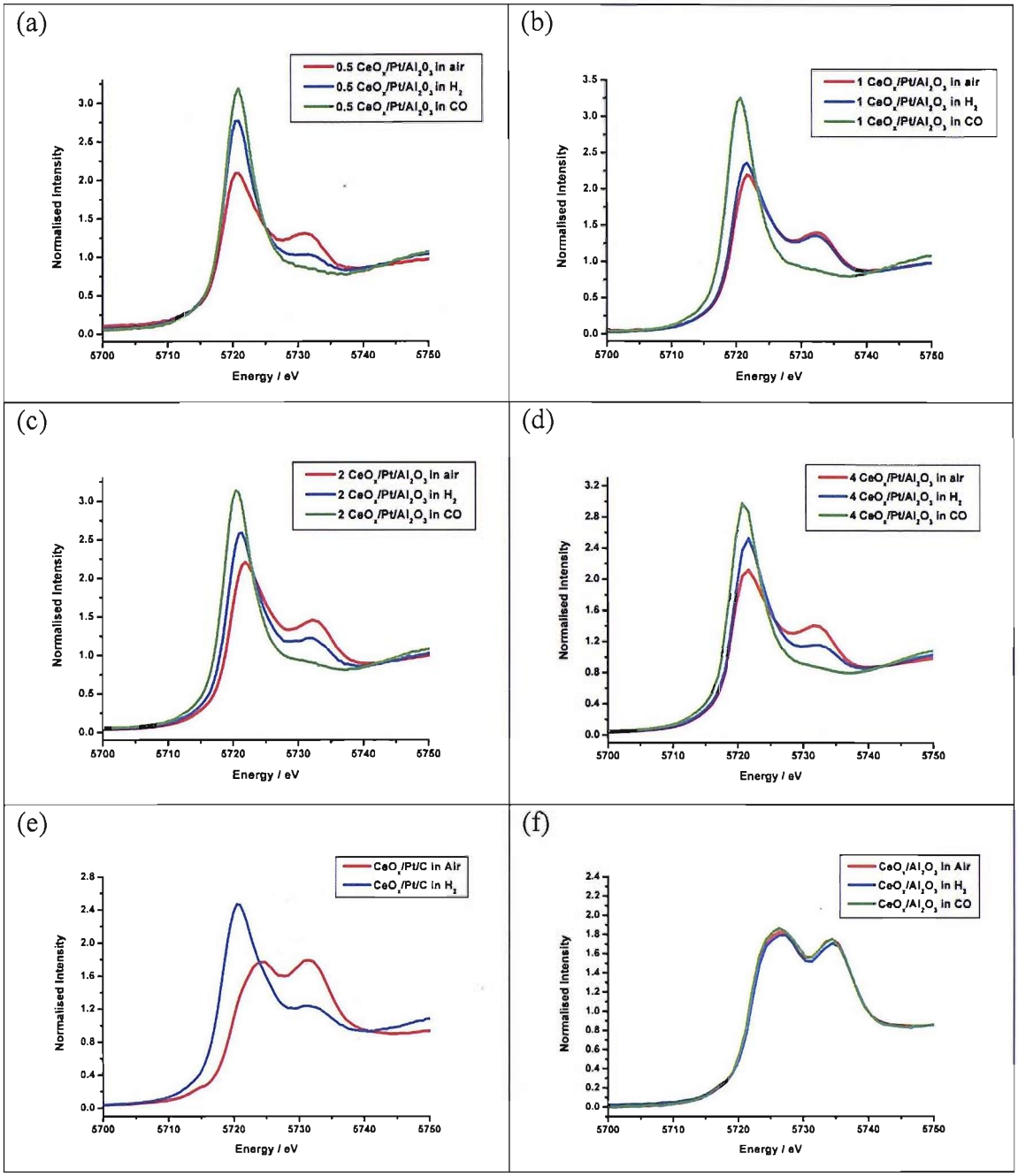

Figure 12 **Normalised Ce L_3 edge XANES spectra of (a) 0.5 $CeO_x/Pt/Al_2O_3$, (b) 1 $CeO_x/Pt/Al_2O_3$, (c) 2 $CeO_x/Pt/Al_2O_3$, (d) 4 $CeO_x/Pt/Al_2O_3$, (e) $CeO_x/Pt/C$ and (f) CeO_x/Al_2O_3 in gas environments of air, H_2, and CO at room temperature.**

XANES studies by Jacobs *et al.* [13] on the Pt/CeO_2 system have investigated how the Pt loading affects the ratio of Ce(IV) to Ce(III) species under an atmosphere of H_2/He at temperatures up to 300 °C. The quantitative determination performed by Jacobs *et al.* involved a linear combination of fitting Ce(III) and Ce(IV) reference materials. A maximum Ce(III) content of 75 % was shown for a 5 wt % Pt/CeO_2 catalyst at 300 °C. This partial reduction of the ceria

support appeared as a slight increase of peak b_2 with respect to peak c for the CeO_2 XANES spectrum. Only a small change in Ce valency is expected due to the large proportion of Ce in the bulk of the support in comparison to the surface. The XANES spectra in figure 11 show that the $CeO_x/Pt/Al_2O_3$ catalysts investigated in this thesis exhibit a large amount of Ce(III) character under normal atmospheric conditions at room temperature. In general, all the $CeO_x/Pt/Al_2O_3$ catalysts show the same degree of Ce reduction in the different gas environments. The proportion of Ce(III) present increases, as the gas environment is changed from H_2 and then to CO. The XANES spectra for the $CeO_x/Pt/Al_2O_3$ catalysts in CO closely resembles the XANES spectrum of $Ce(NO_3)_6$ (figure 10) indicating that almost the entirety of the Ce in the catalyst is present as Ce(III). This shows that the Ce is well dispersed as any agglomeration would give rise to sub-surface Ce(IV). As the Ce is well dispersed at the surface these catalytic systems are ideal to study the affect of Pt on the oxidation state of the Ce as there is little bulk Ce to dilute the response.

For the CeO_x/Al_2O_3 system prepared as the control sample the Ce is present as entirely Ce(IV) in all the environments of air, H_2, and CO. The absence of Ce(III) character in these XANES spectra provides evidence that the presence of Pt is facilitating the reduction of Ce(IV) to Ce(III) for the $CeO_x/Pt/Al_2O_3$ catalysts. The observation of this effect is indicative that the Ce and Pt are in close proximity to each other on the alumina surface and may indicate that the mechanism of CeO_x deposition differs in the presence and absence of Pt.

The *in-situ* XANES studies carried out on Pt/CeO_2 by Jacobs *et al.* [13] utilised aggressive reducing conditions to observe a partial reduction of the ceria support. It is of interest that a partial reduction of Ce(IV) to Ce(III) is observed in air at room temperature for the $CeO_x/Pt/Al_2O_3$ catalysts, whilst no reduction was observed for the CeO_x/Al_2O_3 catalyst (as discussed above) and also the $CeO_x/Pt/C$ catalyst. Thus, the partial reduction requires the presence of both Pt and Al_2O_3. This observation may reflect differences in the distribution of CeO_x on the two supports. On carbon the CeO_x is less able to spread across the surface of the support, resulting in larger clusters of CeO_x or encapsulation of the Pt

particles, either of which would decrease the fraction of the Ce present in the +3 oxidation state.

In a gas environment of H_2, the reduction of Ce(IV) to Ce(III) species is more pronounced than that in air for all of the $CeO_x/Pt/Al_2O_3$ catalysts, with the exception of the 1 $CeO_x/Pt/Al_2O_3$ catalyst. As a further reduction is noted for all the other catalysts the result for the 1 $CeO_x/Pt/Al_2O_3$ catalysts seems anomalous and may be the result of a leak in the gas cell, or insufficient purging with hydrogen. The additional reduction observed for the other $CeO_x/Pt/Al_2O_3$ catalysts may be caused by the dissociation of H_2 over surface Pt sites. The resultant hydrogen could then subsequently spill over onto neighbouring Ce atoms, causing the formation of the bridging –OH groups. Thus, creating the proposed active sites for the WGS reaction proceeding by the formate mechanism [13].

Experiments performed in an environment of CO, show signs of further reduction of Ce(IV) to Ce(III). Jacobs *et al.* [13] noted a similar effect after a reduction pre-treatment in CO for Pt/Ceria catalysts. This observation was attributed to the ability of CO to remove capping oxygen atoms at the ceria surface. As no partial reduction is observed for the CeO_x/Al_2O_3 this infers that the Pt is required for the CO to reduce Ce(IV) or that previously formed Ce(III) species at the surface are required.

3.5 WGS Testing

WGS testing was carried out in a fixed bed reactor at conditions designed for testing LTS catalysts. The temperature was ramped at a rate of 5 °C min^{-1}, with a total gas flow of 300 cm^3 min^{-1}, comprised of 5 % CO, 30 % steam, and 65 % N_2 by volume, and a catalyst load of 0.45 g. The results of the WGS testing are shown in figure 13 and the temperature at which 50 % conversion was attained (T_{50}) shown in table 4.

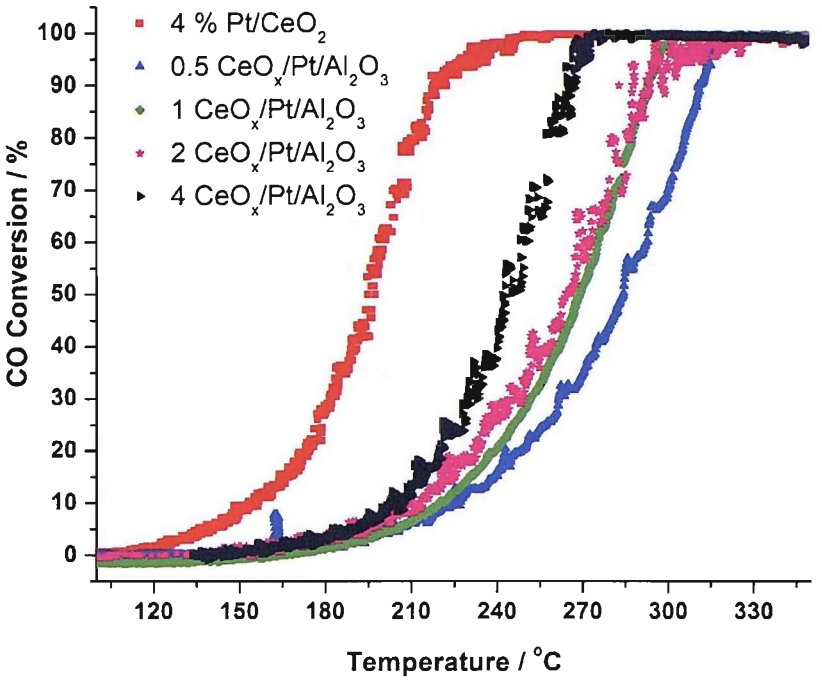

Figure 13 **WGS testing results for different $CeO_x/Pt/Al_2O_3$ catalysts. Data for 4 wt % Pt/CeO_2 is included for comparison. Data for Pt/Al_2O_3 (not shown) gives a zero/baseline response over this temperature range.**

Table 4 **Temperature at 50 % CO conversion for the WGS testing results.**

Catalyst	T_{50} / °C
4 wt % Pt/CeO_2	193.5
0.5 $CeO_x/Pt/Al_2O_3$	285.1
1 $CeO_x/Pt/Al_2O_3$	269.3
2 $CeO_x/Pt/Al_2O_3$	263.5
4 $CeO_x/Pt/Al_2O_3$	245.5

The WGS testing results show that the modification of Pt/Al_2O_3 with CeO_x greatly enhances the activity of the catalyst. The response of an unmodified Pt/Al_2O_3 catalyst over the same temperature range gives a baseline response and exhibits no activity towards the WGS reaction. It is of great interest that the addition of ~ 0.35 wt % Ce, as is the case with the 0.5 $CeO_x/Pt/Al_2O_3$, has such a pronounced affect on the activity of the catalyst. As the Ce loading is increased

the activity of the catalyst towards the WGS rises accordingly. Looking at the formate and the surface redox mechanism, both processes suggest that as the number of surface Ce sites increases the amount of active sites should increase and thus increase the performance towards the WGS reaction. However, it is only in the surface redox process that Pt plays a direct role in the WGS reaction. The formate mechanism claims the reaction proceeds solely on the active bridging OH groups on the Ce, with the Pt facilitating the formation of these species. The XANES analysis shows there is a sufficient amount of Pt present to cause similar levels of reduction for all of the $CeO_x/Pt/Al_2O_3$ catalysts. It would be of interest to see if the same modification were performed on a Pt/Al_2O_3 catalyst with a lower Pt loading whether the extent of Ce reduction would remain constant and how the performance towards the WGS would be affected.

The prepared catalysts show promising activity but do not reach the performance levels of a conventional Pt/CeO_2 catalyst. The Al_2O_3 support should aid the stability of the catalyst and offer a solution to the current deactivation that conventional Pt/CeO_2 catalysts suffer. Trials in WGS reactor conditions over much larger timescales would be needed to prove this benefit. Further tailoring of the catalyst could help to improve the activity towards the WGS reaction. This tailoring could involve the use of mixed oxide supports or the addition of other components to the catalyst surface. Choung *et al.* have shown that the use of PtRe bimetallic particles rather than Pt alone supported on CeO_2 - ZrO_2 resulted in an increase in the performance towards the WGS reaction [4]. It is not documented in this work but the controlled surface modification procedure has been successfully used in our group to deposit Re onto the surface of Pt/C, via the use of the $Re(Cp)(CO)_3$ precursor. This method could also be used to incorporate Re into the $CeO_x/Pt/Al_2O_3$ catalysts to enhance the performance towards the WGS reaction.

3.6 CO Oxidation Testing

The CO oxidation testing was carried out using the reactor described in chapter 2, section 7.1. The inlet gases were a mixture of N_2, 1% CO in N_2, and air with a

total flow of 300 cm^3 min^{-1}. A large excess of air was used and kept constant, the flows of N_2 and CO were adjusted to control the mole fraction of CO (X_{CO}). The reactor was cooled with liquid nitrogen until the CO monitor showed no signs of CO conversion. The temperature was then ramped manually, simultaneously heating the furnace and cooling with liquid nitrogen to facilitate a very slow heating rate and combat the exothermic reaction conditions. The CO oxidation testing results are shown below in figure 14.

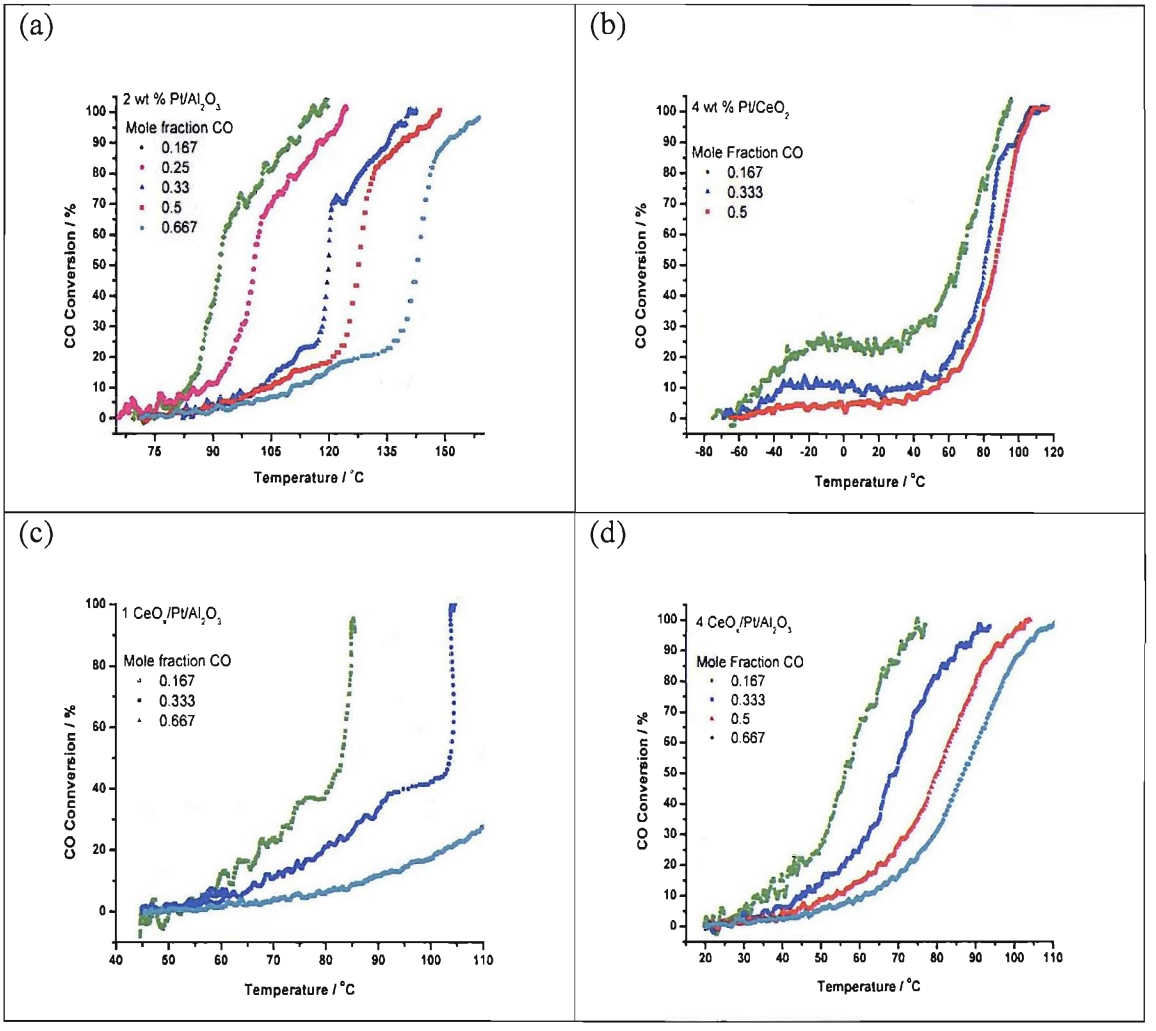

Figure 14 **CO oxidation testing results for (a) 2 wt % Pt/Al_2O_3, (b) 4 wt % Pt/CeO_2, (c) 1 $CeO_x/Pt/Al_2O_3$, and (d) 4 $CeO_x/Pt/Al_2O_3$.**

Table 5 **Temperature at which 50 % CO conversion was attained (T_{50}) for the CO oxidation testing at different mole fractions of CO for different catalysts.**

Catalyst	T_{50} at different values of X_{CO} / °C			
	$X_{CO} = 0.167$	$X_{CO} = 0.33$	$X_{CO} = 0.5$	$X_{CO} = 0.667$
4 % Pt/CeO_2	65	82	87	-
2 % Pt/Al_2O_3	92	120	128	143
1 $CeO_x/Pt/Al_2O_3$	83	104	-	-
4 $CeO_x/Pt/Al_2O_3$	56	69	80	87

Figures 14 (a) and (b) show the CO conversion plots for 4 wt % Pt/CeO_2 and 2 wt % Pt/Al_2O_3. It can be seen that both plots show a characteristic light off feature where there is a sharp increase in the conversion of CO. This light off feature is much more pronounced for the 2 wt % Pt/Al_2O_3 catalyst compared to the 4 wt % Pt/CeO_2 catalyst. The sharp feature associated with Pt/Al_2O_3 is also present in the CO conversion plots for 1 $CeO_x/Pt/Al_2O_3$ (figure 13c). The CO conversion plots for 1 $CeO_x/Pt/Al_2O_3$ differ from that of the 2 wt % Pt/Al_2O_3 catalyst as there is a larger amount of CO conversion before the light off occurs, and the light off takes the CO conversion close to 100 % in comparison to a conversion of 70 % for the 2 wt % Pt/Al_2O_3. Looking at the T_{50} values for $X_{CO} = 0.33$ it can be seen that 50 % conversion occurs at 104 °C for the 1 $CeO_x/Pt/Al_2O_3$ catalyst. This may be compared to 120 °C for the Pt/Al_2O_3 catalyst and 80 °C for the Pt/CeO_2 The 4 $CeO_x/Pt/Al_2O_3$ is the most active catalyst and has a T_{50} value of 69 °C for $X_{CO} = 0.33$. The CO conversion plot for the 4 $CeO_x/Pt/Al_2O_3$ is more like that for the Pt/CeO_2 catalyst in appearance as with a more gradual increase in CO conversion with increasing temperature than the intense light off feature associated with Pt/Al_2O_3. However, the CO conversion plots for the 4 $CeO_x/Pt/Al_2O_3$ catalyst are absent of any CO conversion at temperatures lower than 20 °C, as exhibited by the Pt/CeO_2 catalyst.

By performing the experiments in a large excess of O_2 (air) relative to CO, the concentration of O_2 can be assumed to be constant despite the conversion of CO to CO_2. Thus, plots (figure 15) of Log rate against Log mole fraction CO, can be

used to calculate the reaction orders with respect to CO. Due to the sharp light off feature in the CO conversion plot for the Pt/Al_2O_3 catalyst and the conversion at low temperatures for the Pt/CeO_2 catalyst there were no suitable points to choose for the reaction order assessment.

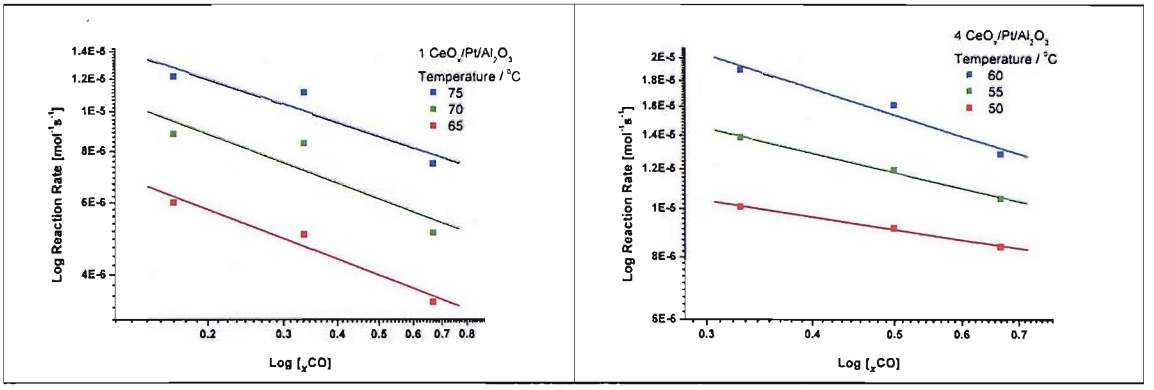

Figure 15 **Plots to determine the reaction order for the CO oxidation with respect to CO for 1 $CeO_x/Pt/Al_2O_3$ and 4 $CeO_x/Pt/Al_2O_3$.**

The reaction orders determined for 1 $CeO_x/Pt/Al_2O_3$ and 4 $CeO_x/Pt/Al_2O_3$ are -0.27 to -0.40 and -0.27 to -0.54, respectively. The reaction order for CO oxidation with respect to CO for unmodified Pt/Al_2O_3 catalysts has been reported as -1, over the temperature range used in these experiments [25]. Thus, a decrease in the reaction order with respect to CO for the $CeO_x/Pt/Al_2O_3$ catalysts is observed in comparison to unmodified Pt/Al_2O_3. A change in reaction order indicates a change in the reaction mechanism. The partial negative reaction orders reported here are similar to those for the $Pt/CeO_2/Al_2O_3$ catalysts reported elsewhere [25]. As the change in reaction order is the same for the $Pt/CeO_2/Al_2O_3$ catalysts it can be inferred that the reaction mechanism is the same when CeO_2 is present at the surface or as part of mixed oxide support. However, the change in reaction order observed is also indicative of the CeO_x and Pt components being in close proximity to each other.

4 Conclusions

The controlled surface modification of Pt/Al_2O_3 using the $Ce(acac)_3 \cdot H_2O$ precursor is successful in creating catalysts which exhibit good activity towards the WGS and CO oxidation reactions. The characterisation of the catalysts establishes an ambiguous picture of their overall structure. The control reactions illustrate that the reaction will proceed on the Al_2O_3 support in the absence of Pt, but not on a carbon support. It is proposed that the reason for this reaction between the Ce precursor and the alumina is the reducibility of the alumina support. The TEM is unable to produce a clear picture of the co-locality of the different components in the system. This is not aided by the low proportions of Ce present and the small particle size of the Pt catalysts. There is substantial anecdotal evidence in the form of the XANES characterisation and WGS and CO oxidation activities that the Ce is in close proximity of the Pt. The XANES analysis of the data obtained in air, H_2, and CO showed there was a substantial proportion of Ce(III) present in the catalyst. The XANES spectra in the same gas environments for the CeO_x/Al_2O_3 catalyst showed no reduction of Ce(IV). This is confirmation that the Pt is facilitating the reduction of Ce(IV) to Ce(III). It is expected that the Pt and Ce sites would need to be in close proximity to one another for this effect to be observed. The change in reaction order with respect to CO observed for the oxidation of CO for the $CeO_x/Pt/Al_2O_3$ catalysts is also consistent with Pt and Ce sites being in close proximity.

The performance of the catalysts towards the WGS reaction, although encouraging, do not have the same level of performance as conventional Pt/CeO_2 catalysts. As the Ce loading was increased the performance of the $CeO_x/Pt/Al_2O_3$ catalysts improved. However, the Ce saturated, 8 $CeO_x/Pt/Al_2O_3$ was unable to be tested as access to the rig was not possible at the point of time this catalyst was prepared. It is unclear whether the activity of this catalyst would be close to that of Pt/CeO_2. It is believed that further tailoring of the catalysts in the form of using mixed oxide supports, and additional alloying components with Pt could increase the activity still further.

Despite not attaining the same level of performance as conventional Pt/CeO_2 catalysts it is believed that the work carried out on the $CeO_x/Pt/Al_2O_3$ catalysts offers valuable mechanistic information pertaining to the WGS reaction. It is believed that the performances of the $CeO_x/Pt/Al_2O_3$ catalysts are consistent with the formate mechanism, assuming that on addition of four equivalent monolayers of CeO_x there are more Ce surface sites than Pt surface sites. With an excess of Ce sites available it unlikely that an increase in performance will be observed following the surface redox mechanism, as it is reliant upon the presence of both Ce and Pt surface sites. Thus, the improved WGS activity observed on increasing the Ce loading, reported in this work, is consistent with the formate mechanism.

5 References

1. Ladebeck, J.R. and J.P. Wagner, *Chapter 16: Catalyst Development for Water Gas Shift*, in *Handbook of Fuel Cells - Volume 3: Fuel cell technology and applications*. 2003, John Wiley & Sons.
2. Farrauto, R., S. Hwang, L. Shore, and W. Ruettinger, Ann. Rev. Mater. Res., 2003. **33**: p. 1.
3. Ghenciu, A.F., Current opinion in solid state and materials science, 2002. **6**: p. 389.
4. Choung, S.Y., M. Ferrandon, and T. Krause, Catal. Today, 2005. **99**(3-4): p. 257.
5. Shido, T. and Y. Iwasawa, J. Catal., 1993. **141**(1): p. 71.
6. Shido, T. and Y. Iwasawa, J. Catal., 1992. **136**(2): p. 493.
7. Jacobs, G., E. Chenu, P.M. Patterson, L. Williams, D. Sparks, G. Thomas, and B.H. Davis, Appl. Catal. A-Gen., 2004. **258**(2): p. 203.
8. Jacobs, G., L. Williams, U. Graham, G.A. Thomas, D.E. Sparks, and B.H. Davis, Appl. Catal. A-Gen., 2003. **252**(1): p. 107.
9. Jacobs, G., P.M. Patterson, L. Williams, E. Chenu, D. Sparks, G. Thomas, and B.H. Davis, Appl. Catal. A-Gen., 2004. **262**(2): p. 177.
10. Jacobs, G., P.M. Patterson, U.M. Graham, A.C. Crawford, and B.H. Davis, International Journal of Hydrogen Energy, 2005. **30**(11): p. 1265.

11. Jacobs, G., P.A. Patterson, U.M. Graham, D.E. Sparks, and B.H. Davis, Appl. Catal. A-Gen., 2004. **269**(1-2): p. 63.
12. Jacobs, G., S. Khalid, P.M. Patterson, D.E. Sparks, and B.H. Davis, Appl. Catal. A-Gen., 2004. **268**(1-2): p. 255.
13. Jacobs, G., U.M. Graham, E. Chenu, P.M. Patterson, A. Dozier, and B.H. Davis, J. Catal., 2005. **229**(2): p. 499.
14. Jacobs, G. and B.H. Davis, Appl. Catal. A-Gen., 2005. **284**(1-2): p. 31.
15. Jacobs, G., A.C. Crawford, and B.H. Davis, Catal. Lett., 2005. **100**(3-4): p. 147.
16. Jacobs, G., A. Crawford, L. Williams, P.M. Patterson, and B.H. Davis, Appl. Catal. A-Gen., 2004. **267**(1-2): p. 27.
17. Jacobs, G., L. Williams, U. Graham, D. Sparks, and B.H. Davis, J. Phys. Chem. B, 2003. **107**(38): p. 10398.
18. Hilaire, S., X. Wang, T. Luo, and R.J. Gorte, Appl. Catal. A-Gen., 2001. **215**: p. 271.
19. Gorte, R.J. and S. Zhao, Catal. Today, 2005. **104**(1): p. 18.
20. Bunluesin, T., R.J. Gorte, and G.W. Graham, Appl. Catal. B-Environ., 1998. **15**(1-2): p. 107.
21. Li, Y. and Q. FU, Appl. Catal. B-Environ., 2000. **27**: p. 179.
22. Goguet, A., S.O. Shekhtman, R. Burch, C. Hardacre, E. Meunier, and G.S. Yablonsky, J. Catal., 2006. **237**(1): p. 102.
23. Schumacher, B., Y. Denkwitz, V. Plzak, M. Kinne, and R.J. Behm, J. Catal., 2004. **224**: p. 449.
24. Schubert, M.M., M.J. Kahlich, H.A. Gasteiger, and R.J. Behm, J. Power Sources, 1999. **84**: p. 175.
25. Oran, U. and D. Uner, Appl. Catal. B-Environ., 2004. **54**(3): p. 183.
26. Kahlich, M.J., H.A. Gasteiger, and R.J. Behm, J. Catal., 1998. **182**: p. 430.
27. Goguet, A., F. Meunier, J.P. Breen, R. Burch, M.I. Petch, and A.F. Ghenciu, J. Catal., 2004. **226**(2): p. 382.
28. Fu, L., N.Q. Wu, J.H. Yang, F. Qu, D.L. Johnson, M.C. Kung, H.H. Kung, and V.P. Dravid, J. Phys. Chem. B, 2005. **109**(9): p. 3704.

29. Navarro, R.M., M.C. Alvarez-Galvan, M.C. Sanchez-Sanchez, F. Rosa, and J.L.G. Fierro, Appl. Catal. B-Environ., 2005. **55**(4): p. 229.
30. Kolb, G., H. Pennemann, and R. Zapf, Catal. Today, 2005. **110**(1-2): p. 121.
31. Germani, G., P. Alphonse, M. Courty, Y. Schuurman, and C. Mirodatos, Catal. Today, 2005. **110**(1-2): p. 114.
32. Crabb, E.M. and R. Marshall, Appl. Catal. A-Gen., 2001. **217**(1-2): p. 41.
33. Fonda, E., D. Andreatta, P.E. Colavita, and G. Vlaic, J. Synchrot. Radiat., 1999. **6**: p. 34.
34. Shahin, A.M., T.P. Schuman, F. Grandjean, and G.J. Long, Abstr. Pap. Am. Chem. Soc., 2004. **228**: p. 133.
35. Shahin, A.M., F. Grandjean, G.J. Long, and T.P. Schuman, Chem. Mat., 2005. **17**(2): p. 315.
36. Elfallah, J., S. Boujana, H. Dexpert, A. Kiennemann, J. Majerus, O. Touret, F. Villain, and F. Lenormand, J. Phys. Chem., 1994. **98**(21): p. 5522.
37. Balasubramanian, M., C.A. Melendres, and A.N. Mansour, Thin Solid Films, 1999. **347**(1-2): p. 178.

Chapter Six: Conclusions and Further work

The principle aim of this project was to use the controlled surface modification procedure developed by Crabb *et al.* [1-5] to prepare model catalytic systems to facilitate a better understanding of processes pertinent to the development of PEMFC technology. The catalysts have primarily been characterised using electrochemical and XAS techniques.

Chapter 3 detailed the preparation of Cr and Co modified Pt/C catalysts. The characterisation of the catalysts found that the secondary metal component was targeting the Pt sites, but additional heat treatments were required to form an alloy. The oxygen reduction testing performed using the RDE found that only the catalysts containing the Pt_3M phase exhibited the 2 to 3 fold enhancement reported for PtCr/C and PtCo/C catalysts. Thus, the presence of unalloyed Cr or Co at the surface does not improve the performance of Pt/C catalysts towards the ORR. Additional work should investigate the heat treatment required to form the alloy phase. It would be of interest to confine the alloy phase to as close to the surface as possible and see if the enhancements observed for a Pt_3M phase can be maintained.

Pt modified Pd/C and Pd modified Pt/C samples were detailed in chapter 4, with the main focus of the research on the Pt/Pd/C system. The intention behind the work was to retain/enhance the catalytic properties of Pt, whilst reducing the Pt loading by placing it on the surface of a cheaper core metal. The mass activities reported were less than that of the Pt/C standard tested as a comparison. The characterisation is mainly supportive that the Pt is predominantly on the exterior of the particle. Further studies should involve the modification of much larger Pd core nanoparticles than those used in this study. The Pd particles used in this study were ~ 2 nm diameter in size and did not facilitate a pronounced decrease in the Pt loading as is desired.

Chapter 5 details the preparation of $CeO_x/Pt/Al_2O_3$ catalysts for the WGS reaction. The XANES studies carried out indicated that the presence of Pt facilitates the reduction of Ce(IV) to Ce(III) in atmospheres of air, H_2, and CO. The activities of these catalysts are far superior to the unmodified Pt/Al_2O_3 catalyst, but fail to attain the same performance offered by Pt/CeO_2. It is believed that $CeO_x/Pt/Al_2O_3$ catalysts offer valuable mechanistic information about the WGS reaction for Pt/CeO_2 systems under these conditions. It is proposed that the improved performance of the catalysts on increasing the CeO_x content is consistent with the formate mechanism. The $CeO_x/Pt/Al_2O_3$ catalysts should offer improved stability in comparison to the Pt/CeO_2 system with further catalyst testing and lifetime studies required to support this claim.

The use of the controlled surface modification procedure has branched away from its origins of using simple alkyl-metal compounds [3, 4] and has progressed to the use of metallocenes [1] and acac complexes. The reaction was initially believed to proceed by the physisorption of the organometallic precursor onto the pre-reduced metal surface, followed by cleavage of the organic fragment on further heating under an atmosphere of hydrogen. The cleavage of the organic fragment for the metallocene and alkyl compounds was followed using gas chromatography [3, 4, 6]. However, such methods have not been used to gain an insight into the reaction that occurs when using the acac complexes. Additional studies into the reaction mechanism for the controlled surface modification procedure would prove beneficial and improve the understanding of interaction between the organometallic precursor and the unmodified platinum catalyst.

References

1. Crabb, E.M., M.K. Ravikumar, D. Thompsett, M. Hurford, A. Rose, and A.E. Russell, Phys. Chem. Chem. Phys., 2004. **6**(8): p. 1792.
2. Crabb, E.M., M.K. Ravikumar, Y. Qian, A.E. Russell, S. Maniguet, J. Yao, D. Thompsett, M. Hurford, and S.C. Ball, Electrochem. Solid State Lett., 2002. **5**(1): p. A5.

3. Crabb, E.M. and M.K. Ravikumar, Electrochim. Acta, 2001. **46**(7): p. 1033.
4. Crabb, E.M., R. Marshall, and D. Thompsett, J. Electrochem. Soc., 2000. **147**(12): p. 4440.
5. Crabb, E.M. and R. Marshall, Appl. Catal. A-Gen., 2001. **217**(1-2): p. 41.
6. Qian, Y., Preparation of Platinum based bimetallic catalysts for the oxygen reduction reaction for PEM fuel cells, PhD Thesis, 2004, The Open University